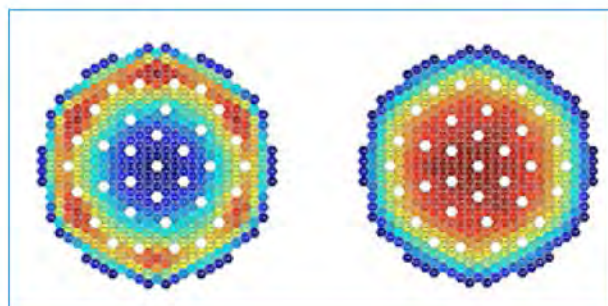
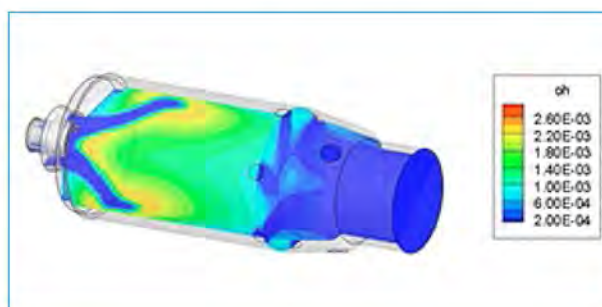
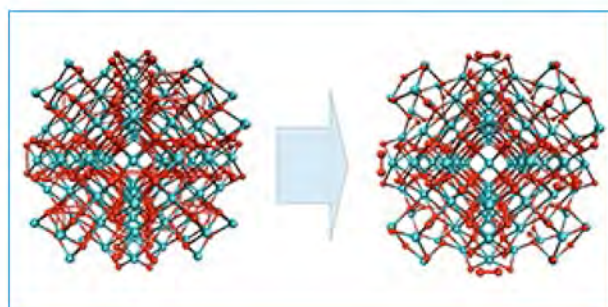
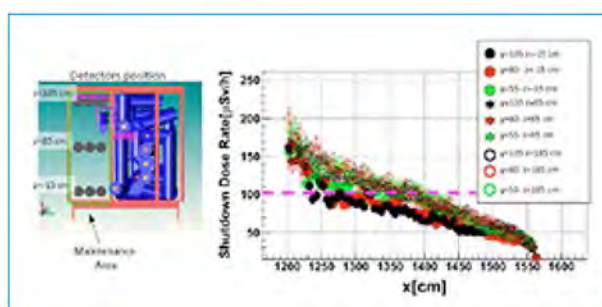
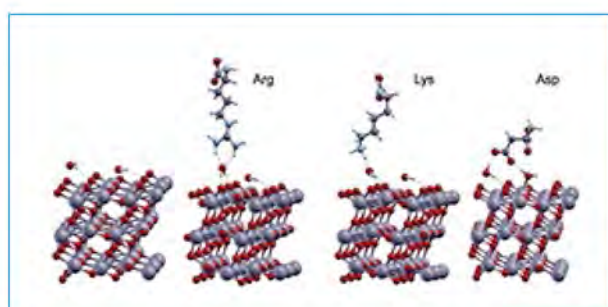


# High Performance Computing on CRESCO infrastructure: research activities and results 2013



Contributions provided by a selection of users of the CRESCO infrastructure.

Scientific Editor: *Agostino Funel*, ENEA, UTICT-HPC, CR Portici

Acknowledgements: We wish to thank *Daniela Alderuccio* and *Filippo Palombi* who contributed to the editing of this Report.

Cover: *Amedeo Trolese*, ENEA, UTICT-PRA, CR Frascati

ISBN: 978-88-8286-312-8

## Contents

<b>Foreword</b>	<b>6</b>
<b>The ideal tensile strength of tungsten and tungsten-rhenium alloy by first-principles calculations</b>	<b>7</b>
<i>S. Giusepponi, M. Celino</i>	
<b>Structure of metal dioxide nanoparticles and investigation on the origin of their structural disorder</b>	<b>13</b>
<i>R. Grena</i>	
<b>Ab-initio modeling of methane adsorption at Ca impurities on a carbon nanotube side-wall</b>	<b>17</b>
<i>F. Gala, G. Zollo</i>	
<b>A Generalized Turbulent Combustion Model for Large Eddy Simulation of Turbulent Premixed Flames</b>	<b>32</b>
<i>E. Giacomazzi, D. Cecere, F. R. Picchia, N. M. Arcidiacono</i>	
<b>Modelling the exchange flow dynamics through the Turkish Strait System</b>	<b>37</b>
<i>G. Sannino, A. Sözer, E. Özsoy</i>	
<b>Voting Dynamics as an Open Problem in Non-equilibrium Statistical Mechanics</b>	<b>42</b>
<i>F. Palombi, S. Toti</i>	
<b>Benchmark of the CPMD code on the CRESCO clusters in ENEA-GRID environment</b>	<b>49</b>
<i>R. Vujasin, J. G. Novakovic, N. Novakovic, S. Giusepponi</i>	
<b>Activities made by the MoLNaC (Molecular Lab for Nanomaterials and Catalysis)</b>	<b>56</b>
<i>L. Cavallo, G. Milano, A. Correa, R. Credendino, M. Byskin, A. De Nicola, F. Ragone, L. Falivene, A. Pizzirusso, A. Poater</i>	
<b>Simulation of the adsorption mechanism of titanium-binding peptide to TiO<sub>2</sub> anatase surface</b>	<b>61</b>
<i>L. Agosta, C. Arcangeli, F. Buonocore, M. Celino, F. Gala, G. Zollo</i>	
<b>CFD investigation of advanced cooling techniques in gas turbine blades</b>	<b>67</b>
<i>D. Borrello, F. Rispoli, P. Venturini, A. Salvagni</i>	
<b>Direct Numerical Simulation of a premixed CH<sub>4</sub>/H<sub>2</sub> – Air slot flame</b>	<b>72</b>
<i>D. Cecere, E. Giacomazzi, F. R. Picchia, N. Arcidiacono</i>	

<b>Nuclear Analysis of the ITER Cryopump Ports</b>	<b>80</b>
<i>F. Moro, R. Villari, D. Flammini, S. Podda</i>	
<b>Structural and energetical analysis of a prismatic cadmium sulfide nanocluster</b>	<b>86</b>
<i>E. Burresi, M. Celino</i>	
<b>First principles study of the stability of Graphane deposited on a copper surface using QUANTUM-ESPRESSO on CRESCO HPC</b>	<b>91</b>
<i>F. Buonocore</i>	
<b>First-principle study of amorphous germanium under pressure</b>	<b>97</b>
<i>G. Mancini, M. Celino, A. Di Cicco</i>	
<b>Icosahedral structure and mean-square displacement in Cu<sub>64</sub>Zr<sub>36</sub> metallic glass</b>	<b>106</b>
<i>J. Zemp, M. Celino, J. F. Löffler, B. Schönfeld</i>	
<b>Particle simulation of Alfvén mode dynamics in nuclear fusion devices</b>	<b>112</b>
<i>S. Briguglio, G. Fogaccia, G. Vlad, X. Wang</i>	
<b>Structural, electronic and optical properties of low dimensional systems</b>	<b>117</b>
<i>A. Mosca Conte, C. Violante, V. Garbuio, I. Kupchak, M. Marsili, P. Gori, O. Pulci</i>	
<b>Validation of the Monte Carlo model of TAPIRO Fast Reactor using MC-NPX on ENEA-GRID/CRESCO facility</b>	<b>122</b>
<i>N. Burgio, A. Santagata, M. Frullini</i>	
<b>Benchmark performances of CRESCO4 HPC system</b>	<b>129</b>
<i>F. Ambrosino, A. Funel, S. Giusepponi, G. Guarnieri, G. Ponti</i>	
<b>The new ENEA CRESCO3 and CRESCO4 HPC systems</b>	<b>144</b>
<i>F. Ambrosino, G. Bracco, A. Colavincenzo, A. Funel, G. Guarnieri, B. Mastroianni, S. Migliori, G. Ponti</i>	
<b>Progress on Inertial Confinement Fusion studies</b>	<b>152</b>
<i>A. Schiavi, A. Marocchino, S. Atzeni</i>	
<b>Application of the MINNI Atmospheric Model System (AMS) at high resolution over Italy</b>	<b>155</b>
<i>M. Adani, G. Briganti, A. Cappelletti, M. D'Isidoro, M. Mircea, L. Vitali</i>	
<b>Electronic properties at complex interfaces</b>	<b>163</b>
<i>G. Cantele, D. Ninno, R. N. D'Amico</i>	

<b>Dynamical Downscaling of GCM Seasonal Forecasts over the Greater Horn of Africa</b>	<b>168</b>
<i>S. Calmanti, M. V. Struglia</i>	
<b>Synchronization phenomena in complex networks</b>	<b>174</b>
<i>J.A. Almendral, S. Boccaletti, R. Gutiérrez, I. Leyva, J. M. Buld, A. Navas, I. Sendiña-Nadal</i>	
<b>Use of Monte Carlo to Evaluate Signal and Radiation Damage to Corium Detector in PWR Severe Accident Scenario</b>	<b>179</b>
<i>K. W. Burn</i>	
<b>Boosting conformational sampling in lipid bilayer simulations using Hamiltonian Replica Exchange</b>	<b>183</b>
<i>C. Cardelli, A. Barducci, P. Procacci</i>	
<b>Nuclear Analysis for ITER TBM PORT #16</b>	<b>192</b>
<i>B. Caiffi, R. Villari</i>	
<b>Simulation of a Square Boiling Channel Using NEPTUNE_CFD</b>	<b>198</b>
<i>A. Cervone</i>	
<b>CFD testing of a conventional gas turbine burner operating in oxy-fuel combustion</b>	<b>203</b>
<i>G. Calchetti, A. Di Nardo</i>	
<b>Contributions to CRESCO Annual Report 2013</b>	<b>208</b>
<i>F. Paglia, D. Schiariti</i>	
<b>Sodium fast reactor core design using MCNPX<sup>TM</sup> code and CRESCO HPC infrastructure</b>	<b>212</b>
<i>C. Parisi, G. Abbate, B. Fresilli</i>	
<b>Hydrogen diffusion in rutile TiO<sub>2</sub></b>	<b>217</b>
<i>R. Vujasin, J. G. Novaković, S. Giusepponi, N. Novaković</i>	
<b>CeO<sub>2</sub> electronic properties from first principles: an introductory study</b>	<b>223</b>
<i>F. Rizzo, G. de Marzi, L. Morici</i>	
<b>Magneto-Thermo-Structural optimization of the Large-Bore 8T Superconducting Magnet for the Nafassy Test Facility</b>	<b>229</b>
<i>G. Tomassetti, M. Perrella, A. Anemona, V. Corato, A. della Corte</i>	

## Foreword

During the year 2013 CRESCO high performance computing clusters have provided more than 27 million hours of "core" computing time, at a high availability rate, to more than one hundred users, supporting ENEA research and development activities in many relevant scientific and technological domains. In the framework of joint programs with ENEA researchers and technologists, computational services have been provided also to academic and industrial communities.

This report, the fifth of a series started in 2008, is a collection of papers illustrating the main results obtained during 2013 using CRESCO HPC facilities in various fields as material science, computational fluid dynamics, climate research, nuclear technology, plasma physics, complex system physics and biophysics. The report shows the variety of the applications of high performance computing, which has become an enabling technology for science and engineering.

ENEA Portici Research Centre near Naples is the location hosting the main ENEA computational resources since 2008. This is a result of the CRESCO Project (Computational Centre for Research on Complex Systems), co-funded, in the framework of the 2001-2006 European Regional Development Funds Program by the Italian Ministry of Education, University and Research (MIUR).

The Project CRESCO provided the resources to set up the first HPC x86\_64 Linux cluster in ENEA, achieving a computing power relevant on Italian national scale (it ranked 126 in the HPC Top 500 June 2008 world list, with 17.1 TFlops and 2504 CPU cores). It was later decided to keep CRESCO as the signature name for all the Linux clusters in the ENEAGRID infrastructure which integrates all ENEA scientific computing systems, and is currently distributed in six Italian sites.

In 2013 the ENEAGRID computational resources attained the level of 6000 computing cores (in production) and other 5000 in the final test phase. The raw data storage reached 900 TB. Both values show an increase of factor 3 in respect to the past and the increase was made possible by various projects, LAMRECOR, IT@CHA, TEDAT and VIS4FACTORY - funded by MIUR in the framework of the 2007-2013 European Regional Development Funds Program. More specifically, in 2013 the cluster CRESCO3, 2016 AMD cores, was opened to users and a new cluster CRESCO4, 4864 Intel cores, 100 TFlops peak, was installed and certified, being ready for service in 2014.

The success and the quality of the results produced by CRESCO stress the role that HPC facilities can play in supporting science and technology for all ENEA activities, national and international collaborations, and the ongoing renewal of the infrastructure provides the basis for a similar role in the forthcoming years.

Unità Tecnica Sviluppo Sistemi per l'Informatica e l'ICT  
Il Gruppo di Lavoro CRESCO

# The ideal tensile strength of tungsten and tungsten-rhenium alloy by first-principles calculations

*Simone Giusepponi<sup>1\*</sup>, Massimo Celino<sup>2</sup>*

<sup>1</sup>*ENEA, UTITC-HPC C.R. Casaccia  
Via Anguillarese 301, 00123 Rome, Italy*

<sup>2</sup>*ENEA, UTMAT-DIAG C.R. Casaccia  
Via Anguillarese 301, 00123 Rome, Italy*

**ABSTRACT.** Both mechanical and structural properties of bcc crystal tungsten in presence of different concentrations of rhenium substitutional defects has been investigated by using accurate first-principles total energy methods based on density functional theory.

## 1 Introduction

There is a widespread consensus in considering tungsten (W) and W alloys as good candidates for structural and shield material in the future nuclear fusion reactors [1, 2]. Indeed W alloys are characterized by thermal properties, such as good thermal conductivity, high melting temperature and low sputtering erosion, of great interest in fusion applications. The main requirement on tungsten materials for structural applications is to be ductile within the operation temperature range. An armor material needs high crack resistance under extreme thermal operation conditions [3, 4] and compatibility with plasma-wall interaction phenomena [5].

Thus a deep understanding of the mechanical properties of W and of their atomic-scale modifications in presence of impurities is unavoidable step for the use of W under extreme conditions. In this framework, the determination of the ideal tensile strength, that is an inherent property of materials, can help to identify those aspects of mechanical behavior that are tightly linked to crystal structure and bonding. However, the ideal tensile strength represents the stress at the elastic instability, thus only an upper limit to the yield strength in real materials mainly affected by the complex interplay of defects, such as dislocations and cracks.

---

\*Corresponding author. E-mail: [simone.giusepponi@enea.it](mailto:simone.giusepponi@enea.it).

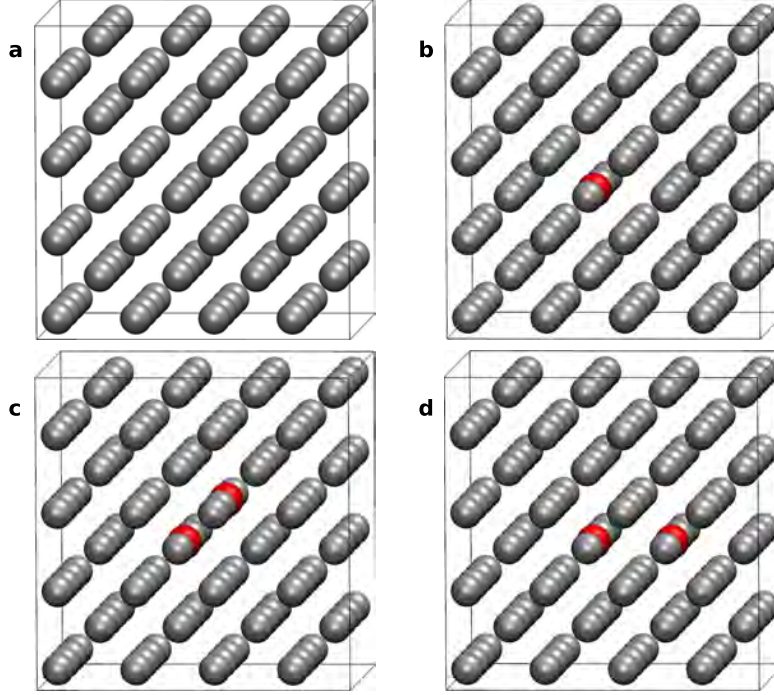


Figure 1: Simulation cell of the crystalline structure, tungsten atoms are the gray spheres, rhenium atoms are the red spheres: a) crystalline tungsten b) one substitutional Re atom; c) two 1NN substitutional Re atoms; d) two 2NN substitutional Re atoms.

## 2 Computational details

The first-principles PWscf (Plane-Wave Self-Consistent Field) code of the Quantum Espresso suite has been used [6, 7] to accurately characterize W properties. PWscf performs many different kinds of self-consistent calculations of electronic-structure properties within Density-Functional Theory (DFT), using a Plane-Wave (PW) basis set and pseudopotentials (PP) [8, 9]. A reliable physical model for W has been developed to accurately compute lattice parameters, bulk modulus, enthalpy of atomization and ideal tensile strengths of W and W alloy with different concentrations of Re. We used the W and Re Goedecker norm-conserving pseudopotentials [10, 11, 12] with Perdew-Burke-Ernzerhof (PBE) [13] approximating GGA exchange–correlation potential, available in the Quantum Espresso library [7]. 6 and 7 electrons are explicitly taken into account in the wave functions for tungsten and rhenium atoms respectively. All the calculations are performed in the supercell approximation with periodic boundary conditions meant to mimic an infinitely extended system. We considered a cubic supercell composed by a  $4 \times 4 \times 4$  array of bcc conventional cells and 128 W atoms. The electronic wave functions were expanded in a plane-wave basis set with a kinetic energy cut-off equal to 80 Ry and a  $3 \times 3 \times 3$  Monkhorst-Pack mesh of  $k$  points was employed [14]. We used Marzari-Vanderbilt smearing [15] with a width of 0.008 Ry. The kinetic energy cut-off, the  $k$  sampling and the smearing width were optimized by preliminary calculations on tungsten and rhenium pseudopotentials.



As shown in Fig.1, the role of rhenium substitutional defect in tungsten bulk is investigated removing one and two W atoms respectively.

Thus we considered four systems:

- a) Tungsten without defects: a supercell of 128 W atoms (Fig. 1a);
- b) One substitutional defect case: a supercell of 127 W atoms in which a W atom is replaced with one Re atom (Fig. 1b);
- c) Two substitutional defects 1NN case: a supercell of 126 W atoms in which a couple of first-nearest-neighbor (1NN) W atoms are replaced with two Re atoms (Fig. 1c). The replaced atoms are in the  $[1\ 1\ 1]$  direction at distance  $\frac{\sqrt{3}}{2}a_0$ ;
- d) Two substitutional defects 2NN case: a supercell of 126 W atoms in which a couple of second-nearest-neighbor (2NN) W atoms are replaced with two Re atoms (Fig. 1d). The replaced atoms are in the  $[1\ 0\ 0]$  direction at distance  $a_0$ .

$a_0$  is the lattice constant of the W bcc crystal structure at zero temperature and zero loading.

By using first-principles zero-temperature total energy calculations we computed lattice constant  $a$ , bulk modulus  $B$ , enthalpy of atomization  $H_a$  as described in Ref. [16]. Moreover, repeating the procedure used in Ref. [16], we calculated the ideal tensile strength  $\sigma_m$  plotting the energy per atom  $E - E_0$  versus strain  $\epsilon$  (see Fig. 2), where  $E_0$  is the ground-state energy of the unloaded material.  $E$  is the total energy of the loaded system in the relaxed condition. The relaxed condition for the crystalline structure is achieved when, after elongation along the loading axis by a fixed amount  $\epsilon$  (unrelaxed condition), except that in the tensile direction (relaxed condition) all the others components of the stress tensor vanish. This procedure is adopted for the test-cases to ensure optimal uniaxial loading.

This approach was repeated for bcc tungsten and for tungsten with different concentration of rhenium, to obtain the total energy-strain relations shown in the Fig. 2. The ideal tensile strength  $\sigma_m$  corresponds to the maximum of the stress-strain relation, and it is related to the inflexion point in the total energy-strain relation. We fitted total energy-strain relation with a polynomial cubic function to determine its inflexion point (by vanishing of the second order derivative) corresponding to the the strain  $\epsilon_m$ , and then the  $\sigma_m$  value. The behavior of the energy per atom  $E - E_0$  versus  $\epsilon$  along the loading axis is shown in Fig. 2. Green symbols are the energies in unrelaxed conditions, black symbols are the energies in relaxed conditions and black solid lines are the cubic fitting functions.

## 2.1 Results and discussion

The calculated equilibrium lattice parameter for bcc W is  $a_0 = 3.23\ \text{\AA}$  and the calculation for the bulk modulus gives  $B = 282.2\ \text{GPa}$ . The enthalpy of atomization is  $H_a = 882.9\ \text{kJ/mol}$  and the values of the ideal tensile strength and related strain in the  $[0\ 0\ 1]$  direction are  $\sigma_m = 26.34\ \text{GPa}$  and  $\epsilon_m = 13.6\%$  respectively. The full set of our results

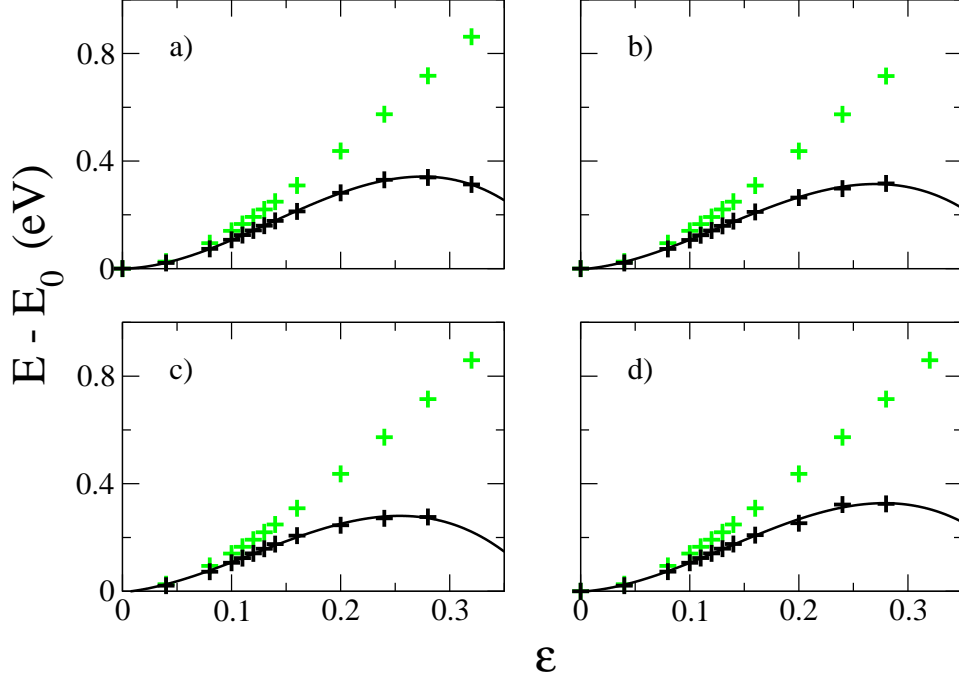


Figure 2: Total energy  $E - E_0$  per atom versus strain  $\epsilon$  for uniaxial deformation: a) crystalline tungsten; b) one substitutional Re atom; c) two 1NN substitutional Re atoms; d) two 2NN substitutional Re atoms.  $E_0$  is the ground-state energy of the systems. Energies for unrelaxed conditions are shown in green symbols, those for relaxed conditions are shown in black symbols. Solid lines are the fitting functions.

for tungsten are reported in the first row of the Table 1. Having checked the reliability of our numerical model, we study the structural and mechanical properties of tungsten with different concentrations of rhenium to understand their effects on bulk properties.

In all the considered cases the substitution of tungsten atoms with rhenium atoms does not cause variation in the sizes of the systems. The value of the lattice parameter remains the same  $a_0 = 3.23 \text{ \AA}$ . The enthalpy of atomization is slightly influenced by the point defects, the values of  $H_a$  are in the range 882.9-883.4 kJ/mol. However, we observe an increase of  $H_a$  with the number of substituted atoms. On the contrary the presence of substitutional defects affects the values of bulk modulus  $B$ , ideal tensile strength  $\sigma_m$  and related strain  $\epsilon_m$ .

In the case b) in which a single W atom is replaced with a Re atom, the bulk modulus  $B$  is reduced of about 0.2%: from 282.4 GPa for pure W system to 281.8 GPa. We also observe a decrease of about 1.3% in the ideal tensile strength  $\sigma_m$ : from 26.34 to 26.01 GPa. The results are reported in the second row of the Table 1. The behavior of the energy per atom versus strain along the crystallographic axis  $[0\ 0\ 1]$  is shown in Fig. 2b.

When two first neighbours W atoms are removed in  $[1\ 1\ 1]$  direction to create the 1NN substitutional Re atoms cluster, the reduction of the bulk modulus  $B$  from 282.4 to 281.4 GPa is raised with a decrease of about 0.35% (see third row of the Table 1). Also the reduction

Table 1: Calculated values of lattice parameter  $a$ , bulk modulus  $B$ , enthalpy of atomization  $H_a$ , ideal tensile strength  $\sigma_m$  and related strain  $\epsilon_m$  for the four systems of Fig. 1.

system	$a$ (Å)	$B$ (GPa)	$H_a$ (kJ/mol)	$\sigma_m$ (GPa)	$\epsilon_m$ (%)
a)	3.23	282.4	882.9	26.34	13.6
b)	3.23	281.8	883.2	26.01	12.9
c)	3.23	281.4	883.3	25.62	11.9
d)	3.23	281.4	883.4	25.68	11.5

of the ideal tensile strength  $\sigma_m$  is valuable of consideration: from 26.34 to 25.62 GPa (about 2.7%). In Fig. 2c it is shown the dependence of the energy versus the strain along the crystallographic axis  $[0\ 0\ 1]$ .

The final case is when we remove two W atoms in  $[1\ 0\ 0]$  direction to have the 2NN substitutional Re atoms cluster. The value of the bulk modulus  $B=281.4$  GPa is the same as that of the 1NN substitutional Re atoms case. Also the ideal tensile strength  $\sigma_m=25.68$  GPa is close to the previous case with a decrease of about 2.5% compared to the tungsten system without point defects (see fourth row of the Table 1). In Fig. 2d it is shown the dependence of the energy versus the strain along the crystallographic axis  $[0\ 0\ 1]$ .

In conclusion the substitution of tungsten atoms with rhenium atoms causes a variation in the mechanical properties of the material. The reduction in the values of the bulk modulus  $B$  are less than 0.5%, more evident are the decreases in the values of the ideal tensile strength  $\sigma_m$  that are in the range 1.3-2.7%. Moreover, it is interesting to note the linear increase of the value of the variations with the number of substituted atoms.

## References

- [1] Rieth M. *et al.* J. Nuc. Mater. 442 (2013) S173.
- [2] Rieth M. *et al.* J. Nuc. Mater. 432 (2013) 482.
- [3] Wittlich K. *et al.* Fusion Eng. Des. 84 (2009) 1982.
- [4] Hirai T., Pintsuk G., Linke J., Batilliot M. J. Nucl. Mater. 390-391 (2009) 751.
- [5] Roth J. *et al.* J. Nucl. Mater. 390-391 (2009) 1.
- [6] Giannozzi P. *et al.* J. Phys.: Condens. Matter. 21 (2009) 395502.
- [7] [www.quantum-espresso.org](http://www.quantum-espresso.org)
- [8] Hohenberg P., Kohn W. Phys. Rev. 136 (1964) B864.

- [9] Kohn W., Sham L. J. Phys. Rev. 140 (1965) A1133.
- [10] Goedecker S., Teter M., Hutter J. Phys. Rev. B 54 (1996) 1703.
- [11] Hartwigsen C., Goedecker S., Hutter J. Phys. Rev. B 58, (1998) 3641.
- [12] Krack M. Theor. Chem. Acc. 114 (2005) 145.
- [13] Perdew J. P., Burke K., Ernzerhof M. Phys. Rev. Lett. 77 (1996) 3865.
- [14] Monkhorst H. J., Pack J. D. Phys. Rev. B 13 (1976) 5188.
- [15] Marzari N., Vanderbilt D., De Vita A., Payne M. C. Phys. Rev. Lett. 82 (1999) 3296
- [16] Giusepponi S., Celino M. J. Nucl. Mater. 435 (2013) 52.

# Structure of metal dioxide nanoparticles and investigation on the origin of their structural disorder

*Roberto Grena\**

*ENEA UTRINN-PCI C. R. Casaccia,  
Via Anguillarese 301, 00123 Rome (Italy)*

**ABSTRACT.** The structure of nanoparticles with a diameter around 2 nm of three metal dioxides ( $\text{TiO}_2$ ,  $\text{ZrO}_2$ ,  $\text{CeO}_2$ ) is investigated, checking two hypotheses for the different levels of structural disorder found in the three nanoclusters.

## 1 Introduction

Metal dioxide nanoparticles attracted much interest due to studies and applications in various fields, such as electronics, energy generation, use as additives in nanofluids or other materials, and study of their biological effects. However, the structure of oxide nanoclusters of size lower than few nanometers remains elusive. Beside the complex polymorphism often shown by bulk metal dioxides, another cause of difficulties is the unusual form of structural disorder that can appear below a certain size, and substantially modifies the properties of the material, so that clusters cannot simply be considered as small pieces of bulk material. The problem of determining the structure of nanoparticles is far from being solved to date [1]. In particular, the structural deviations relative to the ideal structure are not well characterized because no experimental techniques, X-ray and neutron diffraction for instance, can give univocal information for such small objects [2]. Consequently, this problem cannot be tackled with experimental methods only but needs extra-information coming from theoretical modeling methods. An example of the difficulties and variability of the nanocluster structure can be observed considering the difference between  $\text{ZrO}_2$  and  $\text{TiO}_2$  nanoclusters.  $\text{TiO}_2$  is a well-studied material for catalysis and energy applications; it is a well known fact that, despite the greater stability of rutile structure for bulk material, nanoparticles assume anatase structure, maintaining a fairly ordered crystalline structure. The anatase structure is clearly recognizable even for extremely small clusters ( $\leq 1$  nm), as shown by computations [3]. The situation is completely different for  $\text{ZrO}_2$ : despite the similarity of the chemical properties of Zr and Ti, recent studies [4] shows that small clusters (around 1.3 nm) of  $\text{ZrO}_2$  does not preserve any regular structure, and the most stable configurations seems to be amorphous.

---

\*Corresponding author. E-mail: [roberto.grena@enea.it](mailto:roberto.grena@enea.it).

Different hypotheses can be made on the origin of the different behaviour: from structural considerations (anatase structure is very different from the tetragonal structure favoured by  $\text{ZrO}_2$  clusters of larger size), to chemical considerations (Ti, beside the "natural" oxidation number 4, can easily assume oxidation number 3, while Zr with oxidation state 3 is more unstable). So, in order to investigate the question, an oxide with structural properties similar to  $\text{ZrO}_2$  of a metal which can easily assume oxidation number 3 should be considered: if the nanocluster results disordered the first hypothesis (structural differences) is the most likely one, while if the cluster retains its order the second hypothesis (chemical differences) is corroborated. The choice fell on  $\text{CeO}_2$ . So, the study of three nanoclusters ( $\text{TiO}_2$ ,  $\text{ZrO}_2$ ,  $\text{CeO}_2$ ) was started. A stoichiometric, roughly spherical nanoparticle, with a size slightly below 2 nm, was chosen for each of the three materials. The nanoparticles are quite "large" for ab-initio simulations (342 atoms for  $\text{TiO}_2$ , 314 atoms for the other two oxides) and are near the upper limit of the computational possibilities with standard DFT (no linear-scaling) methods. The choice of "large" clusters was made for two reasons: the first reason is the desire to study existing objects (metal oxide nanoparticles below 1.5 nm are not realistic), the second reason is to emphasize the different behaviours of the materials (with smaller clusters all the materials exhibit a certain amount of amorphization, and larger clusters become fairly ordered for all the materials; a size around 2 nm is in the range in which the different behaviours are more striking). The comparison among the results will give an indication on the origin of the structural disorder.

## 2 Methods

The study of the clusters was made using Car-Parrinello molecular dynamics as an optimization tool, since standard geometrical optimizations (BFGS/GDIIS) was too unstable when dealing with such large systems. Quantum Espresso software was used [5]. In the optimization, the cluster evolves according to a fictitious molecular dynamics with a thermostat at a very low temperature (10 K), in order to achieve a local energy minimum with a smooth dynamics. The computations are heavy: the computation of a minimum requires from 20 to 80 24-hour runs (depending on the disorder of the cluster: if the structure is far from the crystalline structure, longer computations are needed) on 288 CPU cores. The computation of a single minimum is not sufficient, since it could be only a local minimum; so, cycles of simulated annealing (heating-cooling cycles) are then made to find different minima. Even if it is not possible to find the global minimum for such large systems (unless the system retains a crystalline structure), the properties of the first 3-4 minima is sufficient to observe the tendency to disordered structures of the cluster.

## 3 Results

The first minima of the three structures found give a strong hints on the correct hypothesis on the disorder origin. The three structures found are shown in Fig. 1- 3 , together with the starting configurations. As expected, the  $\text{TiO}_2$  structure retains its anatase structure, with only a rearrangement of the surface atoms. The study of  $\text{ZrO}_2$  confirms the tendency of

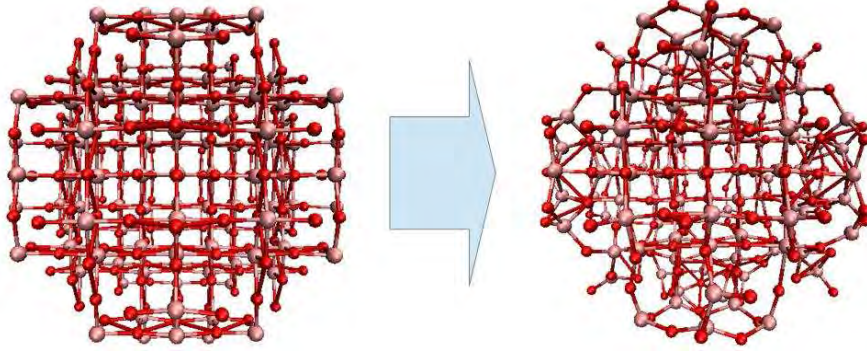


Figure 1: Structure of the  $\text{TiO}_2$  nanocluster: initial (left) and optimized (right) configurations.

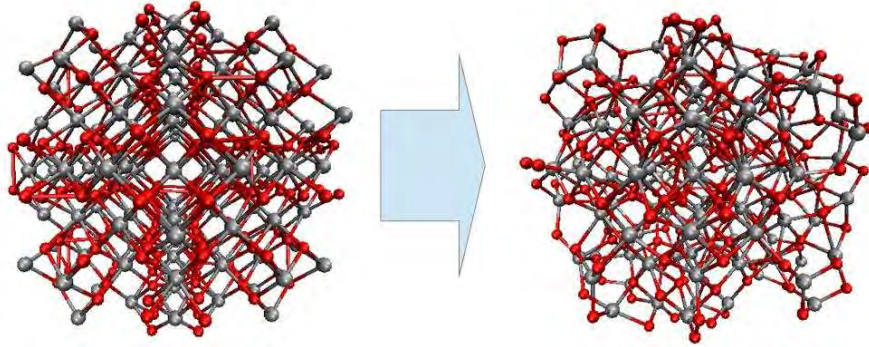


Figure 2: Structure of the  $\text{ZrO}_2$  nanocluster: initial (left) and optimized (right) configurations.

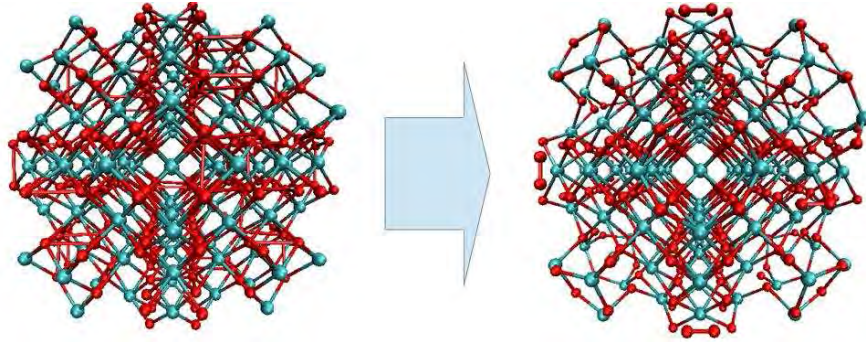


Figure 3: Structure of the  $\text{CeO}_2$  nanocluster: initial (left) and optimized (right) configurations.

the cluster to disordered structures: this is not a trivial fact, since no ab-initio studies were made on such large clusters up to now, and the tendency to disorder was found considering a structure with about  $1/3$  of the atoms. So, we can conclude that increasing the size (up to 2 nm) does not stabilize the structure of  $\text{ZrO}_2$  and the tendency to disorder persists. The most interesting result is obtained for the  $\text{CeO}_2$  structure. The starting structure was the same of  $\text{ZrO}_2$  cluster; however, the minimization procedure took far less time and the resulting final structure is almost perfectly ordered. This fact shows that disorder

is more likely induced by the difference in chemistry than by structural properties. The differences in ordering between  $\text{TiO}_2$  and  $\text{ZrO}_2$  are not induced by differences in structure or coordination numbers, since a structure identical to  $\text{ZrO}_2$  structure ( $\text{CeO}_2$ ) produces clusters almost perfectly ordered. The difference is likely due to chemical difference.  $\text{ZrO}_2$  crystalline structure is disrupted since Zr atoms on the surface have a pending bond, and they have a strong tendency to saturate the bond; on the contrary, the other two elements can easily assume oxidation number 3, and this fact stabilizes the surface.

## 4 Conclusions

The preliminary results of the work allows to give useful hints on the origin of structural disorder in small size nanoclusters, discerning between two competing hypotheses (crystal structure or chemical differences). Of course, the work is far from complete: it is required a better definition of disorder (possibly quantitative), the investigation of other minima, and possibly the test of other metal dioxide to confirm the hypothesis. For example, it should be interesting to study a cluster with the same structure as  $\text{TiO}_2$  of a metal with chemical properties similar to  $\text{ZrO}_2$ ; unfortunately, anatase is not a common structure and no examples has been found. However, even the first results show the potential of the ab-initio methods for clarifying the origin of structural properties of nanoclusters.

## References

- [1] Juhas P., Cherba D. M., Duxbury P. M., Punch W. F., and Billinge S.L.J. Ab initio determination of solid-state nanostructure. *Nature*, 440:655–658, 2006.
- [2] Billinge S. L. J. and Levin I. The problem with determining atomic structure at the nanoscale. *Science*, 316:561–565, 2007.
- [3] Iacomino A., Cantele G., Ninno D., Marri I., and Ossicini S. Structural, electronic, and surface properties of anatase  $\text{TiO}_2$  nanocrystals from first principles. *Physical Review B*, 78:075405, 2008.
- [4] Grena R. Structure and molecular dynamics of a spherical cluster  $\text{Zr}_{43}\text{O}_{86}$ . *High performance Computing on CRESCO infrastructure: research activities and results 2010-2011*, pages 179–186, 2012.
- [5] Giannozzi P. et al. QUANTUM ESPRESSO: a modular and open-source software project for quantum simulations of materials. *Journal of Physics: Condensed Matter*, 21:395502, 2009.



# Ab-initio modeling of methane adsorption at Ca impurities on a carbon nanotube side-wall

*Fabrizio Gala\*, Giuseppe Zollo*

*Università di Roma “La Sapienza”*

*Dipartimento di Scienze di Base e Applicate per l’Ingegneria (Sezione di Fisica)  
Via A. Scarpa 14–16, 00161 Rome Italy*

**ABSTRACT.** Methane adsorption at Ca decorated single wall carbon nanotubes has been studied by ab-initio total energy calculation based on the density functional theory. The adsorption configurations have been studied using various exchange correlation energy functionals including also two possible long-range interaction correction schemes. Our calculations show that methane adsorption at Ca decorated carbon nanotubes is markedly enhanced when impurity atoms are considered as individual adsorption sites. We demonstrate that up to six CH<sub>4</sub> molecules can bind at a single Ca impurity at room temperature. The phenomenon responsible of the measured adsorption energy is recognized as a Kubas-type interaction that involves the orbital overlap between the Ca *d* state and the methane  $\sigma$  molecular orbitals. The adsorption values obtained with the different energy functionals used are discussed showing that LDA, often employed in the recent literature for similar adsorption problems, is affected by severe limitations when orbital overlap and physisorption co-exist. Lastly the well known problem of Ca clustering is studied and discussed showing that, differently to the hydrogen case, it does not induce any molecular dissociation.

## 1 Introduction

Nanoporous carbon-based materials have been shown to be particularly attractive as solid media for gas storage purposes thanks to their large surface/volume ratio and peculiar geometry. Accordingly, both crystalline and disordered carbon nano-structures have been subject of investigation for gas supply and sensing [1], with remarkable emphasis on two carbon allotropes: single walled carbon nanotubes (SWCNTs) and graphene. The storage problem has been especially focused on gaseous species of interest for energetic applications such as molecular hydrogen (H<sub>2</sub>) and methane (CH<sub>4</sub>). Concerning hydrogen, that is the most promising energy source alternative to fossil fuels, however, pristine carbon nano-structures have exhibited physical limits preventing them for practical use as hydrogen storage media: indeed H<sub>2</sub> molecules are weakly bound with a low adsorption heat on pristine carbon materials through long-range dipolar forces. As a consequence, when considered in the context of adsorption/desorption cycles of the so-called delivery process involving storage and release, pure carbon nano-structures are unfit for hydrogen storage

---

\*Corresponding author. E-mail: [fabrizio.gala@uniroma1.it](mailto:fabrizio.gala@uniroma1.it).

purposes [2]. Such limitations appear to be less stringent in the methane case due to the larger adsorption heat measured in carbon nano-structured media: it has been demonstrated, indeed, that  $\text{H}_2\text{-CH}_4$  mixtures (hythane) can be stored in slitlike pores and CNTs achieving the volumetric stored energy threshold of  $5.4 \text{ MJ/cm}^3$  useful for alternative automotive fuel systems as established by the US Freedom Car Partnership [1]. However, because methane is commonly employed as a precursor for SWCNT synthesis at high temperature, its storage in SWCNT media might be affected by dissociation phenomena occurring at the tube side-wall; this phenomenon, that should be taken into account as a source of atomic hydrogen chemisorption by methane catalytic dissociation, may affect the methane molecular stability for high temperature storage systems [3].

A common strategy to improve the carbon nanomaterials storage performance in the  $\text{H}_2$  case consists in decorating the nano-structures with light alkali metals, either of the first group, such as Li [4], or of the second group, such as Ca [5]. The latter solution has revealed as the most appealing due to the larger  $\text{H}_2$  binding energy on Ca than Li impurity sites in carbon nano-structures (roughly 17% more) as a consequence of a genuine nonclassical phenomenon: the so called Kubas interaction [6, 5]. In this case the binding occurs through the orbital hybridization involving the empty  $d$  states of the alkali metal and the  $\sigma$  orbital of the  $\text{H}_2$  molecule and is accompanied also by a charge back donation from the  $d$  state to the molecular  $\text{H}_2 \sigma^*$  antibonding state. The benefit of Ca doping, however, is affected by the marked tendency of Ca atoms to form metallic clusters [5] at the SWCNT side-wall thus altering dramatically the nature of the  $\text{H}_2$  adsorption process and causing the molecule dissociation. Atomistic modeling has demonstrated that Ca clustering can be suppressed on zig-zag graphene nano-ribbons (ZGNR) because individual alkali impurities are stably adsorbed on both sides of the zig-zag edge [7]. However a practical exploitation of this finding is still to come because large-area graphene structures have been obtained by chemical vapor deposition only on solid substrates so far [8, 9], making impractical the assumption of Ca atoms decorating both sides of a graphene sheet. While the Ca clustering problem is still an open problem, a question arises concerning the possible role played by Ca decorated carbon nanostructures in the methane adsorption: are Ca impurities able to enhance also the adsorption of methane molecules? And if so, at which extent? The answer to these questions would be important to characterize the uptake performance of alkali doped carbon nano-structured media, originally designed for hydrogen storage, also for the storage of methane and hythane.

Therefore, in this paper we have taken into consideration the possibility of enhancing the methane storage in SWCNT media by Ca doping and we have investigated if, similarly to the  $\text{H}_2$  case, a Kubas-type interaction between the involved orbitals arises that may increase the binding energy of the  $\text{CH}_4$  molecule on a SWCNT. Moreover, Ca clustering phenomena has been also considered concerning the way they affect the interaction between the methane molecules and the alkali doped SWCNT.

## 2 Theoretical Method

Methane adsorption at a semiconducting SWCNT decorated with a Ca atom, has been investigated by *ab-initio* Density Functional Theory (DFT), together with norm-conserving

pseudopotentials, constructed using the Troullier-Martins scheme [10], and a plane wave basis set expansion scheme. The Ca semicore  $3s$  and  $3p$  states have been explicitly taken into account as valence shell in the construction of the corresponding pseudopotential. First-principles calculations have been performed using the QUANTUM-ESPRESSO package [11], with an energy cut-off of 120 Ry for the wave functions and periodic boundary conditions (PBCs) have been employed together with a  $1 \times 1 \times 3$  Monkhorst-Pack  $k$ -point grid [12] for the Brillouin zone sampling. The adopted supercell is tetragonal with  $a = b = 30$  Å in the plane orthogonal to the tube axis. The supercell size along the tube axis has been chosen  $c = 8.45$  Å i.e. two (11,0) CNT unit cells, when considering up to 2 methane molecules adsorbed while it has been increased to  $c = 12.69$  Å i.e. three (11,0) CNT unit cells, for the cases involving  $n \geq 3$  methane molecules. The used  $k$ -point sampling scheme and supercell sizes have been checked for convergence giving a maximum error-bar of 8 meV (obtained in the case of the most crowded configuration) for the values of the adsorption energy that have been calculated and are reported below; this error is negligible with respect to the adsorption energy values obtained (see below).

It is commonly recognized that the Local Density Approximation (LDA) [13, 14] and Generalized Gradient Approximation (GGA) [15] schemes give respectively the lower and the upper bound values for the binding energies of weak interacting systems. Thus we have used both the schemes choosing the Perdew-Burke-Ernzerhof (PBE) formula [16] for the GGA case. While the LDA scheme is commonly used in adsorption problems because it has been found to behave surprisingly well, we have found, on the contrary, that the usage of the PBE exchange-correlation functional gives an unrealistic small value for the adsorption energy of a methane molecule on a bare SWCNT; this is basically due to the inadequacy of GGA schemes to treat long range Van der Waals (VdW) dispersion forces that are expected to play a major role in both the adsorption geometries and energetics of weak interacting surface/molecule systems; as a consequence, we have also used two correction schemes to handle long-range interactions using either a semi-empirical correction (vdw-D) [17] or a fully density functional approach that includes also an additional self-consistent dispersion interaction term (vdw-DF) [18, 19] in the context of the PBE XC functional scheme.

The ground state configurations have been fully relaxed using the Broyden-Fletcher-Goldfarb-Shanno (BFGS) method [20] together with the Hellmann-Feynman forces acting on the ions. The ionic minimization has been done until the convergence threshold of 0.001 a.u. on the total force was reached.

Previous investigations [5] have shown that the binding energy of Ca on CNTs has little to do with the chirality of the carbon nanotube and thus we have taken into account a semiconducting (11,0) SWCNT as a prototypical case for our study.

The adsorption energy of a  $\text{Ca}_m$  cluster on a SWCNT has been computed as:

$$E_a^{\text{Ca}_m} = E(\text{SWCNT}_{\text{Ca}_m}) - E(\text{SWCNT}_{\text{Ca}_{m-1}}) - E(\text{Ca}) \quad \text{with } m = 1, 2$$

while the adsorption energy of  $n$   $\text{CH}_4$  molecules on a carbon nanotube decorated with a  $\text{Ca}_m$  cluster, has been calculated as:

$$E_a^{(m,n)} = E(\text{SWCNT}_{\text{Ca}_m} + n\text{CH}_4) - E(\text{SWCNT}_{\text{Ca}_m}) - nE(\text{CH}_4)$$

### 3 Results and Discussion

First of all the adsorption of a single methane molecule on a bare SWCNT has been considered. The focus on this case study, besides its obvious importance as a reference system for the adsorption of methane, has been oriented also to check the reliability of the schemes used, especially concerning the XC functional and the treatment of the long range dispersion forces. Thus we have checked the four schemes adopted, namely the LDA, the PBE, the semi-empirical (vdw-D) and the density functional (vdw-DF) corrected PBE, by calculating the total energy of the methane-SWCNT system statically (i.e. with no atomic relaxation) as a function of the  $\text{CH}_4$  distance  $d$  from the CNT side-wall.

The obtained adsorption energy values are reported in Fig.1 and show that PBE XC functional (red line) gives an unfeasible value of -15 meV of the adsorption energy at the wall minimum. LDA results (black line in Fig.1), on the contrary, seem much more robust with a well defined adsorption energy wall that is in agreement with the findings of methane adsorption on graphene reporting an adsorption energy evaluated at LDA level close to the experimental value [21]. Green and blue line in Fig. 1 report the vdw-D and vdw-DF results respectively.

The static curves obtained with the vdw-D and vdw-DF schemes coincide asymptotically, as expected, but show some differences at short distances even though the adsorption energy at the wall minimum are similar (respectively -0.1 eV and -0.11 eV) and close to the LDA value (-0.093 eV). The adsorption wall minimum occurs at 3 Å for LDA, 3.25 Å and 3.55 Å for vdw-D and vdw-DF respectively evidencing that the equilibrium distance of methane is at larger distance for PBE corrected schemes than for LDA. It is interesting to note that, while the LDA adsorption energy is below the PBE value in the whole range, Van der Waals corrected schemes evidence two domains: at short distance PBE corrected schemes overestimate the LDA results while at large distance the opposite occurs. Then the major difference between vdW-D and vdw-DF results are the methane equilibrium distance (the adsorption energy at this distance differ as well but at a smaller extent) and the short range behavior that, as expected, resembles the pure PBE behavior more closely for vdw-DF than for the semi-empirical corrected scheme. On the basis of the above considerations and on the fact that vdw-DF scheme imply only a moderate heavier workload, we have chosen to perform all the calculations involving also the Ca impurities using the LDA, the PBE and the vdw-DF schemes.

After accurate optimization run, the ground state configuration of one Ca impurity placed on the SWCNT side-wall has been found to be the "hollow" one (i.e. the Ca impurity is located above the centre of a hexagon at the tube side wall) for each of the three different XC flavors used. The calculated adsorption energy values  $E_a^{\text{Ca1}}$  are -1.14 eV (LDA), -0.53 eV (PBE) and -0.23 eV(vdw-DF), evidencing a strong dependence on the XC functional chosen, the LDA value being double of the PBE one. The optimized geometries, on the contrary, are quite similar, with distances from the SWCNT sidewall of  $\sim 2.1$  Å (LDA),  $\sim 2.2$  Å (PBE) and  $\sim 2.4$  Å (vdw-DF). For all the XC energies considered, Ca adsorption results in a slight deformation of the nanotube, as well as in a charge transfer of  $\sim 0.5 e^-$  from the Ca atom to the SWCNT, as shown by the Löwdin population analysis performed on each of the ground state configurations studied.

Then we have addressed the problem of the adsorption of a single  $\text{CH}_4$  molecule on a Ca atom decorating the nanotube; again, the optimized structures are qualitatively similar, as evidenced by a comparison of the geometrical parameters indicated in Fig.2(a), whose values are reported, together with the corresponding adsorption energies, in Fig.1.

The adsorption energy gain  $\Delta E_a$  with respect to the case of methane absorption on a pristine nanotube is considerable; it is quite different in the three cases treated ranging from 60 meV in the vdw-DF case to 360 meV in the LDA case with the PBE case being intermediate with 165 meV. The charge on the Ca impurity measured for the three cases (between  $\sim 0.40 e^-$  and  $\sim 0.48 e^-$ ) does not correlate with the energy gain data indicating that the phenomenon observed is not barely electrostatic and should be explained by orbitals interaction. The projected density of states (PDOS) of the ground state adsorption configurations of a methane molecule on a Ca decorated site on the (11,0) SWCNT side wall have been calculated for the three exchange-correlation functionals; and are reported in Fig.3. Here the projections on the Ca  $s$ ,  $p$  and  $d$  valence orbitals and on the  $\text{CH}_4$  orbitals are reported for the three cases studied evidencing an overlap between the methane  $\sigma$  molecular orbitals (either the  $\sigma_{ss}$  orbitals located near -15 eV or the  $\sigma_{sp}$  located near -8 eV) and the  $s$ ,  $p$  and  $d$  states of the Ca atom. Indeed the Ca 3d state, that is the highest occupied molecular orbital (HOMO) found in the Ca decorated SWCNT, shows an increased electron population when  $\text{CH}_4$  is adsorbed that is accompanied by an increased PDOS in the energy ranges where the methane  $\sigma_{ss}$  and  $\sigma_{sp}$  molecular orbitals reside thus indicating the formation of hybrids involving the Ca  $d$  state and the methane orbitals. The above described orbital hybridization is quite similar to the Kubas-type interaction occurring in the hydrogen case and briefly described in the Introduction. Differently from the  $\text{H}_2$  case, however, we have measured an almost negligible charge back donation from the Ca  $d$  state to the methane  $\sigma^*$  state near the highest occupied molecular orbital (HOMO), as evidenced in the inset of Fig.3; thus, differently from the hydrogen case, this circumstance seems to indicate that the methane molecular stability against dissociation (that might be caused by the interaction with the impurity) should be preserved.

Subsequently we have obtained by accurate optimization the adsorption configurations on a Ca decorated SWCNT involving more than one  $\text{CH}_4$  molecule up to six. Up to five molecules adsorbed, the ground state configurations found are quite similar for the three X-C functionals used, except for the relative distances measured between the Ca impurity and the methanes; on the contrary, the ground state configuration with six methane molecules exhibits a different global geometry in the LDA case with respect to the other two.

The optimized geometry of two  $\text{CH}_4$  adsorbed at the Ca impurity is characterized by the two molecules lying in a plane orthogonal to the tube axis, and symmetrically placed with respect to the Ca atom; the Ca- $\text{CH}_4$  distances are roughly equal to the corresponding ones reported in Table 1 for the single  $\text{CH}_4$  molecule. In the  $3\text{CH}_4^{\text{ad}}$  optimized configuration, a third methane is located along the tube axis and the optimized configurations are slightly different in the three cases: using LDA, indeed, the Ca- $\text{CH}_4$  distances are nearly equal for the three molecules being  $\sim 2.7 \text{ \AA}$  for the other two XC functionals, instead, the Ca- $\text{CH}_4$  distance is greater for the molecule along the tube axis (about 20% and 30% more for PBE and vdw-DF respectively) than the ones of the molecules in the plane orthogonal to

the tube axis. A similar trend is also found in the case with four  $\text{CH}_4$  molecules; here the optimized geometry is characterized by two couples of molecules: one couple is in the plane orthogonal to the tube axis and the molecules are symmetrical with respect to the Ca atom; the other couple is made of molecules placed along the tube axis at different distances from the Ca impurity. Three of the four molecules basically keep the same configuration found in the  $3\text{CH}_4^{\text{ad}}$  case while the Ca- $\text{CH}_4$  distance of the fourth molecule, that is located along the tube axis, is much different from the others and varies with the XC functional employed in the optimization, ranging from 4.1 Å in the PBE case, to 4.6 Å in the LDA case. Due to the large distance measured between the Ca impurity and the fourth  $\text{CH}_4$  molecule, this configuration could be, in principle, affected by a larger interaction between methane molecules belonging to adjacent supercells; therefore we have further checked this configuration against the supercell size along the tube axis using a larger supercell with  $c = 16.93$  Å. The configuration found does not differ significantly and the adsorption energy correction obtained is discussed below. The ground state configuration involving five  $\text{CH}_4$  molecules is nearly the same independently on the XC functional chosen with the fifth  $\text{CH}_4$  molecule occupying the top position above the Ca impurity. The distances of the methane molecules lying along the tube axis and in the plane orthogonal to it are quite similar to the  $4\text{CH}_4^{\text{ad}}$  case while the fifth top molecule is placed at a distance that is larger in the LDA and PBE cases (3.82 Å and 5.0 Å respectively) than the one in the vdw-DF case (3.25 Å); in particular it should be noted that the PBE case largely overestimates such distance reflecting a marked inadequacy in such cases where chemisorption and physisorption coexists. In the  $6\text{CH}_4^{\text{ad}}$  case the optimized geometries are different; the LDA configuration shows five  $\text{CH}_4$  molecules arranged in a distorted pentagon centered on the Ca impurity (with relative Ca- $\text{CH}_4$  distances of 2.73 Å, 2.74 Å, 2.83 Å, 2.83 Å, 4.77 Å) and the sixth  $\text{CH}_4$  molecule in the top position above the Ca atom at 3.78 Å from it (see Fig.4(a) for details); in both PBE and vdw-DF cases, on the contrary, the ground state configuration is obtained from a distorted  $5\text{CH}_4^{\text{ad}}$  configuration (as shown in Fig.4(b)) with relative distances of 2.84 Å, 2.85 Å, 3.60 Å, 4.32 Å, 5.90 Å, and 6.15 Å (2.94 Å, 2.95 Å, 4.40 Å, 4.64 Å, 5.03 Å, and 3.64 Å) in the PBE (vdw-DF) case.

The adsorption energy of the various configurations studied as functions of the number of methane molecules involved is reported in Fig.5(a). It is shown that the adsorption energy of  $n\text{CH}_4^{\text{ad}}$  molecules at the Ca decorated SWCNT approaches a saturation value for  $n \geq 6$  for the PBE and the vdw-DF cases while in the LDA case no saturation occurs in spite of the large equilibrium distance measured, typical of a simple physisorption, concerning the last  $\text{CH}_4$  molecule added. Such a behavior is more clearly evidenced by drawing the adsorption energy of the last added molecule shown in Fig.5(b): the curves concerning both the PBE and the vdw-DF cases show, except for the first point, a monotonically increasing behavior of the adsorption energy that approaches zero: in the PBE case, the adsorption energy of the sixth added molecule is already quite small while in the vdw-DF case it is about 60 meV that is still larger than the thermal energy at RT indicating that, according to vdw-DF results, six methane molecule can stay adsorbed at the Ca impurity at RT. It must be emphasized, however, that the binding energy of the sixth methane molecule is lower than the one of a methane molecule at the SWCNT side-wall. Therefore it is likely that the methane adsorption starts at the Ca impurity where five molecules are adsorbed, then it proceeds at the SWCNT side-wall where the eventual

pristine adsorption sites are saturated and finally it completes with the sixth methane molecule at the Ca adsorption site. The usage of the PBE scheme, instead, does not catch the physisorption of the two last added molecules and therefore can be considered reliable only for adsorption configurations involving  $n \leq 3$  molecules where the orbital overlap play a mayor role in the adsorption configuration. The monotonic increasing behavior of the last adsorbed methane molecule that is expected to occur in such cases is completely missed with the LDA XC functional that, in the recent literature, has been often used in adsorption studies. The above results reported in Fig.5 show, on the contrary, that such scheme severely overestimates the binding energy and does not evidence the expected behavior concerning the adsorption energy. The measured Ca-CH<sub>4</sub> distances for the vdw-DF cases concerning the configurations with five and six methane molecules show that these configurations are characterized by three "short ranged" methane molecules with distances less than 4 Å and two or three long range molecules with distances greater than 4 Å. The PDOS of the configurations involving five and six molecules show that the "long range" molecules barely interact with the Ca impurity via an enforced long range interaction that does not involve any orbital hybridization phenomenon (see Fig.6) while for the the three "short range" molecules a Kubas-type interaction is responsible of the observed adsorption feature. Thus, the saturation of the adsorption energy when the number of CH<sub>4</sub> molecules exceeds four is related to a less pronounced Kubas type interaction as evidenced by the PDOS involving the CH<sub>4</sub> molecules that are arranged nearly above the Ca impurity shown in Fig.6: indeed we observe that the  $\sigma_{sp}$  molecular orbitals of the "long range" methane molecule undergo a shift upward with respect to the Ca d-states in the energy range [-9,-6] eV confirming the absence of any orbital overlap, as also expected due to the relative distance. On the contrary the "short range" top methane molecule still exhibits some overlap in the same range between the  $\sigma_{sp}$  methane molecular orbitals and the Ca d, p and s states. The binding energy of the long range molecules is definitely related to an enhanced electrostatic interaction due to the charge transfer involving the Ca impurity and the CNT. However when the number of CH<sub>4</sub> molecules exceeds 4, the hybridization between the Ca *d* state and the CH<sub>4</sub>  $\sigma$  states becomes less pronounced. As mentioned above, particular attention has been paid to the PBE (vdw-DF) case with  $n \geq 4$  because in these cases one physisorbed methane molecules is located along the axis at a distance from the Ca impurity larger than 4 Å. This circumstance could, in principle, affect the adsorption energy by a spurious interaction between CH<sub>4</sub> molecules belonging to adjacent supercells with respect to the one containing only three methanes. Therefore we have checked the adsorption configuration with  $n = 6$  CH<sub>4</sub> molecules in a larger supercell (see above) obtaining that such a such a spurious interaction affects the adsorption energy by only 10 meV, thus nearly the same error as the convergence error discussed in section 2. The same correction should be applied also to the  $n = 4$  and  $n = 5$  cases while it does not affect at all the  $n \leq 3$  cases. Hence the adsorption energy difference curve is slightly affected only for the  $n = 4$  case.

The last deal addressed is the problem of the Ca<sub>2</sub> clustering at the carbon nanotube side-wall that may affect the above described scenario when more impurity atoms are employed; the three XC functionals chosen give basically the same results, with a Ca-Ca distance ranging from 3.28 Å (LDA and PBE) to 3.32 Å (vdw-DF), while the distance between the Ca<sub>2</sub> mid-bond and the tube sidewall is 1.82 Å (LDA), 1.94 Å (PBE), and 2.01 Å (vdw-

DF) respectively; the LDA case shows the lowest adsorption energy  $E_a^{\text{Ca}_2}$  (-2.23 eV) with respect to the other two cases, namely -1.84 eV and -0.96 eV for the PBE and vdw-DF cases respectively, which also reflects the short distance measured between the dimer and the SWCNT sidewall in this case. On the other hand the binding energy of the Ca dimer, measured as  $E_b = E(\text{SWCNT}_{\text{Ca}_2}) - E(\text{SWCNT}) - 2E(\text{SWCNT}_{\text{Ca}})$  is almost constant, being -0.737 eV (LDA), -0.781 (PBE), and -0.812 (vdw-DF) confirming the general trend of Ca atoms of being clustered on the sidewall of a nanotube instead of being individually dispersed on it.

Then we fully relaxed the configuration obtained from the previous one by adding a single methane molecule for each of the employed XC functionals. The obtained results exhibit a marked dependence on the XC scheme chosen with the PBE and vdw-DF cases substantially in agreement among each other concerning the optimized geometries, the adsorption energies and the PDOS while the LDA case is quite different: indeed the LDA adsorption energy value (reported in Table 2 together with the corresponding geometrical parameters shown in Fig.2(b) ) is much greater than both the PBE and vdw-DF corresponding values. The observed different behavior is clarified by looking again at the corresponding PDOS: while in the LDA case the stronger interaction is accompanied by the overlap between the methane molecular orbitals and the Ca s, p and d states, this feature is completely absent in the PBE and the vdw-DF cases indicating that in these cases there is no Kubas-type interaction (see Fig.7, the vdw-DF case, being qualitatively similar to the PBE case, has not been reported). The existence of a Kubas-type interaction in the LDA case is also evidenced by the reduced distance between the  $\text{CH}_4$  molecule and the  $\text{Ca}_2$  dimer occurring in this case. On the basis of the above reported results, we can support the idea that the LDA features shown in the present case must be taken with care and that they are most likely artifacts due to the LDA inadequacy to represent such a complicated adsorption scenario where physisorption and orbital hybridization co-exist. We must notice, however, that for none of the adopted schemes, Ca clustering induces any weakening of the adsorbed molecule that, on the contrary, occurs for hydrogen molecules close to a Ca dimer at the SWCNT side-wall.

Indeed, differently from the case of  $\text{H}_2$  adsorption where the aggregation of the two Ca atoms results in the dissociation of the molecular hydrogen, here the Ca clustering results only in a marked reduction of the adsorption energy without any molecular dissociation. Such a reduction is basically due to the disappearing of any Kubas-type interaction for both the PBE and vdw-DF schemes and no hybridization between the Ca and  $\text{CH}_4$  states occurs.

There is, however, a certain similarity between the adsorption phenomena involving a  $\text{CH}_4$  molecule and a  $\text{H}_2$  molecule (at least at PBE/vdw-DF level) when they interact with a Ca decorated SWCNT, with either the same kind of interaction (i.e. the Kubas interaction) or the same problems (Ca clustering); such a similarity suggests that the possible solutions of the clustering problem, invoked through many different mechanism, that have been proposed for the molecular hydrogen storage problem (i.e. by doping the CNT with boron atoms or by producing defects on the SWCNT [5]) can be successfully employed also for the methane storage.



## 4 Conclusions

In conclusion, we have demonstrated, on the basis of ground state *ab-initio* calculations, that Ca decorated SWCNT can be employed as CH<sub>4</sub> storage media because they evidence an improved methane uptake (up to six molecules) per Ca impurity. Similarly to the H<sub>2</sub> adsorption case, the empty *d* states of Ca are mostly responsible of the enhanced adsorption via a Kubas-type interaction involving the methane molecular orbitals and the s, p and d states of Ca. The employed XC functional schemes, namely LDA, PBE and van der Waals corrected PBE have been discussed critically evidencing the inadequacy of the LDA scheme, that is still employed in adsorption studies, in the 6CH<sub>4</sub><sup>ad</sup> case due to overbinding. Generally speaking, our results show that the electron exchange and correlation energy functionals commonly applied in density functional calculations (i.e. LDA and PBE) behave differently, especially for what concerns the adsorption energies and the Ca clustering problem, which is the major limiting factor that reduces the application of carbon based nanostructures as solid tank fuels for molecular hydrogen or hydrocarbons. In presence of a gaseous methane environment, indeed, LDA predicts that Ca clustering does not prevent the occurrence of a Kubas-type interaction between a CH<sub>4</sub> molecule and the Ca<sub>2</sub> dimer, while, at PBE/vdw-DF level, Ca clustering suppresses such enhanced interaction. Moreover the XC functionals here employed, predict that up to six CH<sub>4</sub> molecules can be adsorbed at a single Ca impurity being reasonably stable at room temperature, except for the PBE case. A critical evaluation of the presented results make us confident that the van der Waals corrected PBE results are consistent and reasonable while LDA results must be taken with care in such cases where physisorption and orbital overlap may coexist. Experimental results concerning Ca decorated SWCNTs for methane storage are highly desirable to confirm our predictions.

## References

- [1] Zollo G. and Gala F. Atomistic modeling of gas adsorption in nanocarbons. *J. Nanomat.*, 2012(32):152489–1–32, 2012.
- [2] Bhatia S. K. and Myers A. L. Optimum conditions for adsorptive storage. *Langmuir*, 22(4):1688–1700, 2006.
- [3] Bagolini L., Gala F., and Zollo G. Methane cracking on single-wall carbon nanotubes studied by semi-empirical tight binding simulations. *Carbon*, 50(9):411–20, 2012.
- [4] Dag S., Ozturk Y., Ciraci S., and Yildirim T. Adsorption and dissociation of hydrogen molecules on bare and functionalized carbon nanotubes. *Phys. Rev. B*, 72(8):155404–1–8, 2005.
- [5] Lee H., Ihm J., Cohen M. L., and Louie S. G. Calcium-decorated carbon nanotubes for high-capacity hydrogen storage: First-principles calculations. *Phys. Rev. B*, 80(5):115412–1–5, 2009.

- [6] G. J. Kubas. Metal-dihydrogen and  $\sigma$ -bond coordination: the consummate extension of the dewar-chatt-duncanson model for metal-olefin  $\pi$  bonding. *J. Organomet. Chem.*, 635(37):37–68, 2001.
- [7] Lee H., Ihm J., Cohen M. L., and Louie S. G. Calcium-decorated graphene-based nanostructures for hydrogen storage. *Nano Lett.*, 10(6):793–98, 2010.
- [8] Wood J. D., Schmucker S. W., Lyons A. S., Pop E., and Lyding J. W. Effects of polycrystalline cu substrate on graphene growth by chemical vapor deposition. *Nano Lett.*, 11(8):4547–54, 2011.
- [9] Park H. J., Meyer J., Roth S., and Skákalová V. Growth and properties of few-layer graphene prepared by chemical vapor deposition. *Carbon*, 48(7):1088–94, 2010.
- [10] Troullier N. and Martins J. L. Efficient pseudopotentials for plane-wave calculations. *Phys. Rev. B*, 43(14):1993–06, 1991.
- [11] Giannozzi P., Baroni S., Bonini N., Calandra M., Car R., Cavazzoni C., Ceresoli D., Chiarotti G. L., Cococcioni M., Dabo I., Dal Corso A., de Gironcoli S., Fabris S., Fratesi G., Gebauer R., Gerstmann U., Gougoussis C., Kokalj A., Lazzeri M., Martin-Samos L., Marzari M., Mauri F., Mazzarello R., Paolini S., Pasquarello A., Paulatto L., Sbraccia C., Scandolo S., Sclauzero G., Seitsonen A. P., Smogunov A., Umari P., and Wentzcovitch R. M. Quantum espresso: a modular and open-source software project for quantum simulations of materials. *J. Phys.: Condens. Matter*, 21(19):395502–1–19, 2009.
- [12] Monkhorst H. J. and Pack J. D. Special points for brillouin-zone integrations. *Phys. Rev. B*, 13(5):5188–92, 1973.
- [13] Ceperley D. M. and Alder B. J. Ground state of the electron gas by a stochastic method. *Phys. Rev. Lett.*, 45(4):566–69, 1980.
- [14] Perdew J. P. and Zunger A. Self-interaction correction to density-functional approximations for many-electron systems. *Phys. Rev. B*, 23(32):5048–79, 1981.
- [15] Martin R. M. *Electronic Structure: Basic Theory and Practical Methods*. Cambridge University Press, 2008.
- [16] Perdew J. P., Burke K., and Ernzerhof M. Generalized gradient approximation made simple. *Phys. Rev. Lett.*, 77(4):3865–68, 1996.
- [17] Grimme S. Semiempirical gga-type density functional constructed with a long-range dispersion correction. *J. Comput. Chem.*, 27(15):1787–99, 2006.
- [18] Dion M., Rydberg H., Scröder E., Langreth D. C., , and Lundqvist B. I. Van der waals density functional for general geometries. *Phys. Rev. Lett.*, 92(4):246401–1–4, 2004.
- [19] Román-Pérez G. and Soler J. M. Efficient implementation of a van der waals density functional: Application to double-wall carbon nanotubes. *Phys. Rev. Lett.*, 103(4):096102–1–4, 2009.

- [20] Fletcher R. A new approach to variable metric algorithms. *The Computer Journal*, 13(6):317–22, 1970.
- [21] Thierfelder C., Witte M., Blankenburg S., Rauls E., and Shmidt W. G. Methane adsorption on graphene from first principles including dispersion interaction. *Surf. Sci.*, 605(4):746–49, 2011.

## 5 Tables

Table 1: Geometrical parameters, together with the adsorption energies for a relaxed  $\text{CH}_4$  molecule adsorbed on a  $\text{SWCNT}_{\text{Ca}}$  as a function of the XC correlation energy employed.

	$d_1$ (Å)	$d_2$ (Å)	$\theta$ (°)	$E_a$ (meV)
LDA	2.1	2.6	110	-460
PBE	2.2	2.8	113	-180
vdw-DF	2.4	2.9	102	-187

Table 2: Geometrical parameters for a relaxed  $\text{CH}_4$  molecule adsorbed on a  $\text{SWCNT}$  decorated with a  $\text{Ca}_2$  dimer as a function of the XC correlation energy employed.

	$d_{\text{Ca}_2}$ (Å)	$d_1$ (Å)	$d_2$ (Å)	$\theta$ (°)	$E_a$ (meV)
LDA	3.32	1.79	2.57	112.0	-350.9
PBE	3.28	1.94	4.61	95.9	-31.6
vdw-DF	3.31	2.01	4.53	95.7	-54.2

## 6 Figures

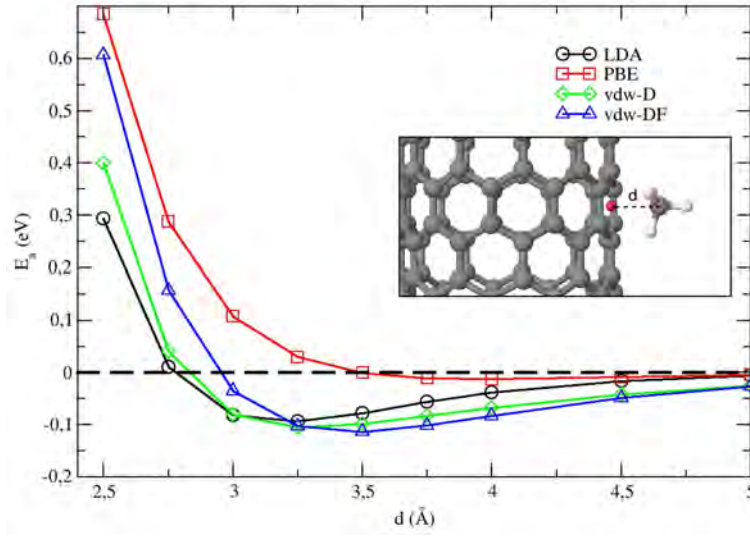


Figure 1: (Color online) Variation of the adsorption energy with respect to the distance between the  $\text{CH}_4$  molecule and the SWCNT sidewall.

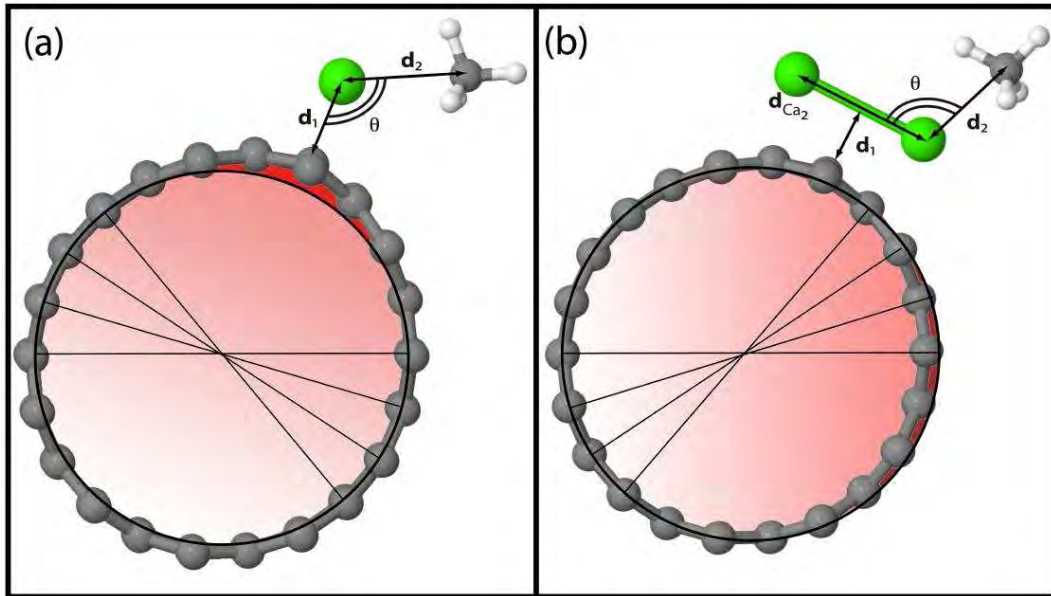


Figure 2: (Color online) Methane molecule adsorbed on a Ca atom (a) and a  $\text{Ca}_2$  dimer (b) decorating the hollow position of a SWCNT. See Table 1 and Table 2 for the different values of the geometrical parameters of interest in the adsorption for the XC correlation energies employed in the optimization.

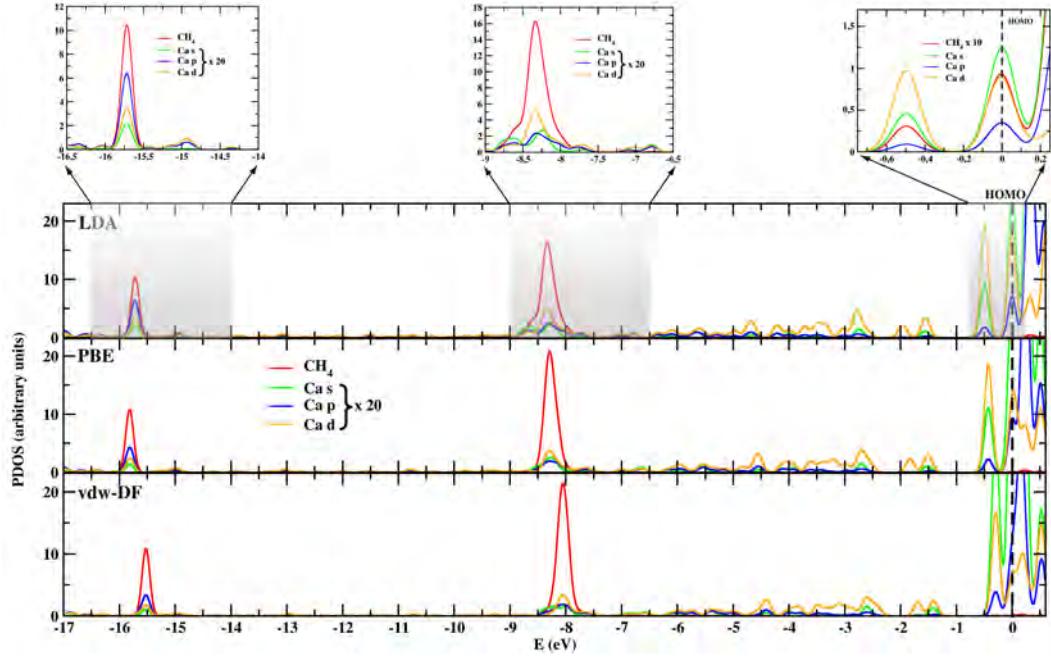


Figure 3: (Color online) PDOS over Ca and CH<sub>4</sub> orbitals involved in the adsorption decorating a SWCNT for the three XC functionals chosen. The energy regions where the overlap between the Ca and CH<sub>4</sub> orbitals occurs have been enlarged for the LDA case only, as for the other two XC functionals the situation is qualitatively the same. For the sake of clarity the insets have different scales, the HOMO level of the entire system has been set to zero, and last PDOS spectra have been convoluted with a gaussian function.

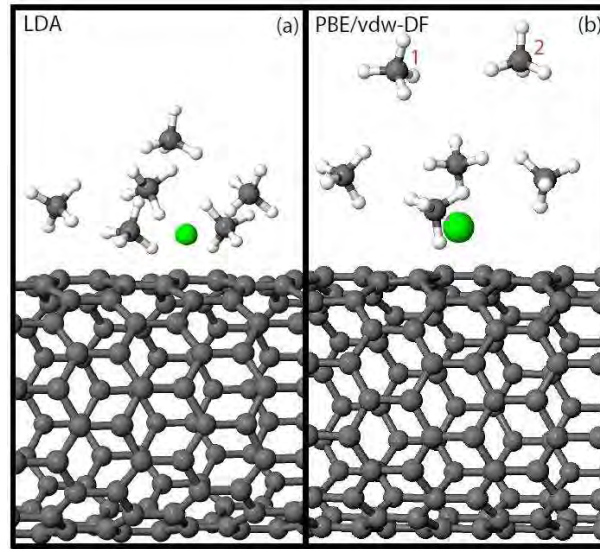


Figure 4: (Color online) Relaxed structures of the adsorption configurations involving six CH<sub>4</sub> molecules at a Ca decorated site of SWCNT in the LDA case(a) and in the PBE/vdw-DF case(b). The two methane molecules labeled as 1 and 2 in (b) are those sharing the top position above the Ca impurity.

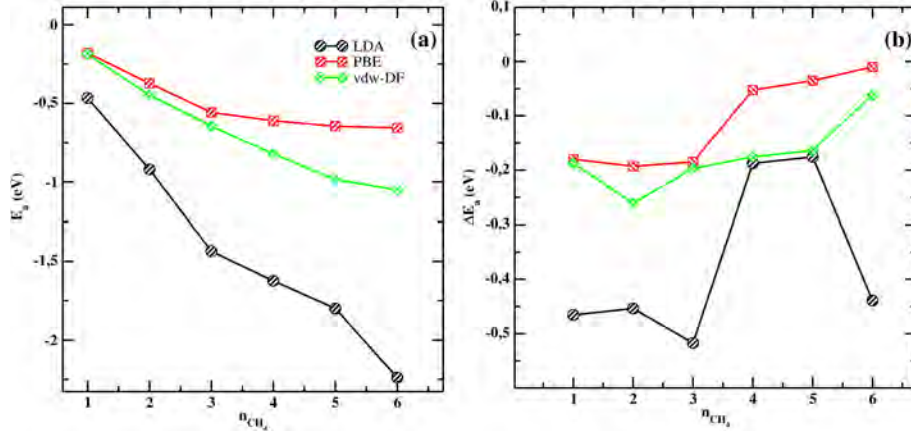


Figure 5: (Color online) Total adsorption energies as a function of the number of  $\text{CH}_4$  molecules adsorbed on a single Ca atom decorating a SWCNT (a) and adsorption energy values of the last added methane molecule (b).

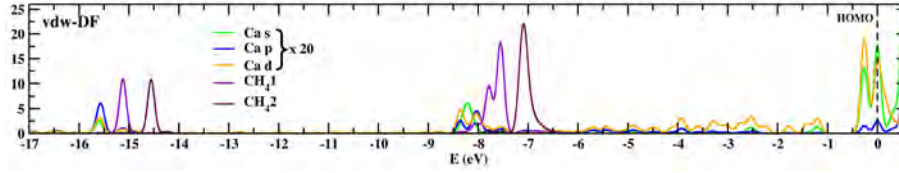


Figure 6: (Color online) Gaussian convoluted PDOS over Ca and  $6\text{CH}_4$  molecules for the vdw-DF case. The methane labelled  $\text{CH}_4 2$  is the "long range" one (see Section 3 for the details) being at  $5.03 \text{ \AA}$  from the Ca impurity. The zero of the energy has been set to the HOMO level of the entire system.

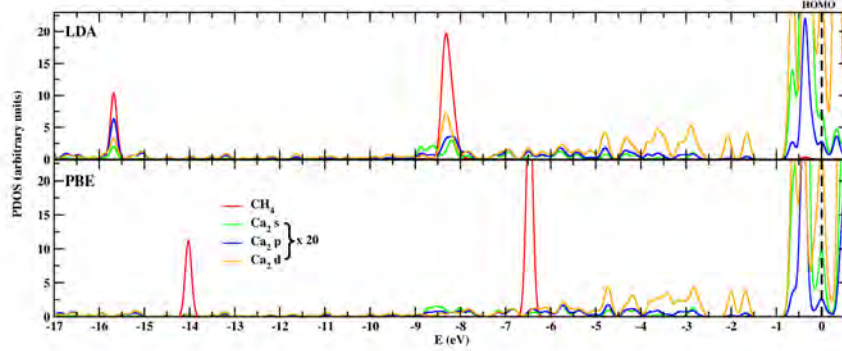


Figure 7: (Color online) PDOS over  $\text{Ca}_2$  and  $\text{CH}_4$  orbitals involved in the adsorption decorating a SWCNT for both LDA and PBE calculations. For the sake of clarity the HOMO level of the entire system has been set to zero and the spectra have been convoluted with a gaussian function.

# A Generalized Turbulent Combustion Model for Large Eddy Simulation of Turbulent Premixed Flames

*E. Giacomazzi\*, D. Cecere,  
F. R. Picchia, N. M. Arcidiacono*

*ENEA, UTTEI-COMSO  
S.P. 081, Via Anguillarese 301, 00123, S.M. Galeria (Rome), Italy*

**ABSTRACT.** This work validates a subgrid scale model for Large Eddy Simulation of turbulent premixed flames. The model, developed by the same authors, is the Localised Turbulent Scale Model (LTSM), that proposes a unified (generalized) closure of the chemical source term covering all the regimes of turbulent premixed combustion. This model founds on the estimation of the local reacting volume fraction of a computational cell, that is related to the local turbulent and laminar flame speeds and to the local flame thickness. Simulations were performed on CRESCO3 and CRESCO4 platforms.

## 1 Modelling the Chemical Source Term

The Localised Turbulent Scale Model (LTSM) developed by these authors aims to model the chemical source terms in the reactive Navier-Stokes equations for turbulent combustion. The Favre filtered chemical source term in the energy and single species transport equations is here modelled as  $\tilde{\omega}_i \approx \gamma^* \omega_i^*$ ,  $\gamma^*$  and  $\omega_i^*$  being the local reacting volume fraction of the computational cell and the reaction rate of the  $i$ -th chemical species, respectively.

The local reacting volume fraction is defined as  $\gamma^* = \mathcal{V}_{\mathcal{F}}^* / \mathcal{V}_{\Delta}$ ,  $\mathcal{V}_{\mathcal{F}}^*$  and  $\mathcal{V}_{\Delta}$  being the reacting and the total volumes of the computational cell. In particular, the suggested Localized Turbulent Scales Model (LTSM) estimates the local reacting volume fraction  $\gamma^*$  assuming that a flame front having a surface area  $\mathcal{A}_{\mathcal{F}}$  and thickness  $\delta_{\mathcal{F}}$  is contained in a computational cell volume of characteristic size  $\Delta = \mathcal{V}_{\Delta}^{1/3}$ , i.e.,

$$\gamma^* = \frac{\mathcal{V}_{\mathcal{F}}^*}{\mathcal{V}_{\Delta}} \approx \frac{\mathcal{A}_{\mathcal{F}} \delta_{\mathcal{F}}}{\mathcal{V}_{\Delta}} \approx \frac{\mathcal{S}_{\mathcal{T}}}{\mathcal{S}_{\mathcal{L}}} \mathcal{A}_{\mathcal{L}} \frac{\delta_{\mathcal{F}}}{\mathcal{V}_{\Delta}} \approx \frac{\mathcal{S}_{\mathcal{T}}}{\mathcal{S}_{\mathcal{L}}} \Delta^2 \frac{\delta_{\mathcal{F}}}{\Delta^3} = \frac{\mathcal{S}_{\mathcal{T}}}{\mathcal{S}_{\mathcal{L}}} \frac{\delta_{\mathcal{F}}}{\Delta}. \quad (1)$$

This expression has been obtained with two main assumptions. The first is that within a wrinkled flame front the iso-surfaces of the progress variable are parallel. The second assumption is that the ratio between the turbulent and the laminar flame surface areas scales as the ratio between the associated flame speeds, i.e.,  $\mathcal{A}_{\mathcal{F}} / \mathcal{A}_{\mathcal{L}} \equiv \mathcal{A}_{\mathcal{T}} / \mathcal{A}_{\mathcal{L}} \approx \mathcal{S}_{\mathcal{T}} / \mathcal{S}_{\mathcal{L}}$ .

---

\*Corresponding author. E-mail: [eugenio.giacomazzi@enea.it](mailto:eugenio.giacomazzi@enea.it).



With this modeling, subgrid flame front wrinkling and curvature effects are synthesized in this ratio. It is reminded that the laminar flame speed can be estimated as  $\mathcal{S}_{\mathcal{L}} \approx (\alpha/\tau_{ch})^{1/2}$ , the laminar flame thickness as  $\delta_{\mathcal{L}} \approx (\alpha\tau_{ch})^{1/2}$ , and that these two expressions imply  $\frac{\delta_{\mathcal{L}}\mathcal{S}_{\mathcal{L}}}{\alpha} = 1$ . The quantity  $\alpha = k/(\rho C_p)$  is the thermal diffusivity, with  $k$  being the thermal conductivity,  $\rho$  the density and  $C_p$  the specific heat at constant pressure.

It is observed that the local flame at the base of Eqn. (1) may be laminar or turbulent, wrinkled or not, thickened by turbulence or not, depending on the local conditions of the flow. In particular, for a local laminar (planar) flame Eqn. (1) reduces to  $\gamma^* \approx \delta_{\mathcal{F}}/\Delta$ . When combustion is locally volumetric,  $\gamma^* = 1$ . Equation (1) refers to a laminar or turbulent wrinkled flame front with  $\gamma^* < 1$ .

An extinction or flame stretch factor  $\mathcal{G}_{ext} \leq 1$  is introduced to take into account flame quenching due to subgrid scales. This factor has effect on  $\gamma^*$  that is finally given by  $\gamma^* = \mathcal{G}_{ext} \frac{\mathcal{S}_{\mathcal{L}}}{\mathcal{S}_{\mathcal{L}}} \frac{\delta_{\mathcal{F}}}{\Delta}$ . The problem of  $\gamma^*$  estimation becomes the problem of estimating the characteristics of the local flame front in terms of its turbulent flame speed, laminar flame speed and thickness (turbulent or laminar) from the filtered conditions of the flow and depending on the related local premixed combustion regime. Models (not reported here) to derive the turbulent quantities are proposed within the Localised Turbulent Scale Model. To derive such models, interaction between vortices and a flame front is analysed. The range of scales that can interact with a flame front, and eventually enter into, is identified to model local flame thickening due to turbulence. The smallest turbulent scales that apply the highest strain rate and curvature wrinkling onto the flame front are also identified to model local flame quenching due to turbulence. Three main combustion regimes are identified based on the comparison between the local laminar flame front  $\delta_{\mathcal{L}}$ , the local turbulent macro-scale  $l_{\Delta}$ , and the local turbulent dissipative scale  $\eta$ . These regimes are named  $\mathcal{V}_{\mathcal{R}}$  from *Volumetric Regime*,  $\mathcal{TTC}_{\mathcal{R}}$  from *Thickened, Turbulence – Thickened, Corrugated Regimes*,  $\mathcal{W}_{\mathcal{R}}$  from *Wrinkled Regime*. The LTSM models the local reacting volume fraction in these regimes.

## 2 Model Validation

The Localised Turbulent Scale Model has been validated by simulating a test case defined and simulated by these authors using the Direct Numerical Simulation approach. In particular, the time average and rms fluctuation of some quantities resulted from the LES simulation were compared with their DNS counterpart.

The test case consists in an unconfined and atmospheric Bunsen flame developing along the streamwise direction ( $z$ ), as shown in Fig. 1. This premixed flame is produced by three adjacent rectangular slot burners whose size is undefined in the spanwise direction ( $x$ ) and that are separated along the transversal direction ( $y$ ) by means of two 0.17 mm thick walls. The central slot burner injects a fresh mixture of methane, hydrogen and air, while the two side burners inject hot combustion products of the same central mixture. This test case was selected because a slot Bunsen flame represents one of the major categories of turbulent premixed combustion. It is also interesting to analyse the effect of hydrogen added to methane, due to the increasing interest in hydrogen enriched natural gas.

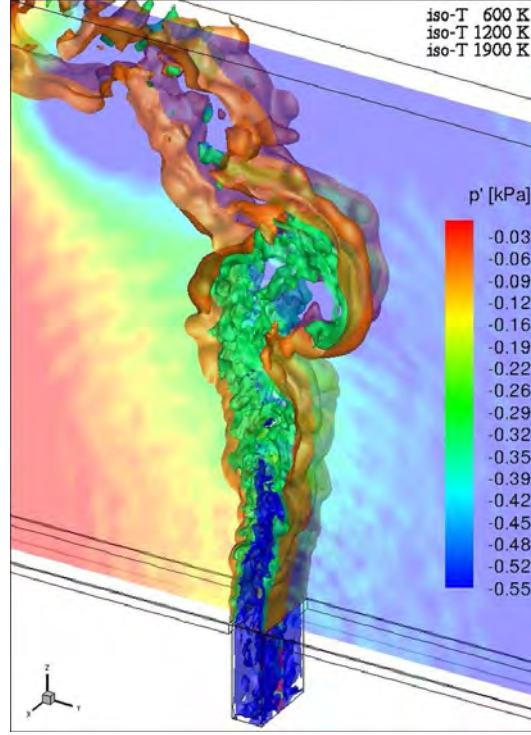


Figure 1: Instantaneous temperature iso-surfaces and pressure fluctuations in the middle plane.

The reactant mixture, with an equivalence ratio  $\Phi = 0.7$  and with 0.2 mole fraction of hydrogen, is injected from the central slot with a bulk velocity of  $100 \text{ m s}^{-1}$  and at  $600 \text{ K}$ . The velocity of the coflow stream is  $25 \text{ m s}^{-1}$ . The central jet Reynolds number is 2264, based on the width of the jet,  $1.2 \text{ mm}$ , its bulk velocity, and the kinematic viscosity  $5.3 \cdot 10^{-5} \text{ m}^2 \text{ s}^{-1}$ . Homogeneous isotropic turbulence is forced at the inlet. Such turbulence is artificially produced by means of a synthetic turbulence generator implemented from [1]. In particular, the spatial correlation length scales and velocity fluctuations provided as input to this generator are:  $L_{zz} = 0.8 \text{ mm}$ ,  $L_{xx} = L_{yy} = L_{zz}/2 = 0.4 \text{ mm}$ ,  $u'_z = u'_x = u'_y = 12 \text{ m s}^{-1}$  with no shear stresses (the Reynolds stress tensor is diagonal).

The actual velocity fluctuation at the end of the injection channel is  $u' \approx 12 \text{ m s}^{-1}$ , and the turbulent length scale is  $l_t \approx 1 \text{ mm}$ . These data are used in the calculation of the characteristic numbers associated to the present jet premixed flame.

The central jet turbulent Reynolds number is 226, based on the rms velocity fluctuation,  $12 \text{ m s}^{-1}$ , the integral scale,  $1 \text{ mm}$ , and the previous kinematic viscosity. The Kolmogorov length scale is  $\eta \approx 17.22 \mu\text{m}$ . The adiabatic flame temperature is  $2071 \text{ K}$ . The laminar flame speed and flame front thickness at these conditions are  $\mathcal{S}_{\mathcal{L}} = 0.96 \text{ m s}^{-1}$  and  $\delta_{\mathcal{F}} = 0.386 \text{ mm}$ , respectively. Hence,  $u'_{rms}/\mathcal{S}_{\mathcal{L}} = 12.5$  and  $L_t/\delta_{\mathcal{F}} = 2.6$ ;  $Ka_{\eta} = 503$ ,  $Da_{L_t}^I = 0.21$ .

This test was performed on a three-dimensional computational domain with 61 nodes in the

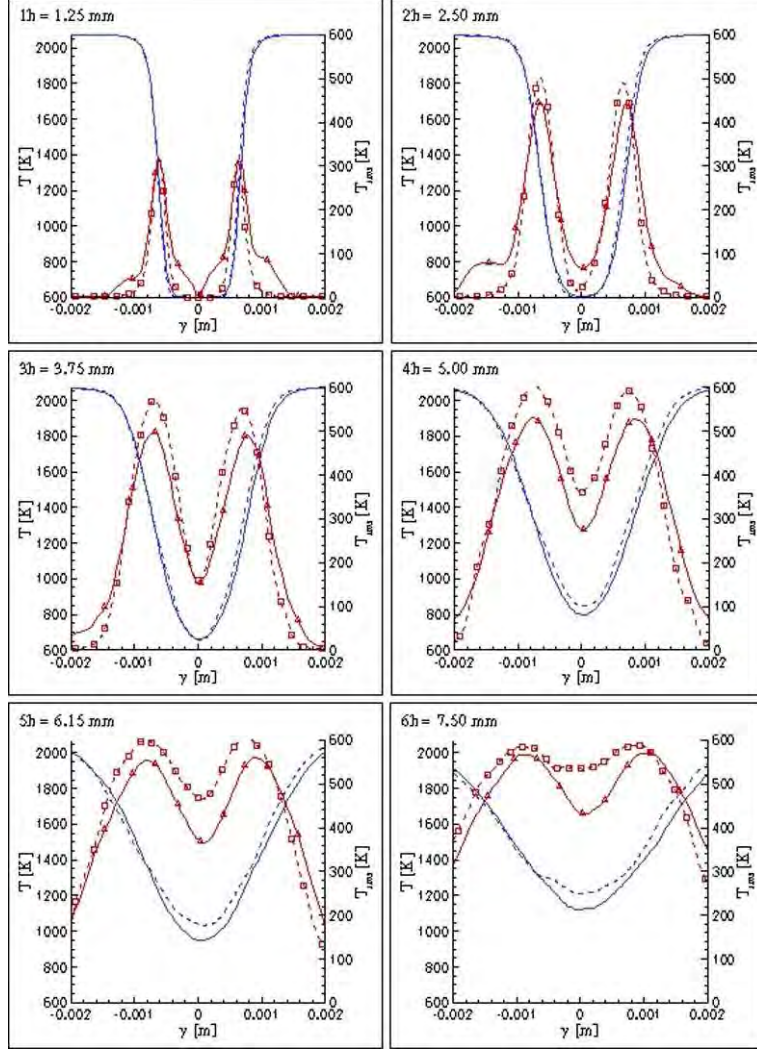


Figure 2: Transversal average and rms temperature profiles at several heights above injection: comparison between LES (solid lines) and DNS data (dashed lines). Lines with symbols are rms fluctuations.

spanwise direction ( $x$ ), extending from  $-1.5$  to  $1.5$  mm, and along which periodic boundary conditions are forced. The computational domain has four zones: a central injection zone extending from  $-4$  mm to  $0$  in the streamwise direction ( $z$ ) with a width (along  $y$ ) of  $1.2$  mm and with  $60 \times 35$  nodes ( $zy$ ); two surrounding zones extending from  $-0.4$  mm to  $0$  in the streamwise direction and from the central slot external wall (wall thickness  $0.17$  mm) up to  $18$  mm outward in the transversal direction ( $y$ ) with  $8 \times 89$  nodes ( $zy$ ); a main mixing and reacting zone downstream of the injection extending from  $0$  to  $24$  mm in the streamwise direction and from  $-18$  mm to  $18$  mm in the transversal direction with  $241 \times 221$  nodes ( $zy$ ). The whole computational domain has  $56785 \times 61 = 3463885$  nodes.

Seventeen species are transported:  $\text{CH}_4$ ,  $\text{H}_2$ ,  $\text{O}_2$ ,  $\text{N}_2$ ,  $\text{OH}$ ,  $\text{O}$ ,  $\text{H}$ ,  $\text{HO}_2$ ,  $\text{H}_2\text{O}_2$ ,  $\text{CH}_3$ ,  $\text{CH}_2$ ,

CH, CH<sub>2</sub>O, HCO, CO, CO<sub>2</sub>, H<sub>2</sub>O. The chemical mechanism adopted for combustion is a skeletal mechanism having 58 reactions [2]. The walls are assumed viscous and adiabatic. Partially non-reflecting outflow boundary conditions were imposed at the open boundaries of the computational domain. The subgrid scale model adopted for the turbulence closure is the dynamic Smagorinsky model.

Temperature, streamwise and transversal velocities and mass fractions predicted through the LES simulation were compared with DNS data, in terms of their time averages and rms fluctuations transversal profiles at different heights above injection (see Fig. 2 for example). The comparison shows the goodness of the LTSM model.

## References

- [1] Klein M., Sadiki A., and Janicka J. A digital filter based generation of inflow data for spatially developing direct numerical or large eddy simulations. *J. of Comp. Physics*, 186:652–665, 2003.
- [2] Smooke M. D., Puri I. K., and Seshadri K. A comparison between numerical calculations and experimental measurements of the structure of a counterflow diffusion flame burning diluted methane in diluted air. In *Proceedings of the 22nd Symposium International on Combustion, The Combustion Institute*, volume 21, pages pp. 1783–1792, 1988.

# Modelling the exchange flow dynamics through the Turkish Strait System

*Gianmaria Sannino<sup>1\*</sup>, Adil Sözer<sup>2</sup>, and Emin Özsoy<sup>2</sup>*

*<sup>1</sup>ENEA Casaccia Research Center, UTMEA  
Via Anguillarese 301, 00123 – Rome, Italy*

*<sup>2</sup>Institute of Marine Sciences, Middle East Technical University (IMS-METU)  
Erdemli, Mersin, Turkey*

**ABSTRACT.** The system composed by the two narrow Straits, Dardanelles and Bosphorus, and the Marmara Sea is known as the Turkish Straits System (TSS). The scientific questions on the role of the TSS in coupling the adjacent basins of the Mediterranean and Black Seas with highly contrasting properties and in a region of high climatic variability can only be answered by model predictions of the processes that determine the integral properties of the coupled sub-systems. This can only be achieved if the entire TSS is modelled as a finely resolved integral system that appropriately accounts for the high contrasts in seawater properties, steep topography, hydraulic controls, fine and meso-scale turbulence, nonlinear and non-hydrostatic effects, thermodynamic states and an active free-surface in the fullest extent, based on well represented fluid dynamical principles. In this study the MITgcm (MIT General Circulation Model) is used at very high resolution to study this extreme environment that needs to be represented as a whole and with the full details of its highly contrasting properties. The capability of MITgcm to represent the two-layer exchange dynamics both in the straits and in the Marmara Sea is examined. The non-uniform grid and the vertical resolution implemented have demonstrated to be suitable to capture the fine scales within the two Straits and also to well represent mesoscale in the Marmara Sea. The response of the currents and density structure over the water column to different net flow is also examined through the setup of experiment with varying net barotropic volume fluxes.

## 1 Introduction

In this work the Massachusetts Institute of Technology general circulation model (MIT-gcm, <http://mitgcm.org>) is used to study TSS with full details of its contrasting properties. The model domain chosen extends over the entire TSS, including also parts of the north-east Aegean Sea and the Black Sea at its two ends. A non-uniform curvilinear orthogonal grid covers the domain at variable resolution: from less than 50 m in the two Straits up to about 1 km in the Marmara Sea. To adequately resolve the complex hydraulic dynamics of the TSS, the model grid is made by 100 inhomogeneous distributed

---

\*Corresponding author. E-mail: [gianmaria.sannino@enea.it](mailto:gianmaria.sannino@enea.it).

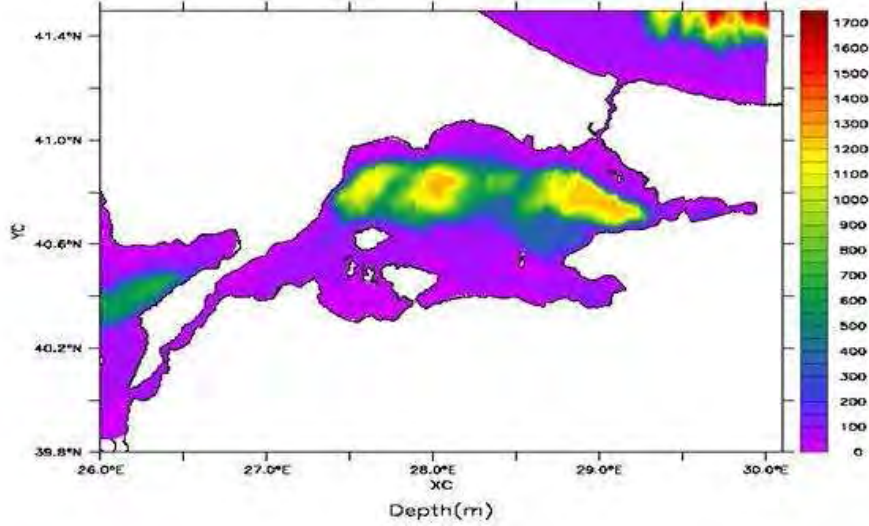


Figure 1: Model bathymetry (colorbar: depth in m).

vertical  $z$ -levels. The thickness exponentially ranges from 1.2 m at the surface to 80 m at the bottom with most of the levels concentrated in the first 100 m. The very high horizontal resolution adopted in MITgcm, together with the partial cell formulation result in a very detailed description of the bathymetry (Fig. 1). The model has been initialized with three different water masses filling the western part of the domain, the Marmara Sea and the eastern side of the domain respectively, with vertical profiles selected from CTD casts obtained during the cruise of the R/V BILIM of the Institute of Marine Sciences in June–July 2013. With the initial condition specified as lock-exchanges at the two straits, the model is left free to adjust to the expected two-way exchange. No-slip conditions were imposed at the bottom and lateral solid boundaries. The very high resolution adopted in the current model configuration forced the authors to use both the CRESCO and PRACE (Partnership for Advanced Computing in Europe) facilities. In particular part of the simulations showed in this report have been carried out on the IBM Power 775 (called Boreasz) installed at the Maciej Cytowski, ICM, University of Warsaw.

## 2 Results

The non-uniform curvilinear orthogonal grid and the vertical resolution implemented have demonstrated to be sufficient to capture the fine scales within the two Straits and also to well represent mesoscale in the Marmara Sea. The response of the currents and density structure over the water column to different net flow is also examined through the setup of experiments with varying net barotropic volume flux values ( $Q = -9600, 0, 5600, 9600, 18000$  and  $50000 \text{ m}^3/\text{s}$  respectively). Positive values of  $Q$  represent flow from the Black Sea towards the Mediterranean, while negative values represent net flow in the opposite direction. The free surface variations in the Marmara Sea, corresponding to configurations initialized with vertical profiles representative of the three basins selected from CTD casts in June–July 2013 and variable values of net barotropic flow values are shown in Fig. 3.



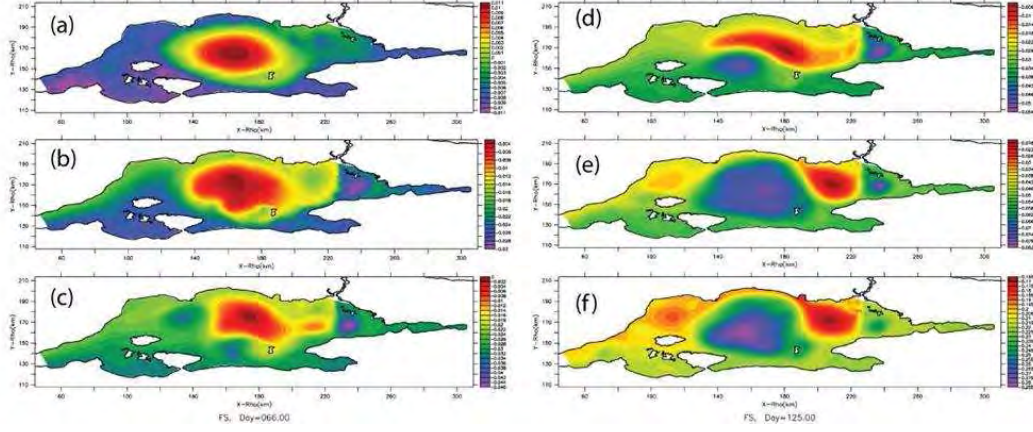


Figure 2: The free surface variations in the Marmara Sea for varying net barotropic volume flux values of: (a)  $Q = -9600 \text{ m}^3/\text{s}$ , day=67, range=2.2 cm; (b)  $Q = 0 \text{ m}^3/\text{s}$ , day=100, range=2.7 cm; (c)  $Q = 5600 \text{ m}^3/\text{s}$ , day=66, range=4.5 cm; (d)  $Q = 9600 \text{ m}^3/\text{s}$ , day=22, range=4.8 cm; (e)  $Q = 18000 \text{ m}^3/\text{s}$ , day=65, range=6.4 cm; (f)  $Q = 50000 \text{ m}^3/\text{s}$ , day=125, range=12.0 cm.

### 3 Discussion

For the studied flows driven solely by the net flux, an *S*-shaped current first moving south from the Bosphorus, later turning northwest and finally exiting from the Dardanelles Strait appears to be the basic character of the circulation. With a negative flux of  $Q = -9600 \text{ m}^3/\text{s}$ , such that the net flow is towards the Black Sea, the upper layer flow from the Bosphorus into the Marmara Sea is still positive, and sufficient to generate an anticyclonic net circulation in the midst of the Marmara Sea, as shown in Fig. 2.

For zero net flux, the same structure is preserved and as the positive values of the barotropic flux is increased further the size of the central gyre is reduced and the flow becomes increasingly more attached to the northern coast of the Marmara Sea. As the flux is increased to  $9600 \text{ m}^3/\text{s}$ , the central anticyclonic circulation cell takes an elongated form. For the extreme flux values of  $Q = 18000 \text{ m}^3/\text{s}$  and  $Q = 50000 \text{ m}^3/\text{s}$ , the lower layer flow in the Bosphorus becomes blocked, and qualitative changes occur in the circulation of the Marmara Sea, with a smaller anticyclone near the Bosphorus exit, a jet attached to the northern coast, and a secondary anticyclone further west, and a cyclonic circulation emerging in the south. For these cases, the circulation pattern looks more like the buoyancy driven flow along the coast adjacent to the mouth of a river. The generation of a basic anticyclonic circulation in the Marmara Sea for lower net fluxes, evolving towards a more balanced circulation of cyclonic–anticyclonic eddies appears to be a result of the vorticity balance of the basin.

As shown by [1], and studied by [2], the net basin circulation is sensitively determined by the potential vorticity (PV) imports and exports of the basin. From this point of view, the reduction of interface depth (or upper layer thickness) from the Black Sea to the Marmara Sea implies a decrease in fluid vorticity, or anticyclonic circulation assuming the

Net Flux $Q$ ( $\text{m}^3/\text{s}$ )	Bosphorus (TSS) sea level difference $\Delta\eta$ (cm)	Dardanelles (TSS) sea level difference $\Delta\eta$ (cm)	Bosphorus (ROMS) sea level difference $\Delta\eta$ (cm)
-9600	2	1.5	-
0	8	5	14
5600	10	7	18
9600	14	11	22
18000	22	16	30
50000	85	32	-

Table 1: Sea Level Difference at both edges of the two straits as a function of net flux.

input to have zero vorticity. The behaviour of the buoyant plume entering the Marmara Sea, initially shooting south and hitting the opposite coast is displayed in all cases in Fig. 2, although the later turning of the flow to the west is typical of buoyant plumes at this scale. Buoyant flows entering the sea are typically attached to the right hand coast (looking out from the exit in the northern hemisphere, especially for initial vorticity zero below a critical limit e.g. [3, 4]). Often a bulge of the buoyant fluid is formed, as the flow turns right to follow the coast, as often observed at river mouths (e.g. [5]). In a two-layer system with variable bottom topography and dynamically active layers, the circulation may develop differently, with topography influencing the lower layer flow, and the resultant interface topography influencing the upper layer flow [6]. As the net flux is increased in Fig. 2, the changes in the circulation pattern may be a result of this kind of interactive adjustment of the flow layers to bottom and interface topography. The qualitative change in the circulation towards a series of anticyclonic and cyclonic eddies following the meander of the currents, when the flux is increased to  $18000 \text{ m}^3/\text{s}$  and  $50000 \text{ m}^3/\text{s}$  is reminiscent of the Alboran Sea, where similar gyres filling the basin develop under high fluxes [1]. The sea level differences that develop at the two straits, Bosphorus and Dardanelles are given in Table 1, in relation to the net barotropic fluxes and the values obtained from the TSS model are compared with the ROMS model results for the Bosphorus [7]. While the total range of sea level in the Marmara Sea between cyclonic and anticyclonic areas varies between 2–12 cm (Fig. 2), the net sea level differences across straits are much larger, varying between 2–85 cm in the Bosphorus and 1–32 cm in the Dardanelles, while the results for the Bosphorus compare well between the two models. These results would imply sea level differences of about 0–120 cm between the Black Sea and the Aegean Sea, for the range of net transport tested. Finally a comparison is made of the upper-layer ( $Q_1$ ) and lower-layer ( $Q_2$ ) volume fluxes through the Bosphorus, based on observational data and the results from the Bosphorus model (ROMS) of Sözer (2013) and the TSS (MITgcm) models. Although the Bosphorus model is more specific to the Strait and has better resolution, the TSS model results perform even better in comparison with observations.



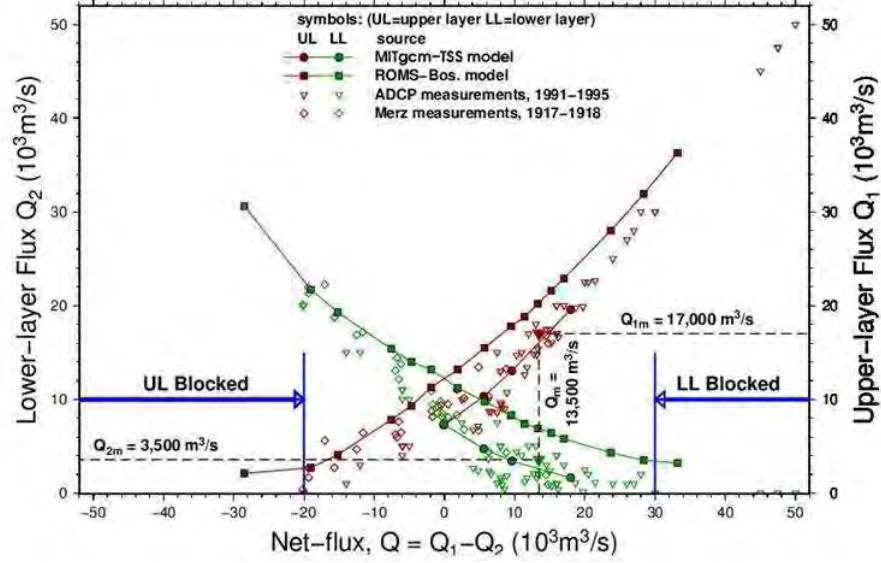


Figure 3: Upper-layer ( $Q_1$ ) and lower-layer ( $Q_2$ ) volume fluxes through the Bosphorus as a function of the net flux ( $Q = Q_1 - Q_2$ ), based on observational data and compared with the results from the Bosphorus model (ROMS) of Sözer (2013) and the TSS (MITgcm) models.

## References

- [1] Spall M. and Price J. F. Mesoscale variability in denmark strait: The pv outflow hypothesis. *J. Phys. Ocean.* 28, pages 1598–1623, 1998.
- [2] Morrison A. Upstream basin circulation of rotating, hydraulically controlled flows. *2011 Summer Program in Geophysical Fluid Dynamics, WHOI, 429pp.*, 2011.
- [3] Nof D. On geostrophic adjustment in sea straits and wide estuaries: Theory and laboratory experiments. Part II – Two-Layer System. *J. Phys. Ocean.* 8, pages 861–872, 1978.
- [4] Stern M., Whitehead J., and Hua B. The intrusion of a density current along the coast of a rotating fluid. *J. Fluid Mech.* 123, pages 237–265, 1982.
- [5] Huq P. Buoyant outflows to the coastal ocean, handbook of environmental fluid dynamics, volume one. *edited by H. J. S. Fernando. CRC Press, Taylor & Francis Group, LLC*, pages 1:207–215, 2013.
- [6] Beardsley R. C. and Hart J. A simple theoretical model for the flow of an estuary on to a continental shelf. *J. Geophys. Res.*, 83, pages 873–883, 1978.
- [7] Sözer A. Numerical modeling of the bosphorus exchange flow dynamics. *Ph.D. thesis, Institute of Marine Sciences, Middle East Technical University, Erdemli, Mersin, Turkey*, 2013.

# Voting Dynamics as an Open Problem in Non-equilibrium Statistical Mechanics

Filippo Palombi<sup>1\*</sup> and Simona Toti<sup>2</sup>

<sup>1</sup>*ENEA Frascati Research Center, UTICT-HPC  
Via E. Fermi 45, 00044 – Frascati, Italy*

<sup>2</sup>*Italian National Institute of Statistics  
Via C. Balbo 16, 00184 – Rome, Italy*

**ABSTRACT.** Results of political elections can be regarded as snapshots of a complex social dynamics. Our computational activity on CRESCO focused on the possibility of understanding whether and to what extent empirical vote distributions can be reproduced by stochastic models based on agents interacting over complex networks.

## 1 New frontiers in Statistical Mechanics

A quantitative description of interacting many-body systems has been the goal of statistical mechanics since the pioneering work by Boltzmann. As universally known, if a particle system with Hamiltonian coordinates  $(q, p)$  and energy  $\mathcal{H}(q, p)$  is coupled to a thermal *reservoir* at temperature  $T$ , the probability of finding the system in a small region around  $(q, p)$  is given by

$$dP(q, p) = \frac{\exp \left\{ -\frac{\mathcal{H}(q, p)}{k_B T} \right\} dq dp}{\int \exp \left\{ -\frac{\mathcal{H}(q, p)}{k_B T} \right\} dq dp}, \quad (1)$$

with  $k_B$  denoting the universal Boltzmann constant. A system behaving according to eq. (1) wanders in thermal equilibrium around the minimum  $(\bar{q}, \bar{p})$  of  $\mathcal{H}$ , with fluctuations exponentially damped at a rate proportional to the energy of the system (measured in units of thermal energy). While the configuration space endowed with the Boltzmann measure eq. (1) is known as the *canonical ensemble*, the above is just one possible formulation of equilibrium statistical mechanics, others being the *microcanonical ensemble* and the *grancanonical* one [1].

Although the Boltzmann law eq. (1) governs a universe of physical systems (with application domains ranging from material science to elementary particle physics), there is a number of many-body systems, mostly made of living organisms, which have nothing to

---

\*Corresponding author. E-mail: [filippo.palombi@enea.it](mailto:filippo.palombi@enea.it).

do with eq. (1), as they do not admit any Hamiltonian description nor are they in thermal equilibrium with any kind of *reservoir*. Among countless examples, the reader could take as references complex systems such as firing neurons in animal brains, human beings interacting in social networks, biological (computer) viruses spreading across communities (WAN), *etc.*

Such systems have attracted the interest of statistical physicists over the past years, for several good reasons. One main motivation is represented by the lack of universal laws such as eq. (1) to describe non-Hamiltonian systems; another one is the very possibility of statistically describing systems, where each degree of freedom differs from all the others to an essential extent. Just as an example, take a pot of boiling water: all  $H_2O$  molecules, which are part of the system, are perfectly identical, thus a statistical description of the system on a macroscopic scale does not seem to be unreasonable. By contrast, think about neurons in a human brain: each neuron has a unique position in the neural network and a specific functionality, which makes it almost unique in its environment. Is a mathematical description of such a system in terms of statistical laws even just conceivable? Questions like this lie at the heart of what is currently known as *non-equilibrium statistical mechanics*.

## 2 Voting dynamics in real elections

A complex non-equilibrium phenomenon of the kind described in the previous section is represented by the voting behaviour of people in political elections. The reader could hardly imagine statistical regularities emerging in a voting process. Yet, it was shown in ref. [2] that a high degree of universality characterizes proportional elections with open lists. Recall that in proportional elections political parties compete by proposing lists of local candidates in different electoral constituencies. Votes are assigned to parties and preferences to candidates. House seats are then decided on a proportional basis. The number of candidates in an open list depends by definition on the party and the electoral constituency.

---

*Now, if  $v$  denotes the number of preferences assigned to a candidate in a constituency,  $Q$  represents the number of candidates proposed by the party in a constituency and  $N$  is the total number of votes assigned to the party in a constituency, then the average number of votes per candidate is given by  $N/Q$  and the variable  $x = vQ/N$  describes the excess of votes received by a candidate with respect to the average of all competitors from the same party. It turns out that the statistical distribution  $\mathcal{F}(x)$  of  $x$  is universal: it has been the same in a large number of elections held across different countries (Italy, Poland, Finland, Denmark, Estonia, etc.) in the course of time, see ref. [2] for details.*

---

While non-trivial and remarkable, the universal shape of  $\mathcal{F}(x)$  is not unrelated to the voting rules. Indeed, a recent extension of the analysis performed in [2] to countries implementing proportional electoral systems with open lists *and additional (and/or slight variations of the) voting rules*, shows that universality can be broken in various ways [3]. An interesting case is represented by Brazil, whose political elections have been first studied in [4]. Here, the distribution of the excess of votes breaks the universality pattern only

for  $x < 1$ . Since the only deviation from standard proportional systems with open lists introduced by Brazil is that voting is there compulsory, the Brazilian case can perhaps help shed light on the origin of the observed universality.

### 3 The Voter model

A simple mathematical framework to describe voting processes is represented by the voter model (VM). The original construction, proposed by Clifford and Sudbury in 1973 [5] and by Holley and Liggett in 1975 [6] is an agent-based binary model with a Markovian stochastic dynamics. Agents can cast their votes for the Democratic Party or the Republican Party. At the beginning, votes are assigned at random among the agents. The system evolves afterwards via agent-agent interactions. On each step of the dynamics, an agent chooses a partner from her neighbours and just inherits her vote. This plain interaction rule encodes the idea that human interactions bring people closer to each other. Owing popularity to its exact solvability on a lattice in any dimension, the VM has been studied in a number of variants. We refer the reader to ref. [7] for a comprehensive review of the relevant literature.

### 4 Candidates and community-based networks

Since the beginning of 2013 we are committed to a project aimed at understanding whether and to what extent voter models defined over heterogeneous networks are suitable to describe results of real political elections, see [8, 9]. Since agents express a political preference at each time, the VM looks indeed suitable to describe real proportional elections with compulsory voting, such as the Brazilian ones. Is this statement correct? It is not easy to figure out the answer. First, in order to adapt the VM to the Brazilian electoral system, at least two modifications have to be introduced:

- the VM is a binary model, unfit to describe elections with more than two candidates. Turning to a multi-state variant, such as considered for instance in [10] is however of no problem;
- the stochastic dynamics of both the binary VM and its multistate variant drives ultimately the system towards consensus, a uniform state where all agents share the same political preference. The simplest way to avoid this seems to be the use of committed agents (also known in the literature as *zealots*), that is to say agents who never change political position, while taking part in the stochastic dynamics as opinion donors. Zealots have been originally introduced in [11] in the framework of the binary VM and have been subsequently used by several authors to investigate various aspects of opinion dynamics. It is legitimate to interpret political candidates as zealots and in practice it is sufficient to insert  $Q$  zealots (representing candidates from the same party list) among the voters to avoid consensus states.

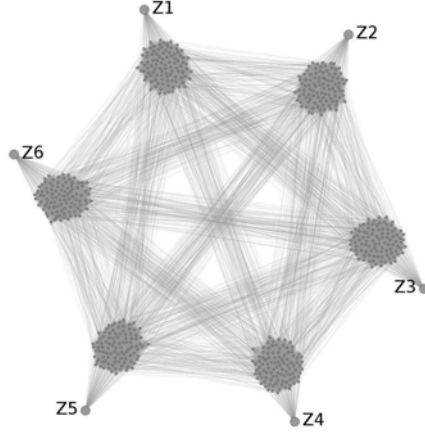


Figure 1: An example of the network topology considered in ref. [8] with  $Q = 6$ .

Now, the model is completely defined once we assign a social network, *i.e.* we specify the set of neighbours of each agent. How should this be done? There various considerations to take into account. First of all, we expect that the stochastic dynamics of the system depends on the chosen network; the extent to which results hang on the network topology is however largely unknown. Secondly, if a candidate takes a favoured topological position among the voters, we expect her to have more chances to polarize the whole network in her favour; the lack of *a priori* information suggests therefore to restrict the attention to symmetric networks only. Thirdly, the network should be stochastically assigned. Fourthly, if we aim at understanding the suitability of the VM to describe real proportional elections, the topological structure of the network should be sufficiently simple to allow for analytic calculations. To fulfill the above and other indications, detailed in [8], we have considered the multi-state voter model with zealot candidates over a community-based network, represented by a graph  $G = (V, E)$  such as depicted in Fig. 1. Each node of it belongs to one of  $Q$  non-overlapping cliques (all having equal size  $\omega_1 = |V|/Q$ ); it is connected with certainty to any other node in its own clique and with finite probability  $p$  to nodes belonging to other cliques, apart from the  $Q$  zealots  $\{Z_k\}_{k=1}^Q$ . The latter distribute one-per-clique; they are connected with certainty to the nodes of their own clique, but never to the other nodes.

If  $v_k^{(m)}$  denotes the number of votes assigned to  $Z_k$  from the *dynamical* voters belonging to the  $m$ -th clique, then  $\phi_k^{(m)} = Qv_k^{(m)}/|V| = \omega_1^{-1}v_k^{(m)}$  represents the corresponding scaling variable in the language of ref. [2]. The equilibrium probability density of the system was shown in ref. [8] to obey with good approximation a multi-clique Fokker-Planck equation, namely

$$\begin{aligned}
0 = & - \sum_{i=1}^Q \sum_{\ell \neq i}^{1 \dots Q} \partial_\ell^{(i)} \left[ A_\ell^{(i)}(\bar{\phi}) \mathcal{P}(\bar{\phi}) \right] \\
& + \frac{1}{2} \sum_{i=1}^Q \sum_{\ell, m \neq i}^{1 \dots Q} \partial_\ell^{(i)} \partial_m^{(i)} \left[ B_{\ell m}^{(i)}(\bar{\phi}) \mathcal{P}(\bar{\phi}) \right] = \mathcal{L}_{\text{FP}} \cdot \mathcal{P}(\bar{\phi}), \tag{2}
\end{aligned}$$

where  $\partial_\ell^{(i)} \equiv \partial/\partial\phi_\ell^{(i)}$  and  $\mathcal{L}_{\text{FP}}$  denotes the stationary Fokker–Planck operator. Drift and diffusion coefficients are given respectively by

$$A_\ell^{(i)} = -[1 + \omega_1\omega_2(1 - \omega_1^{-1})]\phi_\ell^{(i)} + \frac{\omega_1\omega_2(1 - \omega_1^{-1})}{Q-1} \left\{ \sum_{k \neq i, \ell}^{1\dots Q} \phi_\ell^{(k)} - \sum_{k \neq \ell}^{1\dots Q} \phi_k^{(\ell)} \right\} + \frac{\omega_1\omega_2(1 - \omega_1^{-1})^2}{Q-1}, \quad (3)$$

$$\begin{aligned} B_{\ell m}^{(i)} = & -2(1 - \delta_{\ell m})\phi_\ell^{(i)}\phi_m^{(i)} \\ & - (1 - \delta_{\ell m})\frac{\omega_2}{(Q-1)} \left[ \phi_\ell^{(i)} \left( 1 - \omega_1^{-1} + \sum_{k \neq i, m}^{1\dots Q} \phi_m^{(k)} - \sum_{k \neq m}^{1\dots Q} \phi_k^{(m)} \right) \right. \\ & \quad \left. + \phi_m^{(i)} \left( 1 - \omega_1^{-1} + \sum_{k \neq i, \ell}^{1\dots Q} \phi_\ell^{(k)} - \sum_{k \neq \ell}^{1\dots Q} \phi_k^{(\ell)} \right) \right] \\ & + 2\delta_{\ell m}\phi_\ell^{(i)} \left[ 1 + \frac{\omega_2(1 - \omega_1^{-1}) - \omega_1^{-1}}{2} - \phi_\ell^{(i)} \right] \\ & + \delta_{\ell m}\frac{\omega_2}{(Q-1)} \left( 1 - \omega_1^{-1} - 2\phi_\ell^{(i)} \right) \left[ 1 - \omega_1^{-1} + \sum_{k \neq i, \ell}^{1\dots Q} \phi_\ell^{(k)} - \sum_{k \neq \ell}^{1\dots Q} \phi_k^{(\ell)} \right], \quad (4) \end{aligned}$$

where  $\bar{\phi} = \{\bar{\phi}^{(k)}\}_{k=1}^Q$  denotes the global state vector of the system,  $\bar{\phi}^{(m)} = \{\phi_k^{(m)}\}_{k \neq m}^{1\dots Q}$  represents the local state vector of the  $m$ -th clique and  $\omega_2 = p(Q-1)$  is an inter-clique coupling constant.

Having simulated the Fokker–Planck equation numerically, as described in ref. [8], we are currently working on the possibility of deriving semi-analytic solutions [9].

## 5 Monte Carlo simulations of the model

As explained above, competing candidates prevent the system from reaching exit configurations. The extremal states  $\sum_{k=1}^Q \phi_\ell^{(k)} = \omega_1^{-1}$  behave like reflecting boundaries in coordinate space. They make the microscopic dynamics of the model run endlessly. After a transient depending on the initial state, the voter configuration reaches a dynamic equilibrium governed by  $\mathcal{P}(\bar{\phi})$ . We explored this numerically by means of Monte Carlo simulations, run on CRESCO3 and CRESCO<sub>f</sub>. In the thermodynamic limit, defined by  $Q \rightarrow \infty$  and  $(\omega_1, \omega_2) = \text{const.}$ , the parameter space of the model is represented by the pairs  $(\omega_1, \omega_2)$ . At finite  $|V|$  the adjacency matrix of the network becomes denser as  $\omega_1$  and/or  $\omega_2$  increase. Simulations become in this limit more and more demanding, owing to both an increasingly severe memory requirement to host the model on a machine and an intrinsic enhancement of the autocorrelation time.

According to such restrictions and the computing power in our availability, we chose to simulate the model at  $\omega_1 = 1, 000.0, 2, 000.0$  and  $\omega_2 = 0.3, 0.6, 0.9$ . For each pair  $(\omega_1, \omega_2)$ ,

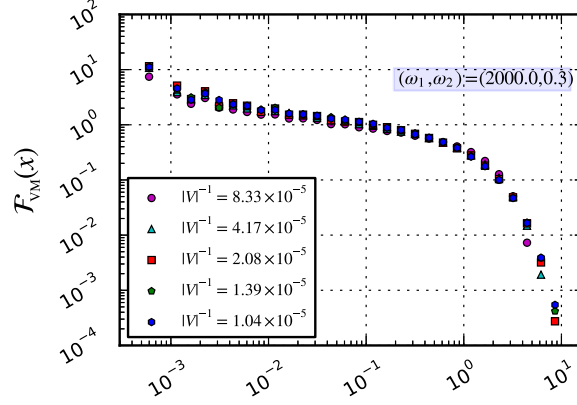


Figure 2: Distribution of the excess of votes at  $\omega_1 = 2,000.0$  and  $\omega_2 = 0.3$ .

we performed simulations at five values of  $|V|$ , so as to be able to observe clearly how the system approaches the thermodynamic limit. For each set of simulation parameters, we extracted randomly 20 network samples at  $\omega_1 = 1,000.0$  and 40 network samples at  $\omega_1 = 2,000.0$  and averaged results over them. All simulations started from a random configuration of voters, with political preferences assigned independently with a flat probability of  $1/Q$ . As an example, in Fig. 2 we show the distribution of the intra-party excess of votes at  $\omega_1 = 2,000.0$  and  $\omega_2 = 0.3$ . The plot resembles qualitatively the distribution observed in real Brazilian elections.

## 6 Conclusions

The present contribution reports on an ongoing project aimed at understanding whether and to what extent voter models over heterogeneous networks are suited to describe results of real political elections. In ref. [8], we explored the stochastic dynamics of the multi-state voter model over a social network, where people belong to cliques dominated by zealot candidates and contacts among different cliques are static and random. In the thermodynamic limit, the model is characterized by two parameters, representing respectively the size of the cliques and the frequency of the random contacts. We studied the equilibrium distribution of the vote variables by means of numerical simulations and analytic arguments based on mean field theory. We are currently involved in an attempt to derive (semi-)analytic solutions of the model [9].

## References

- [1] Huang Kerson. *Statistical Mechanics*. John Wiley & Sons, 2 edition, 1987.
- [2] Fortunato S. and Castellano C. Scaling and universality in proportional elections. *Phys. Rev. Lett.* 99, 138701, 2007.

- [3] Chatterjee A., Mitrović M., and Fortunato S. Universality in voting behavior: an empirical analysis. *Sci. Rep.* 3, 1049, 2013.
- [4] Costa Filho R. N., Almeida M. P., Andrade J. S., and Moreira J. E. Scaling behavior in a proportional voting process. *Phys. Rev. E*, 60(1):1067–1068, 1999.
- [5] Clifford P. and Sudbury A. A model for spatial conflict. *Biometrika*, 60(3):581–588,, 1973.
- [6] Holley R. and Liggett T. M. Ergodic theorems for weakly interacting infinite systems and the voter model. *The Annals of Probability*, 3(4):643–663, 1975.
- [7] Castellano C., Fortunato S., and Loreto V. Statistical physics of social dynamics. *Rev. Mod. Phys.* 81:591–646, 2009.
- [8] Palombi F. and Toti S. Stochastic dynamics of the multi-state voter model over a network based on interacting cliques and zealot candidates. *Journal of Statistical Physics*, Vol. 156, Issue 2, pages 336–367, 2014.
- [9] Palombi F. and Toti S. Use of dirichlet distributions and orthogonal projection techniques for the fluctuation analysis of steady-state multivariate birth-death systems. *arXiv:1411.5207*, 2014.
- [10] Starnini M., Baronchelli A., and Pastor-Satorras R. Ordering dynamics of the multi-state voter model. *J. Stat. Mech.*, P10027, 2012.
- [11] Mobilia M. Does a single zealot affect an infinite group of voters? *Physical Review Letters*, 91:028701, 2003.



# Benchmark of the CPMD code on the CRESCO clusters in ENEAGRID environment

*Radojka Vujasin<sup>1</sup>, Jasmina Grbovic Novakovic<sup>1</sup>, Nikola Novakovic<sup>1</sup>,  
Simone Giusepponi<sup>2\*</sup>, Massimo Celino<sup>2</sup>, Amelia Montone<sup>2</sup>*

<sup>1</sup>*University of Belgrade, Vinča Institute of Nuclear Sciences  
Department of Materials Science, P.O. Box 522, 11001 Belgrade, Serbia*

<sup>2</sup>*ENEA, C.R. Casaccia, via Anguillarese 301, 00123 Rome, Italy*

**ABSTRACT.** Hydrogen desorption from a hydride matrix is still an open field of research. For this purpose, we want to set up a numerical model to perform first principle calculations based on the density functional theory, using CPMD code. To evaluate the suitable computational demand, we performed benchmarks of the CPMD code on the HPC ENEA CRESCO computing facilities taking in to account also the energy cost issue.

## 1 Introduction

Recent research in terms of replacement of fossil fuels with alternative energy sources goes in favour of widespread use of hydrogen as an energy source. However, there are technological problems of hydrogen storage primarily for mobile applications, i.e. in the automotive industry. Storing hydrogen in gas cylinders and cryogenic tanks have safety problem due to high pressure and low temperature, respectively [1]. In the case of storage in a solid state, hydrogen is stored in the form of chemical compounds (metal/intermetallic and complex hydrides), or adsorbed on materials with large specific surface area, such as carbon nanostructures and nano-porous materials [2, 3, 4]. Solid state storage is the safest and the most effective way of hydrogen handling. However, this method for hydrogen storage has also disadvantages such as slow sorption process and high temperature of desorption in case of hydrides, and small volumetric density in solids with large specific surface area. Magnesium hydride ( $\text{MgH}_2$ ) is attractive material for hydrogen storage since it has suitable properties like high gravimetric (7.6 wt%) and volumetric densities ( $130 \text{ kg H}_2/\text{m}^3$ ), abundance, low price and non-toxicity. However, this hydride has not found wide industrial application because of its stability (enthalpy of formation is  $-75 \text{ kJ/mol H}_2$ ) and high desorption temperature  $T_d=720 \text{ K}$ , which give rise to slow hydrogenation/dehydrogenation kinetics. Various physical and chemical processes can be used to enhance  $\text{MgH}_2$  formation by promoting destabilization of  $\text{MgH}_2$  lattice or surface modification and/or structural deformation. Mechanical milling without or with additives, and using ion irradiation are

---

\*Corresponding author. E-mail: [simone.giusepponi@enea.it](mailto:simone.giusepponi@enea.it).

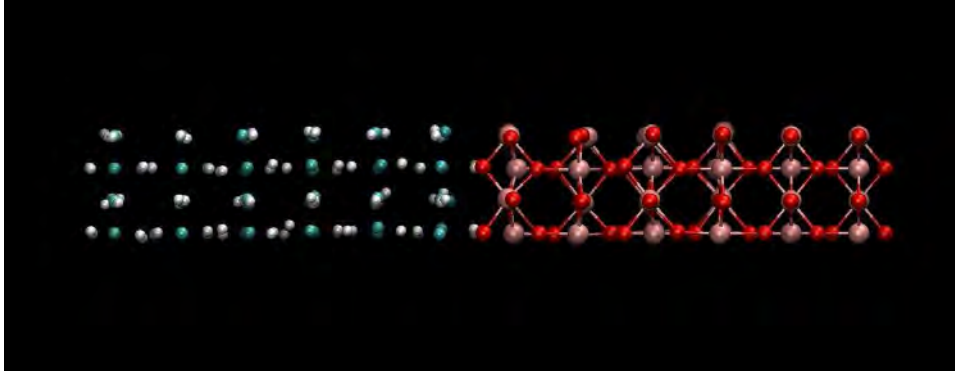


Figure 1: 1x1(110) slab supercell of  $\text{MgH}_2\text{-TiO}_2$  interface after geometry relaxation. Mg atoms are in light blue, H atoms are in white, Ti atoms are in pink and O atoms are in red.

some of the methods for destabilization of  $\text{MgH}_2$  structure [5, 6, 7, 8]. The most commonly used additives are transition metals and transition metal oxides [9, 10, 11, 12]. A number of experimental studies confirm that the addition of  $\text{TiO}_2$  has beneficial effect on destabilization of  $\text{MgH}_2$  matrix and can cause improvement of kinetic properties of this material [13, 14]. Several numerical studies on hydrogen motion on and through titanium oxide surface has been done to understand the mechanism of the reaction [15, 16]. Namely, hydrogen interaction with  $\text{TiO}_2$  surface is peculiar because the maximum H monolayers coverage on  $\text{TiO}_2$  (110) surface is only 70% at room temperature, regardless of applied partial pressure of hydrogen, and during the heating of the hydrogenated sample, there no hydrogen desorption with temperature rise. The most probable cause is H diffusion into subsurface area. However, mechanism of the effect of  $\text{TiO}_2$  on improving the kinetics properties of  $\text{MgH}_2$  is still unknown. This is the reason why we performed numerical studies on  $\text{MgH}_2\text{-TiO}_2$  interface. *Ab-initio* calculation based on density functional theory (DFT) implemented in Car-Parrinello Molecular Dynamics (CPMD) code was used [17, 18].

## 2 Computational details

CPMD code is an *ab-initio* electronic structure and molecular Dynamics (MD) program which uses a plane wave/pseudopotential implementation of DFT [19, 20]. In *ab-initio* MD simulation, the forces acting on atoms are calculated from an electronic structure calculation repeated every time step (on the fly). Thanks to electronic structure calculation which uses density functional methods, simulations of large systems with hundreds of atoms are now standard.

We use the CPMD compiled with Intel Fortran Compiler, MKL (Math Kernel Library), ACML (AMD Core Math Library) and MPI (Message Passing Interface) parallelization on the high performance ENEA CRESCO computing facilities [21]. We tested the CPMD code by using the system representing a  $\text{MgH}_2\text{-TiO}_2$  interface constituted by 48 atoms of Ti and Mg, and 96 atoms of O and H. The whole system was consisted of 288 atoms. For all the calculations we employed the CPMD code with Martins-Troullier norm-conserving

pseudopotentials for all atoms, together with The Perdew-Burke-Ernzerhof exchange-correlation functional [22, 23]. The electronic wave functions are expanded in a plane-wave basis set with a kinetic energy cut-off equal to 80 Ry.

### 3 Results and discussion

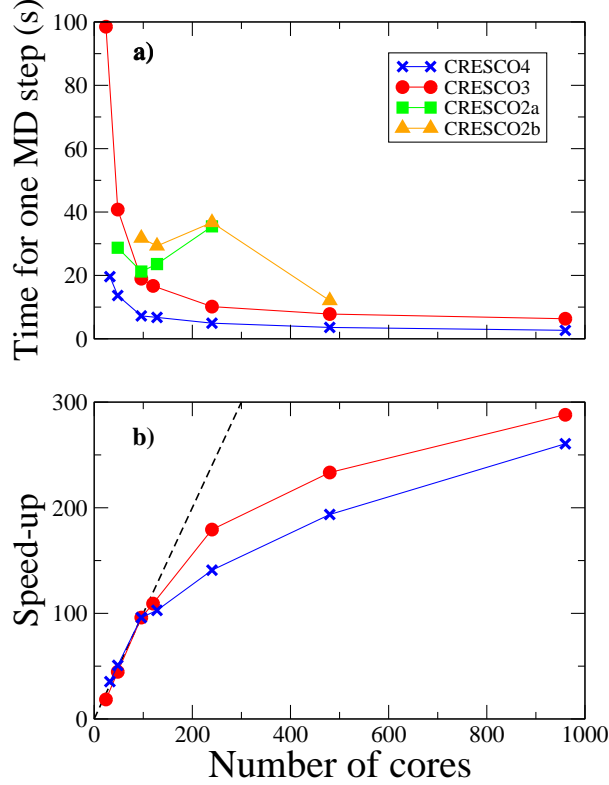


Figure 2: a) Average time for one MD step for different CRESCO clusters. b) Speed-up for CRESCO4 and CRESCO3 clusters.

Slab supercell of  $\text{TiO}_2$  and  $\text{MgH}_2$  surface was constructed by 45 degree rotation of rutile  $\text{TiO}_2$  (or rutile  $\text{MgH}_2$ ) unit cell around x-axis in order to expose its (110) plane. This cell was extended in x-direction, containing 12 atomic layers. A void region was on each side of the surface preventing the interaction between the external free surfaces. The final supercell parameters were  $L_x = 50.4 \text{ \AA}$ ,  $L_y = 12.6 \text{ \AA}$ , and  $L_z = 6.0 \text{ \AA}$ . Two outer layers in  $\text{TiO}_2$  slab, and two outer layers in  $\text{MgH}_2$  slab were fixed playing the role of bulk.  $\text{TiO}_2$ - $\text{MgH}_2$  interface was constructed using fully relaxed  $\text{TiO}_2$  and  $\text{MgH}_2$  surfaces (see Fig.1). Distance between internal surfaces was varied until the reaching the minimum of total energy of whole system.  $\text{TiO}_2$  and  $\text{MgH}_2$  have the same crystal structure with similar cell parameters and tailoring of interface should be with minimal strain. Total energy of the surfaces and interface was used to calculate work of adhesion  $W_a$  for  $\text{TiO}_2$ - $\text{MgH}_2$  interface and calculated value is  $W_a = 991.66 \text{ J/m}^2$ .

Molecular dynamics calculation was performed from 300 K to 1000 K in step of 100 K.

Table 1: Some of the hardware and software characteristics for the CRESCO clusters.

cores	CRESCO4	CRESCO3	CRESCO2a	CRESCO2b
Processor	Intel E5-2670	AMD 6234TM	Intel E5530	Intel E5345
Clock (GHz)	2.6	2.4	2.4	2.33
TDP (W)	115	115	80	80
Cores for node	$2 \times 8$	$2 \times 12$	$2 \times 4$	$2 \times 4$
RAM for node (GB)	64	64	16	16
Compiler	Ifort 14.0	Ifort 12.1	Ifort 11.0	Ifort 11.0
MPI Flavour	OpenMPI 1.4.3	OpenMPI 1.5.4	OpenMPI 1.2.8	OpenMPI 1.2.8
Math. Lib.	MKL 11.0	ACML 5.3.0	MKL 11.0	MKL 11.0

Table 2: Average time (s) for one MD step for different number of cores and for different CRESCO clusters.

cores	CRESCO4	CRESCO3	CRESCO2a	CRESCO2b
24	-	98.5	-	-
32	19.61	-	-	-
48	13.66	40.8	28.7	-
96	7.22	19.0	21.2	31.8
120	-	16.7	-	-
128	6.74	-	23.6	29.3
240	4.92	10.1	35.5	36.7
480	3.58	7.8	-	12.1
960	2.66	6.3	-	-

Melting of magnesium started at 1000 K, which is in agreement with experimental results.

To evaluate the computational cost of our simulations, some tests have been performed using the physical system previously described on the CRESCO clusters in the ENEAGRID environment. Some of the hardware and software characteristics for the CRESCO clusters are reported in Tab. 1. Further details on ENEAGRID computational infrastructure are in Ref.[21]. We checked the average time spent to perform a single step of MD simulations using different CRESCO clusters (see Tab. 2 and Fig. 2) and varying the number of cores utilized. From the data it is evident that CRESCO4 has the best performance independently from the number of cores. Moreover, in Fig 3a) we compared the data relative to the case in which 96 cores are used. It is highlighted how the times raise considerably changing the CRESCO cluster. Making a comparison respect to the CRESCO4 time, there is an increase of about 160% for the CRESCO3, and an increase of about 195% for CRESCO2a. Even more evident (340%) is the deterioration of the performance for the

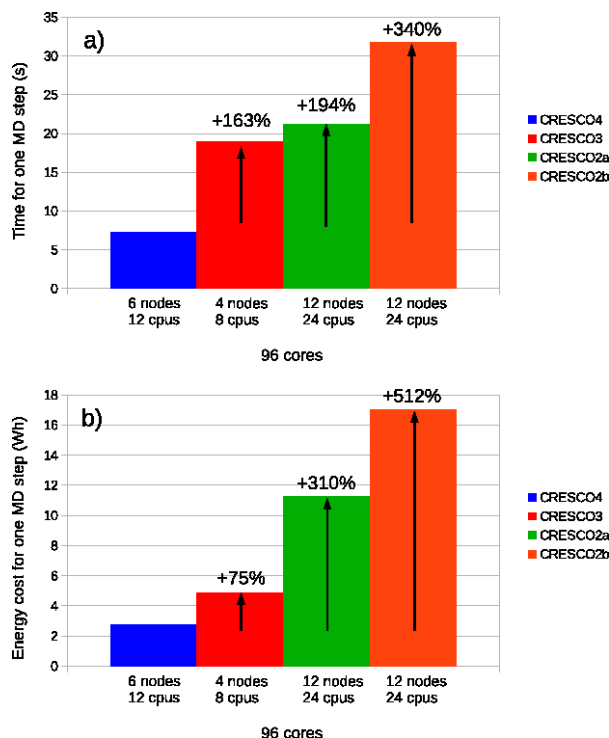


Figure 3: Average time (panel a) for one MD step for different CRESCO clusters using 96 cores and the corresponding energy cost (panel b).

case of CRESCO2b.

Another important point to take in consideration is the energy consumption issue. For this reason we evaluated the power cost for a single MD step. In panel b) of Fig 3 we showed the energy cost for a MD step taking into account that 96 cores correspond to 12 cpus for CRESCO4, 8 cpus for CRESCO3, and 24 cpus for CRESCO2a and CRESCO2b. The different number of cpus utilized changes the evaluation on the CRESCO clusters. CRESCO4 is still the energetically most advantageous choice, however CRESCO3 is a viable alternative, the energy consumption raise is only 75%. On the contrary the CRESCO2 clusters are less energetically favourable choices, in fact they are more slow, and in addition, having each processor four cores, the number of cpus used is 24. This produce an increase of the energetic cost of about 300% and 500% compared to CRESCO4 case.

In conclusion, we performed benchmarks of the CPMD code to evaluate the performance on the HPC CRESCO computing facilities. The benchmarks reveal that CRESCO4 has the best outcome on both time and energy cost,

## Acknowledgements

We acknowledge ENEA-HPC team for supporting our computational activities on the ENEAGRID infrastructure. Part of this work was supported by the Ministry of Education,

Science and Technological Development of the Republic of Serbia under the Grant III 45012. Part of this work was supported by the COST Action MP1103 “Nanostructured materials for solid state hydrogen storage”.

## References

- [1] Schlapbach L., Züttel A. *Nature* 414 (2001) pp. 353-358.
- [2] Züttel A. *Naturwissenschaften* 91 (2004) pp. 157-172.
- [3] Thomas K. M. *Catal. Today* 120 (2007) pp. 389-398.
- [4] Ormio S., Züttel A., Schlapbach L., Mayer G., Fukunaga T. *J. Alloys Comp.* 356-357 (2003) pp. 716-719.
- [5] Huot J., Liang G., Boily S., Van NESTA A., Schulz R. *J. Alloys Comp.* 293-295 (1999) pp. 495-500.
- [6] Montone A., Grbovic J., Vittori Antisari M., Bassetti A., Bonetti E., Fiorini A. L., Pasquini L., Mirengi L., Rotolo P. *Int. J. Hydrogen Energy* 32 (2007) pp. 2026-2934.
- [7] Kurko S., Aurora A., Gattia D. D., Contini V., Montone A., Raskovic-Lovre Z., Novakovic J. G. *Int. J. Hydrogen Energy* 38 (2013) pp. 12140-12145.
- [8] Matovic L., Kurko S., Raskovic-Lovre Z., Vujasin R., Milanovic I., Milosevic S., Grbovic Novakovic J. *Int. J. Hydrogen Energy* 37 (2012) pp. 6727-6732.
- [9] Shang C. X., Bououdina M., Song Y., Guo Z. X. *Int. J. Hydrogen Energy* 29 (2004) pp. 73-80.
- [10] Novakovic N., Grbovic Novakovic J., Matovic L., Manasijevic M., Radisavljevic I., Paskas mamula B., Ivanovic N. *Int. J. Hydrogen Energy* 35 (2010) pp. 598-608.
- [11] Varin R. A., Li S., Chiu C., Guo L., Morozova O., Khomenko T., Wronski Z. *J. Alloys Comp.* 404-406 (2005) pp. 494-498.
- [12] Oelerich W., Klassen T., Bormann R. *J. Alloys Comp.* 315 (2001) pp. 237-242.
- [13] Pandey S. K., Bhatnagar A., Shahi R. R., Hudson M. S. L., Singh M. K., Srivastava O. N. *J. Nanosci. Nanotechnol.* 13 (2013) pp. 5493-5499.
- [14] Crostan D. L., Grant D. M., Walker G. S. *J. Alloys Comp.* 492 (2010) pp. 251-258.
- [15] Leconte J., Mrkovits A., Skalli M. K., Minot C., Belmajdoub A. *Surf Sci* 497 (2002) pp. 194-204.
- [16] Yin X. L., Calatayud M., Qui H., Wang Y., Birkner A., Minot C., Woll C. *ChemPhysChem* 9 (2008) pp. 253-256.
- [17] Car R., Parrinello M. *Phys. Rev. Lett.* 55 (1985) pp. 2471-2474.

- [18] CPMD V3.15.1 Copyright IBM Corp 1990-2011, Copyright MPI fuer Festkoerperforschung Stuttgart 1997-2001.
- [19] Hohenberg P., Kohn W. Phys. Rev. 136 (1964) pp. B864-B871.
- [20] Kohn W., Sham L. J. Phys. Rev. 140 (1965) pp. A1133-A1138.
- [21] [www.cresco.enea.it](http://www.cresco.enea.it).
- [22] Perdew J. P., Burke K., Erzerhof M. Phys. Rev. Lett. 77 (1996) pp. 3865-3868.
- [23] Troullier N., Martins J. L. Phys. Rev. B 43 (1991) pp. 1993-2006.

# Activities made by MoLNac (Molecular Lab for Nanomaterials and Catalysis)

*Luigi Cavallo<sup>1,2</sup>, Giuseppe Milano<sup>1</sup>, Andera Correa<sup>1</sup>,  
Raffaele Credendino<sup>1,2</sup>, Maxim Byskin<sup>1</sup>, Antonio De Nicola<sup>1,3\*</sup>,  
Francesco Ragone<sup>1</sup>, Zhao Ying<sup>1</sup>, Laura Falivene<sup>1,2</sup>,  
Antonio Pizzirusso<sup>1</sup>, Albert Poater<sup>1,2</sup>*

*<sup>1</sup>Dipartimento di Chimica e Biologia, Università di Salerno  
Via Ponte don Melillo, 84084 Fisciano, Italy*

*<sup>2</sup>King Abdullah University of Science and Technology (KAUST)  
Physical Sciences and Engineering, Kaust Catalysis Center  
Thuwal 23955-6900, Saudi Arabia*

*<sup>3</sup>IMAST Scarl-Technological District in Polymer and Composite Engineering  
P.le Bovio 22, 80133 Napoli (NA), Italy*

## 1 Electronic bond tuning with heterocyclic carbenes

We discuss the impact of the nature of the heterocyclic carbene ring, when used as a complex forming ligand, on the relative stability of key intermediates in three typical Ru, Pd and Au promoted reactions. Results show that P-heterocyclic carbenes have a propensity to increase the bonding of the labile ligand and of the substrate in Ru-promoted olefin metathesis, whereas negligible impact is expected on the stability of the ruthenacycle intermediate. In the case of Pd cross-coupling reactions, dissociation of a P-heterocyclic carbene is easier than dissociation of the N-heterocyclic analogue. In the case of the Au-OH synthon, the Au-OH bond is weakened with the P-heterocyclic carbene ligands. A detailed energy decomposition analysis is performed to rationalize these results.

## 2 How does the addition of steric hindrance to a typical N-heterocyclic carbene ligand affect catalytic activity in olefin metathesis?

Density functional theory (DFT) calculations were used to predict and rationalize the effect of the modification of the structure of the prototype 1,3-bis(2,6-diisopropylphenyl)imidazol-

---

\*Corresponding author. E-mail: [adenicola@unisa.it](mailto:adenicola@unisa.it).



2-ylidene) N-heterocyclic carbene (NHC) ligand. The modification consists in the substitution of the methyl groups of ortho isopropyl substituent with phenyl groups, and here we plan to describe how such significant changes affect the metal environment and therefore the related catalytic behaviour. Bearing in mind that there is a significant structural difference between both ligands in different olefin metathesis reactions, here by means of DFT we characterize where the NHC ligand plays a more active role and where it is a simple spectator, or at least its modification does not significantly change its catalytic role/performance.

### 3 Exploring new generations of ruthenium olefin metathesis catalysts: the reactivity of a bis-ylidene ruthenium complex by DFT

Density functional theory calculations were used to predict the behaviour of a potential novel architecture of olefin metathesis catalysts, in which one of the neutral ligands of classical Ru-based catalysts, e.g. a phosphine or an N-heterocyclic carbene, is replaced by an alkylidene group. Introduction of a second alkylidene ligand favors dissociation of the remaining phosphine and the overall energy profile for the metathesis using ethylene as the probe substrate reveals that the proposed bis-alkylidene complexes might match the requirements of a good performing olefin metathesis catalyst.

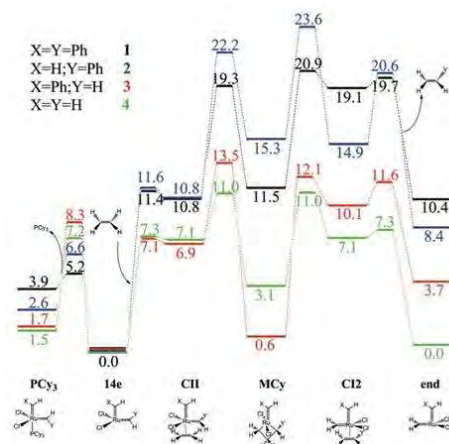


Figure 1: Ethylene metathesis cycle for the putative bis-alkylidene catalysts (free energies in kcal/mol).

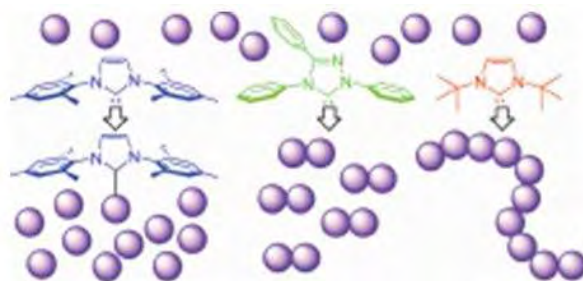
### 4 Catalytic Role of Nickel in the Decarbonylative Addition of Phthalimides to Alkynes

Density functional theory calculations have been used to investigate the catalytic role of nickel(0) in the decarbonylative addition of phthalimides to alkynes. According to

Kurahashi et al. the plausible reaction mechanism involves a nucleophilic attack of nickel at an imide group, giving a six-membered metallacycle, followed by a decarbonylation and insertion of an alkyne leading to a seven-membered metallacycle. Finally a reductive elimination process produces the desired product and regenerates the nickel(0) catalyst. In this paper, we present a full description of the complete reaction pathway along with possible alternative pathways, which are predicted to display higher upper barriers. Our computational results substantially confirm the proposed mechanism, offering a detailed geometrical and energetical understanding of all the elementary steps.

## 5 Organocatalytic Conjugate-Addition Polymerization of Linear and Cyclic Acrylic Monomers by N Heterocyclic Carbenes: Mechanisms of Chain Initiation, Propagation, and Termination

This contribution presents a full account of experimental and theoretical/computational investigations into the mechanisms of chain initiation, propagation, and termination of the recently discovered N-heterocyclic carbene (NHC)-mediated organocatalytic conjugate-addition polymerization of acrylic monomers. The current study specifically focuses on three commonly used NHCs of vastly different nucleophilicity, 1,3-di-tert-butylimidazolin-2-ylidene (ItBu), 1,3-dimesitylimidazolin-2-ylidene (IMes), and 1,3,4-triphenyl-4,5-dihydro-1H-1,2,4-triazol-5-ylidene (TPT), and two representative acrylic monomers, the linear methyl methacrylate (MMA) and its cyclic analog, biomass-derived renewable  $\gamma$ -methyl- $\alpha$ -methylene- $\gamma$ -butyrolactone (MMBL).



For MMA, there exhibits an exquisite selectivity of the NHC structure for the three types of reactions it promotes: enamine formation (single-monomer addition) by IMes, dimerization (tail- to-tail) by TPT, and polymerization by ItBu. For MMBL, all three NHCs promote no dimerization but polymerization, with the polymerization activity being highly sensitive to the NHC structure and the solvent polarity. Thus, ItBu is the most active catalyst of the series and converts quantitatively 1000–3000 equiv of MMBL in 1 min or 10000 equiv in 5 min at room temperature to MMBL-based bioplastics with a narrow range of molecular weights of  $M_n=70\text{--}85$  kg/mol, regardless of the  $[\text{MMBL}]/[\text{ItBu}]$  ratio employed. The ItBu-catalyzed MMBL polymerization reaches an exceptionally high turnover frequency up to  $122\text{ s}^{-1}$  and a high initiator efficiency value up to 1600%. Unique chain-termination mechanisms have been revealed, accounting for the production of rela-

tive high-molecular-weight linear polymers and the catalytic nature of this NHC-mediated conjugate-addition polymerization. Computational studies have provided mechanistic insights into reactivity and selectivity between two competing pathways for each NHC-monomer zwitterionic adduct, namely enamine formation/dimerization through proton transfer vs polymerization through conjugate addition, and mapped out extensive energy profiles for chain initiation, propagation, and termination steps, thereby satisfactorily explaining the experimental observations.

## 6 Liquid-Solid transition of tryglycerides, Molecular Dynamic investigation using CG-models

The current project is focused on Molecular Dynamics simulations of triglycerides using a coarse-grained (CG) modelling approach. These tri-esters of glycerol with fatty acids are important constituents of oils and fats and are widely used in foods, in cosmetics, and medicine as nutrients or matrix materials [1]. In this context we investigated liquid-solid transition both of tripalmitin and tristearin as triglyceride, where force field parameters are obtained in a recent paper through an optimization procedure [2]. Due to the nature of the process we needed to reach microsecond time scale to correct obtain representative equilibrium structures (see Fig. 2).

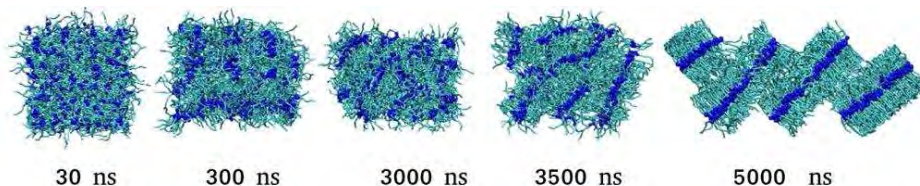


Figure 2: Snapshots of PPP system composed of 270 CG molecule during simulation time.

## 7 Spontaneous insertion of carbon nanotube bundles inside biomambranes: A hybrid particle-field coarse-grained molecular dynamic study

The processes of CNTs bundle formation and insertion/rearrangement inside lipid bilayers, as models of cellular membranes, is described and analyzed in details using simulations on the microsecond scale. Molecular Dynamics simulations employing hybrid particle-field models (MD-SCF) show that during the insertion process lipid molecules [3] coat bundles surfaces. The distortions of bilayers are more pronounced for systems undergoing to insertion of bundles made of longer CNTs. In particular, when the insertion occurs in perpendicular orientation, adsorption of lipids on CNTs surfaces promotes a transient poration. This result suggests mechanism of membrane disruption operated by bundles causing the formation of solvent-rich pockets (Fig. 3).

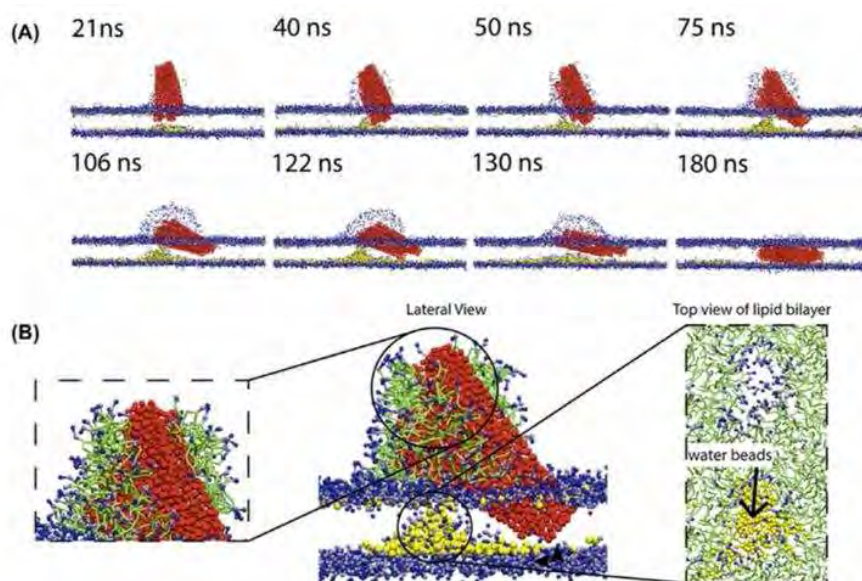


Figure 3: Process of pore formation inside the lipid bilayer during the insertion process of a bundle made of CNTs long 10 nm (A). The lipid orientations corresponding to micelle in water around the CNTs (inset on the left side) and reverse micelle (around the pore including water) aggregates (right side) are highlighted (B).

## References

- [1] Pardeike J., Hommoss A., and Moller R. H. Lipid nanoparticles (sln, nlc) in cosmetic and pharmaceutical dermal products. *International Journal of Pharmaceutics*, 366:170–184, 2009.
- [2] Brasiello A., Criscitelli S., and Milano G. Development of a coarse-grained model for simulations of tridecanoin liquid-solid phase transitions. *Phys. Chem. Chem. Phys.*, 13:16618–16628, 2011.
- [3] Zhao Y., De Nicola A., Kawakatsu T., and Milano G. *J. Comput. Chem.* 33 (2012) 868.

# Simulation of the adsorption mechanism of titanium-binding peptide to TiO<sub>2</sub> anatase surface

*Lorenzo Agosta<sup>1</sup>, Caterina Arcangeli<sup>2,3\*</sup>, Francesco Buonocore<sup>2,3</sup>,  
Massimo Celino<sup>2,3</sup>, Fabrizio Gala<sup>1</sup>, Giuseppe Zollo<sup>1</sup>*

*<sup>1</sup>Department of Fundamental and Applied Sciences for Engineering  
University of Rome "La Sapienza"  
Via A. Scarpa 14-16, I-00161 Rome, Italy*

*<sup>2</sup>NAST Centre c/o University of "Tor Vergata", Department of Physics  
Via della Ricerca Scientifica, 1, I-00133 Rome, Italy*

*<sup>3</sup>ENEA, Italian National Agency for New Technologies,  
Energy and Sustainable Economic Development  
C. R. Casaccia, Via Anguillarese 301, I-00123 Rome, Italy*

**ABSTRACT.** Organic-inorganic interfaces are nowadays playing a major role in several technological fields ranging from photovoltaics to drug-delivery, from microelectronics to composites. However they are very challenging from the experimental point of view because the microscopic features giving raise to their exceptional properties involve very small distances and very small energies. For this reason the modelling approach can act as a powerful microscope to see and measure the relevant physical and chemical quantities. A model for amino acids adhesion on a widely used inorganic surface has been developed and implemented on the high performance computing platform CRESCO.

Abbreviations: MD: Molecular dynamics; DFT: Density Functional Theory; Ala: Alanine; Cys: Cysteine; Arg: Arginine; Lys: Lysine; Asp: Aspartic acid.

## 1 Introduction

Interfaces between biological matter and inorganic materials are now among one of the hottest research topics in various research fields and even in industry. Recent progress in combinatorial biology (e.g. the phage display method) has permitted to select amino acid sequences possessing specific affinities to their target inorganic materials. Among peptide sequences that bind inorganic surfaces the sequence AMRKLPDAPGMHC has been demonstrated to display a large and selective affinity to titanium dioxide [1]. Experimental characterization of the peptide-titania interface has revealed that electrostatic

---

\*Corresponding author. E-mail: [caterina.arcangeli@enea.it](mailto:caterina.arcangeli@enea.it).

interactions play a role and that peptide flexibility may also be important [2, 3]. The understanding of these interfaces paves the way to the design of novel materials engineered at the nanometric scale. In order to shed some light on this interaction, we investigated at atomic level the binding mechanisms between the  $\text{TiO}_2$  anatase surface and the peptide.

## 2 Computational details

The simulation of the peptide-titania interface consisted of three stages: 1) the modeling of the peptide folding through classical MD simulations in water, starting from a totally unfolded molecular conformation. 2) DFT calculations to characterize the hydrated inorganic surface and the adhesion of the amino acids (relevant to the binding) on the  $\text{TiO}_2$  anatase in the presence of water molecules. 3) MD simulations of the folded peptide adsorbed onto the  $\text{TiO}_2$  surface in water solution and steered MD simulations to better investigate the force of the interaction between the peptide and the  $\text{TiO}_2$  surface. The DFT calculations and MD simulations were carried on CRESCO HPC cluster by using the Quantum Espresso code and the highly optimized parallel version of GROMACS (version 4.5.4), respectively.

## 3 Results and Discussions

### 3.1 Modeling the peptide folding by MD simulation

MD simulation of the folding of the peptide in water were performed starting from a totally unfolded conformation. Most of the residues of the peptide assumes a bended conformation that is maintained stable during the last 5 ns of simulation (Fig. 1). An intra-molecular hydrogen bond between the N atom of the Ala1 and the O atom of the terminal carboxyl group of Cys13 stabilizes the bended peptide [4].

### 3.2 DFT calculations

The  $\text{TiO}_2$  (101) anatase surface was reconstructed with adsorbed water molecules (Fig. 2). The adsorption energy of water molecules was calculated as -0.729 eV/molecule. Therefore it is expected that in water solution, water molecules mediate the peptide adsorption. As a first step towards the understanding of the peptide adhesion, we considered the adsorption properties of the three isolated amino acids as if they were charged according to their charge states in neutral water solution. The water molecules completely mediate the adhesion process [5] (Fig. 2). DFT calculations show that the three amino acids have negative adsorption energy (i.e. stay stacked on the surface spontaneously). However Lys and Arg are largely more stable than the Asp. While on the dry surface Lys and Arg have nearly the same adsorption energy [5] on the hydrated surface Arg is more stable than Lys by nearly 220 meV (Table 1). Then it is likely that the main responsible of the peptide adhesion is Arg even though this conclusion is drawn without taking into account the peptide structure that might play a significant role.

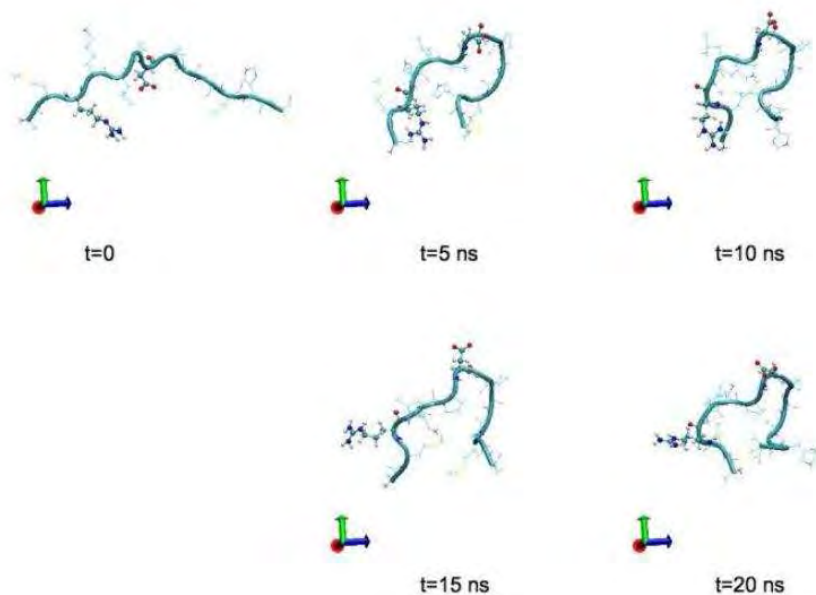


Figure 1: Snapshots of the peptide at selected time points of the MD simulation. The peptide backbone is shown as a cyan tube while the Arg3 and Asp7 are represented through CPK model. The movie of the folding simulation is at <https://www.afs.enea.it/project/cmast/index.php>.

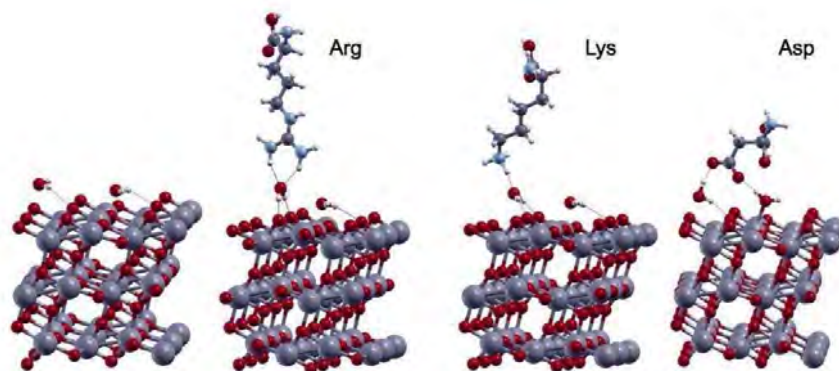


Figure 2: Relaxed configuration for two water molecules on (101) anatase surface and adsorption of amino acids relevant for the adhesion on the hydrated  $\text{TiO}_2$  surface.

### 3.3 MD simulation of the peptide- $\text{TiO}_2$ interface

The folded peptide was placed close to the  $\text{TiO}_2$  surface ( $d=1.0$  nm)[4]. The configuration of the adsorbed folded peptide onto the surface after 5 ns of MD simulation (Fig. 3 left) shows that the interfacial water molecules are stable and oriented on the surface to form a hydrogen bonding network induced by the surface (white dashed lines). The side-chains of Asp7 and Arg3 adsorb on the surface mediated by the interfacial water layer. The effect of the adsorbed peptide on the structure of the interfacial water was investigated. The plane



	Arg	Lys	Asp
Dry(101)	-2.297	-2.362	-1.277
Hydrated (101)	-1.703	-1.923	-0.427

Table 1: Adsorption energies (eV) of amino acids on the (101) anatase surface with and without water.

containing the surface ranges from 1.9 to 2.5 nm and defines two interfaces. The left water-surface is free from the peptide; the right water-surface is affected from the presence of the peptide. The density profiles for both exposed surfaces show distinct peaks corresponding to different hydration layers (Fig. 3 right). The presence of the peptide causes a decrease of the local water density. The atoms of the Arg3 and Asp7 are in the 1st and 2nd adsorbed water layer (Fig. 3 right b). To better investigate the force of the interaction between the peptide and the surface, the peptide was detached from the surface along the z-direction by pulling on the COM using  $k = 5000$  kJ/mol/nm<sup>2</sup> and a pull rate of 0.0005 nm/ps.

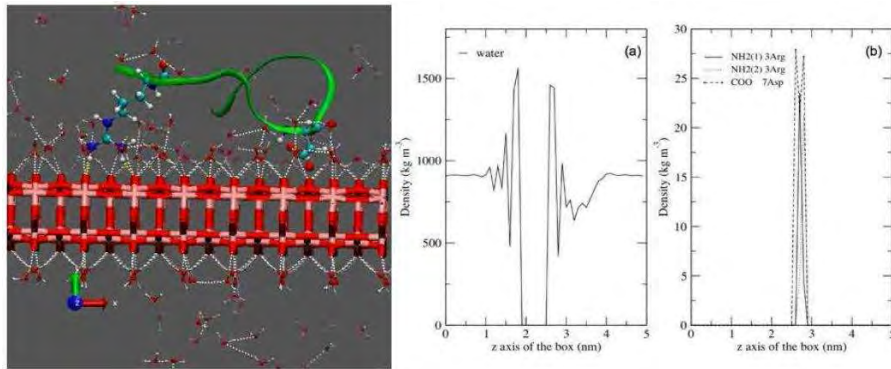


Figure 3: Left: Snapshots of side view (left) of the adsorbed peptide onto TiO<sub>2</sub> (101) anatase surface taken at 5 ns. Right: Density profile as a function of z-axis for water (a) and peptide atoms (b).

The pulling force builds up until three breaking points are reached, at which the interactions between the Cys13, Asp7 and Arg3 with the metal surface are disrupted, allowing the peptide to dissociate from the metal surface (Fig. 4). A similar behaviour has been observed for desorption of the hexapeptide RKLPGA from a natively oxidized TiO<sub>2</sub> surface [6]. The dissociation pathway is shown in Fig. 5.



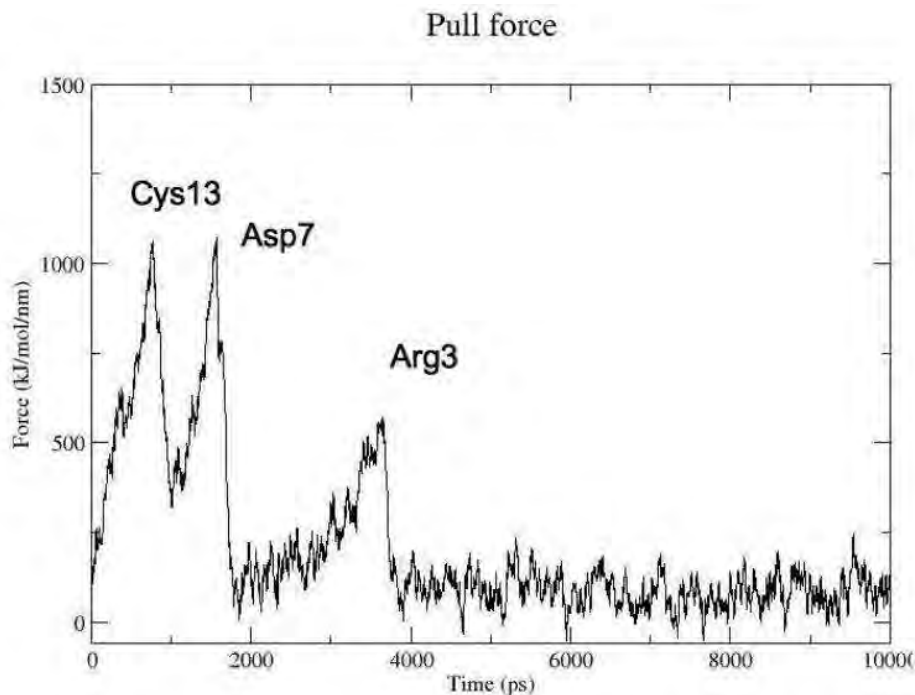


Figure 4: Pulling force applied as a function of simulation time.

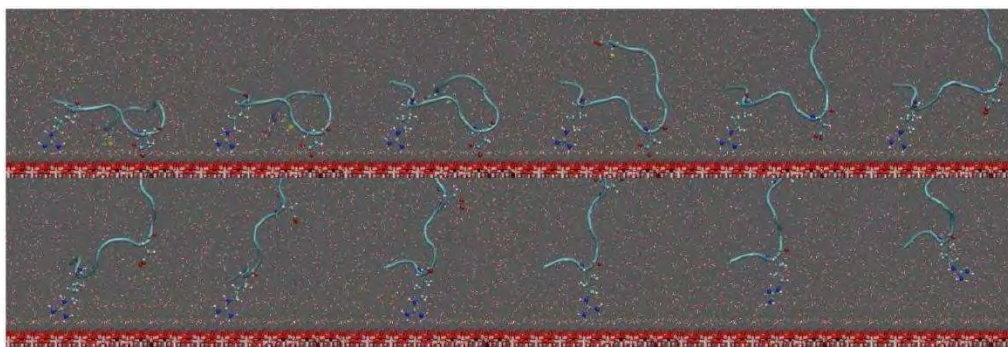


Figure 5: Snapshots of the dissociation pathway (from the top left to the bottom right) of the peptide from the  $\text{TiO}_2$  surface.

## 4 Conclusions

Atomic scale modelling is able to provide interesting insights in the design of novel materials. In the case of biomolecules interacting with inorganic surfaces, modelling can compute the adhesion properties and how these influence the physical and chemical properties. By means of accurate and extensive DFT simulations, we confirm the major role of the electrostatic interactions to the binding mechanism. Classical MD simulations of the interface enlighten that the adhesion mechanism is mediated by the interfacial waters. The dissociation pathway, obtained by steered MD simulations, suggests an anchoring of the peptide

to the surface via Cys13 Asp7 and Arg3 residues. Our results may have important implications for nanotechnology and material science applications offering a rational design of material-selective peptides.

## Acknowledgements

This work was supported by META-Materials Enhancement for Technological Application-Project (FP7-PEOPLE-2010-IRSES-Marie Curie Actions, PIRSES-GA-2010-269182). We acknowledge the technical support of the ENEA-ICT team who provided the access to the ENEA-CRESCO high-performance computing facility ([www.cresco.enea.it](http://www.cresco.enea.it)). We thank Dr. S. Giusepponi for helpful discussions and suggestions.

## References

- [1] Sano KI. and Shiba K. A hexapeptide motif that electrostatically binds to the surface of titanium. *J Am Chem Soc*, 125:14234–5, 2003.
- [2] Hayashi T et al. Mechanism underlying specificity of proteins targeting inorganic materials. *Nano Letters*, 6:515–9, 2006.
- [3] Fukuta M. et al. The adsorption mechanism of titanium-binding ferritin to amphoteric oxide. *Colloids Surface*, B(102):435–40, 2013.
- [4] Arcangeli C. et al. Organic functionalization of metal oxide surfaces: An atomic scale modeling approach. *Nanosci Nanotech Lett*, 5:1147–54, 2013.
- [5] Agosta L. et al. Submitted to Physical Chemistry Chemical Physics 2014.
- [6] Schneider J. et al. Specific material recognition by small peptides mediated by the interfacial solvent structure. *J Am Chem Soc*, 134:2407–13, 2012.

# CFD investigation of advanced cooling techniques in gas turbine blades

*D. Borrello\*, F. Rispoli, P. Venturini, A. Salvagni*

*Dipartimento di Ingegneria Meccanica e Aerospaziale  
Università "Sapienza" di Roma, Via Eudossiana, 18, 00184 Roma, Italy*

**ABSTRACT.** The present contribution aims to illustrate the research activities carried out in 2013 by the group working at the Department of Mechanical and Aerospace Engineering, "Sapienza" University of Rome, using the CRESCO computational resources. The research group has a long record of publication in the field of Computational Fluid Dynamics and it is cooperating with ENEA groups since 2001. During 2013, the numerical investigations were focused on the LES-like investigations of the flow in turbomachinery relevant flows. Two main research lines were pursued in this field: a) thermo-fluid-dynamic investigation of a blade vane in presence of film cooling [1] ; b) analysis of the flow in a rotating rib-roughened duct reproducing the internal cooling mechanism in a turbine blade [2]. Both of these activities led to a production of two papers presented to peer-reviewed International Conferences and now submitted for publication in journals or selection of papers. In the following a brief description of the two simulation is carried out.

## 1 Thermo-fluid-dynamic investigation of a blade vane in presence of film cooling

First stage of a turbine vane is generally subjected to the hot gas reached from the combustor. Thus, an adequate cooling system is required to prevent blade failure. Simulation of the flow around a General Electric Energy Efficient Engine (E3) High Pressure Turbine (HPT) vane with and without film cooling was performed. Firstly, we focused on a simplified 2D geometry reproducing the middle section of the turbine blade (Fig. 1.a).

Fig. 1.b shows the computational domain which includes six film cooling holes. The domain was composed of 444,980 2D structured cells thickened around the holes. Although a 2D simulation is not satisfactory at all for this type of configuration, it is possible to carry out some interesting conclusions from this investigation (which does not include any 3D effects), before the analysis of the 3D configuration.

In Fig. 2, the flow and the temperature field close to the leading edge are shown. The influence of the cooling jets is clearly visible. The changes in velocity distribution strongly affects the temperature field that reduces its maximum value to 800 K in the cooled zones.

---

\*Corresponding author. E-mail: domenico.borello@uniroma1.it.

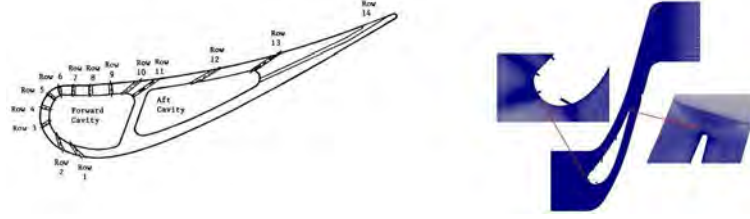


Figure 1: a) EEE blade vane-vane profile; b) EEE blade vane-computational domain with cooling holes.

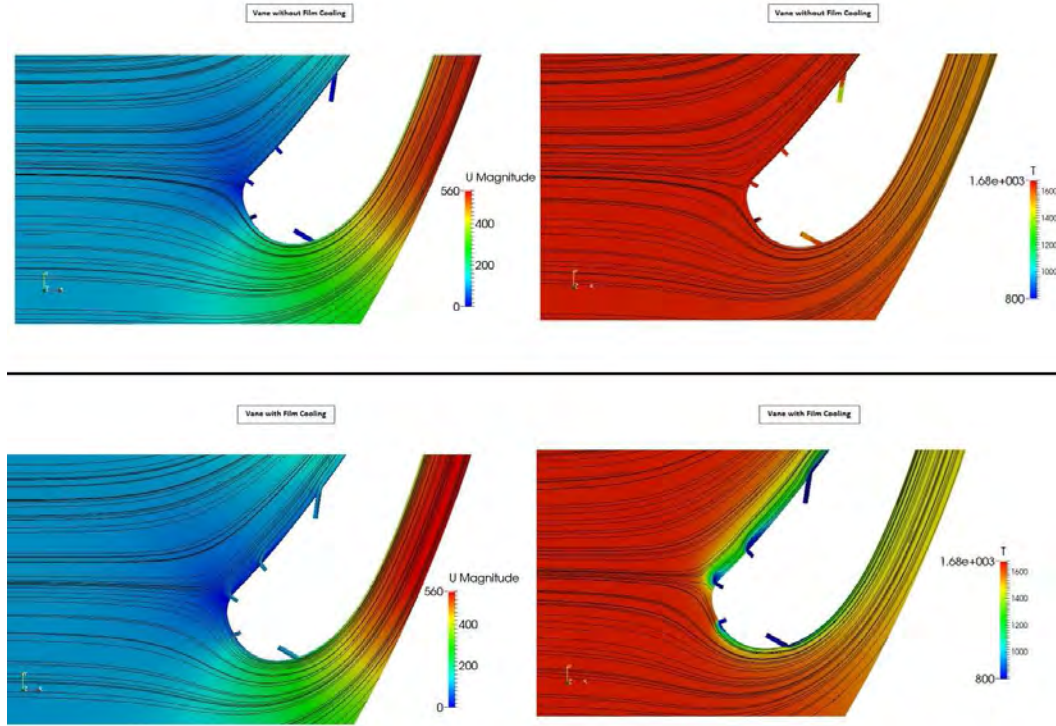


Figure 2: Velocity (left) and Temperature (right) distribution and streamlines for the turbine simulation; up: without film cooling; down: with film cooling.

It is important to note that there is a region close to the stagnation zone where the cooling jets are not able to remove heat efficiently. This depends on the flow direction and the position of the stagnation line. From Fig. 2 it is evident that film cooling creates a barrier all along the blade, and the hot gas.

Then, most of the solid particles carried by the flow are not able to reach the blade surface. Then, we analysed a portion of the blade (1/6 of the hub-to-tib height of the blade, Fig. 3.a). A 3D block-unstructured tetrahedral grid was used for discretizing the computational domain (Fig. 3.b). The grid has 7,343,000 tetrahedral cells.

In Fig. 4, the temperature distribution on the pressure side is shown. In the cooled con-



Figure 3: a) EEE blade vane-vane profile; b) EEE blade vane-computational domain with cooling holes.

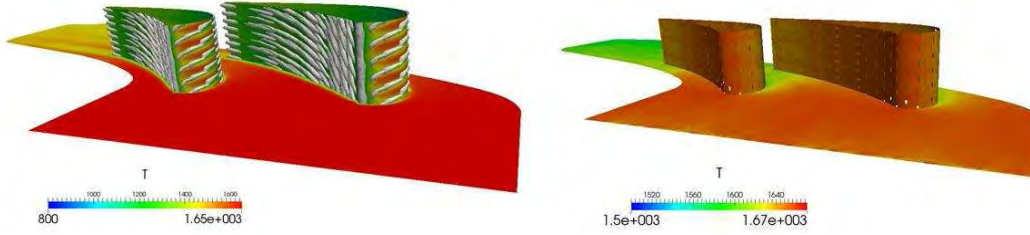


Figure 4: Temperature distribution along the pressure side: left-cooled configuration, the temperature isosurfaces at 1200 K are indicated in grey; right-uncooled configuration.

figuration, the presence of film cooling is put in evidence by the presence of temperature isosurfaces. The influence of film cooling is made evident by lack of temperature uniformity along the span. In the non-cooled case, the blade temperature is more uniform (we changed the temperature range in the plots) and the small reduction of blade temperature is only related to the influence of flow temperature variation. For this application we used OpenFOAM 2.1.0 code that is available on the CRESCO machines. As we were interested in mean properties, we used a U-RANS approach.

## 2 LES of flow in a rotating rib-roughened channel

For this application we used T-FlowS, a FV unstructured parallel research code developed by some of the authors. We implemented, checked and validated T-FlowS on the CRESCO machines since 2007. The test case is particularly relevant for the analysis of internal cooling efficiency in the first stages of turbine blades. A refined LES analysis is required in this case due to the presence of very small structures generated by the interaction of the several walls and the influence of rotation. The grid used has 9 Mo. cells. Here we present the results of the case without rotation, with anti-clockwise rotation (corresponding to a destabilizing effect on the ribbed surface) and with clockwise rotation (corresponding to a stabilizing effect on the ribbed surface). The rotational number is equal to 0.3. The channel has an aspect ratio equal to 0.9 and the ribs generate a blockage factor of 0.1,  $h$  is the rib height. The Navier-Stokes equations system is solved in dimensionless



variables. As reference variables we used duct hydraulic diameter, bulk flow velocity and air properties at 20 C. The ensuing Reynolds number is equal to 15,000. A Crank-Nicolson/CDS scheme was adopted to obtain a second-order accurate solution. Fully coupled solution of the Navier-Stokes system was obtained using the SIMPLE scheme, while the Preconditioned BiCG solver is adopted for the solution of the algebraic linearized equation system. Periodic boundary conditions were imposed at the inlet and outlet surface in stream-wise conditions. On the solid walls no-slip conditions were set. The non-dimensional time step was selected equal to  $10^{-4}$ . The maximum CFL number is smaller than 0.3. The computations were performed on the CRESCO3 cluster at Portici (ENEA) using 64 processors. Computations were performed for 2 flow through times (FTT) before starting to collect statistics.

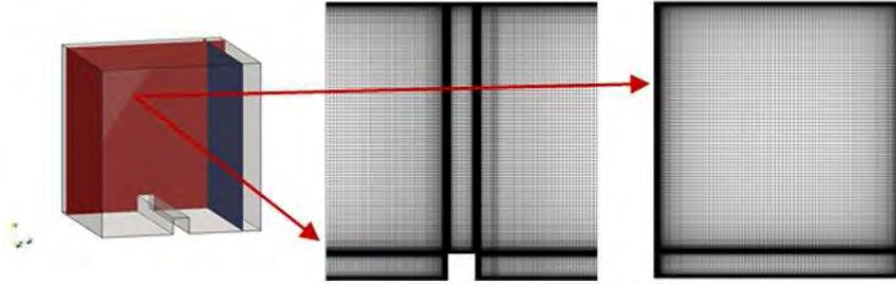


Figure 5: Grid discretisation - details of the cross planes: a) 5.8 Million cells; b) 8.8 Million cells.

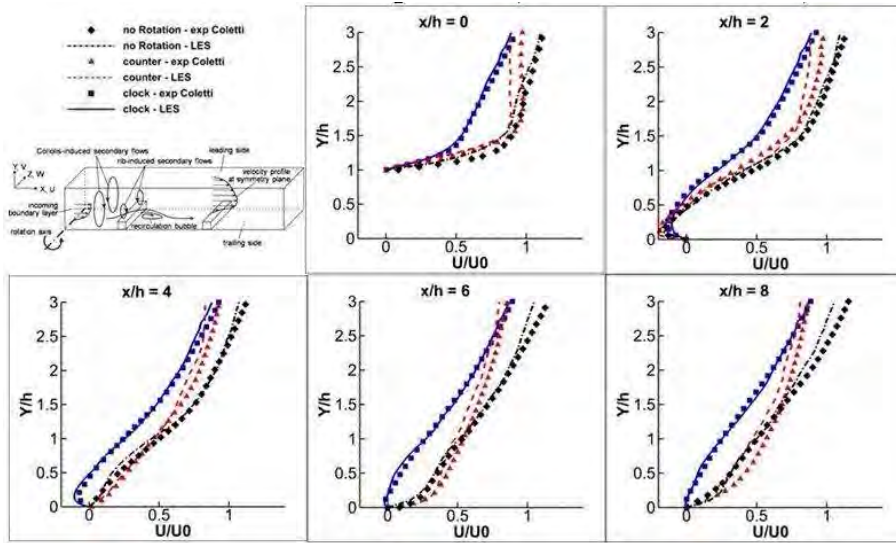


Figure 6: Top left: sketch of the flow configuration (from Coletti et al. 2011). Mean streamwise velocity profiles at  $x/h = 0, 2, 4, 6$  and  $8$ : Symbols: experiments (PIV, Coletti et al. 2011); lines: present LES.

Fig. 6 shows a comparison of the LES-computed mean velocity profiles with the experimental data of Coletti et al. (2011). The latter are available only for the region close to the ribbed wall. For an overall impression, Fig. 6 shows also a sketch of the whole flow config-

uration with typical flow patterns and main vortical systems. The agreement between the computed and measured profiles at five stream-wise locations for all three cases considered can be regarded as satisfactory. In fact the stabilizing and the non-rotating cases were reproduced very well and the destabilizing case reasonably well. The stabilized rotation makes the profiles less turbulent and the opposite occurs for the destabilizing rotations. The LES returns very satisfying results especially in predicting the recirculating boundary layer in the first measurement sections and the successive development downstream from the reattachment point.

### 3 Summary and Conclusions

The authors used the CRESCO computational resources in 2013 for studying turbomachinery applications. The analysis allowed to obtain relevant details about the turbulence structures via an U-RANS in a first stage blade vane and an LES in a rib-roughened rotating channel. The results of the simulations allowed to produce two papers presented in peer-reviewed International Conferences and that will be delivered to indexed publications (journals or edited books).

### References

- [1] Borello D., D'Angeli L., Salvagni A., Venturini P., and Rispoli F. Study of particles deposition in gas turbine blades in presence of film cooling. ASME TurboExpo 2014, 16-20 June 2014, Düsseldorf, Germany, to be submitted to AIAA J. of Prop.
- [2] Borello D., Rispoli F., Salvagni A., and Hanjalic K. Effects of rotation on flow in a rib-roughened channel: Les study. Engineering Turbulence Modelling and Measurement 10, 17-19 September 2014, Marbella, Spain, selected for publication on IJHFF.

# Direct Numerical Simulation of a premixed $\text{CH}_4/\text{H}_2$ -Air slot flame

*D. Cecere\*, E. Giacomazzi, F. R. Picchia and N. Arcidiacono*

*Laboratorio per la Combustione Sostenibile e Processi (UTTEI-COMSO)  
ENEA, C. R. Casaccia, Via Anguillarese 301, 00123 - S.M. Galeria (Roma)*

**ABSTRACT.** In recent years, due to the advent of high-performance computers and advanced numerical algorithms, direct numerical simulation (DNS) of combustion has emerged as a valuable computational research tool, in concert with experimentation. The role of DNS in delivering new scientific insight into turbulent combustion is illustrated using results from a recent 3D turbulent premixed flame simulation. To understand the influence of turbulence on the flame structure, a 3D fully-resolved DNS of a spatially-developing lean  $\text{CH}_4/\text{H}_2$  – air turbulent slot flame was performed in the thin reaction zones regime. A detailed chemical model for methane-air chemistry consisting of 22 resolved species and 73 elementary reactions was adopted for the current simulation together a compact high order staggered scheme for the solution of compressible Navier-Stokes equations.

## 1 Introduction

In many practical devices for power generation, such as stationary gas turbines, or propulsive systems, there has been a strong interest in achieving more efficiency and low pollutants emissions. For this purpose lean combustion burners are developed. The advantages of operating at lean mixture conditions are high thermal efficiency and low emissions of  $\text{NO}_x$  due to lower flame temperatures. Unfortunately at leaner conditions the flame tends to be thicker and propagate more slowly, suffering of flame instability. Local flame extinction occurs as a consequence of lean combustion conditions associated with stretching and heat losses. In order to overcome this issue, it is possible to increase the laminar burning velocity adding a small percentage of hydrogen to the lean premixed methane/air flame mixture. The hydrogen's large laminar burning velocity (approximately 7 times that of methane at 300 K and 1 bar) and the wider flammability limits allows the extension of the operational range of the combustion system. However, hydrogen is less energy dense than all other fuels, resulting in a loss of power in proportion to the base fuel substituted. For turbulent flames with hydrogen added to methane the literature is limited; we mention the experimental studies of [1] and the two-dimensional DNS (with a chemical mechanism reduced to 19 species and 15 reactions) by Hawkes and Chen [2]. The topic of hydrogen addition has become important recently, in particular because of the need to increase the knowledge about the effects of addition of  $\text{H}_2$  to regular fuels obtained from biomass and coal gasification.

---

\*Corresponding author. E-mail: donato.cecere@enea.it.



$\phi$	$n_{H_2} = x_{H_2}/(x_{H_2} + x_{CH_4})$	$T_u$ [K]	$T_b$ [K]	$s_L$ [cm s <sup>-1</sup> ]	$\delta_{th}$ [mm]
0.7	0.2	600	2072	103.75	0.3476

Table 1: CH<sub>4</sub>/H<sub>2</sub> – Air laminar flame.

## 2 Problem configuration

The simulation was performed in a slot-burner Bunsen flame configuration. The slot-burner Bunsen configuration is especially interesting due to the presence of mean shear in the flow and is similar in configuration to the burner used in experimental studies [3]. This configuration consists of a central reactant jet through which premixed reactants are supplied. The central jet is surrounded on either side by a heated coflow, whose composition and temperature are those of the complete combustion products of the freely propagating jet mixture. The reactant jet was chosen to be a premixed methane/hydrogen air jet at 600 K and mixture equivalence ratio  $\phi = 0.7$ , with molar fractional distribution of 20% H<sub>2</sub> and 80% CH<sub>4</sub>. The unstrained laminar flame properties at these conditions computed using Chemkin [8] are summarized in Table 1. In this table  $\phi$  represents the multicomponent equivalence ratio of the reactant jet mixture,  $\phi = [(X_{H_2} + X_{CH_4})/X_{O_2}]/[(X_{H_2} + X_{CH_4})/X_{O_2}]_{stoich}$ ,  $T_u$  is the unburned gas temperature,  $T_b$  the products gas temperature,  $s_L$  represents the unstrained laminar flame speed and  $\delta_{th} = (T_b - T_u)/|\partial T/\partial x|_{max}$  is the thermal thickness based on maximum temperature gradient. Preheating the reactants leads to a higher flame speed and allows a higher inflow velocity without blowing out the flame, reducing computational costs. Also, many practical devices such as gas turbines, internal combustion engines, and recirculating furnaces operate at highly preheated conditions. The simulation parameters are summarized in Table 2. The domain size in the streamwise (z), crosswise (y) and spanwise (x) directions is  $L_x \times L_y \times L_z = 24h \times 15h \times 2.5h$ ,  $h$  being the slot width ( $h = 1.2$  mm). The grid is uniform only in the x direction ( $\Delta x = 20 \mu m$ ), while it is stretched in the y and z direction near the inlet duct walls. The DNS was run at atmospheric pressure using a 17 species and 73 elementary reactions kinetic mechanism [4]. The velocity of the central jet stream is 100 m/s, while the velocity of the coflow stream is 25 m/s. The width  $h$  of the central duct, where the inlet turbulent velocity profile may develop, is 1.2 mm and 4 mm long. The width walls of the duct  $h_w$  is 0.18 mm. Velocity fluctuations,  $u' = 12 \text{ ms}^{-1}$ , are imposed on the mean inlet velocity profile, obtained by generating at duct's inlet homogeneous isotropic turbulence field with a characteristic turbulent correlation scale in the streamwise direction of  $\delta_{corr} = 0.0004$  m and a streamwise velocity fluctuation of  $u'_z = 12 \text{ ms}^{-1}$ , are imposed on the mean inlet duct's velocity profile by means of Klein's procedure [5]. The jet Reynolds number based on the centerline inlet velocity and slot width  $h$  is  $Re_{jet} = Uh/\nu = 2264$ . Based on the jet exit duct centerline velocity and the total streamwise domain length, the flow through time is  $\tau_U = 0.218$  ms. Navier-Stokes characteristic boundary conditions (NSCBC) were adopted to prescribe boundary conditions. Periodic boundary conditions were applied in the x direction, while improved staggered non-reflecting inflow and outflow boundary conditions were fixed in y and z directions [6, 7]. The simulation was performed on the linux cluster CRESCO4 (Computational Center for Complex Systems) at ENEA, requir-

Slot width ( $h$ )	1.2 mm
Domain size in the spanwise ( $L_x$ ), cross-wise ( $L_y$ ) and streamwise ( $L_z$ ) directions	$24h \times 15h \times 2.5h$
$N_x \times N_y \times N_z$	$1550 \times 640 \times 140$
Turbulent jet velocity ( $U_0$ )	$110 \text{ m s}^{-1}$
Coflow velocity	$25 \text{ m s}^{-1}$
Jet Reynolds Number ( $Re_{jet} = U_0 h / \nu$ )	2264
Turbulent intensity ( $u' / S_L$ )	12.5
Turbulent length scale ( $l_t / \delta_L$ )	2.6
Turbulent Reynolds Number ( $Re_t = u' \eta_K / \nu$ )	226
Damkohler number ( $s_L L_t / u' L$ )	0.21
Karlovitz number ( $\delta_L / \eta_K$ )	503
Minimum grid space	$9 \mu\text{m}$
Kolmogorov Length Scale $\eta_K$	$17.22 \mu\text{m}$

Table 2:  $\text{CH}_4/\text{H}_2 - \text{Air}$  turbulent flame: the kinematic viscosity used in the calculation of Reynolds number is that of the inflow  $\text{CH}_4 - \text{H}_2/\text{Air}$  mixture  $\nu = 5.3 \cdot 10^{-5} \text{ m}^2 \text{ s}^{-1}$ .

ing several months on 2400 processors. The solution was advanced at a constant time step of 2.3 ns and after the flame reached statistical stationarity, the data were been collected through  $4 \tau_U$ .

### 3 Results and discussion

#### 3.1 General characteristics of the flame

An overall description of the slot flame is given by the evolution, downstream the inlet channel, of the axial and radial velocities  $\tilde{U}_z, \tilde{U}_y$  shown in Fig. 1. At the exit of the channel, the axial velocity  $U_z$  reaches a maximum value of  $110 \text{ m s}^{-1}$  greater than its inlet value, due to formation of the channel boundary layer, that is equivalent to a restriction of the flow section (see Fig.1). Downstream, a crosswise component is generated in the coflow because of the presence of the central jet core (see streamlines in Fig.1 and  $U_y$  velocity profiles in Fig.2b). The blue lines indicates the flame brush thickness identified using a value of progress variable  $c$  between (0.05 – 0.95). The Fig.1b shows the mean shear layer, defined as the velocity gradient in the crosswise direction, and the flame front location, identified with a value of  $c = 0.7$  corresponding to the location of the maximum heat release of the unstrained laminar flame. Due to the presence of wall channel the maximum velocity gradient is located near the internal edges. The average flame front resides outside of the core of the jet near the wall duct and at  $0.009 \text{ mm}$  it moves towards the inside of the shear layer. The effect of the mixture jet expansion at the exit of channel and the coflow entrainment towards the jet core is evidenced in Fig. 2b (solid line). The velocity fluctuation is highest in the middle of the shear layer due to the mean shear of the

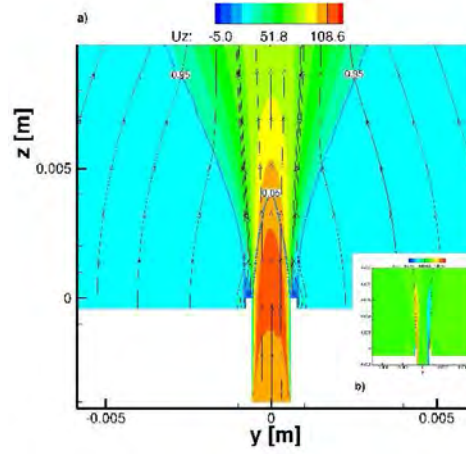


Figure 1: Mean streamwise velocity contour plot at the  $x = 0$  plane. Also shown in the contour plot are the velocities streamlines and the iso-contour of  $\tilde{c} = 0.05 - 0.95$ , indicating the mean flame brush. b) The bottom right shows a zoomed in view of the velocity gradient  $d\tilde{U}_z/dy$  contour and the iso-contour of progress variable  $\tilde{c} = 0.7$ .

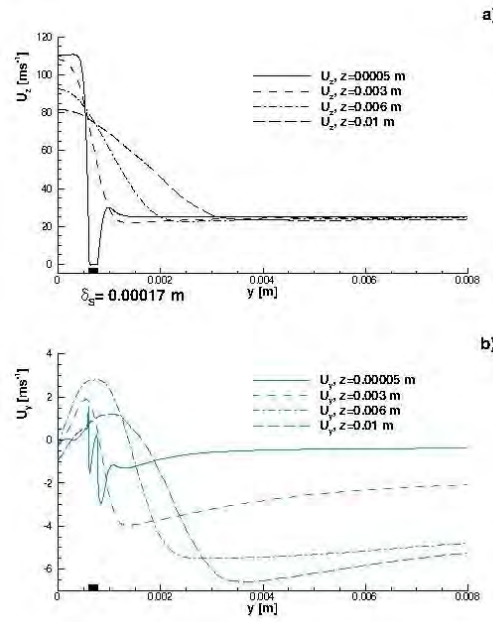


Figure 2: a) Mean streamwise velocity  $U_z$  versus crosswise direction  $y$ ; b) Mean crosswise velocity  $U_y$  versus crosswise direction  $y$ .

jet and to the heat released by the flame, air reaches its maximum value at  $z \sim 0.007\text{m}$  and decreases downstream. Many modeling approaches, describe turbulent premixed flames as an ensemble of flame elements that resemble steadily propagating strained or curved laminar flames. When Karlovitz (Ka) number is between 1 and 100 small eddies can penetrate the diffusion preheating zone of the flame and increase the mixing process, but not the thinner reaction layer that remains close to a wrinkled laminar reaction zone. This regime is identified as "Thickened Reaction Zone (TRZ)" regime.

### 3.2 Displacement speeds

Under the assumptions that a turbulent premixed flame retains locally the structure of a laminar flame but stretched and wrinkled by the surrounding turbulence, it is possible to separate the non linear nature of turbulence with that of the reaction rate defining a reaction progress variable, monotonically varying from 0 in the fresh reactants to 1 in the products. The flame zones are identified with progress variable isosurfaces, on which statistics are extracted. Once the species, that define the normalized progress variable  $c = (\sum_{i \in S} Y_i - \sum_{i \in S} Y_{i,u}) / (\sum_{i \in S} Y_{i,b} - \sum_{i \in S} Y_{i,u})$ , are determined (in this case  $S = \{\text{CO}_2, \text{CO}, \text{H}_2\text{O}\}$ ), and considering that Differential Diffusion is taken into account and Hirschfelder and Curtiss formula for mass diffusion and Soret effect are included, the classical governing transport equation must be revised as:

$$\frac{\partial c}{\partial t} + \mathbf{u} \cdot \nabla c = \frac{1}{\rho} \sum_{i \in S} \nabla \cdot (\rho \frac{W_i}{W_m} D_i \nabla X_i) + \frac{1}{\rho} \sum_{i \in S} \nabla \cdot (\frac{D_i^T}{T} \nabla T) + \frac{\dot{\omega}_c}{\rho} \quad (1)$$

with  $W_m$  the average mixture molecular weight. The mass diffusion term of Eqn. 1 based on the Hirschfelder and Curtiss formula may be split into a normal and tangential term recognizing that is

$$\nabla X_i = \frac{W_m}{W_i} \nabla Y_i + \frac{Y_i}{W_i} \nabla W_m \quad (2)$$

with  $\nabla Y_i = -|\nabla Y_i| \mathbf{n}$ . Further expansion of the divergence operator,  $\nabla \cdot ()$ , yields for Eqn.1 to:

$$\begin{aligned} \frac{\partial c}{\partial t} + \mathbf{u} \cdot \nabla c = & \\ \frac{1}{\rho Y_{c,N}} \sum_{i \in S} (-\mathbf{n} \cdot \nabla (\rho D_i |\nabla Y_i|) - \rho D_i |\nabla Y_i| \nabla \cdot \mathbf{n} + \nabla \cdot (\frac{\rho D_i Y_i}{W_m} \nabla W_m)) + & \\ \frac{1}{\rho Y_{c,N}} \sum_{i \in S} \nabla \cdot (\frac{D_i^T}{T} \nabla T) + \frac{\dot{\omega}_c}{\rho} & \end{aligned} \quad (3)$$

Here,  $\nabla \cdot \mathbf{n}$  is the curvature which may be expressed as the sum of the local inverses of the principal radii of curvature of the isosurface and flame surface curved convex towards

the reactants is assumed to have positive curvature. The same equation can be written in kinematic form for a progress variable isosurface  $c = c^*$  [10]:

$$\left[\frac{\partial c}{\partial t} + \mathbf{u} \cdot \nabla c\right]_{c=c^*} = S_d |\nabla|_{c=c^*} \quad (4)$$

where  $S_d$ , the displacement speed, is the magnitude of the propagation velocity of the isocontour with normal  $\mathbf{n} = -(\nabla c / |\nabla c|)_{c=c^*}$  directed toward the unburnt gas. Considering Eqns. (1-4) the following expression for the displacement speed  $S_d$  is obtained:

$$\begin{aligned} S_d = & \left[ \frac{1}{\rho |\nabla c| Y_{c,N}} (\omega_c + \sum_{i \in S} (-\mathbf{n} \cdot \nabla (\rho D_i |\nabla Y_i|))) + \right. \\ & \sum_{i \in S} (-\rho D_i |\nabla Y_i| \nabla \cdot \mathbf{n}) + \sum_{i \in S} (\nabla \cdot (\frac{\rho D_i Y_i}{W_m} \nabla W_m)) + \\ & \left. \sum_{i \in S} \nabla \cdot (\frac{D_i^T}{T} \nabla T) \right]_{c=c^*}. \end{aligned} \quad (5)$$

This expression shows that  $S_d = S_r + S_n + S_t + S_h + S_{td}$  is determined by five contributions: (a) reaction of progress variable, (b) normal mass diffusion, c) tangential mass diffusion, d) a new term related to Hirschfelder and Curtiss formula for mass diffusion, e) thermal diffusion. The value of the displacement speed changes across the flame normal because of thermal expansion effects, using a density-weighted displacement speed  $S_d^* = \rho S_d / \rho_u$  this effect may be largely reduced. Fig. 3a shows the density weighted mean (averaged

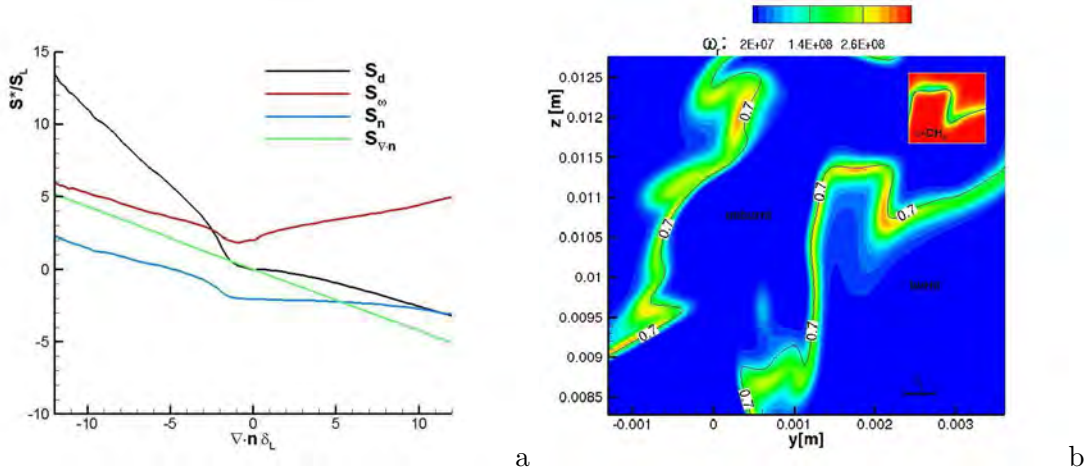


Figure 3: a) Density weighted mean displacement speed plotted against normalized curvature at  $c=0.7$ ; b) Instantaneous heat release  $[\text{W m}^{-3}]$  contour map and zoomed in view of the  $\text{CH}_4$  reaction rate. The maximum of heat release is located at negative curvatures.

on intervals of curvature) displacement speed and its components plotted against normalized curvature at isosurface  $c = 0.7$ . Curvature and flame displacement speed are

negatively correlated and the flame is thermally stable. Flame elements with negative curvatures (curvature center in the unburnt mixture) propagate with faster flame speed than positively curved elements. Even though the local equivalence ratio decrease at negative curvature, due to preferential diffusion of  $H_2$  towards hot regions, the effect of heat focusing at negative curvature increases the reaction rate of  $CH_4$ , as it has shown in Fig. 3b, and consequently the isosurface displacement speed (that is related to reaction rate through  $S_r$  component). The local enrichment of the flame at positive curvature is shown also in Fig.4a where the instantaneous equivalence ratio is shown. While in the laminar flame, the effect of the differential diffusion is only a reduction towards leaner condition of the equivalence ratio, in the tridimensional DNS, the effect of positive curvature produces also local enrichment of the flame.

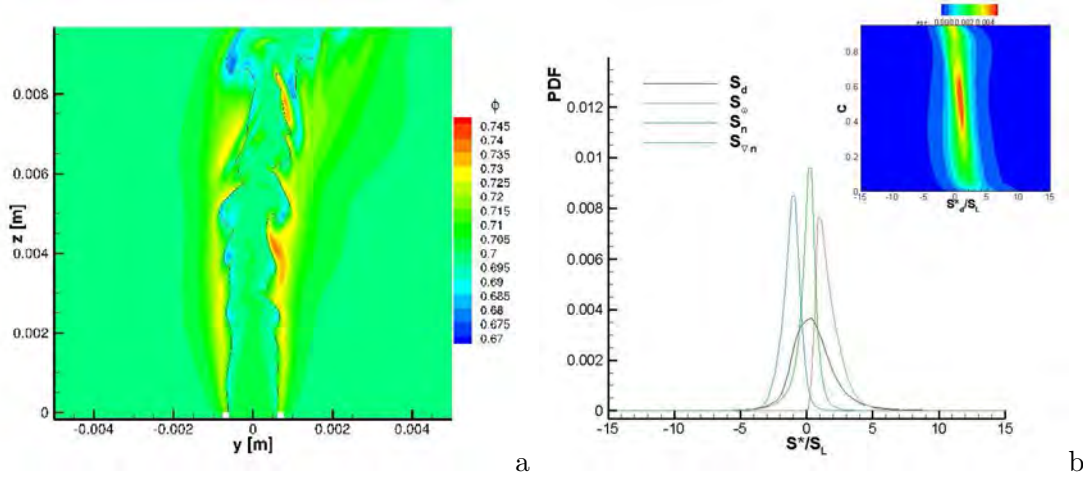


Figure 4: a) Instantaneous snapshot of the equivalence ratio  $\phi$  and isosurface of progress variable  $c = 0.7$ ; b) PDF of the density weighted mean displacement speed  $S_d^*/S_L$  and its three components at  $c = 0.7$ , PDF of  $S_d^*/S_L$  as a function of  $c$ .

In Fig. 3a it is evident that the flame is thermally stable, since the displacement speed of convex curvature regions is smaller than that of negative ones. Fig. 4b shows the Probability Density Function (PDF) of the normalized density weighted mean displacement speed  $S_d^*/S_L$  and its components at  $c = 0.7$ . At  $c = 0.7$ , where the heat release is maximum, the total  $S_d$  is not symmetric around zero, with a skewness towards positive values of displacement speed and its peak is  $S_s \sim 1 ms^{-1}$ . In the pre-heating zone of the flame ( $c < 0.5$ ) the PDF presents a broader range of velocities, thus implying non parallel iso- $c$  surfaces in agreement with the Thin Reaction Regime, where small eddies may affect the pre-heating zone more than the reaction layer.

### 3.3 Conclusions

A 3D slot  $CH_4 - H_2$ /Air flame was simulated with a high-order compact staggered numerical scheme and detailed chemical mechanism. Displacement speeds as function of curvature are examined. Preferential diffusion of  $H_2$  into positively curved flame elements are evidenced, the effect of mass differential diffusion calculated with the Hirschfelder

formula was included in the displacement speed and a new expression was found for the displacement speed in the case of differential diffusion for the species. The lean flame is intrinsically stable as shown by the displacement speed as a function of the curvatures, since negative curvature flame elements present higher velocity than positive ones. Further work is necessary to evaluate quantitative effect of  $H_2$  on structure of the flame. The simulation of the same flame with the Soret effect included in the transport equations is actually running on the CRESCO supercomputer cluster. The analysis done for the flame must be repeated for these results in order to quantify the role of thermal diffusion on statistics and stability of the flame.

## References

- [1] Schefer R. W., Wicksall D. M., Agrawal A. J., Combustion of hydrogen-enriched methane in a lean premixed swirl stabilized burner. *Proc. Comb. Inst.* 2003;29:843-51.
- [2] Hawkes E. R., Chen J. H., Direct numerical simulation of hydrogen-enriched lean premixed Methane-Air Flames, *Combust. Flame* 138 (2004) 242-58.
- [3] Filatyev S. A., Driscoll J. F., Carter C. D., Donbar J. M., Measured properties of turbulent premixed Flames for model assessment, including burning velocities, stretch rates, and surface densities, *Combust. Flame* 141, 1-21, 2005.
- [4] Sankaran R., Hawkes E. R., Chen J. H., Lu T., Law C. K., Structure of a spatially developing turbulent lean methane-air Bunsen flame, *Proc. Combust. Inst.*, 31, (2007) 1291-1298.
- [5] Klein M., Sadiki A., Janicka J., A digital filter based generation of inflow data for spatially developing direct numerical or large eddy simulations, *J. Comput. Phys.* 186, (2003), 652-665.
- [6] Poinso T. J., Lele S. K., Boundary Conditions for Direct Simulations of Compressible Viscous Flow. *J. Comput. Phys.*, 101:104-129 (1992).
- [7] Sutherland J. C., Kennedy C. A., Improved boundary conditions for viscous, reacting, compressible Flows, *J. Comput. Phys.*, 191:502-524, 2003
- [8] Kee R. J., Dixon-Lewis G., Warnatz J., Coltrin M. E., Miller JA, Moffat HK, The CHEMKIN Collection III: Transport, San Diego, Reaction Design, (1998).
- [9] Shu C. W., Osher S., Efficient implementation of essentially non-oscillatory shock-capturing schemes, *J. Comput. Phys.*, 77, 439-471 (1988).
- [10] Echehki T., Chen J. H., Unsteady strain rate and curvature effect in turbulent premixed methane-air flames, *Combust. Flame*, 106, (1996), 184.

# Nuclear Analysis of the ITER Cryopump Ports

*Fabio Moro\*, Rosaria Villari, Davide Flammini, Salvatore Podda*

*ENEA, Fusion Technical Unit, Nuclear Technologies Laboratory  
Via Enrico Fermi 45, 00044 Frascati, Rome, Italy*

**ABSTRACT.** The Cryopump (TCP) system is a fundamental component to ensure optimal plasma performance during ITER operations: its main function is to reduce the pressure inside the vessel; moreover its designed to extract the ashes generated by the deuterium-tritium fusion reactions, that will be processed in the tritium plant. A comprehensive nuclear analysis of the Cryopump Ports #4 and #12 has been carried out by means of the MCNP-5 Monte Carlo code in a full 3-D geometry, providing guidelines for the design of the embedded components. Radiation transport calculations have been performed in order to determine the radiation field inside the Lower Ports, up the Port Cell: 3-D neutrons and gamma maps have been provided in order to evaluate the shielding effectiveness of the Cryopump Housings (TCPHs). Nuclear heating induced by neutron and photons have been estimated on the TCP and TCPH to assess the nuclear loads during plasma operations. The shutdown dose rate in the maintenance area of the Lower Ports has been assessed with the Advanced D1S method to verify the design limits.

## 1 Introduction

The Cryopump system is a fundamental component to ensure optimal plasma performance during ITER operations: its main function is to reduce the pressure inside the vessel; moreover its designed to extract the ashes generated by the deuterium-tritium fusion reactions, that will be processed in the tritium plant. The ITER machine will be equipped with 6 torus Cryopumps (TCP) that are positioned in their Housings (TCPHs), integrated into the Cryostat walls at B1 level in the port cells (Fig. 1).

The Housings structure depends on the port cells in which it will be located: the Lower Ports #4, #10 and #16 will host the pellet injection system, consequently the relative TCPHs present dedicated cut-outs, while the TCPHs in the port cells #6, #12 and #18 have five straight penetrations for diagnostics systems. 1

The aim of the study presented, is to perform a complete assessment of nuclear responses in the Lower Ports #4 and #12 by means of the MCNP-5 Monte Carlo code [1] in a full 3-D geometry. The shielding effectiveness of the TCPHs has been assessed by means of 3-D neutrons and gamma maps; moreover, the nuclear heating induced by neutron and photons has been evaluated on the TCP and TCPH. Dose rate at 12 days after shutdown has been calculated in the maintenance area of the Lower Ports with the Advanced D1S

---

\*Corresponding author. E-mail: [fabio.moro@enea.it](mailto:fabio.moro@enea.it).



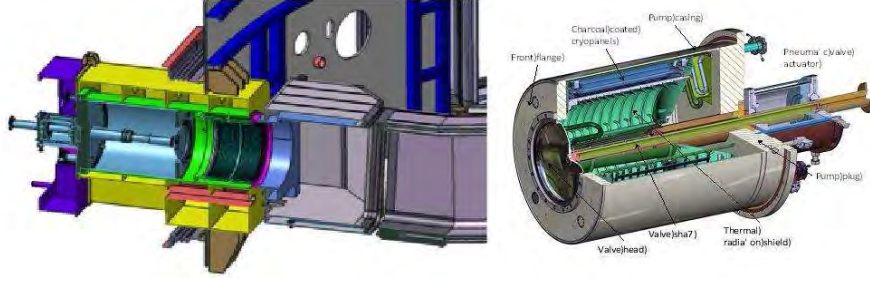


Figure 1: ITER Lower Port #4 (section along its longitudinal axis, left) and ITER torus cryopump (right).

method [2], in order to verify the design target ( $100 \mu\text{Sv/h}$ ). Considering the outcomes of the analyses performed, potential improvements of the shielding configuration aimed at the reduction of the dose level in the Port Cell have been proposed and discussed. The results of the neutronic analysis carried out provide guidelines for the design of the embedded components, in order to guarantee their structural integrity and proper operations.

## 2 Modelling and calculation tools

The simplified MCNP geometries of both the Lower Ports #4 and #12, generated by means of the CAD-to-MCNP interface MCAM 4.8 [3], have been singularly incorporated in the last MCNP ITER 40° reference model B-lite v3 [4], including the Shielding, TCP main components (Fig. 2), the TCPs and all the elements that are present in the area.

The chemical composition of the materials defined in the MCNP inputs includes impurities according to the latest documentation [5]. The volume percentages of the materials in the mixtures as well as the densities are settled on the basis of the masses extracted from the original CATIA files. Furthermore, both the ITER B-lite v3 models have been extended beyond the Bioshield to the port door, integrating details of the Port Cells (Fig. 3).

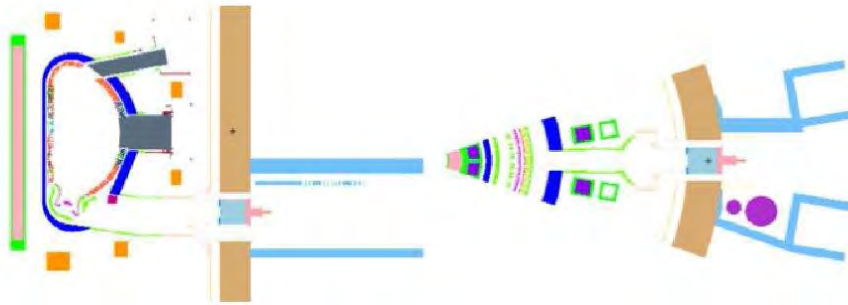


Figure 2: ITER B-lite v3 MCNP model upgraded with the Lower Port #12. Poloidal section along the Cryopump longitudinal axis (left) and toroidal section along the Cryopump mid-plane (right).

The calculations carried out are based on the ITER Deuterium–Tritium plasma source

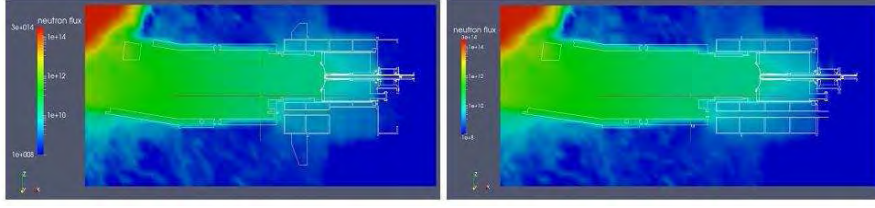


Figure 3: 3-D total neutron flux map ( $\text{n}/\text{cm}^2/\text{s}$ ): poloidal section through the longitudinal axis of the Lower Port #4 (left) and Lower Port #12 (right).

included in B-lite v3 model and normalized to 500MW of fusion power. The shutdown dose rates have been calculated using the irradiation scenario SA2 [6].

MCNP simulations have been run on the ENEA CRESCO HPC facility: the MCNP5v1.6 code, linked to the FENDL 2.1 [7] nuclear data libraries, has been compiled in its parallel version (Open MPI) using the Intel compiler suite and on the CRESCO cluster section 1 and 2. The installation of the code required the application of several patches to the `install` and `makefile` scripts, and the modification of several routines of the native source code in order to remove warnings and errors that prevented the building of the executable. Moreover, several routines in the original `src` directory have been customized in order to obtain the required nuclear responses: in particular, the application of the Advanced D1S method for shutdown dose rate calculations, required the implementation of the modules that treat the gamma transport.

The analyses performed required several 24-hours runs on CRESCO 1 and 2 with 600 cores each, generating  $\sim 109$  particles for neutron/gamma flux and nuclear heating estimation and  $\sim 108$  particles for shutdown dose rate calculations: the high performance computing capability of the CRESCO cluster, together with the application of variance reduction techniques (weight windows) allowed a consistent improvement of the statistics and provided results with sufficient accuracy (statistical errors ranging between within few % and 10% in the area of interest).

### 3 Nuclear analyses

#### 3.1 Neutrons and gamma streaming

Total and fast ( $E > 100\text{keV}$ ) neutron fluxes in the Lower Ports area have been calculated using a mesh tally extended up to the plug of the TCP. The radiation streaming through the Lower Ports structure is well visible in 3-D maps of total neutron flux shown in Fig. 3. The neutron flux decreases of about 4/5 orders of magnitude from the Lower Port shielding to the back end of the TCPs ( $\sim 10^{13} \text{ n}/\text{cm}^2/\text{s}$  in correspondence of the Lower Port entrance,  $\sim 10^8 \text{ n}/\text{cm}^2/\text{s}$  behind the TCP plug). Moreover, 3-D maps of fast neutrons flux highlight the streaming effect through the diagnostic penetrations in the Lower Port #12 (Fig. 5): a slightly higher neutron streaming ( $\sim$  a factor 2) is observed in the lower area of the TCPH.

As far the prompt gamma fluxes is concerned, 3-D maps of the gamma flux ( $\gamma/(\text{cm}^2\text{sec})$ ) have been carried out (Fig. 4): in both cases the gamma flux drops of about 5/6 orders of magnitude along the Lower Port ( $\sim 10^{12}\gamma/\text{cm}^2/\text{s}$  in correspondence of the Lower Port entrance,  $\sim 10^8\gamma/\text{cm}^2/\text{s}$  behind the TCP plug).

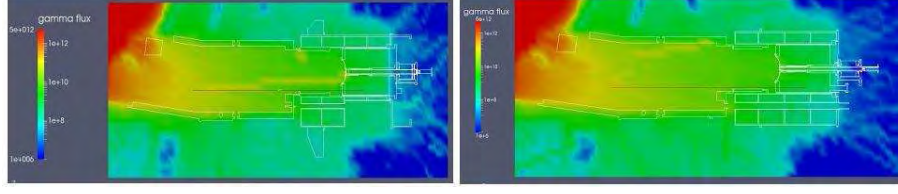


Figure 4: 3-D Gamma flux map ( $\gamma/\text{cm}^2/\text{s}$ ): poloidal section of the Lower Port #4 (left) and Lower Port #12 (right).

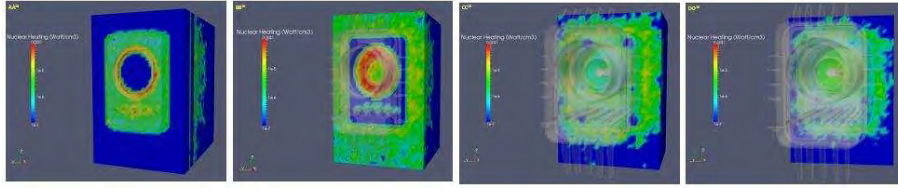


Figure 5: 3-D Nuclear Heating density ( $\text{W}/\text{cm}^3$ ) map: sections of the Lower Port #12 TCP and TCPH.

### 3.2 Nuclear heating

Nuclear heating calculations have been performed on both the Lower Ports TCP and TCPH. The nuclear heating density ( $\text{W}/\text{cm}^3$ ) has been evaluated for neutron and secondary photons in SS and the results are provided in 3-D maps (Fig. 5). The most loaded components in both cases are the TCPHs bellows and the TCP flange ( $\sim 10^{-4} \text{ W}/\text{cm}^3$ ), facing the direct radiation flux from the plasma source. Inside the TCP main body the nuclear load decreases of two orders of magnitude, reaching  $\sim 10^{-6} \text{ W}/\text{cm}^3$  in the TCP back area. Inside the plug, an increase of the heat load is observed, mainly due to the higher density SS composing this element with respect to the one used to define the inner structure of the TCP. Some hotspots are observed around the five diagnostics penetrations, extended along the SS collimators inside the TCPH structure.

### 3.3 Shutdown dose rate

The shutdown dose rate has been calculated using Advanced D1S method at 106 seconds (12 days) after shutdown, considering a total neutron yield of  $3 \times 10^{27}\text{n}$  (whole ITER lifetime [7]) for the Lower Port #12 model, being the less shielded configuration.

The outcome of this analysis (Fig. 6) shows that the dose rate 12 days after shutdown, evaluated in the Port Cell area immediately out of the TCP plug, is generically around  $100\mu\text{Sv}/\text{h}$ , thus very close to the safety requirement for the access zone 1. However,

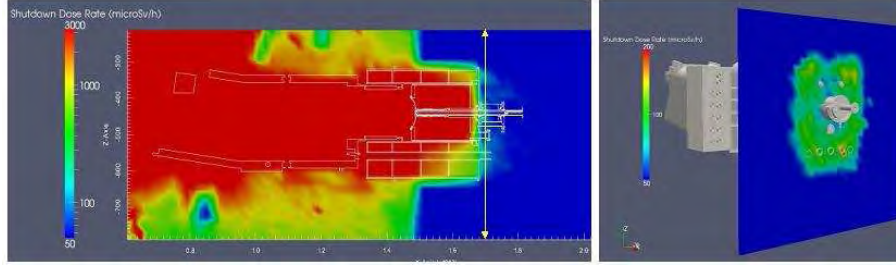


Figure 6: Dose Rate at 12 days after shutdown 3-D map ( $\mu\text{Sv/h}$ ): poloidal section through the longitudinal axis of the Lower Port #12 (left) and section outside the TCP plug (right).

some hot spots have been observed around the TCP plug, mainly due to the void region inside the TCPH (regeneration volume) that reduces its shielding capability. Moreover, the direct neutron flux through the diagnostics penetrations located in the lower area of the TCPH, contributes noticeably to increase the dose level in the Port Cell: this effect will be possibly reduced introducing the diagnostic devices inside the cut-outs that can provide a mitigation of the radiation streaming.

### 3.4 Additional shielding analysis

The studies performed suggest that the present layout of the Lower Ports might need some optimization in order to meet the safety requirements in all positions. In this frame, the study of an additional shielding configuration has been carried out. The proposed option consists of three shielding blocks composed by a mixture of SS316L(N)-IG and water (relative percentage: 80% and 20% respectively), arranged inside the Lower Port #12 to create a dog-leg path inside it.

A systematic analysis with different combinations of the #1, #2 and #3 shielding blocks has been performed, aimed at increasing the shielding efficiency and, at the same time, at minimizing the impact of the integrated blocks on the Lower Port present design and pumping performance. The result of this study showed that integrating in the structure the only shielding block #3, a significant reduction of the neutron streaming ( $\sim 33\%$ ) can be obtained. Moreover a non-negligible mitigation of the shutdown dose rate in the Port Cell has been achieved and the  $100\mu\text{Sv/h}$  design target could be fulfilled (Fig. 7).

Further analyses aimed at verifying the impact on the TCP efficiency are fundamental to evaluate the feasibility of this option.

## 4 Conclusions

A comprehensive nuclear analysis of the Lower Ports #4 and #12 has been performed with the MCNP code in support of the design of the TCP and TCPHs. Results highlighted that the void areas in the inner structure of the TCPHs and the presence of diagnostics penetrations in the Lower Port #12 weaken the shielding efficiency. The evaluated dose

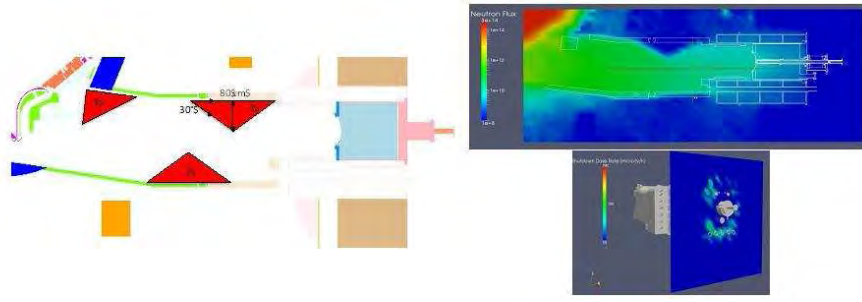


Figure 7: Shielding block configuration for the Lower Ports (left). Impact the shielding block #3 integration in the Lower Port #12: 3-D total neutron flux map ( $\text{n}/\text{cm}^2/\text{s}$ ) poloidal section (upper right) and dose rate at 12 days after shutdown 3-D map ( $\mu\text{Sv}/\text{h}$ ) section outside the TCP plug (lower right).

rate in the Port Cell maintenance area is generically within the design target of  $100\mu\text{Sv}/\text{h}$  12 days after shutdown, nevertheless some hot spots in critical positions are still present: an additional shielding configuration has been proposed in order to satisfy the safety requirements.

## References

- [1] X-5 Monte Carlo Team. Mcnp == a general monte carlo n-particle transport code – version 5. *Los Alamos National Laboratory, Los Alamos, New Mexico, USA*, April 2003.
- [2] Villari R. et al. Shutdown dose rate assessment with the advanced d1s method: development, applications and validation. *Fus. Eng. Des.* 89, pages 2083–2087, 2014.
- [3] FDS Team Wu Y. Cad-based interface programs for fusion neutron transport simulation. *Fus. Eng. Des.* 84, pages 1987–1992, 2009.
- [4] ITER Neutronic model: B-lite v3. *R121217 ITER IDM 9KKVQR*, 2012.
- [5] Moro F. et al. Neutronic analysis of the iter cryopump port. *ITER IDM NC5N3T*, 2014.
- [6] Recommendation on Plasma scenarios. *ITER IDM ITER\_D\_2V3V8G*.
- [7] Lopez Al dama D. et al. Fendl-2.1: update of an evaluated nuclear data library for fusion applications. *Report INDC(NDS)-46 (Vienna: IAEA)*, 2004.

# Structural and energetical analysis of a prismatic cadmium sulfide nanocluster

*E. Burresi<sup>1\*</sup>, M. Celino<sup>2†</sup>*

*<sup>1</sup>ENEA, Faenza Research Laboratories  
Technical Unit for Faenza Material Technologies (UTTMATF)  
Via Ravennana, 186, 48018 Faenza, Italy*

*<sup>2</sup>ENEA, C. R. Casaccia, Via Anguillarese 301, Rome, 00123 Rome, Italy*

**ABSTRACT.** A single wurtzite phase of cadmium sulfide cluster is investigated by ab-initio molecular dynamics simulations at different temperatures. This cluster is built with 324 atoms (162 cadmium and 162 sulfur atoms) with prismatic shape and relaxed at 10 K. After relaxation, this structure is heated under temperature program ranging between 100 K to 340 K. As we already detected for previous CdS cluster with 96 atoms (cluster96), a more stable phase was encountered at 340 K. Formation energy (F.E.) of the cluster confirms this new structure; the gap detected in the F.E. is less with respect to the cluster96. Around 340 K, the MSD (Mean Square Displacement) analysis reveals a large magnitude of the displacement of the atoms with respect the initial positions; this behavior can be due mainly to the larger movement of the superficial atoms. Analysis of the MSD curve for core atoms and superficial atom could help for obtaining this kind of information.

## 1 Introduction

Nanostructured cadmium sulfide quantum dots (CdS QDs) have attracted much attention for their novel optical and electronic properties employed in different technological fields [1]. Structural and electronic properties are not yet completely explained and different phase with different stability could be obtained during the synthesis process. A computational quantum approach can be useful for understanding the behaviors of these phases from atomic and crystallographic point of view. Regarding this problem, in this work, we report a computational study on CdS wurtzite phase nanostructured with prismatic shape. The unrelaxed cluster is built with 162 atoms of cadmium and 162 atoms of sulphur atoms. Subsequently was relaxed at 10 K and heated from 100 K to 340 K by using Car-Parrinello ab-initio molecular dynamics [2] .

---

\*Corresponding author. E-mail: [emiliano.burresi@enea.it](mailto:emiliano.burresi@enea.it).

†Corresponding author. E-mail: [massimo.celino@enea.it](mailto:massimo.celino@enea.it).



## 2 Computational details

Car-Parrinello Molecular Dynamics (CPMD) code which employs the density functional theory was used to heat the CdS cluster from 100 K to 340 K. We used a generalized gradient approximation BLYP for the exchange-correlation functional already implemented in CPMD package. In addition, we applied a norm-conserving pseudopotential approach in the specific case, a Martins-Trouiller type of pseudopotentials in the Kleinman-Bilander form for S and Cd. The structure was studied in an empty simulation cell to mimic isolated molecules with equal number of cadmium and sulfur atoms. The cell is cubic with 40 a.u. in size. The calculation of the average properties for each temperature was done on the equilibrated structure using the last 20000 steps. Generally 216 cores on CRESCO platform for each temperature step are used. The CPU average time employed for each CPMD iteration is 10.48 sec.

## 3 Results and discussion

The unrelaxed structure has been built with a regular geometry with prismatic shape reported in Fig. 1a. After relaxation at 10 K (Fig. 1b), the structure preserves at least the local order which disappears when the cluster is heated, as detected from radial distribution function (RDF) in Fig. 2.

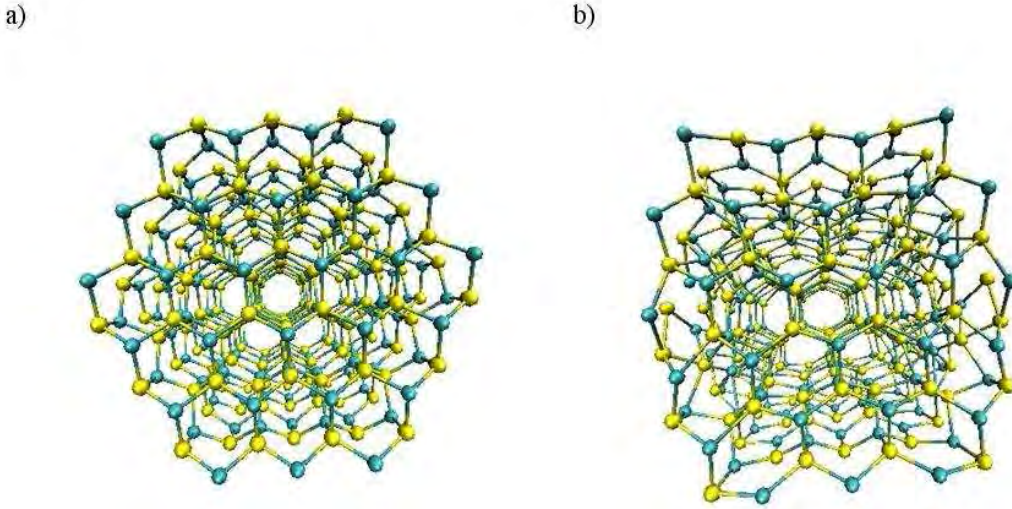


Figure 1: CdS cluster for unrelaxed (a) and relaxed (b) structure.

The system was gently heated up to 340 K; the temperature used for intermediate steps are 100 K, 200 K, 250 K and 300 K.

At 340 K the radial distribution function exhibits a trend which could suggest an initial melting process of the system. The minor peaks in the RDF for relaxed structure (at 10 K) disappear for structure heated at 340 K. By plotting the Kohn-Sham Energy during the simulation at 340 K (Fig. 3), it could be assumed that a new structure is obtained

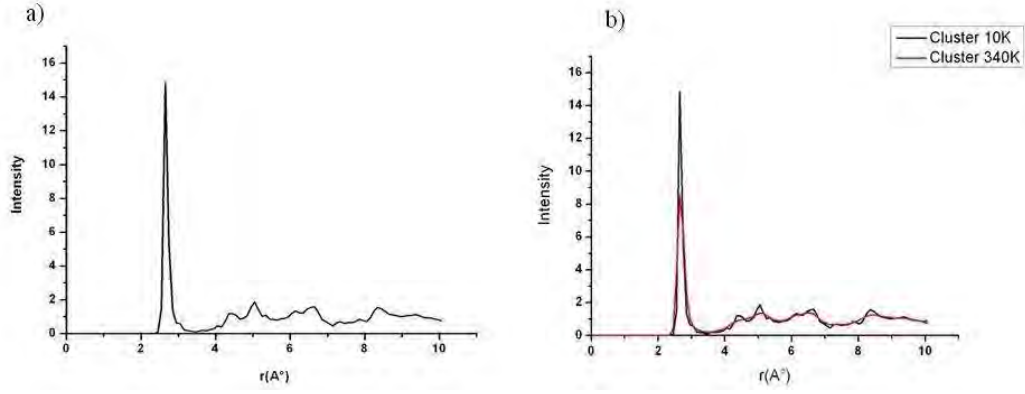


Figure 2: Radial distribution function for relaxed structure at 10 K (a) and heated at 340 K (b).

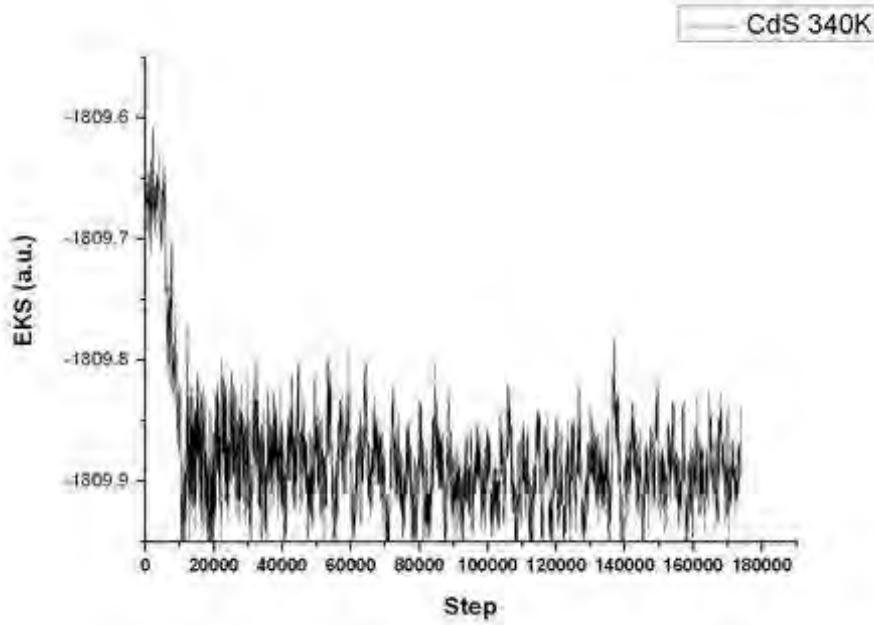


Figure 3: Kohn-Sham Energy of the cluster heated at 340 K.

with respect the initial geometry. From Fig. 4 we can see that this new structure has a formation energy less than the initial one. This temperature is the same we found in our previous work for smaller CdS cluster built with 96 atoms [3, 4].

This liquid-like behavior at high temperature is confirmed by MSD analysis where a strain of the structure at 340 K is detected, as we can note in Fig. 5a. In Fig. 5b we reported a particular view of the cluster heated at 340 K in order to show the difference between core atoms and surface atoms. This figure reveals a clear disorder of the surface while a preserved structural order of the core atoms.

To study deeply what kind of modification occurs on the structure of the cluster, it could



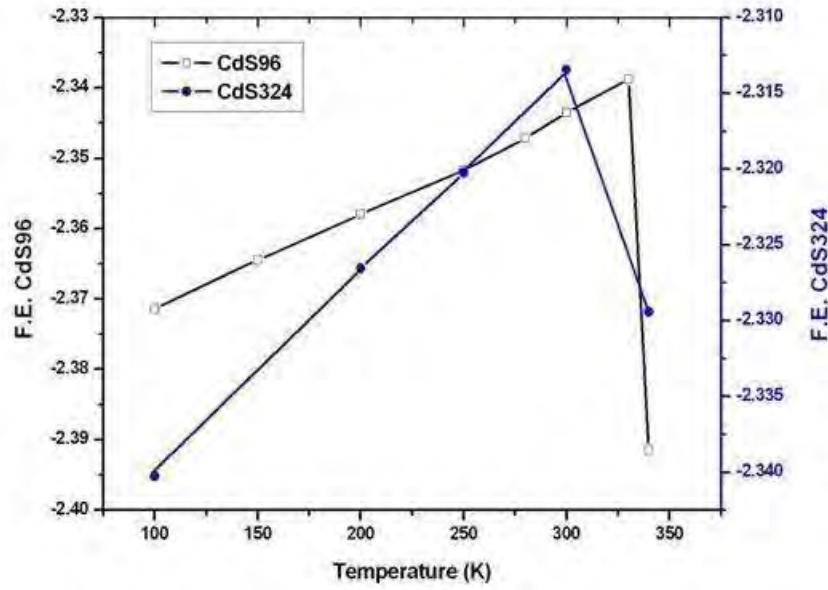


Figure 4: Formation energy (F.E.) of the cluster CdS324 (cluster with 324 atoms) with respect F.E. of the cluster built with 96 atoms (units eV).

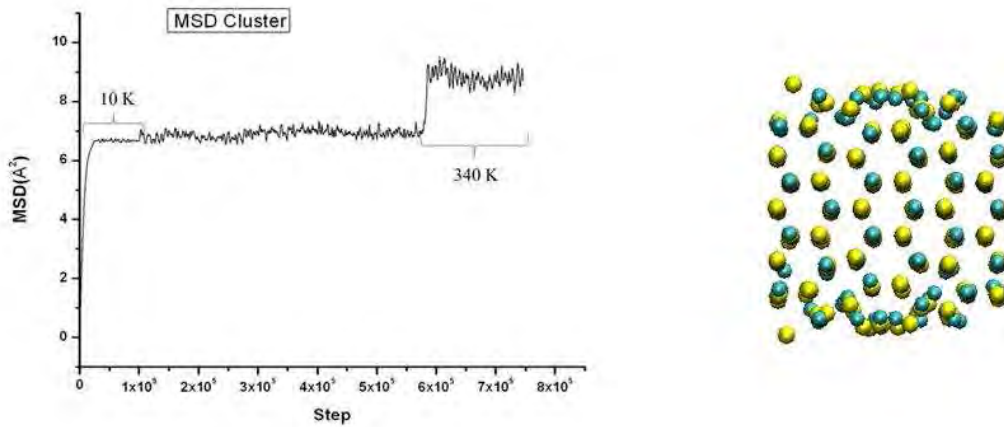


Figure 5: (a) MSD analysis of the total cluster. No meaningful strains have been detected between 100 K and 300 K. The first contribution is the relax of the structure performed at 10 K; (b) special view of the cluster heated at 340 K reveals the liquid-like structure on the surface.

help to divide the contribution of the core and surface atoms to the MSD curve. In this way it is possible to calculate the diffusion of the atoms on the surface, evaluating their contribution to the stability of the new structure of the cluster above 340 K.

## References

- [1] Alivisatos A. P. Prospective on the physical chemistry of semiconductor. *Nanocrystals. J Phys Chem*, 100:13226–13239, 1996.
- [2] CPMD, <http://www.cpmc.org/>, Copyright IBM Corp 1990-2008. Copyright MPI für Festkörperforschung Stuttgart 1997-2001.
- [3] Burresi E. and Celino M. Methodological approach to study energetic and structural properties of nanostructured cadmium sulfide by using ab-initio molecular dynamics simulations. *Solid State Science*, 14:567–573, 2012.
- [4] Burresi E. and Celino M. Surface states and electronic properties for small cadmium sulfide nanocluster. *Nanoscience and Nanotechnology Letters*, 5:1182–1187, 2013.

# First principles study of the stability of Graphane deposited on a copper surface using QUANTUM-ESPRESSO on CRESCO HPC

*Francesco Buonocore\**

*ENEA, Materials Technology Unit, Surface Technology Laboratory  
Casaccia Research Center, Rome, Italy*

**ABSTRACT.** The study of the interface between graphane and catalyst metal surfaces can be pivotal to assess the feasibility of direct CVD growth methods for this material. We investigated the adhesion of graphane to a Cu(111) surface by adopting density functional theory in order to determine the most stable bonding configurations and the change of the graphanes electronic properties. Moreover, we performed a thermodynamic analysis to compare stability of pure and hydrogenated carbon structures. Our calculations requested the use of the high performance computer facility CRESCO.

## 1 Introduction

The direct synthesis of graphene and related materials by using chemical vapor deposition (CVD) is one of the activity pursued in the ENEAs UTTMAT-SUP (Materials Technology Unit, Surface Technology) laboratory. The theoretical study of the interaction of the carbon structures with the metal catalyst and the growth mechanisms plays key role in tuning the growth of novel materials like graphene functionalized by atoms and/or chemical groups. In particular, various forms of hydrogenated graphene have been produced to date by several groups, while the synthesis of pure graphane has not been achieved yet, probably because of the large energy barriers from the reactant elements [1]. Graphane is a two-dimensional hydrocarbon constituted by graphene fully-hydrogenated on both sides of the plane. As an effect of hydrogenation, carbon atoms are displaced onto two distinct planes, where each carbon atom has three single bonds with carbon atoms and one single bond with a hydrogen atom out of plane. Graphane has been demonstrated to be more stable than benzene, the emblem molecule of organic chemistry [1, 2].

However, hopefully in the next future a route for the systematic and reproducible production of graphane monolayers will be found. The bottom-up approach appears to be the most viable for the direct synthesis of pure graphane. This approach would involve the direct synthesis of hydrogenated graphene by using CVD. Within the bottom-up approach, the plasma-assisted CVD in high vacuum of graphane-like films on Ti/Cu substrates at

---

\*Corresponding author. E-mail: [francesco.buonocore@enea.it](mailto:francesco.buonocore@enea.it).

the temperature of 650°C has been reported [3]. Looking forward to the direct CVD synthesis of graphane, in the present report we want to clarify, with the support of density functional theory (DFT) calculations, the nature of the interaction between graphane and the surface of the copper growth substrate. Moreover we perform a thermodynamic study of the graphanes stability in gas environment at high temperatures.

## 2 Computational tools and procedure

### 2.1 Computational package

The computational approach was based on a pseudo-potential plane-wave method using PWSCF code as implemented in the QUANTUM-ESPRESSO package [4]. QUANTUM-ESPRESSO is an integrated suite of computer codes for electronic-structure calculations and materials modeling. It implements a variety of methods and algorithms aimed at a chemically realistic modeling of materials from the nanoscale upwards, based on the solution of the density-functional theory (DFT) [5] problem, using a plane waves (PWs) basis set and pseudopotentials (PPs) [6] to represent electron-ion interactions. The codes are constructed around the use of periodic boundary conditions, which allows for a straightforward treatment of infinite crystalline systems, and an efficient convergence to the thermodynamic limit for aperiodic but extended systems, such as liquids or amorphous materials. Quantum-ESPRESSO code runs on many different computer architectures and allows good scalability till a large number of processors depending on the system size. We use a Quantum-ESPRESSO code compiled with Intel Fortran compiler, Math Kernel Library (MKL) and Message Passing Interface (MPI) parallelization on the high performance computer facility CRESCO [7], with a good scalability up to hundreds of cores.

### 2.2 Computational details

We used the vdW-DF2-C09 exchange-correlation functional that adds the vdW-DF2 correlation [8] to the C09 exchange functional [9]. The vdW-DF2-C09 functional has been demonstrated to be able to include non-local interactions, so that an accurate description of dispersion force for interfaces of graphene related materials with metals is possible [10]. All geometry optimizations were performed with cut-off for the wave functions of 30 Ry, cut-off for the charge density of 300 Ry and 661 Monkhorst-Pack grid. The final self-consistent calculations of the optimized structure properties used a cut-off for the wave functions of 40 Ry, a cut-off for the charge density of 400 Ry and 12121 Monkhorst-Pack grid. The Cu(111) surface was modelled by the repeated slab geometry which contains six Cu atomic layers with the in-plane 22 unit cell for the chair conformer. The vacuum gap between the topmost H atom and the next slab was set to 20 Å. The hydrocarbon structure and the top four copper layers were fully relaxed with a convergence threshold of 0.001 Ryd/Å on the inter-atomic forces.

### 3 Results and discussion

#### 3.1 Graphane/Cu(111) interface

The investigation into the structural properties of copper evidences that a Cu(111) surface exhibits the symmetry and distances required to overlap with the lattice of both graphene and graphane, in analogy with what has been found for Co(111), Fe(1-10) and Ni(111) surfaces [11]. We relaxed six different adsorption geometries for the chair conformer on top of a Cu(111) slab. We discuss the geometrical structures of the most stable configuration. The geometry with the lowest total energy is shown in Fig. 1. The results show that the graphane geometry exhibits poor sensitivity to functional choice and to metal/surface interaction. In general, it is also evidenced that the bottom C-H bonds, nearest to the Cu(111) surface, are larger than the top C-H bonds, with a maximal difference of 0.02 Å. This effect indicates some attraction from the underlying metal to the H atom.

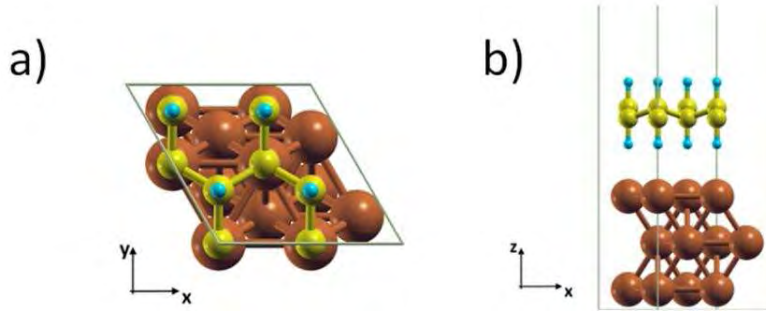


Figure 1: Atomistic periodic model after optimization of the interface of chair conformer of graphane with the Cu(111) slab in (a) top view and (b) side view. Only the first three copper layers are shown. The carbon atoms are shown in yellow, the hydrogen atoms in cyan and the copper atoms in brown.

In Fig. 2 the band structure for the most stable graphane chair conformer onto a Cu(111) surface is reported. The bands associated to graphane resulted to be very similar to the bands of isolated graphane. Therefore the band structure of graphane retains its gap and is not strongly affected by the interaction with the metal; the only important change is in the band gap extension. We found that the band gap of graphane interacting with the metal is 0.5 eV higher than when not interacting, keeping the same lattice parameters of the unit cell for both systems. This is a quite important change in the graphanes band gap, which is due to the interaction with the Cu(111) slab. We have inferred from the calculation of the electronic charge difference that there is an electronic charge stored at the interface at the origin of the band gap enlargement.

#### 3.2 Graphane thermodynamic stability

In order to verify if stable hydrogenated carbon clusters can be formed we compared by first principle calculations the stability of benzene, completely dehydrogenated benzene, graphene and graphane adsorbed on the copper surface and we performed a thermody-

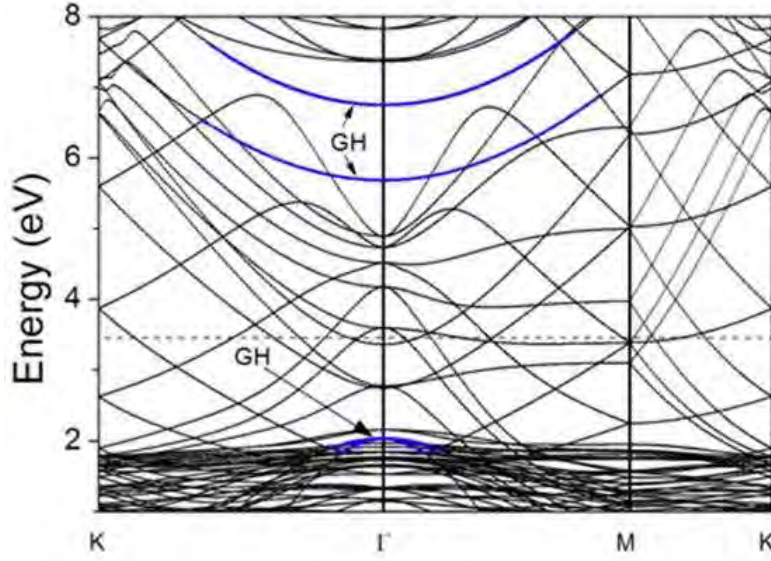


Figure 2: Band structures of chair conformer of graphane onto Cu(111) slab. The top and the bottom of the bands associated to graphene are evidenced by blue color and labeled as GH. The Fermi energy is indicated by dashed line.

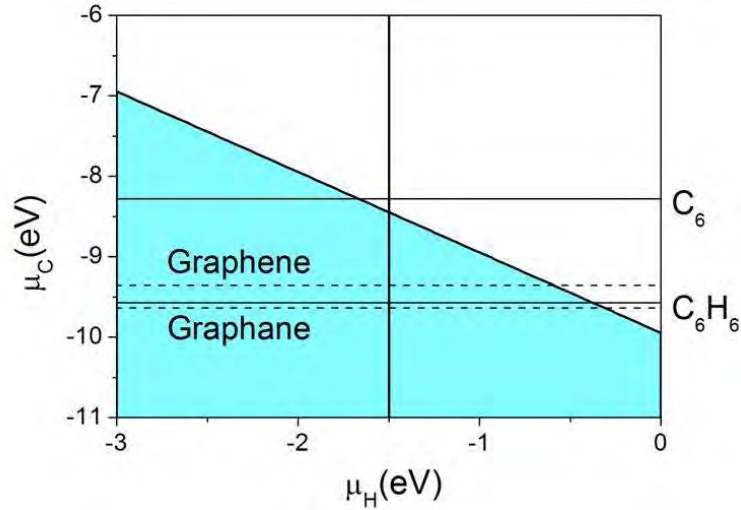


Figure 3: Relationship between carbon and hydrogen chemical potentials for a binary gas constituted by  $\text{C}_2\text{H}_4$  and  $\text{H}_2$  at 1100 K and  $\chi = 1/20$ . The carbon chemical potentials for graphene and graphane (dehydrogenated benzene and benzene) are marked as dashed (solid) horizontal lines. A  $\mu_H$  value corresponding to a  $\text{H}_2$  partial pressure of  $10^{-4}$  bar is marked as a vertical line.

namic analysis to compare thermodynamic stability of pure and hydrogenated carbon structures. In the same scheme developed by Zhang et al. [12], we plot in Fig. 3 the chemical potential  $\mu_C$  of carbon atoms at the equilibrium between  $\text{C}_2\text{H}_4$  and  $\text{H}_2$  gases, as a function of the hydrogen chemical potential  $\mu_H$ . The plot is reported for  $\chi = 1/20$

where  $\chi = P_{C_2H_4}/P_{H_2}$  (ratio of the partial pressures of ethylene and hydrogen). Every carbon structure with a chemical potential of carbon atoms lower than  $\mu_C$  is stable and will not react further with molecular hydrogen.

Our results demonstrate that the chemical potential of carbon atoms is lower for graphane than for graphene, in agreement with the greater stability calculated from the dissociation energy. Therefore the carbon chemical potential drives the growth of graphane rather than graphene. In a similar way we have found that benzene adsorbed on copper is thermodynamically more stable than an adsorbed cluster of carbon atoms ( $C_6$ ). For CVD temperatures around 800C and lower, and below a certain critical cluster size, the CVD growth of graphane appears possible and more favorable than graphene. Conversely, at higher temperatures and above a certain cluster size, dehydrogenated clusters will become the most stable species, giving rise to the preferential (well-established) nucleation and growth of graphene.

## 4 Acknowledgment

We acknowledge the ENEA-ICT team who provided the access to the ENEA-CRESCO high performance computing facility ([www.cresco.enea.it](http://www.cresco.enea.it)).

## References

- [1] Hoffmann R. One shocked chemist. *American Scientist*, 99:116–119, 2011.
- [2] Wen X. D., Hand L., Labet V., Yang T., Hoffmann R., Ashcroft N. W., Oganov A. R., and Lyakhov A. O. Graphane sheets and crystals under pressure. *Proceedings of the National Academy of Sciences USA*, 108:6833–6837, 2011.
- [3] Wang Y., Xu X., Lu J., Lin M., Bao Q., Ozyilmaz B., and Loh K. P. Toward high throughput interconvertible graphane-to-graphene growth and patterning. *ACS Nano*, 4:6146–6152, 2010.
- [4] QUANTUM-ESPRESSO: <http://www.quantum-espresso.org>.
- [5] Parr R. G. and Yang W. Density Functional Theory of Atoms and Molecules. Oxford University Press (1989).
- [6] Pickett W. E. Pseudopotential methods in condensed matter applications. *Computer Physics Reports*, 9:115–197, 1989.
- [7] Please, visit the website for more information: <http://www.cresco.enea.it>.
- [8] Lee K., Murray É. D., Kong L., Lundqvist B. I., and Langreth D. C. Higher-accuracy van der waals density functional. *Physical Review B*, 82:081101 (R), 2010.
- [9] Cooper V. R. Van der waals density functional: An appropriate exchange functional. *Physical Review B*, 81:161104 (R), 2010.

- [10] Hamada I. and Otani M. Comparative van der waals density-functional study of graphene on metal surfaces. *Physical Review B*, 82:153412, 2010.
- [11] Vinciguerra V., Buonocore F., Panzera G., and Occhipinti L. Growth mechanisms in chemical vapour deposited carbon nanotubes. *Nanotechnology*, 14:655–660, 2003.
- [12] Zhang W., Wu P., Li Z., and Yang J. First-principles thermodynamics of graphene growth on cu surfaces. *Journal of Physical Chemistry C*, 115:17782–17787, 2011.



# First-principle study of amorphous germanium under pressure

*G. Mancini<sup>1\*</sup>, M. Celino<sup>2</sup>, A. Di Cicco<sup>1</sup>*

<sup>1</sup>*Università di Camerino Via Madonna delle Carceri 62032, Camerino (MC), Italy*

<sup>2</sup>*ENEA, Ente per le Nuove Tecnologie, l'Energia e lo Sviluppo Economico Sostenibile  
C. R. Casaccia, Via Anguillarese 301, 00123 Roma, Italy*

**ABSTRACT.** In this paper we present the study of the modifications of structural properties of *a*-Ge due to the application of external pressure. The investigations are carried out in the framework of density functional theory via first-principles molecular dynamics (FPMD).

## 1 Introduction

Amorphous germanium (*a*-Ge) has been largely studied in the last decades using a variety of experimental and theoretical methods being a material of undisputed importance in basic science and applications in everyday life. Moreover the investigation of the structure of the condensed phases of germanium is of importance for fundamental science since in the solid state it exhibits polymorphism and pronounced changes in density and bonding upon melting and application of external pressure.

Germanium in its stable crystalline phase at room pressure, has a diamond structure (GeI) in which each atom is surrounded by four covalently bonded first neighbors in a tetrahedral formation. This phase of Ge has a very low density with respect to a close-packed structure and is semiconducting. Upon application of pressure, the tetrahedrally bonded network is broken and both the number of neighbors and the density increase. Around 11 GPa, a phase transition to the metallic  $\beta$ -Sn structure (GeII) occurs and even at higher pressures a hexagonal phase and a close-packed phase are found. Recently, an ab-initio metadynamics approach enlightened the existence of an intermediate phase in the lower pressure regime: the mC16 phase with four-membered rings, less dense than diamond [1]. Upon decompression, the crystalline stable structure is not always recovered, rather metastable crystalline phases are observed. The most common one is called ST12 (GeIII). It is based on tetrahedral structure with 12 atom per unit cell arranged to form fivefold and sevenfold rings. In this phase, Ge has higher density (about 10%) than the underlying stable one as reported in Ref. [2]. It is based on tetrahedral structure with

---

\*Corresponding author. E-mail: [giorgio.mancini@unicam.it](mailto:giorgio.mancini@unicam.it).

12 atom per unit cell arranged to form five-fold and seven-fold rings. As reported in Ref. [3], in case of rapid decompression (about 1 s from the high-pressure phase), a cubic structure characterized by eight atoms per unit cell and called BC8 (or GeIV) is likely to occur [3, 4]. This structure is not stable at room temperature but it transforms to the lonsdaleite structure (hexagonal with four atoms per unit cell) within a few hours.

At room pressure the melting temperature of crystalline Ge is  $T_m \simeq 1210$  K. At the melting transition the tetrahedral network is broken and the average coordination number increases from 4 to about 7, which is still low compared to other liquid metals which typically have coordination number between 9 and 12. Liquid Ge is metallic and amorphous Ge is semiconducting. Amorphous Ge is characterized by a continuous random network of distorted defective tetrahedra. Numerous experimental investigations of the density and bonding changes in different phases of germanium are presented in literature, using both x-ray [5] and neutron diffraction [6] techniques. Bond lengths do not differ more than 1% from the crystalline form and bond angles show a modest spread of the order of 10 degrees about the ideal value of the crystalline counterpart. Moreover *a*-Ge shows a complex behavior when an external pressure is applied, and scattered results are reported in literature. In particular, evidence for a sharp drop in resistivity and crystallization of thin *a*-Ge films was found at about 6 GPa [4, 7]. The x-ray absorption spectroscopy (XAS) technique was used to study the evolution of the local structure at high pressures. Freund et al. [8] showed that *a*-Ge remains amorphous up to 8.9 GPa while more recent XAS measurements showed that at 8 GPa *a*-Ge undergoes a phase transition though remaining amorphous [9]. The glass transitions in Ge under pressure was also studied in recent works both experimentally [10, 11] and through molecular dynamic simulations [12]. The combination of Raman and XAS spectroscopy measurements permitted to confirm that 8 GPa marks the onset of a polyamorphic transition in more homogeneous samples [13]. Moreover, Ref. [13] demonstrates that the actual transitions observed in a given sample depend on the initial morphology of the sample. However, the experiments reported in Ref. 17 were done in a limited pressure range (10–12 GPa) and did not account for the transitions occurring upon depressurization.

Polymorphism of amorphous Ge is reported to occur between the low-density amorphous (LDA) semiconductor and the high-density metallic amorphous (HDA) forms. This intriguing phenomenon is linked to a proposed first-order density- and entropy-driven phase transition in the supercooled liquid state [14]. The LDA-HDA transition has been studied in detail for thin film samples by X-ray absorption, extended X-ray-absorption fine structure (EXAFS), and Raman scattering methods [9, 13, 15]. Nevertheless, a detailed and unambiguous understanding of the complex phenomena taking place in *a*-Ge under pressure has only recently published [15].

In this paper, we report the study of the structural properties of *a*-Ge via first-principles molecular dynamics (FPMD) in the framework of density functional theory. We focus on the structural modification due to the application of the external pressure. An amorphous structure is produced by the quench of a melted, disordered structure at high temperature. After a detailed characterization of the amorphous structure in terms of neutron structure factor, pair correlation function and nearest neighbor analysis, the pressure is applied. During compression a room temperature is kept to mimic real experimental conditions.

The pressure is applied to the amorphous structure up to 14 GPa, but in the range 8-10 GPa, in good agreement with experimental results [13], a phase transition is observed. A detailed characterization of the atomic structure provides insights about phase transition under pressure. During the phase transition, the average coordination number goes from 4 for the *a*-Ge to about 6 of the high pressure phase.

## 2 Computational details

The first-principles molecular dynamics framework is applied to generate and characterize reliable amorphous structures of Ge. The software employed is CPMD (Car-Parrinello Molecular Dynamics) [16, 17]. The self consistent evolution of the electronic structure during the motion is described within density functional theory. A generalized gradient approximation (BLYP-GGA) is adopted for the exchange and correlation part of the total energy [18, 19] and norm conserving pseudopotentials are used for the core-valence interactions. A  $\Gamma$ -point sampling for the supercell's Brillouin-zone integration has been adopted. As shown for similar systems [20], the choice of the  $\Gamma$ -point sampling demonstrated a reasonable one for a 125-atom model. The electronic wave functions were expanded in plane waves up to the kinetic energy cutoff of 60 Ry and an integration time step of 3 a.u. (0.072 fs) was used.

During the equilibration of the liquid and solid structures a Nosé thermostat was used to control the ion temperature [21, 22, 23]. The characteristic frequency for the thermostat was  $1000 \text{ cm}^{-1}$ , which lies close to the peak at 37 THz in the diamond phonon density of states [24]. A second Nosé thermostat was used to control the fictitious electronic kinetic energy [25]. This thermostat prevents the electronic wave functions from drifting away from the instantaneous ground state (the Born–Oppenheimer surface), by removing excess fictitious kinetic energy. This drift is particularly severe for metals. In our simulation the liquid Ge sample possesses no band gap and hence the energy transfer rate is high. The characteristic frequency for the thermostat was  $45000 \text{ cm}^{-1}$  and the target kinetic energy was chosen according to the prescriptions in Ref. [25]. The Noseé thermostat on the electrons was used throughout the simulation and proved to be an effective way of keeping the electrons on the Born–Oppenheimer surface. During the equilibration of the liquid, the cooling of the liquid, and the temporal averaging of the solid, the deviation from the Born–Oppenheimer surface was never more than 0.01 eV/ion, and was often much less. This set of parameters yields accurate and converged properties for Ge crystalline lattices, both diamond and  $\beta$ -Sn.

Amorphous structures have been obtained for a system consisting of  $N=125$  atoms in periodically repeated cubic cells of size  $L=15.61 \text{ Å}$ . The starting density is equal to the experimental value for *a*-Ge at  $T=300 \text{ K}$ :  $\rho=5.51 \text{ gr/cm}^3$  [26]. To ensure that our results are independent on the initial atomic configurations, they are chosen to be drastically different from the crystalline counterpart. Since it is expected that the amorphous structures have a high percentage of Ge atoms four-fold coordinated, the starting configuration has been generated by randomly placing the atoms in the simulation cell. This procedure designs a starting configuration with many defects and many atoms with coordination different from four.

We further disordered the configuration by constant temperature and constant pressure MD equilibration at high temperature ( $T= 4000$  K). During the high temperature simulations, atoms covered a distance as long as about 2 nm ensuring the final configuration retains no memory of the initial geometry. Then we gradually lowered it to  $T= 1278$  K in 10 ps before an additional equilibration for additional 5 ps. The liquid configuration at  $T= 1278$  K, just above the melting temperature, has been used as starting point for the quenching procedure. The amorphous Ge is attained by cooling to 300 K the liquid sample over 0.5 ps. The system was then equilibrated for a further 0.5 ps to gain temporal averages. Two further simulations were performed to study the effect of quench on the atomic structure. One simulation used a slower cooling rate while in the other the liquid was cooled instantaneously to 300 K.

The amorphous structure is then used to produce amorphous structures under pressure. Pressure is applied via the method of Parrinello-Rahman [27] and it is increased by increments of 2 GPa up to 14 GPa. At each pressure the atomic system is relaxed according to the criterion that all the physical quantities are converged.

### 3 Results

#### 3.1 Amorphous structure

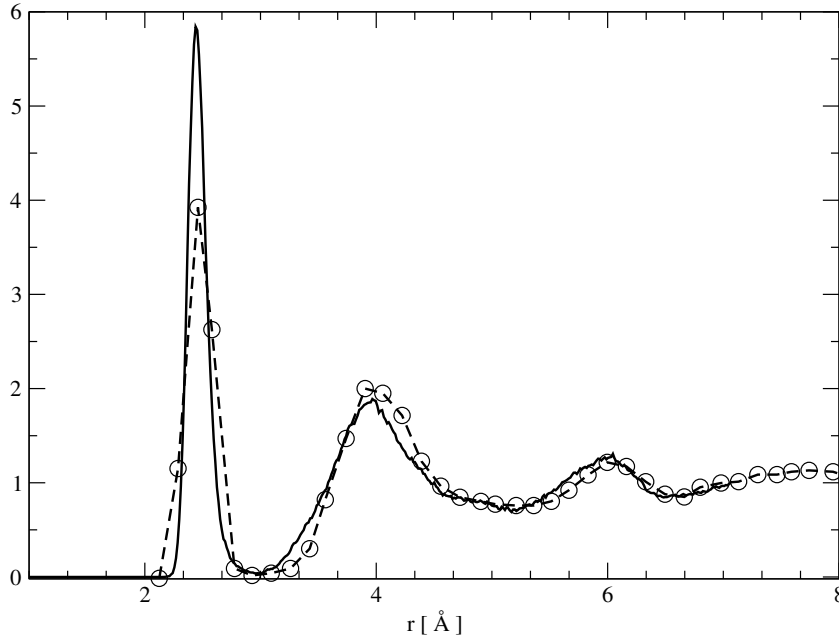


Figure 1: Pair correlation function  $g(r)$  of amorphous Ge at  $T= 300$  K. Full line is the first-principle MD, squares is the experiment Ref. [28].

Constant temperature and constant pressure MD simulations are performed to produce an *a*-Ge via the melt from the quench technique, as discussed in the previous section. The

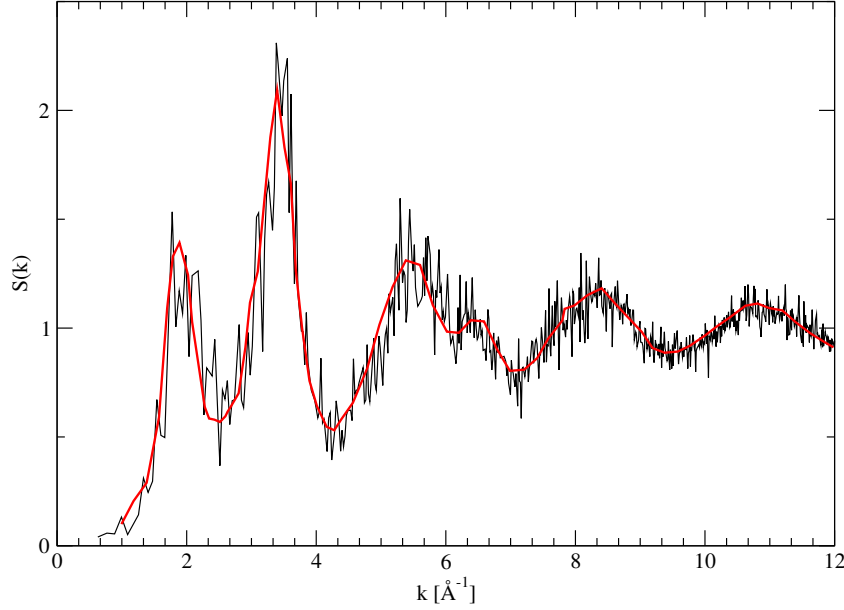


Figure 2: Static structure function  $S(k)$  for amorphous Ge at  $T= 300$  K. Full line is the first-principle MD, squares is the experiment Ref. [26].

good agreement of the calculated  $g(r)$  and  $S(q)$  (Figs. 1 and 2) confirms the reliability of our method.

Moreover the comparison with experiments confirms us that we have produced a good starting point for the simulations of *a*-Ge under an external pressure. The computer generated amorphous sample is slightly overcoordinated ( $N= 4.05$ ), indicating that 5-fold coordinated defects are somewhat more frequent than threefold coordinated sites. Further annealing process increase the agreement with experiment in terms of  $g(r)$  and  $S(q)$  but not in the reduction of the number of defects.

In Fig. 1 the computed pair correlation function is compared with the experimental result from Ref. [28]. There is an overall agreement for what concern both the position of the peaks and their heights. The reliability of our amorphous sample is confirmed by the good agreement between computed total structure factor and the experimental one, on the entire range of  $k$  values (Fig. 2).

### 3.2 LDA-HDA transition

Having verified the reliability of the amorphous configuration at zero pressure, an external pressure has been gradually applied to the atomic system. Each time, the simulation is long enough to allow the system to relax all internal degrees of freedom and to find the volume at equilibrium at each pressure. As shown in the pressure–volume curve given in Fig. 4, the volume changes smoothly up to 8 GPa and at this pressure an abrupt decline of the volume is seen, indicating a phase transition. The volume drop is close to the peculiar change already obtained in diamond to  $\beta$ -Sn transformation from *c*-Ge. Amorphous Ge

transforms from a low-density amorphous phase into a metallic high density phase: the good agreement with experimental results [13], despite the finite size of the simulation cell, is mainly due to the long time scales attained to allow complete equilibration of the atomic systems.

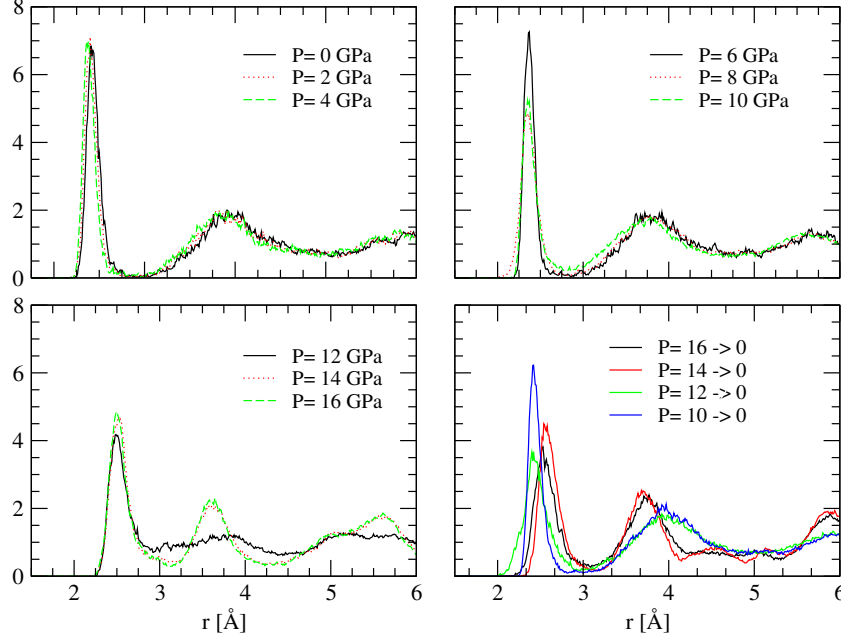


Figure 3: Comparison of the pair correlation functions for different values of the external pressure.

Zero-pressure sample upon rapid decompression is still an amorphous structure, denser than the initial structure because of the volume drop at the transition. Thus we can argue that the path on pressure release is reversible. The structure is found to be denser than the initial amorphous structure, indicating that an irreversible amorphous to amorphous phase transition has been seen.

As for the coordination number, at zero pressure it is centered around the crystalline one. An high percentage of atoms, about 92.8%, has coordination four. Upon application of the pressure the percentage of atoms with coordination 4 lowers and the distribution is slightly broader. At 8 GPa the percentage of atoms with coordination 4 is only 84.6% and there is evidence of 5-fold coordinated atoms (14.6%). During the phase transformation, at 10 GPa, the 4-fold coordinated atoms are about 68% and increase even more the 5-fold coordinated atoms (29.1%). At 12 GPa a new phase appears, as shown by the coordination number, in which 4-fold and 5-fold coordinated atoms are only 1.2% and 13.1%, respectively. On the contrary, percentages of 6-fold, 7-fold, 8-fold coordinated atoms are 41.3%, 33.3% and 10.1%, respectively. Thus the phase transition is characterized by a broader distribution of coordinations centered on coordination 6. Upon decompression partially lower coordination numbers are recovered and the 5-fold coordinated atoms are 49.3%.

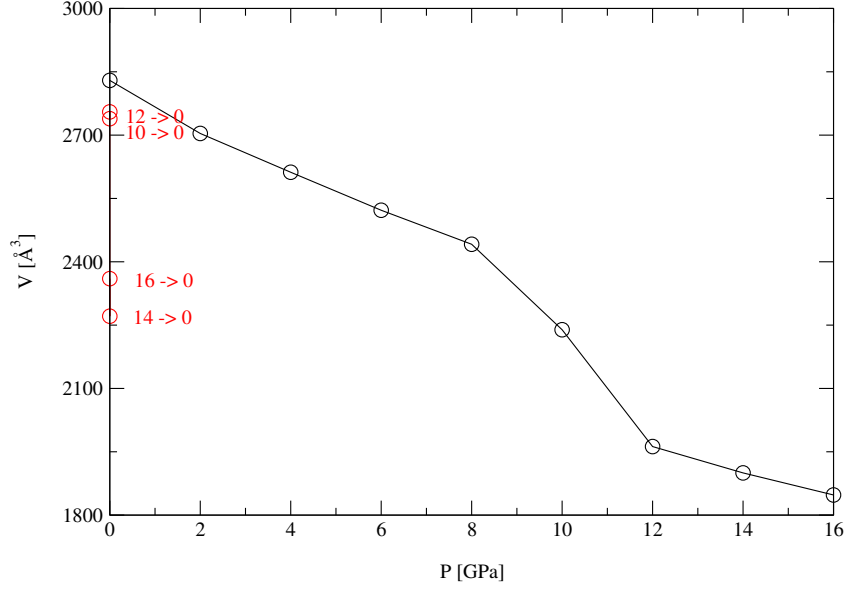


Figure 4: Cell volume versus external pressure. Loading of the pressure up to 16 GPa and unloading in one shot to zero pressure.

## 4 Conclusions

We showed that structural information gathered from molecular dynamics are able to provide an atomic-scale description of the phase transformation under pressure. This leads to a clear picture of the topological differences between systems having the same composition but different chemical nature and systems made of the same species but differing in composition.

The present approach finally provides a general framework for establishing bonding constraints in a neat way via model simulations, and will be used in the future for establishing constraint counting algorithms in more complex glassy materials from Molecular Dynamics.

## 5 Acknowledgements

The calculations were performed by using facilities and services available in the ENEA GRID infrastructure (Italy).

## References

- [1] Selli D., Baburin I. A., Martnak R., and Leoni S. *Scientific Reports*, 3:1466, 2013.
- [2] Bundy F. and Kasper J. S. *Scientific Reports*, 139:340, 1963.

- [3] Nelves R. J., McMahon M. I., Wright N. G., Allan D. R., and Loveday J. S. *Phys. Rev. B*, 48:9883, 1993.
- [4] Shimomura O., Minomura S., Sakai N., Asaumi K., Tamura K., Fukushima J., and Endo H. *Philos. Mag*, 29:547, 1974.
- [5] Filipponi A. and Di Cicco A. *Phys. Rev. B*, 51:12322, 1995.
- [6] Salmon P. S. *J. Phys. F: Met. Phys.*, 18:234, 1988.
- [7] Tanaka K. *Phys. Rev. B*, 43:4302, 1991.
- [8] Freund J., Ingalls R., and Crozier E. D. *J. Phys. Chem.*, 94:1087, 1990.
- [9] Principi E., Di Cicco A., Decremps F., Polian A., De Panfilis S., and Filipponi A. *Phys. Rev. B*, 69:201201(R), 2004.
- [10] Hedler A., Klaumunzer S. L., and Wesch W. *Nature Mater.*, 3:804, 2004.
- [11] Bhat M. H., Molinero V., Soignard E., Solomon V. C., Sastry S., Yarger J. L., and Angell C. A. *Nature (London)*, 448:787, 2007.
- [12] Kga J., Nishio K., Yamaguchi T., and Yonezawa F. *J. Phys. Soc. Jpn.*, 73:388, 2004.
- [13] Di Cicco A., Congeduti A., Coppari F., Chervin J. C., Baudelet F., , and Polian A. *Phys. Rev. B*, 78:033309, 2008.
- [14] Barkalov O. I., Tissen V. G., McMillan P. F., Wilson M., Sella A., and Nefedova M. V. *Phys. Rev. B*, 82:020507(R), 2010.
- [15] Coppari F., Chervin J. C., Congeduti A., Lazzeri M., Polian A., Principi E., and Di Cicco A. *Phys. Rev. B*, 80:115213, 2009.
- [16] Cpmd v3.13.2 copyright ibm corp 1990-2008, copyright mpi für festkörperforschung stuttgart 1997-2001.
- [17] Andreonia W. and Curioni A. *Parallel Computing*, 26:819–842, 2000.
- [18] Becke A. D. *Phys. Rev. B*, 38:3098, 1988.
- [19] Lee C. L., Yang W., and Parr R. G. *Phys. Rev. B*, 37:785, 1988.
- [20] Celino M. and Massobrio C. *Phys. Rev. Lett*, 90:125502, 2003.
- [21] Parrinello M. and Rahman A. *J. Appl. Phys.*, 52:289, 1981.
- [22] Nosé S. *Mol. Phys.*, 52:255, 1984.
- [23] Nosé S. *J. Chem. Phys*, 81:511, 1984.
- [24] Bilz H. and Kress K. *Phonon Dispersion Relations in Insulators*. Springer, Berlin, 1979.
- [25] Blochl P. E. and Parrinello M. *Phys. Rev. B*, 45:9413, 1992.



- [26] Waseda Y. *The structure of non-crystalline materials - liquids and amorphous solids*. McGraw-Hill, New York, 1981.
- [27] Parrinello M. and Rahman A. *Phys. Rev. Lett.*, 45:1196, 198.
- [28] Etherington G., Wright A. C., Wenzel J. T., Dore J. C., Clarke J. H., and Sinclair R. N. *J. Non-Cryst. Solids*, 48:265, 1982.

# Icosahedral structure and mean-square displacement in $\text{Cu}_{64}\text{Zr}_{36}$ metallic glass

*J. Zemp<sup>1\*</sup>, M. Celino<sup>2</sup>, J. F. Löffler<sup>1</sup>, B. Schönfeld<sup>1</sup>*

<sup>1</sup>*Laboratory of Metal Physics and Technology, Department of Materials  
ETH Zurich, 8093 Zürich, Switzerland*

<sup>2</sup>*ENEA Casaccia Research Center, UTMEA  
Via Anguillarese 301, 00123 – Rome, Italy*

**ABSTRACT.** The structure of  $\text{Cu}_{64}\text{Zr}_{36}$  metallic glass is studied by Molecular Dynamics simulations. Using a structure-specific nearest-neighbor histogram the spatial correlation of different local clusters is investigated. Icosahedra show an increased number of nearest neighbors in the range of 2 to 3 Å in comparison to a random distribution. Other cluster types are randomly distributed. Furthermore, the atomic displacements of deformed  $\text{Cu}_{64}\text{Zr}_{36}$  are investigated. Here, the displacements are found enhanced in the shear band region. After unloading structural relaxation takes place leading to a reduction in atomic mobility.

## 1 Introduction

Metallic glasses are produced by rapidly quenching from the melt so that crystallization is avoided. The final structure is often referred to as a *frozen-in* liquid, which is characterized by the lack of long-range translational order. Due to experimental restrictions on the cooling rate, the maximum sample size is limited to a few centimeters in case of the best glass-forming alloys. Still their mechanical properties are very promising for structural applications due to very high yield strength, wear resistance and large elastic strain. A major drawback, however, is their low plasticity. In contrast to crystalline metals, where plasticity is carried by dislocations, plastic deformation in metallic glasses is localized in thin shear bands (SBs). During the formation of a SB topological short-range order is partially destroyed, for example in  $\text{Cu}_{64}\text{Zr}_{36}$  the icosahedral backbone is broken up. The final SB structure shows a lower icosahedra fraction together with a larger Voronoi volume [1]. These structural changes lead to an even lower shear resistance, which manifests itself as strain weakening. To improve plasticity in metallic glasses it is thus important to study the structural processes on the atomic scale. Structural changes, e.g., due to the formation of SB, also influence the atomic motions in the material. Bokeloh et al. [2] in fact found an increase of the atomic diffusion after deformation using radiotracer experiments.

---

\*Corresponding author. E-mail: [jerome.zemp@mat.ethz.ch](mailto:jerome.zemp@mat.ethz.ch).

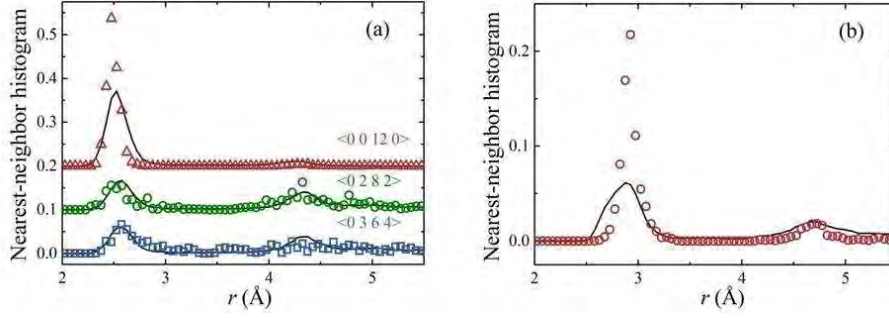


Figure 1: Nearest-neighbor histograms to study (a) the self-correlation of different types of Cu-centered clusters and (b) the cross-correlation of Cu-centered icosahedra and Zr-centered  $\langle 00124 \rangle$  Voronoi polyhedra. Data are taken from [3].

In the first part of this project, the local structure of  $\text{Cu}_{64}\text{Zr}_{36}$  metallic glass is studied by Molecular Dynamics simulations and the use of a structure-specific nearest-neighbor histogram [3]. In the second part, the atomic motions are studied in deformed  $\text{Cu}_{64}\text{Zr}_{36}$ . A SB is simulated as previously shown [4] and the atomic movements of both, Cu and Zr atoms, are followed by calculating the mean-square displacement.

## 2 Method

Molecular Dynamics simulations are carried out using the LAMMPS simulation package [5] and employing the interaction potential developed by Mendelev et al. [6]. The basic simulation procedure is explained in the CRESCO annual reports 2011 [7] and 2012 [4]. In addition, a long-time annealing treatment (300 ns at 800 K) was applied to further relax the amorphous structure. The structural analysis is based on the Voronoi tessellation. At 50 K the amorphous structure is dominated by Cu-centered icosahedra. If a center atom of one icosahedron is again the center atom of a neighboring icosahedron they are called interconnected. The spatial correlation of the Voronoi polyhedra is investigated using structure-specific nearest-neighbor histograms as described by Zemp et al. [3]. To study the atomic motions in and outside a SB, a large simulation box containing 746496 atoms was built from  $2 \times 4 \times 8$  replicas of a the smaller unrelaxed simulation box (11664 atoms). Periodic boundary conditions were applied in  $x$ - and  $z$ -direction but a free surface in  $y$ -direction. The sample was annealed at 850 K for 2 ns and subsequently cooled to 50 K with a cooling rate of 0.01 K/ps. Next, the sample was uniaxially compressed along  $z$ -direction with a strain rate of 107 s<sup>-1</sup> up to a total strain of 14.1% and unloaded. Then, the mean-square displacement is calculated by tracking the atomic positions at 680 K for 1 ns.

To achieve reasonable simulation times, 64 processors were generally required for the small and 256 processors for the large simulation box on the CRESCO infrastructure. All atomic visualization in this work was done using the software OVITO [8].

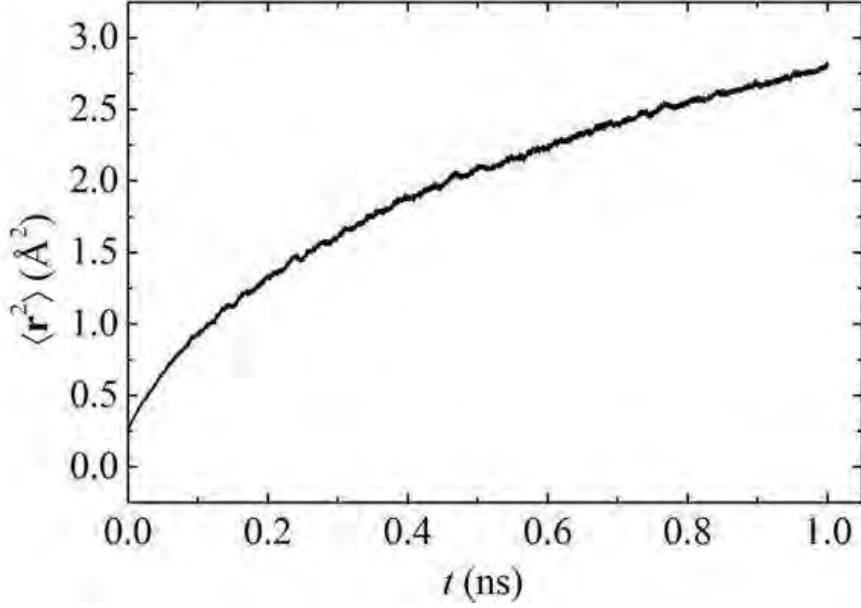


Figure 2: Mean-square displacement in  $\langle r^2 \rangle$  at 680 K. Structural relaxation during the simulation leads to a reduction of the slope with elapsed time.

### 3 Results and Discussion

#### 3.1 Icosahedral superclusters in $\text{Cu}_{64}\text{Zr}_{36}$

Below the glass transition temperature the structure of  $\text{Cu}_{64}\text{Zr}_{36}$  is dominated by Cu-centered icosahedra, which are interconnected and form large icosahedral superclusters. The spatial self-correlation of different structural motifs (such as icosahedra or other Voronoi clusters) is described by the structure-specific nearest-neighbor histogram as shown in Fig. 1a. A comparison of the histogram for icosahedra ( $\langle 00120 \rangle$ ) with a hypothetical random distribution of icosahedra unveils a strong spatial correlation. Icosahedra often occur in the vicinity of other icosahedra, which leads to a highly interconnected structure. On the other hand, other cluster types such as the  $\langle 0282 \rangle$  and  $\langle 0364 \rangle$  Voronoi polyhedra are close to the random distribution and thus no superclustering is observed. In Fig. 1b the cross-correlation of Cu-centered icosahedra and Zr-centered  $\langle 00124 \rangle$  is shown in comparison to a random distribution. The two cluster types are spatially highly correlated. As the  $\text{Cu}_2\text{Zr}$  Laves phase is entirely made up of Cu-centered icosahedra and Zr-centered  $\langle 00124 \rangle$  Voronoi polyhedra, this might be an indication of early stages of crystallization.

#### 3.2 Mean-square displacement in deformed $\text{Cu}_{64}\text{Zr}_{36}$

Fig. 2 shows the average mean-square displacement at 680 K during a simulation time of 1 ns in the entire sample. The data do not follow a linear behavior for two reasons: (i) at very short timescales the atoms move more or less freely inside their potential well

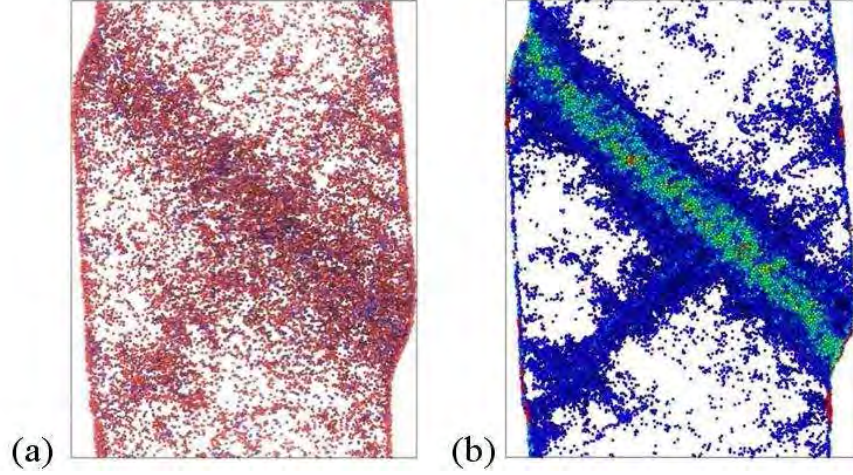


Figure 3: (a) Squared displacements in deformed  $\text{Cu}_{64}\text{Zr}_{36}$  at 680 K after 1 ns. Only atoms with a squared displacement  $> 6 \text{ \AA}^2$  are shown. Red: Cu atoms; Blue: Zr atoms (b) Atomic local shear strain (increasing values from blue to red) for an overall strain of 14.1%. Only atoms with a local strain  $> 0.3$  are shown. The deformation is highly localized in a single shear band.

and (ii) the curve flattens at large times due to structural relaxation happening during the experiment. Fig. 3a shows the squared displacements for each individual atom with a value larger than  $6 \text{ \AA}^2$  after 1 ns. The local atomic shear strain [9] is shown in Fig. 3b. The density of atoms with  $r^2 > 6 \text{ \AA}^2$  is higher in a narrow region, which by comparison of the Figs. 3a and 3b can be identified as the SB. This is further confirmed by calculating a cross-section perpendicular to the SB and averaging the squared displacements in slices with a thickness of  $10 \text{ \AA}$  as shown in Fig. 4. The mean-square displacement shows a peak in the shear band region. Overall Cu atoms show a larger mobility than Zr atoms, which is expected due to their size difference. These results are in good agreement with the experimental findings by Bokeloh *et al.* [2].

## 4 Conclusion and Outlook

The spatial distribution of icosahedra shows a significant amount of superclustering, which is not observed for other cluster types. In addition, Cu-centered icosahedra are spatially correlated to Zr-centered  $\langle 00124 \rangle$  clusters, which might be an indication of crystallization precursors. In conclusion, the structure of  $\text{Cu}_{64}\text{Zr}_{36}$  is topologically heterogeneous. The mean-square displacement in deformed  $\text{Cu}_{64}\text{Zr}_{36}$  metallic glass was studied using Molecular Dynamics simulations. At 680 K structural relaxation already occurs during the simulation time and consequently the mean-square displacement does not show the expected linear behavior. The atomic mobility is larger in the SB than in the rest of the sample, which can be attributed to strain-induced local changes in topological short-range order. In a next step these structural changes will be studied in more detail to better understand the atomic processes of self-diffusion in SBs of metallic glasses.

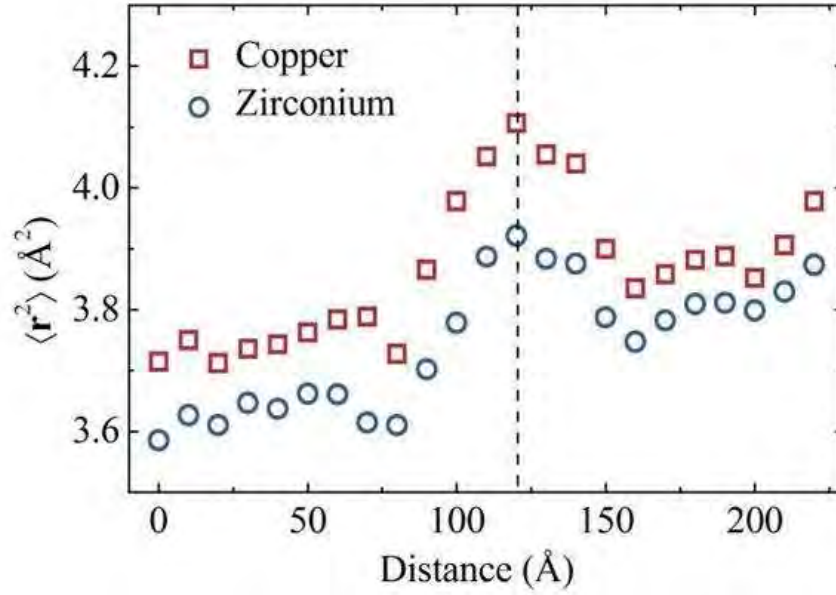


Figure 4: Cross-section perpendicular to the SB of the mean-square displacement in  $\langle r^2 \rangle$  which is calculated by averaging the data from Fig. 2a in slices with a thickness of 10 Å. The dashed line indicates the position of the SB.

## Publications and Conference contributions

1. Zemp J., Celino M., Schönfeld B., Löffler J. F. *Icosahedral superclusters in Cu<sub>64</sub>Zr<sub>36</sub> metallic glass*, accepted by Phys. Rev. B.
2. Zemp J., Celino M., Schönfeld B., Löffler J. F. *Spatial distribution of Icosahedra in a Cu–Zr metallic glass*, DPG Spring Meeting 2014, Dresden, Germany. (Talk)
3. Zemp J., Celino M., Schönfeld B., Löffler J. F. *The Formation of Superclusters in Cu<sub>64</sub>Zr<sub>36</sub> Bulk Metallic Glasses*, TMS 2014, San Diego, USA. (Talk)

## References

- [1] Ritter Y. and Albe K. Thermal annealing of shear bands in deformed metallic glasses: Recovery mechanisms in Cu<sub>64</sub>Zr<sub>36</sub> studied by molecular dynamics simulations. *Acta Mater.* 59, page 7082, 2011.
- [2] Bokeloh J., Divinski S. V., Reglitz G., and Wilde G. Tracer measurements of atomic diffusion inside shear bands of a bulk metallic glass. *Phys. Rev. Lett.* 107, page 235503, 2011.
- [3] Zemp J., Celino M., Schönfeld B., and Löffler J. Icosahedral superclusters in Cu<sub>64</sub>Zr<sub>36</sub> metallic glass. *accepted by Phys. Rev. B.*

- [4] Zemp J., Celino M., Löffler J. F., and Schönfeld B. Shear-band formation in  $\text{Cu}_{64}\text{Zr}_{36}$  metallic glasses under uniaxial compression. *Cresco Progress Report 2012*, ISBN 978-88-8286-302-9.
- [5] Plimpton S. Fast parallel algorithms for short-range molecular dynamics. *J. Comp. Phys.* 117, page 1, 1995.
- [6] Mendelev M. I., Kramer M. J., et al. Development of suitable interatomic potentials for simulation of liquid and amorphous cu-zr alloys. *Phil. Mag.* 89, page 967, 2009.
- [7] Zemp J., Celino M., Löffler J. F., and Schönfeld B. Molecular dynamics simulations of  $\text{Cu}_{64}\text{Zr}_{36}$  metallic glasses. *Cresco Progress Report 2011*, ISBN 978-88-8286-268-8.
- [8] Stukowski A. Visualization and analysis of atomistic simulation data with ovito – the open visualization tool. *Modelling Simul. Mater. Sci. Eng.* 18, page 015012, (Software available on <http://www.ovito.org>) 2010.
- [9] Shimizu F., Ogata S., et al. Theory of shear banding in metallic glasses and molecular dynamics calculations. *Mater. Trans.* 48, page 2923, 2007.

# Particle simulation of Alfvén mode dynamics in nuclear fusion devices

*Sergio Briguglio<sup>1</sup>, Giuliana Fogaccia<sup>1\*</sup>, Gregorio Vlad<sup>1</sup>, Xin Wang<sup>2</sup>*

<sup>1</sup>*ENEA C. R. Frascati,  
Via Enrico Fermi 45, 00044 Frascati, Rome, Italy*

<sup>2</sup>*Max-Planck-Institut für Plasmaphysik  
Boltzmannstrasse 2, D-85748 Garching, Germany*

**ABSTRACT.** The main activities related to particle simulation of electromagnetic turbulence in magnetically confined plasmas for controlled fusion.

## 1 Introduction

The comprehension of the interactions between Alfvén waves and energetic particles produced by nuclear fusion reactions and/or additional heating methods is one of the crucial issues to predict the possibility of realizing a nuclear fusion reactor based on magnetic plasma confinement. One of the most suited approaches for the investigation of such interactions in magnetic confinement devices (in particular, the so called "tokamaks") is represented by particle simulation. It consists in miming the behaviour of the confined plasma by a large set of *numerical* particles, each being representative of all the physical particles belonging to a little portion of the phase space.

The ENEA-Frascati theory group has developed, in the last two decades, a particle simulation code, called HMGC [1] (XHMGC, in its extended version, able to manage several particle species [2]). The code has proved to be one of the most advanced of the same class in the world, and has been applied both to the interpretation of experimental observations in present day tokamaks and the prediction of next generation ones (in particular, ITER). Moreover, it has widely used to get a deeper comprehension of saturation mechanisms of Alfvén waves and the effect these waves produce on fast ion transport, for suited numerical experiments. HMGC is limited to describe systems with magnetic surfaces characterized by circular poloidal section. A second hybrid code has then been developed, dubbed HY-MAGYC [3], able to describe general-shape magnetic surfaces, typical of devices designed to reach advanced confinement regimes.

Both codes are written in Fortran90 and can be compiled using `pgi` and `ifort` compilers. They have been parallelized for distributed-shared memory architectures, with the

---

\*Corresponding author. E-mail: [giuliana.fogaccia@enea.it](mailto:giuliana.fogaccia@enea.it).



distributed-memory level managed by the message-passing library MPI and the shared-memory level by the high-level parallel programming environment OpenMP. MPI library is used by the HMGC code. HYMAGYC, on turn, requires MPI, BLAS and LAPACK libraries. FFTW3 and HIGZ (CERN public libraries) are required by several sources to post process the output results of both codes.

The resources needed for this kind of simulations depend on the typical wavelength of the Alfvén waves described. ITER oriented simulations would require memory resources approximately equal to 2000 GBytes and, in order to maintain the elapsed time for a significant simulation under the limit of 100 hours, a very large architecture of not less than 10000-20000 processors. When running the code on the CRESCO architecture, less ambitious cases have then been investigated (mainly on cluster CRESCO4), with computational requirements one order of magnitude smaller than the ITER-oriented ones. Typical jobs require order 500 processors for 24 hours of elapsed time.

## 2 Dynamics of electron-fishbone modes

The investigation of fishbone modes driven by energetic electrons [4] using the code XHMGC [2] has continued also this year. In particular, it has been explored in some detail the linear dynamics of the electron-fishbone when considering: (a) purely fluid bulk plasma and a population of energetic electrons (peaked on-axis) treated kinetically which drives the mode by deeply trapped particle precession resonance, resulting in a mode which rotates in the electron diamagnetic direction; (b) previous case to which it is added the contribution coming from treating kinetically the thermal ions compressibility, and (c) also treating kinetically the thermal electrons compressibility. For both thermal ions and electrons an isotropic Maxwellian distribution function has been considered, while strongly anisotropic Maxwellian ( $T_{\perp}/T_{\parallel} \ll 1$ ) distribution function is used for the energetic electrons. The thermal ions treated kinetically permit to retain correctly the thermal ion Landau damping and enhanced inertia, and give rise to lower growth-rates with respect to the case in which only energetic electron contribution is retained (see Fig. 1): both co- and counter-passing particles contribute to damp the mode. If also the thermal electrons treated kinetically are retained, the local power exchange between the wave and the thermal electrons is observed to be strongly dependent on the radial shell considered, giving rise to a net positive contribution to the growth-rate; also in this case the dominant contribution to damping and drive is from co- and counter-passing thermal electrons.

Electron fishbones observed experimentally have been mainly observed as modes which rotate in the ion diamagnetic direction, and excited by energetic electrons with off-axis peaked profiles. Preliminary simulations with XHMGC have been performed assuming energetic electrons density profile peaked off-axis and, indeed, a mode which rotates in the ion diamagnetic direction has been observed. Moreover, as expected by theory, the driving resonance is clearly observed to be related to energetic electrons lying close to the trapped/untrapped boundary in velocity space, characterized by precession reversal motion.

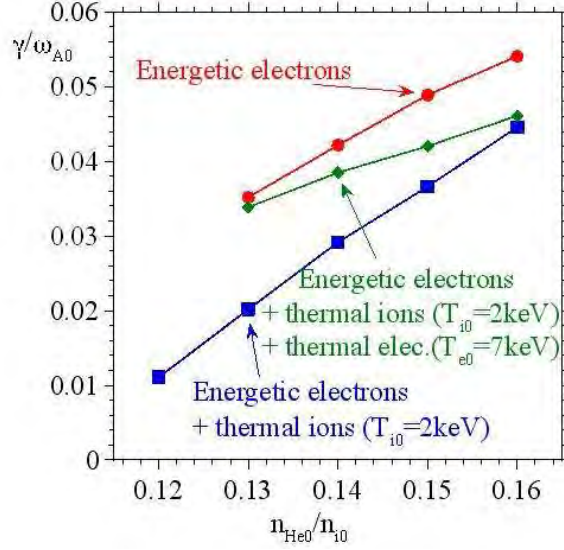


Figure 1: Growth rate of energetic electron fishbone mode vs. energetic electron density (normalized to bulk plasma density). Red curve refers to the case in which only energetic electrons are treated kinetically, blue curve includes thermal ions compressibility treated kinetically, while green curve adds also the thermal electrons compressibility contribution.

### 3 Benchmark of the gyrokinetic module of HYMAGYC

The benchmark activity of the more general code HYMAGYC [3], able to describe general-shape magnetic surfaces, has been continued in 2013.

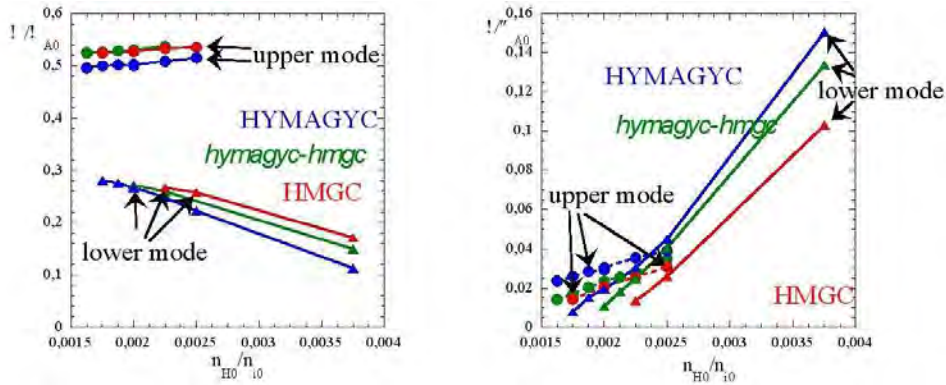


Figure 2: Comparison between HMGC (red symbols), HYMAGYC (blue symbols) and *hymagyc-hmgc* (green symbols) codes: normalized frequency (left) and growth rate (right) vs. normalized energetic particle density.

As the HMGC code, HYMAGYC is formed by a magnetohydrodynamic (MHD) module (which computes the electromagnetic fields in the presence of an energetic particle population) interfaced to a gyrokinetic module (which evolves energetic particles by particle-in-cell methods (PIC) and computes a pressure term need to close MHD equations). In

order to test independently the gyrokinetic module of HYMAGYC, it was extracted and interfaced to the MHD module of the HMGC code (the resulting tool will be indicated, in the following, as "*hymagyc-hmgc*"). The same case of previous benchmark activity has been used as a test case. Varying the energetic particle density, the real frequencies (Fig. 2 left) and the growth rates (Fig. 2 right) of the unstable modes have been compared between HMGC, HYMAGYC and *hymagyc-hmgc*. Good agreement is observed for the "upper" mode, whereas some differences in the growth-rate are observed for the stronger "lower" mode.

## 4 Nonlinear dynamics of Alfvén modes

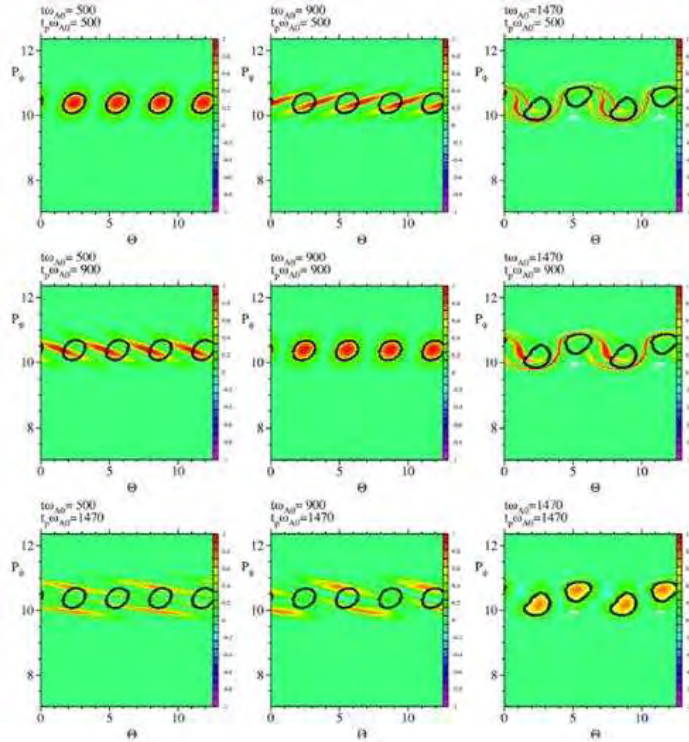


Figure 3: Comparison between the evolution of the resonant structures and that of the particle set contributing to such structures at different times. Particle markers are coloured according to the power they transfer to the wave computed at fixed times ( $t_n$ ) in the linear phase (upper and middle frames) and in the nonlinear one (lower frames). In each row, particles are plotted according to their positions at in the phase-space positions they have at the same three times ( $t$ ). Then, the frames along the diagonal show the resonant structures at the three times considered. The off-diagonal frames show instead the evolution of the "row-time" most destabilising particles at earlier or later times (below and above diagonal, respectively). In each frame, the black boundary contains the region characterised by a particle-to-wave power transfer greater than half of the maximum value obtained at the corresponding time  $t$ .

The issue of the nonlinear saturation of Alfvén modes has been addressed by means of test-particle diagnostics, based on Hamiltonian mapping techniques [5]. Two different modes have been considered: a Toroidal Alfvén Eigenmode in a low-shear equilibrium and an Energetic Particle Mode in a moderate-shear one. It has been shown that, in former case, saturation occurs as the width of the region, around the linear resonance, interested by flattening of the resonant particle density profile the mode becomes comparable with the mode width (*radial decoupling* mechanism). In the latter case, at low growth rates, the resonant layer becomes narrower than the mode; saturation occurs as the width of the flattening region reaches the width of the resonance (*resonance detuning* mechanism).

Several features have been evidenced by the analysis. In particular, the fact that the mode is driven by different particles at different times: the phase-space trajectory of the resonant structures must not be identified with that of the particles that, at a certain time, contribute to those structures. This can be seen from Fig. 3, which directly compares the evolution of resonant structures and particles. It is apparent that the evolution of particles driving the mode is different from that of resonant structures.

## References

- [1] Briguglio S., Vlad G., Zonca F., and Kar C. Hybrid magnetohydrodynamic gyrokinetic simulation of toroidal alfvén modes. *Phys. Plasmas*, 2:3711–3723, 1995.
- [2] WANG X. et al. *Phys. Plasmas* 18, 052504, 2011.
- [3] Vlad G. et al. Toward a new hybrid mhd gyrokinetic code: Progresses and perspectives. Presented at the 11th IAEA Technical Meeting on Energetic Particles in Magnetic Confinement Systems (Kyiv 2009).
- [4] Vlad G., Briguglio S., Fogaccia G., Zonca F., Fusco V., and Wang X. Electron fishbone simulations in tokamak equilibria using xhmgc. *Nuclear Fusion*, 53:083008, 2013.
- [5] Briguglio S., Wang X., Zonca F., Vlad G., Fogaccia G., Di Troia C., and Fusco V. Analysis of the nonlinear behavior of shear-alfvén modes in tokamaks based on hamiltonian mapping techniques. *Phys. Plasmas*, 21:112301, 2014.

# Structural, electronic and optical properties of low dimensional systems

*Adriano Mosca Conte<sup>1,2,3</sup>, Claudia Violante<sup>1,2</sup>, Viviana Garbuio<sup>1,2,3</sup>,  
Ihor Kupchak<sup>4</sup>, Margherita Marsili<sup>1,5</sup>, Paola Gori<sup>1,3,6</sup>, Olivia Pulci<sup>1,2,3\*</sup>*

<sup>1</sup>*European Theoretical Spectroscopy Facility (ETSF)*

<sup>2</sup>*Dipartimento di Fisica, Università di Roma "Tor Vergata"*

<sup>3</sup>*Mediterranean Institute of Fundamental Physics (MIFP)*

<sup>4</sup>*V. Ye. Lashkaryov Institute of Semiconductor Physics of NAS of Ukraine*

<sup>5</sup>*Dipartimento di Fisica "Galileo Galilei", Università di Padova*

<sup>6</sup>*Dipartimento di Ingegneria, Università Roma Tre*

## 1 Introduction

In this report we briefly review the results that have been obtained in the last year also thanks to the use of the ENEA CRESCO facility. All the works concern the calculation of physical properties of materials employing ab-initio theoretical methods based on Density Functional Theory (DFT) [1, 2, 3] for the evaluation of the geometrical properties and ground-state properties in general, and Many Body Perturbation Theory (MBPT, GW method) [4, 5, 6, 7] for the determination of electronic properties. For DFT calculations the free plane-wave code Quantum Espresso ([www.quantum-espresso.org](http://www.quantum-espresso.org)) has been used. Electronic properties have been instead calculated with the CHISIG plane-wave GW code that is interfaced with Quantum Espresso, since the electronic bands are calculated in a perturbative way starting from the Kohn-Sham eigenvalues and eigenvectors computed with Quantum Espresso. In the following sections, we present the results of three different studies: i) Ge nanocluster electronic properties; ii) Geometrical structure of highly doped Si(111)2x1 surface; iii) Infrared optical properties of the bi-dimensional systems graphene, silicene and germanene. While the calculations running on the ENEA CRESCO facility have been mainly carried out by the authors of this report, the complete studies to which we will refer are due to the work of many collaborators, which appear as coauthors in the publications.

---

\*Corresponding author. E-mail: [olivia.pulci@roma2.infn.it](mailto:olivia.pulci@roma2.infn.it).

## 2 Results:

### 2.1 Germanium nano dots

The size dependence of hydrogenated Ge-nanocrystals electronic gap was investigated comparing two first principle methods: the DFT-based  $\Delta_{scf}$  method [8] and the GW method, grounded on many-body perturbation theory [9]. The two methods were thought equivalent in the small cluster limit, although previous studies reported that scf almost systematically underestimated the electronic gap for hydrogenated Si nanocrystals and overestimated it in the case of Ag ones [10, 11]. We found that, upon going from large-diameter to small-diameter dots, the results of the two methods cross. The GW gaps are larger than the  $\Delta_{scf}$  ones for larger nanocrystals, but smaller in the case of  $\text{Ge}_5\text{H}_{12}$  lowest unoccupied molecular orbital (LUMO), which is strongly delocalized away from the cluster. Within the DFT Kohn-Sham scheme this state is above the LUMO level but it becomes the LUMO in the GW picture because its GW quasiparticle corrections are one order of magnitude smaller than the ones pertaining to more localized states (see Fig. 1).

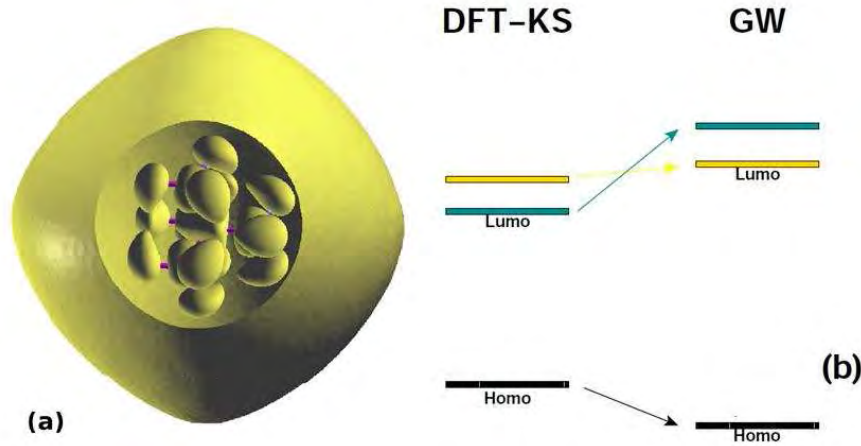


Figure 1: Square modulus of the Kohn-Sham single-particle wave function of the state LUMO+8 of  $\text{Ge}_5\text{H}_{12}$ . The plotted surface is the set of points where the charge density is at the 10% of its maximum value. Note that, to be able to visualize the cluster inside the ball-shaped isosurface, an artificial cut has been performed. (b) Schematic representation of the effect of the GW corrections on the ordering of the KS-levels. The GW corrections change the character of the LUMO.

### 2.2 Isomers of doped Si(111)2x1 surface

The relative energy stability between the two isomers of Si(111)2x1 surface (positive and negative buckling) is still a puzzle: in DFT calculations the isomers are almost degenerate in energy, with the negative buckling (nb) configuration slightly favoured, but this is in contrast to experimental findings, which show that the positive buckling (pb) is the observed structure at low and room temperature [12]. We have investigated the role of the

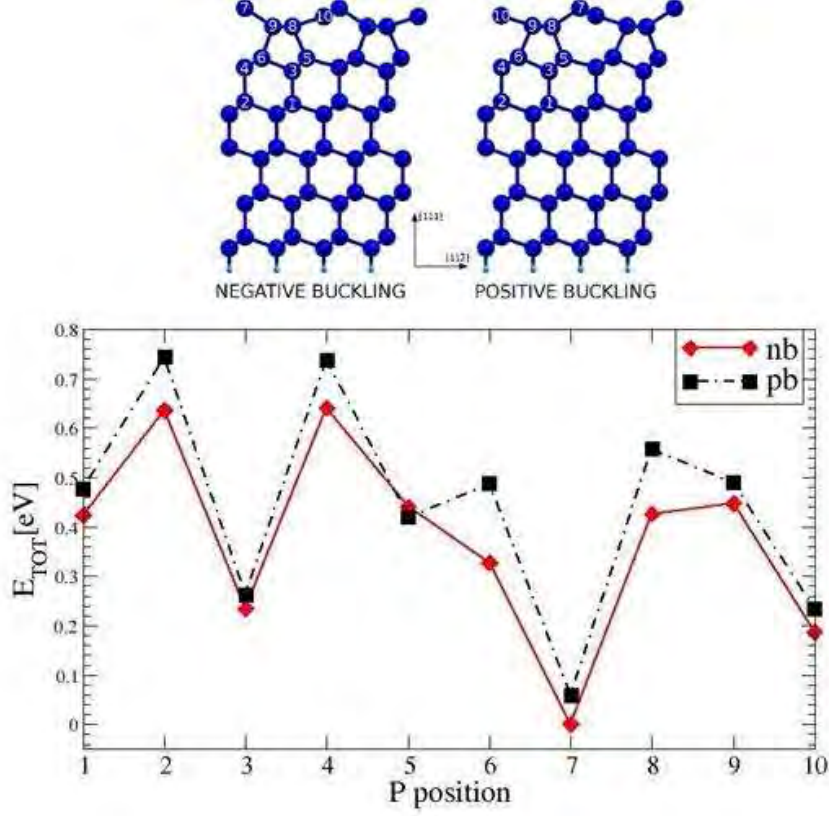


Figure 2: Total DFT energy of negative (nb) and positive (pb) buckling configuration versus the position of the donor atom in the surface.

exchange-correlation (xc) functional and of the presence of donor atoms in DFT calculations concerning ground-state properties [13]. We have found out that the choice of the xc functional plays no essential role in the relative stability, being the nb configuration always slightly lower in energy, but it can affect the geometry of the isomers. The effect of doping has been investigated for several possible positions of the phosphorus (P) donor atom in the surface isomers (see Fig. 2). Considering the most stable position of P (P7), relative stability between the isomers is not strongly affected by doping whereas geometric parameters are different with respect to the no doping case. Further investigations, including electron-phonon interactions, are needed to shed light on the relative stability issue between the two isomers of Si(111)2x1.

### 2.3 Bi-dimensional systems

We have investigated the infrared optical absorbance of 2D-honeycomb materials, namely graphene, silicene, and germanene. Our calculations [14] were boosted by an interesting experiment by Geim and coworkers [15], where it was shown that the infrared transmittance of graphene is quantized, with a 2.3% opacity of each layer. The 2.3% value is given by  $\pi\alpha$ , with  $\alpha = 1/137$  being the fine structure constant. We have shown, by ab-initio



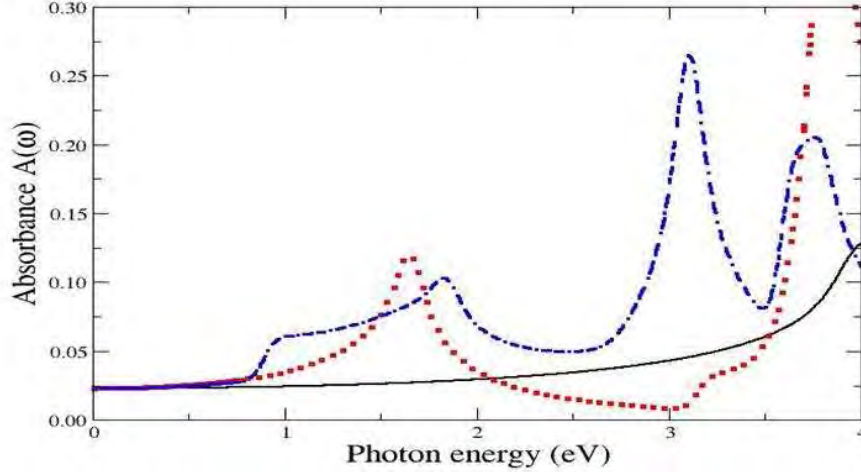


Figure 3: Calculated absorbance of graphene (black solid line), silicene (red dotted line) and germanene (blue dot dashed line). In all three cases the low energy absorbance goes towards the value  $\pi\alpha$ .

DFT calculations, that the infrared absorbance is universal for materials with a Dirac cone, since the infrared absorbance is only due to the linearity of the bands near the absorption onset. In particular, this applies also to silicene and germanene, as shown in Fig. 3.

## References

- [1] Hohenberg P. and Kohn W. Inhomogeneous electron gas. *Phys. Rev. B*, (136):864, 1964.
- [2] Dreizler R. M. and Gross E. K. U. *Density Functional Theory*. 1990.
- [3] Kohn W. and Sham L. J. Self-consistent equations including exchange and correlation effects. *Phys. Rev. A*, (140):1113, 1965.
- [4] Fetter L. and Walecka J. D. *Quantum Theory of Many Body Systems*. 1981.
- [5] Hedin L., "New Method for Calculating the One-Particle Green's Function with Application to the Electron-Gas Problem", *Phys. Rev. A* 139, 796 (1965); Mattuck R. D., "A Guide to Feynman Diagrams in the Many Body Problem", (McGraw-Hill, New York, 1976).
- [6] Hedin L. and Lundquist B. J., in: *Solid State Physics*, Vol. 23, edited by Ehrenreich H., Seitz F., and D. Turnbull (Academic Press, New York, 1969), p. 1.
- [7] Aryasetiawan F. and Gunnarsson O., "The GW method", *Rep. Prog. Phys.* 61, 237 (1998); Johsson L. and Wilkins J. W., "Quasiparticle Calculations in Solid", *Solid State Phys.* 54, 1-218 (2000).



- [8] Jones R. O., Gunnarsson O., Rev. Mod. Phys. 61, 689 (1989).
- [9] Marsili M., Botti S., Palumbo M., Degoli E., Pulci O., Weissker H-C, Marques M. A. L., Ossicini S., and Del Sole R. Ab-initio electronic gaps of ge nanodots: The role of self-energy effects. *Journal of Physical Chemistry C*, (117):14229, 2013.
- [10] Tiago M. L., Chelikowsky J. R., Phys. Rev. B 73, 205334 (2006).
- [11] Tiago M. L., Idrobo J. C., Ogut S., Jellinek J., Chelikowsky J. R., Phys. Rev. B 79, 155419 (2009).
- [12] Violante C., Mosca Conte A., Bechstedt F., and Pulci O., Phys. Rev. B 86, 245313 (2012).
- [13] Violante C., Chiodo L., Mosca Conte A., Bechstedt F. and Pulci O., Surf. Sci. 621, 123-127 (2014).
- [14] Matthes L. et al. Phys. Rev. B 87, 035438 (2013).
- [15] Nair R. R. et al., Science 320, 1308 (2008).

# Validation of the Monte Carlo model of TAPIRO Fast Reactor using MCNPX on ENEAGRID/CRESCO facility

*N. Burgio<sup>1\*</sup>, A. Santagata<sup>1</sup>, M. Frullini<sup>2</sup>*

<sup>1</sup>*ENEA, UT-FISST-REANUC, C.R. Casaccia  
Via Anguillarese 301, 00123 Rome, Italy*

<sup>2</sup>*DIAEE Sapienza University of Rome  
Corso Vittorio Emanuele II 244, 00186 Rome, Italy*

**ABSTRACT.** After Fukushima events, the Italian nuclear program has been redefined leaving space only to activities related to Generation IV nuclear systems. Accordingly with this renewed national scenario, TAPIRO fast reactor facility is gaining a relatively major strategic role. A program is in fact being proposed to host in TAPIRO benchmark experimental activities related to the development of Lead fast reactor and Accelerator Driven Systems. A first step of this program would consist on the validation of neutronic codes, cross section data and reactor models to be adopted for its analysis. Along this line in this work the results of a simulation study has been made relevant to the measurements performed in the SCK-CEN/ENEA experimental campaign carried out in the 1980-1986 period. The calculations have been made using a MPI parallel implementation of the Monte Carlo code MCNPX 2.7.0 on the ENEAGRID speeding up the calculations significantly with respect to scalar implementations.

## 1 Introduction

In the current Research and Development activities the needs of scoping studies where concept and experimental designs are tested to be representative of technological, political and economic project requirements, become stringent. After Fukushima accident, the government initiative for exploitation of the Italian Nuclear industry (2nd and 3rd generation) have been drastically reduce in favour of the validation activities of the totally innovative Generation 4 nuclear systems. The new situation furnishes a motivation to focus all the ENEA and CIRTEN past activities on Lead Fast Reactor (LFR) and Accelerator Driven System (ADS) in a more harmonized design frame where the control the main design and scope requirements allows the cutting of costs, the increase of safety and the preservation of experiments representativity [1]. Aim of this report is the reinterpretation of the experimental campaign of 1980-1986 on TAPIRO reactor held by ENEA and SK-CEN [2]

---

\*Corresponding author. E-mail: [nunzio.burgio@enea.it](mailto:nunzio.burgio@enea.it).

by using a Monte Carlo model of the reactor. In our opinion, the adjustment of neutronic models of relatively simple experimental systems, such as TAPIRO [3], constitutes the basis to develop well-designed experience and calibration methodology in support of LFR and ADS activity. To fulfil this scope, a very detailed TAPIRO model has been implemented as MCNPX [4] input deck to reproduce the late experimental configurations on which the measurements have been performed. The model outcomes, in terms of criticality analysis (Keff, control rods worth), neutron flux intensity, neutron spectra and reaction rates in the irradiation channels have been compared with the measurements finding an overall good agreement. As conclusion, the model set-up appear to be sufficiently accurate to allow the detailed design of experiences in the irradiation facility of TAPIRO reactor.

## 2 Brief description of the MCNPX TAPIRO model

TAPIRO reactor, located in the ENEA-Casaccia Research Center of Rome-Italy, is a fast neutron spectrum irradiation facility. Since 1971, TAPIRO has been used to design shielding solutions for fast nuclear reactors, test of radiation damage for electronic components and dosimetry studies. TAPIRO nominal power is of 5 kWth and the neutron flux at the core center is  $4 \cdot 10^{12} \text{ [n] [cm}^{-2} \text{] [s}^{-1} \text{]}$ .

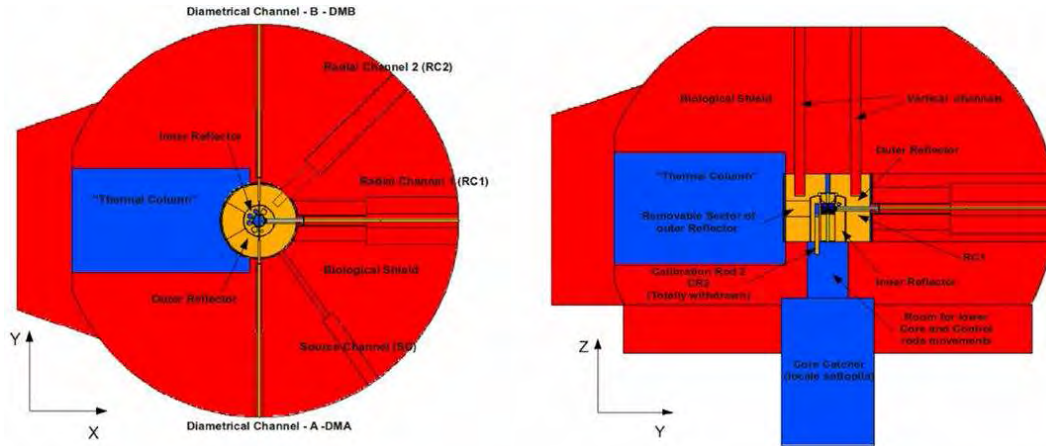


Figure 1: Cross sections from MCNPX geometry: plant (left) and side (right) views of the model.

The core is a cylinder of UraniumMolybdenum (98.5% U, 1.5% Mo) alloy that is completely surrounded by a copper reflector. The upper core block is constituted by two fuel disks (fixed core). The lower disk of the fixed core has a passing hole connected with the experimental diametrical channel (see Fig. 1). The subsequent five disks form the movable core that, jointly with the lower part of inner reflector, could be separated from the fixed core allowing a further reserve of negative reactivity for emergency shut-down or for special reactor physics measurements. The core is cooled by Helium gas that flows on the lateral surfaces of the fuel disks clad. The control rod system, housed in the copper inner reflector, is constituted by five movable cylindrical sectors: 2 SR (safety rods), 2 CR (control rods) and 1 RR (regulation rod). The control rods system regulates the reactor

power by increasing or reducing the neutrons escape from the core. A second cylindrical shell of copper constituted the outer reflector. As reported in Fig. 1, the DM (diametrical channel) passes through the entire core diameter, at mid-plane height, allowing samples irradiation in neutron fission spectrum. RC1 and RC2 (radial channels 1 and 2) are two radial channels coplanar to DM. They have different inner diameter and minimum penetration distances to the core center. The reactor start up neutron source is housed in a radial channel symmetrical to RC2 (see Fig. 1- source channel). The Thermal column room may host nuclear grade graphite block for irradiation experiments in thermal neutron spectrum (see Fig. 1). Two vertical channels penetrate from the top of reactor down to the outer surface of the copper reflector. The materials compositions have been expressed at isotopic level. Structural material elemental composition and density have been obtained from the reference documentation of the facility and the isotopic composition has been derived assuming, for each atomic species (except fuel), the natural isotopic abundance. Since the amount of fission products is relatively low and the fuel thermal coefficient is of the order of  $-1 \text{ pcm}/^{\circ}\text{C}$ , all the simulations have been executed in clean and cold condition (i.e. neglecting fission products and at  $0^{\circ}\text{C}$  of temperature).

### 3 MCNPX implementation on ENEAGRID

The source code version of MCNPX 2.7.0 has been loaded into the AFS home directory of the authorized users (an agreement regarding an export controlled code license must be signed with U.S. Department of Energy on personal basis). The compressed directory is then unzipped and through the "configure" standard utility a dedicated Makefile has been prepared. The executable has been built using Portland Group FORTRAN90 and C/C++ compilers (version 10.2 for linux86-64), and linked with the OPENMPI-1.4.1 (lib64). The compilation and installation of the executable request less than hour. The typical running time for the problems reported in this work were of 5-12 hours, depending of the degree of precisions requested for the results, allocating 64 to 256 cores. MCNPX can be considered as production code, and the above reported calculation times fit very comfortable in our production cycle.

### 4 Comparisons of simulations results with measurements

The comparison as been carried out in term of criticality analysis (i.e. the ability of the model to simulates a stable chain reaction) and estimation of neutron reaction rate responses. During the experimental campaign neutron induced fission ( $^{235}\text{U}$ ,  $^{238}\text{U}$ ,  $^{239}\text{Pu}$  and  $^{237}\text{Np}$ ) and activation rates (Au, Ni, Co and Sc) have been measured by miniature fission chambers and metallic foils along traverses in various channels. In particular, in the present work, reaction rate traverses measured along RC1 (Radial Channel 1 ) have been compared with the results relevant to the TAPIRO simulation calculations. To avoid the dependency from day to day reactor power fluctuations, measured reaction rates have been normalized to the response of a large  $^{235}\text{U}$  fission chamber called MMC (Main Monitor Counter) [2] . However, there is no mention of the exact position and amount of

<b>Simulation description</b>	<b><math>k_{eff}</math></b>	<b>Standard deviation</b>	<b><math>\Delta k/k</math> [pcm]</b>
Shim rods at 10 cm of insertion, RR at 0.55. Fuel Pellet in Diametrical channel	1.00098	0.00008	98

Table 1:  $K_{eff}$  estimations with rods positions as reported in [2]-Fig. 8.2.4.

<b>Control Rod</b>	<b>Experimental Rod worth [pcm]</b>	<b>Simulated Rod worth [pcm]</b>	<b>Standard Deviation of simulated rod</b>
<b>Regulation Rod</b>	326	303	11.31
<b>Shim rods bunch</b>	990	854	16.00
<b>Shim rod 1</b>	462	432	11.31

Table 2: Comparisons of the measured rods worth with the simulated ones.

the active fissile mass of the MMC in the reported experimental layout. In the present work the results have been compared in relative, normalizing the traverses to their own maximum. In a subsequent activity this inconvenient has been solved by using a dedicated normalization procedure [5].

#### 4.1 Critical Analysis

A first preliminary set of runs has been executed to estimate the  $k_{eff}$  with the TAPIRO core maintained at room temperature and assuming the absence of fission products (clean and cold conditions). Tab. 1 reports the the  $k_{eff}$  result for a simulation executed with rods positioned in a configuration that experimentally realizes criticality ( $k_{eff}=1.0000$  - stationary fission reaction chain).

It is evident that the model tends to estimates as slightly supercritical (98 pcm) the experimental configuration. Tab. 2 reports the comparison of the experimental rods worth (see [6]) with the MCNPX model estimations.

The perturbation analysis reported in [5] clearly shows that the excess of reactivity and the rods worth uncertainties estimated by the model are statistically congruent with the experimental uncertainty on the TAPIRO critical mass. Consequently the model agreement with the real reactor, in terms of criticality and rods worth, is quite satisfactory in the limits of the experimental data knowledge.

#### 4.2 Reaction rates traverses on RC1 (Radial Channel 1)

Despite simulated and experimental measurements have been performed in the same ranges of positions, they are generally not coincident. Consequently, the simulated data have been post processed accordingly with the following algorithm:

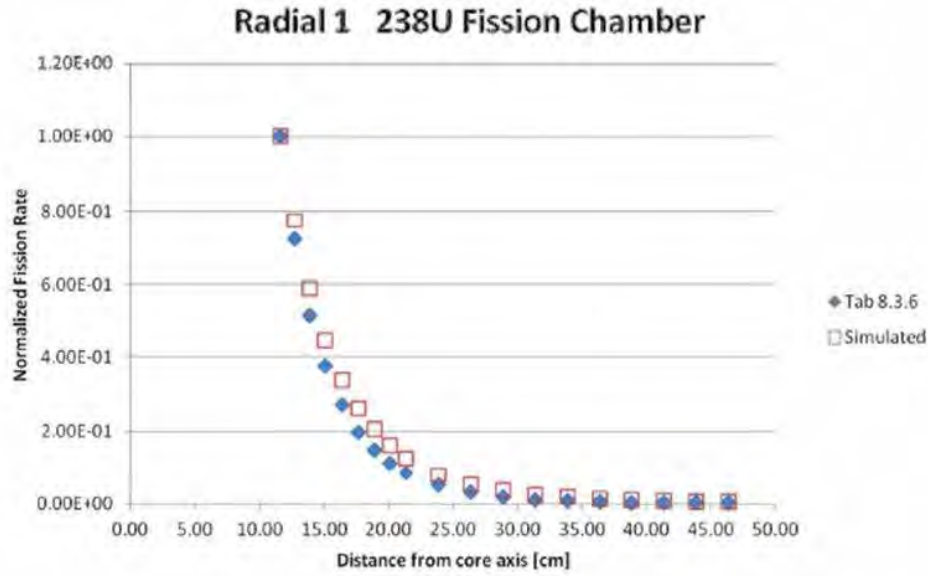


Figure 2: Comparison of experimental vs. simulated responses of  $^{238}\text{U}$  fission chambers along Radial Channel 1.

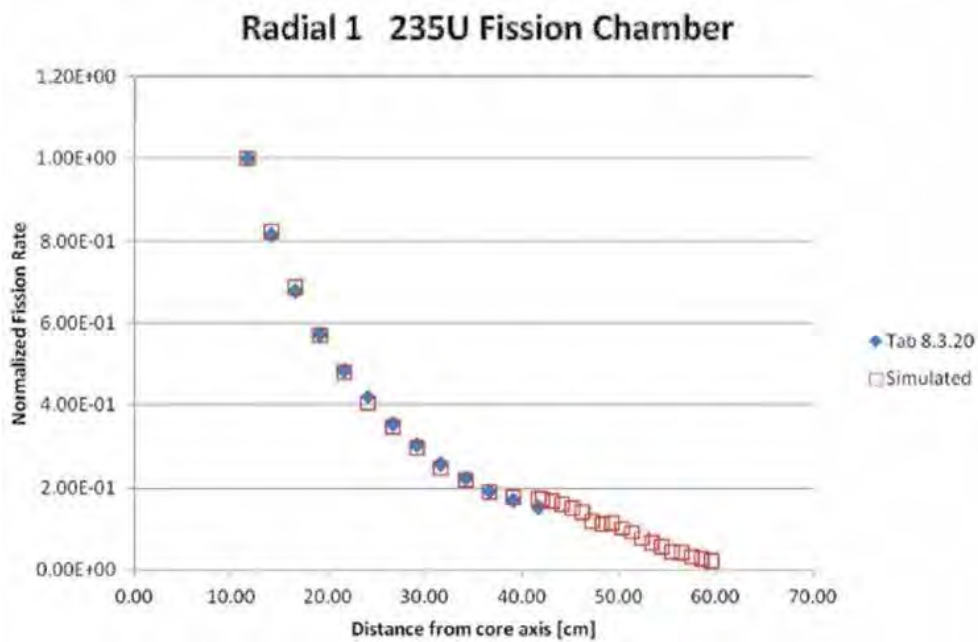


Figure 3: Comparison of experimental vs. simulated responses of U fission chambers along Radial Channel 1.

- The  $\beta$ -splines coefficients of the simulated mesh data have been calculated for each considered reaction along the traverses of each channel [7].
- The values of the simulated reaction rates were calculated by spline interpolation

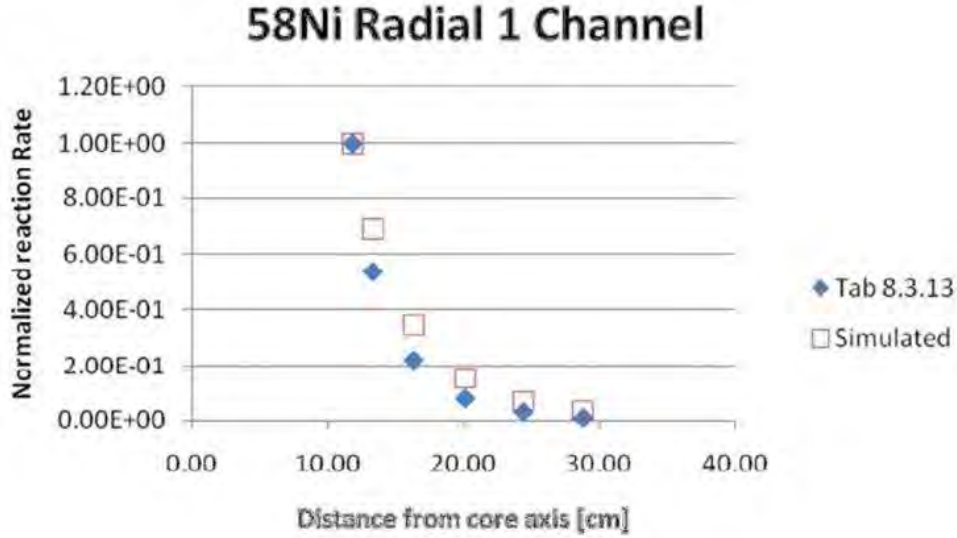


Figure 4: Comparison of experimental vs. simulated responses for  $^{58}\text{Ni}(n,p)^{58}\text{Co}$  reaction rate in radial channel.

exactly in the same positions where measurements have been performed.

- Both measured and simulated data sets were normalized at their respective maximum.
- Measured and simulated data are reported in graphical formats for comparison.

Experimental data are taken from the various tables reported in Volume 2, section 8 of reference [2].

As reported in Fig. 2,  $^{238}\text{U}$  fission rates show a satisfactory agreement with the experimental data. The simulated behaviour tends to overestimate the experimental data in the zone of major rate change of the fission curve (distance range of 10 cm to 22 cm).  $^{235}\text{U}$  fissions (Fig. 3) data are in good agreement with experimental findings. Fig. 4 shows that also the simulated  $^{58}\text{Ni}(n,p)^{58}\text{Co}$  reaction rates are in general agreement with the trends of the experimental findings. As already noted for the  $^{238}\text{U}$  fission rates, the model tends to overestimate the experimental findings in the zone between 12 and 22 cm of distance from core axis. Since both  $^{238}\text{U}$  fissions and  $^{58}\text{Ni}$  have relatively high cross sections for fast neutrons, it can be argued that the models tends to overestimates the fast neutron population ( $E > 1 \text{ MeV}$ ) present in the radial channel.

## 5 Conclusions

- TAPIRO MCNPX model succeed in the evaluation of experimental control rods worth and criticality. Simulations errors are quite below the experimental uncertainties.

- As expected, the energy spectra of the neutron flux, estimate along traverses radial channel 1 show a progressive departure from the fission spectrum as the slow down action of the copper reflector increases with the distance from the core centre. Both flux intensity and spectra are in agreement with experimental findings.
- The ENEAGRID/CRESCO system appear to be effective and reliable tool also for problems that request low to moderate calculation loads.

## References

- [1] Gandini A. Uncertainty analysis and experimental data transposition methods based on perturbation theory. Handbook of Uncertainty Analysis, Y. Ronen Ed., CRC Press, Boca Raton, Florida, 1988.
- [2] Fabry A. Editor: "Neutronic characterization of the TAPIRO fast-neutrons source reactor - Final Report" - Volumes 1-4.
- [3] "Rapporto di sicurezza per il R.S.V. TAPIRO vol. 1°: Descrizione", CNEN - Class. 0-3 - Arch. 57 - 26/09/1969.
- [4] X-5 Monte Carlo Team "MCNP: A General Monte Carlo Transport Code" LA-CP-03-245 April 24,2003 (Revised 10/3/05).
- [5] Burgio N., Cretara L., Frullini M., Gandini A., Peluso V., and Santagata A. Monte carlo simulation analysis of integral data measured in the sck-cen/enea experimental campaign on the tapiro fast reactor. experimental and calculated data comparison. *Nuclear Engineering and Design*, 273:350–358, 2014.
- [6] "Prove Nucleari eseguite con il Reattore TAPIRO", CNEN - Laboratorio Fisica e Calcolo Reattori, 1971.
- [7] Eaton J. W., Bateman D., and Hauberg S. "GNU Octave Manual Version 3" Network Theory Ltd. ISBN 0-9546120-6-X.



# Benchmark performances of CRESCO4 HPC system

*F. Ambrosino<sup>1\*</sup>, A. Funel<sup>1†</sup>, S. Giusepponi<sup>2‡</sup>,  
G. Guarnieri<sup>1§</sup>, G. Ponti<sup>1¶</sup>*

<sup>1</sup>*ENEA UTICT-HPC  
P.le E. Fermi 1, 80055 Portici (Naples), Italy*

<sup>2</sup>*ENEA - UTICT HPC  
Via Anguillarese 301, 00123 S. Maria di Galeria (Rome), Italy*

**ABSTRACT.** We study the performances of CRESCO4 cluster, the new HPC infrastructure of ENEAGRID. The system consists of 4864 Intel E5-2670 cores interconnected with a high speed InfiniBand 4xQDR (40 Gbps) network. The peak computing power of the machine amounts to 101 Tflops. Performances are studied both with standard benchmarks and real applications related to some of the scientific areas of major interest for ENEAGRID users.

## 1 Introduction

The aim of this article is the study of the performances of the High Performance Computing (HPC) cluster CRESCO4 [1] belonging to ENEAGRID [2] infrastructure. A supercomputing system is made up by many components, both hardware and software, which need to be carefully configured to make it a powerful tool. The design of a HPC cluster is often driven by the necessity to accomplish computational tasks related to a particular area of employment. Instead, CRESCO4 has been designed for researchers and modellers working in many different fields. In this context it is not easy to say what it means "good performances" because one has to provide a multi-purpose computing facility capable of achieving remarkable results with many different applications each of which stressing its own combination of available resources (CPU, memory, network, file systems etc.). However, the characterization of a supercomputer often relies upon standard benchmarks used by the HPC community. Thus we analyzed the performances of CRESCO4 regarding both standard metrics and real applications used in scientific research, focusing only on certain of them related to some areas of major interest for ENEAGRID users. As standard benchmarks we used High Performance Linpack (HPL) [3, 4], oriented to measure

---

\*Corresponding author. E-mail: [fiorenzo.ambrosino@enea.it](mailto:fiorenzo.ambrosino@enea.it).

†Corresponding author. E-mail: [agostino.funel@enea.it](mailto:agostino.funel@enea.it).

‡Corresponding author. E-mail: [simone.giusepponi@enea.it](mailto:simone.giusepponi@enea.it).

§Corresponding author. E-mail: [guido.guarnieri@enea.it](mailto:guido.guarnieri@enea.it).

¶Corresponding author. E-mail: [giovanni.ponti@enea.it](mailto:giovanni.ponti@enea.it).

the computing power of CPU; Intel MPI Benchmarks (IMB) [5] and Ohio State University Micro Benchmarks (OSU) [6] for analyzing the performances of the high speed InfiniBand (IB) [7] network. As real scientific applications we tested OpenFOAM [8, 9], an open source computational fluid dynamics (CFD) software, and Carr-Parrinello Molecular Dynamics (CPMD) [10, 11] a code used in materials science. We hope our analysis may provide hints to users on how to set up their own codes, and what they should expect by running them on CRESCO4 cluster.

## 2 Architecture of CRESCO4

CRESCO4 is composed by 38 Supermicro F617R3 Fat-Twin chassis, each hosting 8 computing nodes (4 rack units). Each node hosts a dual-socket 8 cores CPU Intel E5-2670 processor (codenamed Sandy Bridge) which operates at a clock frequency of 2.6 GHz. The RAM memory per node is 64 GB (4 GB per core). The total number of cores is 4864. Computing nodes access a DDN S2A9900 storage system for a total storage area of 480 TB, and are interconnected via an IB 4xQDR Qlogic/Intel 12800-180 switch(432 ports, 40 Gbps). CRESCO4 has been purchased with part of the financial resources of the TEDAT project included in the Italian National Operational Programme (PON) 2007-2013.

## 3 Standard benchmarks

Standard benchmarks are used to test under stress the components of a HPC system in order to verify whether its performances correspond to what claimed by the manufacturer; also, benchmarks are useful to foresee the behaviour of the system while running heavy load jobs and, in case, adopt solutions for preventing failures. The HPC community uses standard benchmarks to classify a supercomputer according to accepted metrics.

### 3.1 HPL

The HPL benchmark is used in the HPC community for ranking supercomputers according to its computing power in terms of floating point operations per second (flops). The most powerful systems over the world are reported in the Top500 List [12]. The flops rate is evaluated by solving in parallel a dense linear system of order  $n$ :

$$A \cdot X = B, \quad A \in \mathbb{R}^{n \times n}, \quad X, B \in \mathbb{R}^n$$

using LU factorization [13, 14] with row partial pivoting of the  $n$  by  $n + 1$  coefficient matrix:

$$P[A, B] = [[L, U], Y].$$

P is the permutation matrix representing the row pivoting and L is the lower triangular matrix. P and L are applied to B as the factorization progresses. The solution is obtained by solving the upper triangular system:

$$U \cdot X = Y.$$

The maximum theoretical peak  $p_{th}$  is given by:

$$p_{th} = N_c \times f \times \omega$$

where  $N_c$  is the number of cores,  $f$  is the CPU clock frequency and  $\omega$  is the number of floating point operations per clock cycle (which for Intel Sandy Bridge E5-2670 processor is 8).

Nodes/Cores	Theoretical peak (Gflops)	Measured peak (Gflops)	Efficiency
1/16	$3.328 \times 10^2$	$3.027 \times 10^2$	91%
8/128	$2.662 \times 10^3$	$2.363 \times 10^3$	89%
15/240	$4.992 \times 10^3$	$4.537 \times 10^3$	91%
40/640	$1.331 \times 10^4$	$1.198 \times 10^4$	90%
64/1024	$2.130 \times 10^4$	$1.922 \times 10^4$	90%
288/4608	$9.585 \times 10^4$	$8.177 \times 10^4$	85%

Table 1: Results of HPL benchmark for CRESCO4 cluster.

Under very general assumptions it can be shown that the HPL algorithm makes the leading term of time to solution  $t_s$  of order  $O(n^3)$ . The time spent for communication is of order  $O(n^2)$ . The HPL benchmark scales very well with the size  $n$  and the scaling does not depend strongly on the communication volume.

The HPL benchmark was compiled with the Intel compiler (ver. 13.1.2). As mathematical and parallel libraries we used the Intel 64 bit MKL (ver. 11.0) and MPI (ver. 4.1.0.30), respectively. In order to fully exploit shared memory we used OpenMP [15] multithreading. More precisely, parallel runs were configured with one MPI process and eight threads for each socket. The compiler optimization flags used are `-xAVX -fomit-frame-pointer -O3 -funroll-loops -openmp`. The Advanced Vector Extensions `-xAVX` flag allows Single Instruction Multiple Data (SIMD) operations for processing multiple pieces of data in a single step.

In Tab.1 are reported the best measured HPL results. We observe that the efficiency of CRESCO4 cluster is, on average, about 90% and does not depend strongly on the number of the computing nodes. In order to quantify the effect of communication, in terms of power consumption, HPL was also ran standalone (without inter-nodes data transfers), at the same time on each node of the cluster and we estimated  $\sim 10$  kW the electrical power

needed by IB fabrics, switches and HCAs. Considering that the total electrical power consumed by CRESCO4 under a heavy parallel HPL run is  $\sim 100$  kW we can say that the communication accounts for  $\sim 10\%$  of total electrical power.

### 3.2 IMB

The IMB benchmark is largely used to evaluate the network and I/O performances for HPC systems. It consists of a family of benchmarks written as MPI applications. In particular, we used the IMB-MPI1 benchmark to evaluate the performances of the IB interconnection among the nodes of CRESCO4. This application tests the point-to-point and collective communication functions defined in the MPI standard.

As mentioned in Section 2, the nodes of the cluster are interconnected by an high speed IB 4xQDR (40 Gbps) network. The benchmark was compiled in OpenMPI 1.4.3-Intel 14.0.1 environment. The OpenMPI library used was compiled with the support for PSM (Performance Scaled Messaging) library.

We want to focus our attention on the results produced by the `Alltoall` benchmark. This test is based on the use of the `MPI_Alltoall`, one of the MPI's function defined for collective communication. This function is invoked when every process of a parallel application has to communicate with all the others and for this reason the network infrastructure is intensively stressed by the call.

The test proceeds for steps, at each iteration we have a growing number of active processes (proceeding by powers of 2) with the remaining processes in a barrier, until the step in which all application processes are active in the `MPI_Alltoall`. For each iteration buffers of increasing size are created and exchanged between processes and the execution times of the various exchanges are registered. As example, in the following Tables 2, 3 and 4 we show the values of the execution times of the `Alltoall` with 1024, 2048 and 3600 active processes.

Buffer size[bytes]	Iterations	t_min[ $\mu$ s]	t_max[ $\mu$ s]	t_avg[ $\mu$ s]
1024	442	23957.15	23980.80	23960.32
16384	35	278897.37	279464.71	278992.29
131072	7	1521213.29	1523635.73	1522496.60

Table 2: Results of `Alltoall` benchmark for CRESCO4 cluster with 1024 active processes.

The execution time of the `Alltoall` benchmark is a function of the buffer size and the number of active processes. For a given buffer size it is possible to express the execution time of the `Alltoall` benchmark as a function of the number of active processes. To evaluate the performance of the network infrastructure when the number of active processes increases, we can assume that the execution time is a parabolic function of the number of active processes:

Buffer size[bytes]	Iterations	t_min[ $\mu$ s]	t_max[ $\mu$ s]	t_avg[ $\mu$ s]
1024	236	48504.00	48521.63	48511.18
16384	14	935953.99	940919.08	936256.36
131072	3	3838384.31	3846776.33	3843144.14

Table 3: Results of **Alltoall** benchmark for CRESCO4 cluster with 2048 active processes.

Buffer size[bytes]	Iterations	t_min[ $\mu$ s]	t_max[ $\mu$ s]	t_avg[ $\mu$ s]
1024	20	415565.41	415990.65	415735.52
16384	7	1575460.43	1577713.73	1576324.90
131072	2	8705240.01	8721863.51	8714565.17

Table 4: Results of **Alltoall** benchmark for CRESCO4 cluster with 3600 active processes.

$$t_{Alltoall} = a * n_{procs}^2 + b * n_{procs}$$

If we choose 128 MB as buffer size, we can find the values of a and b with the values of the execution times for 1024 and 2048 active processes and then we can estimate the execution time for 3600 active processes. In this way, we can see that the estimated time for 3600 active processes is 8874324.00  $\mu$ s while the measured time is 8714565.17  $\mu$ s. So we can conclude that the network infrastructure has a stable behavior when the number of processes that communicate through it grows.

### 3.3 OSU

In preparing the qualification criteria for the tender specifications we had a very useful contact with QLogic staff. After discussions and some preliminary tests we follow their suggestion to set up the requirement on bandwidth and latency as measured by the OSU benchmark. The OSU suite is a collection of MPI message passing performance benchmarks developed at the Ohio State University and can be used for measuring latency and bandwidth in point-to-point and collective communications.

Follows the description of the test that we conducted on the IB fabric.

The benchmarks adopted were: **osu\_bw** and **osu\_latency**.

We had to test:

1. the IB connection among all the nodes of CRESCO4 cluster;

2. the connection among the the nodes of the CRESCO4 cluster and the storage installed in the old data center.

We ran the test number 1 using the first node of the cluster as a reference.

The requirement to be met on the bandwidth was 3300 MB/s ( $\pm 10\%$ ) for buffer  $> 65$  kB. The maximum deviation from the requested value was -3.3%, measured with a buffer of 131 kB.

The requirement to be met on the latency was 2.4 microseconds for small buffers ( $< 16$  B). The results show that for all nodes the measured latency for small buffer was lower than or equal to  $1.8 \mu\text{s}$ . We observed that if the nodes involved by the test were attached on the same leaf of the switch, the value of the latency typically was 1.3/1.4  $\mu\text{s}$ , while if the nodes were attached on different leaf of the switch, the value of the latency typically was 1.7/1.8  $\mu\text{s}$ .

For this reason we decided to set a policy on the scheduler to reorder the computing nodes assigned to a job according with the network topology. Thanks to this policy, we have achieved an improvement of efficiency using 4352 cores that has grown from 38% to 57% on a real case application (Hearts code, developed by the combustion technical unit).

We ran the test number 2 using one of the NSD servers of the GPFS cluster installed in the old data center as a reference.

The requirement to be met on the bandwidth was 3300 MBs ( $\pm 10\%$ ) for buffer  $> 65$  kB. The maximum deviation from the requested value was -7.8%, measured with a buffer of 131 kB.

The requirement to be met on the latency was 3.4  $\mu\text{s}$  for small buffers ( $< 16$  B). The results show that for all nodes the measured latency for small buffer was lower than or equal to 2.85  $\mu\text{s}$  with a mean value of 2.49 microseconds and minimum value of 2.38  $\mu\text{s}$ .

## 4 Application benchmarks

In this section we analyze the performances of CRESCO4 with real scientific codes in the fields of CFD and material science. The criteria often used to quantify the computational performances of a HPC system are: rating, speed-up and efficiency.

*Rating (R)*: is an index that represent “the speed” absolute performance of the simulation; it is the number of simulation steps that can run in a day

$$R = \frac{24 \times 60 \times 60}{t_n} \quad (1)$$

where  $t_n$  is the simulation time when  $n$  cores are used.

*Speed-up (S)*: for parallel simulations with  $n$  cores, is the ratio between the serial  $t_s$  and the parallel  $t_n$  execution time

$$S = \frac{t_s}{t_n}. \quad (2)$$

*Efficiency (E)*: is the speed-up normalized to the number of cores

$$E = \frac{S}{n}. \quad (3)$$

## 4.1 OpenFOAM

The OpenFOAM (Open Field Operation and Manipulation) Toolbox is a free, open source CFD software package which has a large user base across most areas of engineering and science, from both commercial and academic organisations. OpenFOAM has an extensive range of features to solve anything from complex fluid flows involving chemical reactions, turbulence and heat transfer, to solid dynamics and electromagnetics. It includes tools for meshing, notably **snappyHexMesh**, a parallelized mesher for complex CAD geometries, and for pre- and post-processing. Almost everything (including meshing, and pre- and post-processing) runs in parallel as standard, enabling users to take full advantage of computer hardware at their disposal. For this purpose the code is capable of running on very large HPC clusters. The code is written in C++ and being open, it offers users complete freedom to customise and extend its existing functionalities. The core technology includes numerical methods, linear and ODE (Ordinary Differential Equations) system solvers, dynamic mesh, physical models and so on. OpenFOAM includes over 80 solver applications that simulate specific problems in engineering mechanics and over 170 utility applications that perform pre- and post-processing tasks, e.g. meshing, data visualisation, etc. We performed benchmarks of the two different OpenFOAM solvers on the HPC ENEA CRESCO4 computing facility. We compiled the code on CRESCO4 (Intel E5-2680) with the GCC v4.8.2 compiler and OpenMPI v1.6.5 library.

### 4.1.1 Physical systems

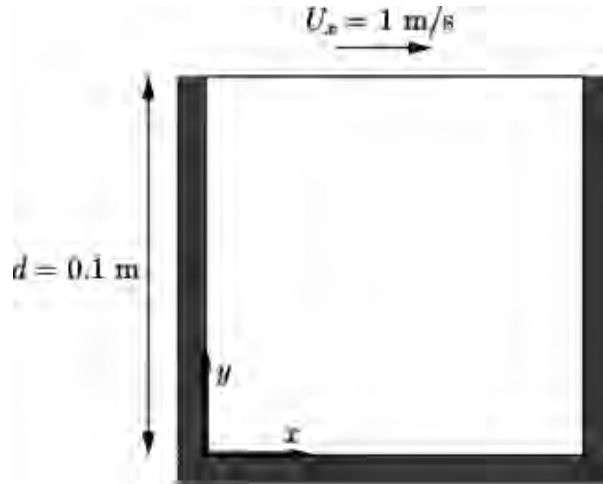


Figure 1: Cavity case description as shown in [9].

Two test cases have been studied in order to measure HPC performances for different CFD algorithms among the several standard solutors implemented in the OpenFOAM library.

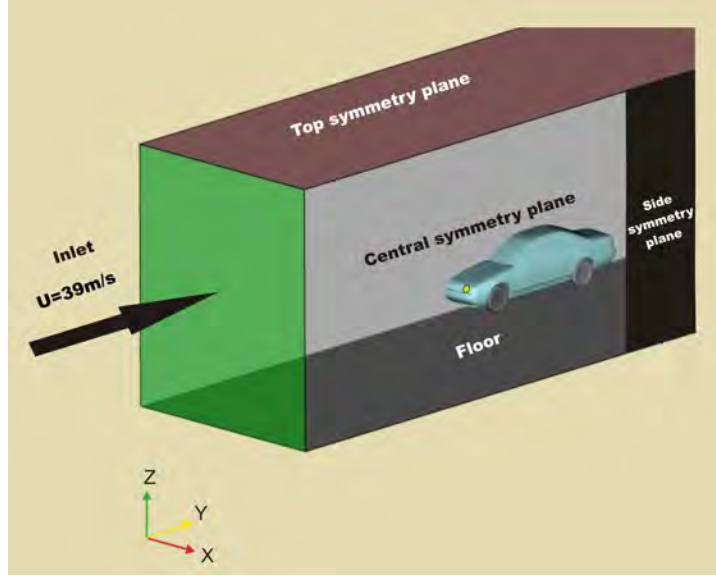


Figure 2: Car case description.

Both cases are very large in terms of size of computational work. The first test case we adopted is called "cavity" and is described in [9] and involves isothermal, incompressible flow in a two-dimensional square domain; geometry and boundary conditions of the original case are shown in Fig. 1. In our simulations some geometric and thermodynamic characteristics are changed in order to have a structured mesh of about 10 million cells and a Reynolds number ( $Re$ ) of the same order of magnitude of the original case ( $Re = 10$ ). The two dimensions of the cavity have been changed to  $6.4\text{ m}$  and the fluid cinematic viscosity has been set to  $\nu = 0.5\text{ m}^2/\text{s}$ , so  $Re = 12.8$ . In each of the two dimensions the cavity has been meshed with 3200 hexahedral cells of the same size. The solver used is `icoFoam` that solves the transient incompressible laminar Navier-Stokes equations using the PISO algorithm.

The second case we adopted as benchmark is called "car" and concerns the airflow over a commercial car. Such a kind of simulations are used in automotive industry to model the shape of cars. This test case was already used as HPC benchmarks in [16]. Geometry and boundary conditions are described in Fig. 2. The air enters perpendicularly to the inlet at a velocity  $U=39.0\text{ m/s}$ . The operating pressure is  $P=1\text{ atm}$ . The computational domain consists of a mesh of about 30 millions tetrahedral cells. The solver used is `simpleFoam` that is a steady-state solver for incompressible, turbulent flow using the SIMPLE algorithm; the turbulent model is the standard  $k - \varepsilon$ .

#### 4.1.2 OpenFOAM results

In both benchmarks the same simulation has been done with an increasing number of cores; specifically the number of used cores are  $n = \{1, 4, 16, 32, 48, 64, 96, 128, 192, 256, 384, 512, 768, 1024, 1536, 2048, 4096\}$ .



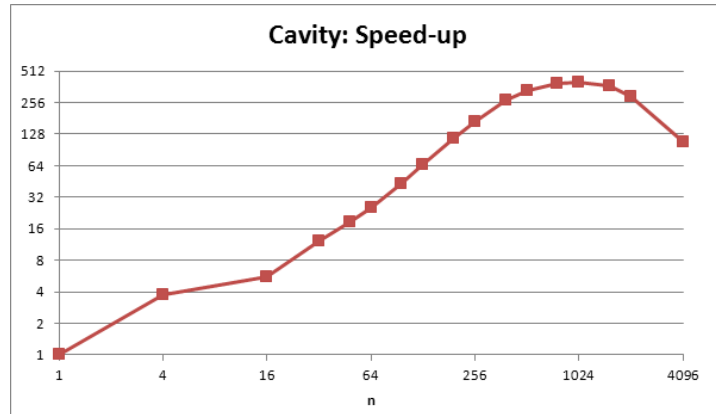


Figure 3: Cavity simulations: speed-up versus number of cores (notable is the effect of hardware acceleration functions on intra-node simulations).

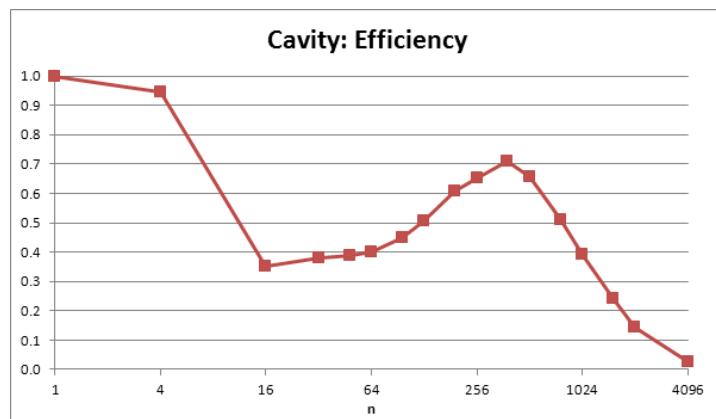


Figure 4: Cavity simulations: efficiency versus number of cores (notable is the effect of hardware acceleration functions on intra-node simulations).

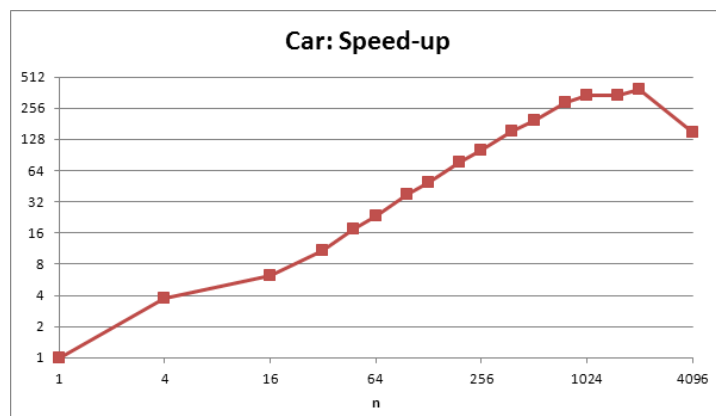


Figure 5: Car simulations: speed-up versus number of cores (notable is the effect of hardware acceleration functions on intra-node simulations).

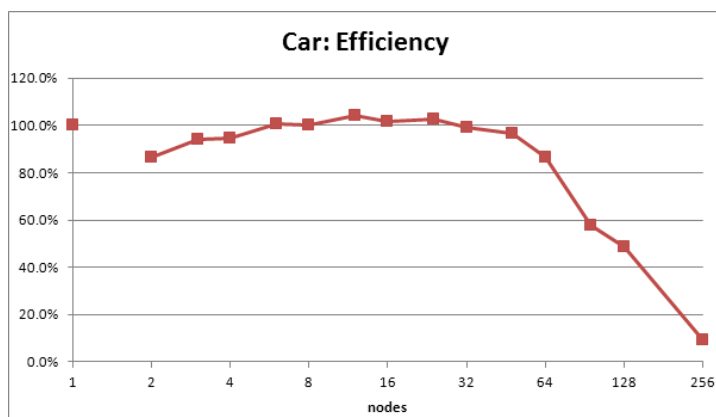


Figure 6: Car simulations: efficiency versus number of nodes (each node has 16 cores).

In the case of cavity benchmark the simulation unit is considered a sequence of 20 time-steps starting from time zero. Fig. 4 shows that the efficiency decreases at around 35% of the serial one in the single node simulation (16 cores) and it goes up to around 70% in the 384 cores simulation; increasing the number of cores the efficiency decreases to very low values: indeed, as shown in Fig. 3, the speed-up decreases when  $n$  is higher than 1024 cores.

In the case of car benchmark the simulation unit is considered a sequence of 100 iterations starting from time zero. Speed-up and efficiency reach higher values probably due to the larger computational domain in terms of mesh size. The speed-up is almost linear up to 1024 cores as shown in Fig. 5. As shown in Fig. 4 the efficiency decreases significantly passing from 1 core to a full single node (16 cores): this is probably due to various hardware accelerated functions of the serial simulation (such as Intel Turbo Boost Technology [17]). A similar behaviour occurs for the efficiency of the car benchmark: if we consider the efficiency related to the full node simulation (16 cores), instead of the serial one, we obtain the Fig. 6 in which a large range of numbers of nodes is characterized by efficiency values of about 100% that are compatible with the almost linear speed-up behaviour.

## 4.2 CPMD

CPMD is an *ab-initio* electronic structure and molecular dynamics (MD) program using a plane wave-pseudopotential implementation of Density Functional Theory (DFT) [18, 19]. It is mainly targeted at Car-Parrinello MD simulations, but also supports geometry optimizations, Born-Oppenheimer MD (BOMD), path integral MD (PIMD), response functions, excited states and calculation of some electronic properties. In *ab-initio* Molecular Dynamics simulation, the forces acting on atoms are calculated from an electronic structure calculation repeated every time step (on the fly). Thanks to electronic structure calculation by using Density Functional methods, simulations of large systems with hundreds of atoms are now standard. Originally developed by Roberto Car and Michele Parrinello for applications in solid state physics and material science, this method has also been used with great success for the study of molecular systems. Applications of *ab-initio*

Car-Parrinello Molecular Dynamics simulations range from the thermodynamics of solids and liquids to the study of chemical reactions in solution and on metal and oxide surfaces. CPMD code runs on many different computer architectures and allows good scalability till a large number of processors depending on the system size [20, 21, 22]. To evaluate the most suitable computational demand, we performed benchmarks of the CPMD code on the HPC ENEA CRESCO4 computing facility. We compiled the code on CRESCO4 (Intel E5-2680) with Intel Fortran Compiler ver.12.1.4, MKL library and OpenMPI ver. 1.4.3.

#### 4.2.1 Physical system

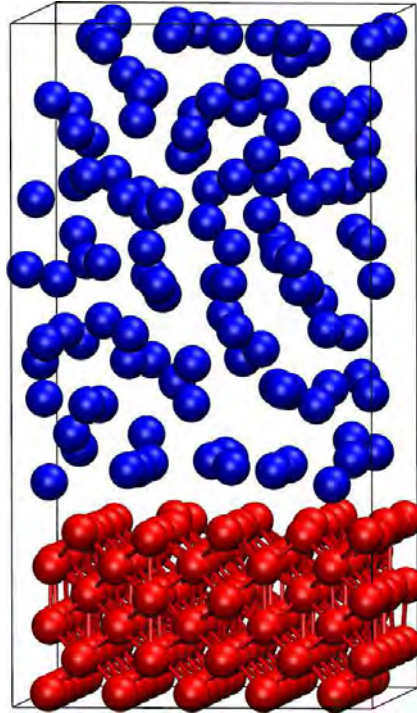


Figure 7: Simulation cell of the solid iron–liquid lead interface. Iron atoms are in red; lead atoms are in blue.

Liquid metal corrosion is one of the key factors that have to be considered when using liquid metal as a heat transfer medium such as the primary coolant in advanced nuclear reactors. Liquid metal corrosion is a physical or physical-chemical process, involving species dissolution and transport, chemical reactions and new phase formation. The corrosion behaviors of steels in high temperature lead have been investigated experimentally so far, but the interaction mechanism between the steels and lead has not been made clear yet [23, 24, 25]. Thus, a study at atomic level is necessary to have a better understanding of the interaction mechanism between these two materials. For these reasons we set up an *ab-initio* numerical model to simulate the behavior of liquid lead on solid iron.

We considered an interface between solid iron (Fe) and liquid lead (Pb) at 600 °C. The

system is made of a solid slab of  $5 \times 5 \times 3$  bcc conventional cell of iron (150 Fe atoms) and a slab of liquid lead at density  $D = 10.317 \text{ g/cm}^3$  (120 Pb atoms). The system is shown in Fig. 7, iron atoms are in red and lead atoms are in blue. We employed the CPMD code with Martins-Trouiller [26] pseudopotentials for iron and lead, together with Perdew-Burke-Ernzerhof gradient corrected exchange-correlation potentials [27]. All the calculations are performed in the supercell approximation with periodic boundary conditions (PBC) meant to mimic an infinitely extended system. The electronic wave functions are expanded in a plane-wave basis set with a kinetic energy cut-off equal to 80 Ry. The latter value was optimized by preliminary calculations on the crystalline structures of metallic iron and lead. In these kind of calculations, the more considerable part of the computation is devoted to the calculation of the Fast Fourier Transforms (FFTs). For our system, the mesh of the real space used for the FFTs is  $320 \times 160 \times 160$ . CPMD distributes calculation and data structures across cores on the basis of the first index of the mesh. To have a well-balanced computational load it is useful to utilize a number of cores that are divisors of 320. Setting the number of groups to be used in the calculation with the entry CP\_GROUPS (CP) it is possible to increase conveniently the number of cores.

#### 4.2.2 CPMD results

$n$	CP	$t_n(s)$	$E(\%)$	$n$	CP	$t_n(s)$	$E(\%)$
32	1	134.14	100	40	1	103.68	104
64	1	66.62	101	64	2	78.80	85
80	1	61.51	87	80	2	64.34	83
160	1	35.66	75	160	2	33.67	80
160	4	40.87	66	320	1	18.98	71
320	2	19.15	70	320	4	21.99	61
320	8	28.18	48	640	1	28.78	23
640	2	9.93	67	640	4	11.53	58
640	8	14.42	47	640	16	23.75	28
1280	1	32.96	10	1280	2	18.49	18
1280	4	7.80	42	1280	8	9.37	36
1280	16	14.38	23	2560	2	21.52	8
2560	4	11.98	14	2560	8	7.38	23
2560	16	9.87	17				

Table 5: Results for CPMD benchmark. The average time  $t_n$  for a single simulation step as a function to the number of cores  $n$  are reported. Moreover, the calculated values of the Efficiency  $E$  are shown.

To evaluate the best choice in term of time and number of cores utilized, we performed some BOMD simulations of our system on CRESCO4 cluster. In Tab. 5 are reported the

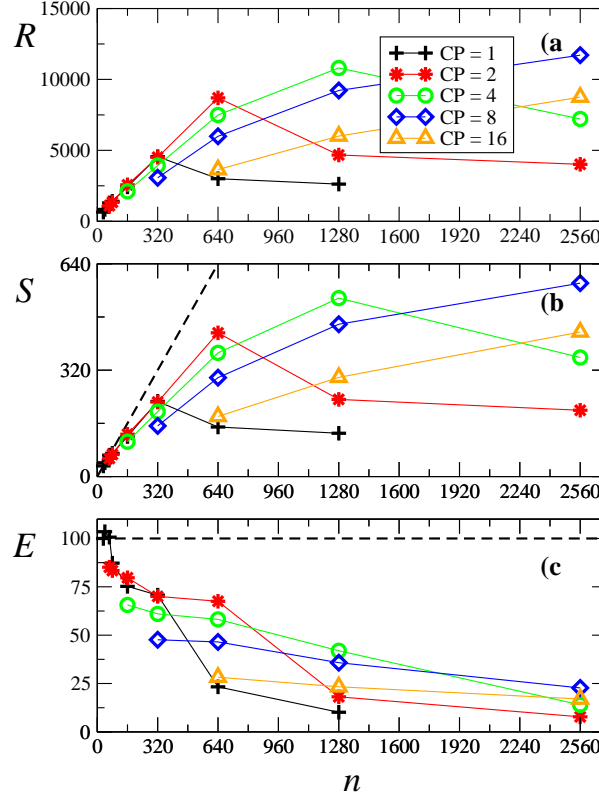


Figure 8: Calculated values of the *Rating*, *Speed-up* and *Efficiency* are shown for the CPMD benchmark in panel a), b) and c), respectively. CP set the number of groups of cores used in the calculation.

average time  $t_n$  for a single simulation step as a function to the number of cores. Using the equations (1), (2) and (3) we calculated the Rating, Speed-up and Efficiency. The corresponding values are shown in panels a), b) and c) of Fig. 8, respectively. We had to use at least 32 cores otherwise the available RAM was not enough for our calculations. Thus, the  $S$  and  $E$  are calculated on the basis of the time  $t_n$  with  $n=32$ . From the results we observed a very good scalability of the code up to 160 core with a efficiency of 80%. In this situation each core has two plane in the real mesh for the calculation of the FFTs. Thanks to the possibility to put together groups of cores with CP\_GROUPS, it is possible to reach good efficiency ( $\sim 70\%$ ) up to 640 cores. The simulation times can be further reduced using a greater number of cores, but with a very low efficiency: 42% for 1280 cores and 23% for 2560 cores.

## References

- [1] <http://www.cresco.enea.it/>.
- [2] <http://www.eneagrid.enea.it/>.

- [3] Petitet A., Whaley R. C., Dongarra J., and Cleary A. Hpl: A portable implementation of the highperformance linpack benchmark for distributed-memory computers.
- [4] Dongarra J., Luszczek P., and Petitet A. The linpack benchmark: past, present and future. *concurrency and computation. Practice and Experience*, 15(9):803–820, 2003.
- [5] [http://software.intel.com/en-us/articles/intel-mpi\\_benchmarks](http://software.intel.com/en-us/articles/intel-mpi_benchmarks).
- [6] <http://mvapich.cse.ohio state.edu/benchmarks/>.
- [7] <http://www.infinibandta.org/>.
- [8] Weller H. G., Tabor G., Jasak H., and Fureby C. A tensorial approach to computational continuum mechanics using object orientated techniques. *Computers in Physics*, 12(6):620–631, 1998.
- [9] <http://www.openfoam.com/>.
- [10] Carr R. and Parrinello M. Unified approach for molecular dynamics and density-functional theory. *Phys. Rev. Lett.*, 55:2471–2474, 1985.
- [11] Copyright IBM Corp 1990-2008. Copyright MPI für Festkörperforschung Stuttgart 1997-2001. CPMD [www.cpmc.org](http://www.cpmc.org).
- [12] <http://www.top500.org/>.
- [13] Dongarra J., Van de Geijn R. A., and Walker D. W. Scalability issues affecting the design of a dense linear algebra library. *J. Parallel Distrib. Comput.*, 22(3):523–537, 1994.
- [14] Dongarra J. and Petitet A. Algorithmic redistribution methods for block-cyclic decompositions. *IEEE Transactions on Parallel and Distributed Systems*, 10(12):201–220, 1999.
- [15] <http://openmp.org/wp/>.
- [16] Ambrosino F. and Funel A. Openfoam computational performances for large parallel distributed simulations. *High Performance Computing on Cresco infrastructure: research activities and results 2009-2010*, pages 85–89, 2011.
- [17] <http://www.intel.it/content/www/it/it/architecture-and-technology/turbo-boost/turbo-boost technology.html>.
- [18] Hohenberg P. and Kohn W. Inhomogeneous electron gas. *Phys. Rev.*, 136:B864–871, 1964.
- [19] Kohn W. and Sham L. J. Self-consistent equations including exchange and correlation effects. *Phys. Rev.*, 140:A1133–1138, 1965.
- [20] Andreoni W. and Curioni A. New advances in chemistry and material science with cpmd and parallel computing. *Paral. Comp.*, 26:819, 2000.

- [21] Hutter J. and Curioni A. Dual-level parallelism for *ab-initio* molecular dynamics: Reaching teraflop performance with the cpmd code. *Paral. Comp.*, 31:1, 2005.
- [22] Giusepponi S., Celino M., Cleri F., and Montone A. Hydrogen storage in mgh<sub>2</sub> matrices: a study of mg-mgh<sub>2</sub> interface using cpmd code on enea-grid. *Il Nuovo Cimento C*, 32:139, 2009.
- [23] Martinelli L., Balbaud-Célérrier F., Terlain A., Delpech S., Santarini G., Favergeon J., Moulin G., Tabarant M., and Picard G. Oxidation mechanism of a Fe-9Cr-1Mo steel by liquid Pb-Bi eutectic alloy (Part I). *Corrosion Science*, 50:2523, 2008.
- [24] Martinelli L., Balbaud-Célérrier F., Terlain A., Bosonnet S., Picard G., and Santarini G. Oxidation mechanism of an Fe-9Cr-1Mo steel by liquid Pb-Bi eutectic alloy at 470 °C(Part II). *Corrosion Science*, 50:2537, 2008.
- [25] Martinelli L., Balbaud-Célérrier F., Picard G., and Santarini G. Oxidation mechanism of a Fe-9Cr-1Mo steel by liquid Pb-Bi eutectic alloy (Part III). *Corrosion Science*, 50:2549, 2008.
- [26] Troullier N. and Martins J. L. Efficient pseudopotentials for plane-wave calculations. *Phys. Rev. B*, 43:1993, 1991.
- [27] Perdew J. P., Burke K., and Ernzerhof M. Generalized gradient approximation made simple. *Phys. Rev. Lett.*, 77:1996, 1991.

# The new ENEA CRESCO3 and CRESCO4 HPC systems

*F. Ambrosino, G. Bracco, A. Colavincenzo, A. Funel,  
G. Guarnieri, B. Mastroianni, S. Migliori, G. Ponti*

*D. Abate, G. Aprea, T. Bastianelli, F. Beone, R. Bertini, M. Caporicci,  
B. Calosso, M. Chinnici, R. Ciavarella, A. Cucurullo, P. D'Angelo, D. De Chiara,  
M. De Rosa, P. De Michele, G. Furini, D. Giammattei, S. Giusepponi, R. Guadagni,  
A. Italiano, S. Magagnino, A. Mariano, G. Mencuccini, C. Mercuri, P. Ornelli,  
F. Palombi, S. Pecoraro, A. Perozziello, S. Pierattini, S. Podda, F. Poggi,  
A. Quintiliani, A. Rocchi, C. Scio', F. Simoni*

*Technical Unit for IT and ICT Systems Development  
ENEA — Italian National Agency for New Technologies,  
Energy and Sustainable Economic Development  
Lungotevere Thaon di Revel 76 – 00196 Rome, Italy*

**ABSTRACT.** We introduce CRESCO3 and CRESCO4 clusters, the new HPC systems in ENEA Portici Research Center. CRESCO3 has been released in May 2013, whereas CRESCO4 has been installed, configured and tested after the summer 2013. They both represent the latest offspring of ENEA CRESCO HPC systems, the ENEA x86\_64 cluster family, fully integrated in ENEAGRID, the infrastructure which contains all the computational facilities located at several ENEA sites in Italy. CRESCO3 is installed in the old data center room which also hosts CRESCO1 and CRESCO2 clusters, whereas CRESCO4 is hosted in its newly built computer room, with a dedicated power supply and cooling subsystem.

## 1 Introduction

ENEAGRID is a distributed hardware/software infrastructure which allows to gather, connect and seamlessly make available to users all ENEA computing facilities, i.e., HPC clusters, and specific research instruments, such as lab equipment and remote rendering machines. Year by year, ENEAGRID evolves, reshaping and redefining itself according to ENEA strategic goals, continuously acquiring computational resources and software, keeping up the pace with world HPC trends.

Here we introduce CRESCO3 and CRESCO4, the latest ENEA x86\_64 Linux operated HPC system, hosted at Portici Research Center, the major ENEAGRID computational site. CRESCO3 and CRESCO4 have been purchased in the framework of the projects of Italian National Operational Programme (PON) 2007-2013, that are IT@CHA and LAM-RECOR for CRESCO3, and TEDAT for CRESCO4 [1, 2, 3]. Moreover unlike previous



CRESCO HPC systems, CRESCO4 has been designed and configured in-house in all its elements, the HPC core (computing nodes, Ethernet and Infiniband networks, storage system), the computer room, the cooling and the power supply subsystems, with separate tenders for each of the main items and with a good and effective interaction with each of the vendors. In this way we have full control of all the crucial components with great advantages for the definition of the tender specifications and for all the subsequent phases: installation, testing and operation.

The paper is structured as follows: CRESCO3 and CRESCO4 HPC systems are described in Section 2, regarding computing nodes architectural details and a brief description of the ENEAGRID infrastructure. Section 3 details the new data center room itself, including the cooling and the fire suppression systems. The power supply is described in Section 4. Finally, conclusions are drawn in Section 5.

## 2 Architecture of CRESCO3 and CRESCO4

The CRESCO computing laboratory at Portici Research Center consists of various Linux x86\_64 Clusters. As the name suggests, CRESCO3 cluster is the third member of the CRESCO HPC systems hosted in ENEA Portici Research Center [4].



Figure 1: The ENEA CRESCO3 cluster.

It is composed by 84 server nodes distributed into two racks (as in Fig. 1), and each node has the following characteristics:

- 2 sockets CPU, processor type AMD Opteron 6234TM 12 cores 2.4 GHz;
- 1 local HD of 500 GB SATA II;
- 1 Infiniband QDR 40 Gbps interface;
- 2 GbE interfaces;
- BMC/IPMI 2.0 support and software for remote console managing and control.

The whole CRESCO3 cluster has a total number of 2016 cores, and reaches a peak computing power of the machine amounts to  $R_{\text{peak}} = 19$  Tflops and its measured HPL efficiency is 75%.



Figure 2: The ENEA CRESCO4 cluster.

CRESCO4 is its fourth and latest member [4], consists of six racks: five are dedicated to computing nodes and one hosts the main InfiniBand switch, as shown in Fig. 2.

Here are some technical specifications of the machine. The system is composed by 38 Supermicro F617R3-FT chassis, each hosting 8 dual CPU nodes. The whole CRESCO4 cluster has a total number of 4864 cores. The peak computing power of the machine amounts to  $R_{\text{peak}} = 101$  Tflops and its measured HPL efficiency is 85%. Each node hosts:

- a dual-socket 8 core CPU, processor type Intel E5-2670 (codenamed Sandy Bridge) with an operational frequency of 2.6 GHz;
- 64 GB of RAM memory (4 GB per core);
- 1 local HD of 500 GB;
- 1 Infiniband QDR 40 Gbps interface;
- 2 GbE interfaces;
- BMC/IPMI 1.8 support and software for remote console managing and control.

The computing nodes access a DDN S2A9900 storage system, for a total storage amount of 480 TB. The computing nodes are interconnected based via an Infiniband 4xQDR QLogic/Intel 12800-180 switch (432 ports, 40 Gbps). The single node architecture is summarized by Fig. 3. In Fig. 4 is shown the configuration of the InfiniBand network of CRESCO3 and CRESCO4 .

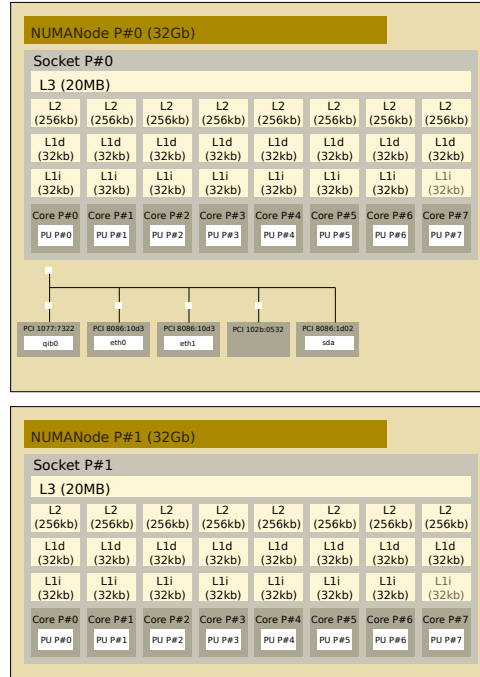


Figure 3: CRESCO4 single node architecture.

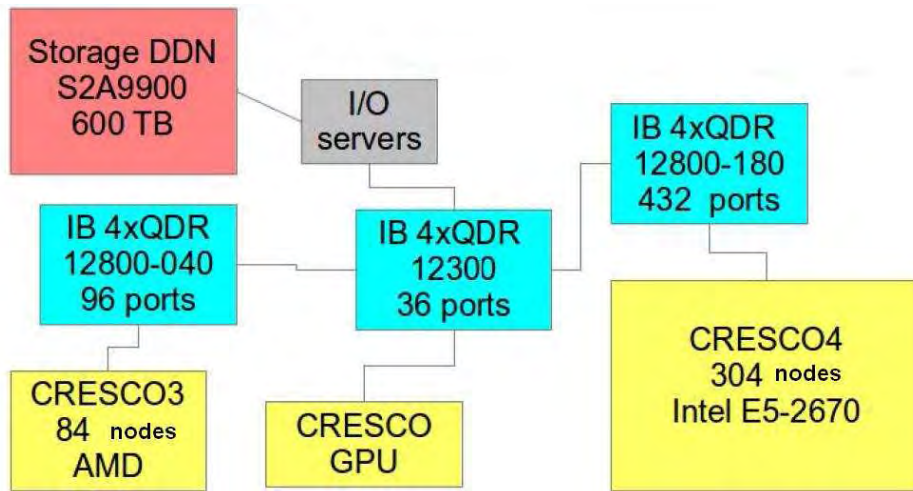


Figure 4: The IB 4xQDR (40 Gbps) network of CRESCO3 and CRESCO4 clusters.

## 2.1 Integration within ENEAGRID

As well as its predecessors CRESCO systems, CRESCO3 and CRESCO4 are also integrated within ENEAGRID, a large infrastructure which includes all the ENEA computing resources installed at the various ENEA research centres in Italy, altogether 6 sites distributed across the whole country, interconnected via the GARR network. ENEAGRID infrastructure is shown in Fig. 5.

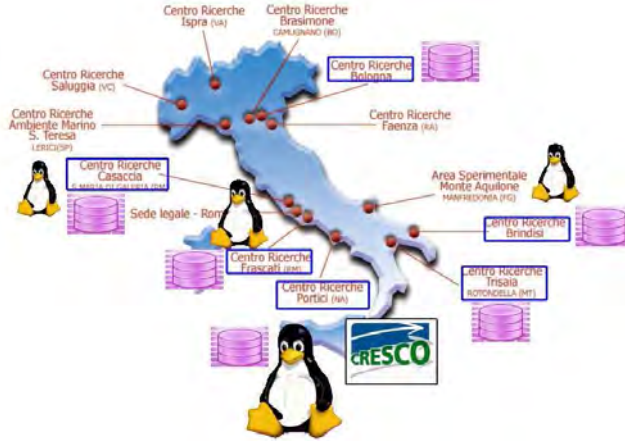


Figure 5: Geographical map of the ENEAGRID sites.

ENEAGRID is characterized by solid structural components, offering reliability and easy management, and by web interfaces which have been developed in-house and customized so as to ensure a friendly user environment:

- authentication via Kerberos v5;
- geographic filesystems: AFS/OpenAFS;
- GPFS parallel file system also on WAN among different clusters and sites;
- resource management via LSF Multicluster;
- system monitoring via Zabbix;
- web access via in-house FARO interface, see [5];
- user management via in-house WARC interface, see [4].

The computing resources currently provided to the users are x86-64 Linux systems (the CRESCO HPC gather more than  $\sim 10,000$  cores) and dedicated systems (e.g. GPU systems). The computing resources spread essentially across four ENEA research centres, that are

- ENEA Portici: CRESCO1 (672 cores), CRESCO2 (2496 cores), CRESCO3 (2016 cores), CRESCO4 (4864 cores)
- ENEA Frascati: CRESCOF (480 cores)
- ENEA Casaccia: CRESCOC (192 cores)
- ENEA Brindisi: CRESCOB (88 cores)

The new CRESCO3 and CRESCO4 clusters are located in the ENEA Portici site, where the largest fractions of computing and man power concentrate. ENEA Portici is connected to the Internet through the PoP GARR of Napoli–Monte S. Angelo thanks to two 1 Gbps links (GARR is the Italian Research & Education Network, planning and operating the national high-speed telecommunication network for University and Scientific Research, see [6]). In 2012 the in-/out- data transfers amounted to 230 TB, equivalent to an average bandwidth of 60 Mb/s, while the transfer peak value reached 80% of the available bandwidth. In 2013 an increase of 30% of the overall network traffic was observed with respect to 2012, due to the entrance of new users and to changes in software applications.

### 3 Data center room and cooling system

The CRESCO4 computing facility is located in a new and dedicated computer room, adjacent to the room in which are located the other three CRESCO clusters. Computing and cooling systems are located in the section of the room having the highest ceiling. In figure 6 is represented the space arrangement of the computing and cooling facilities.

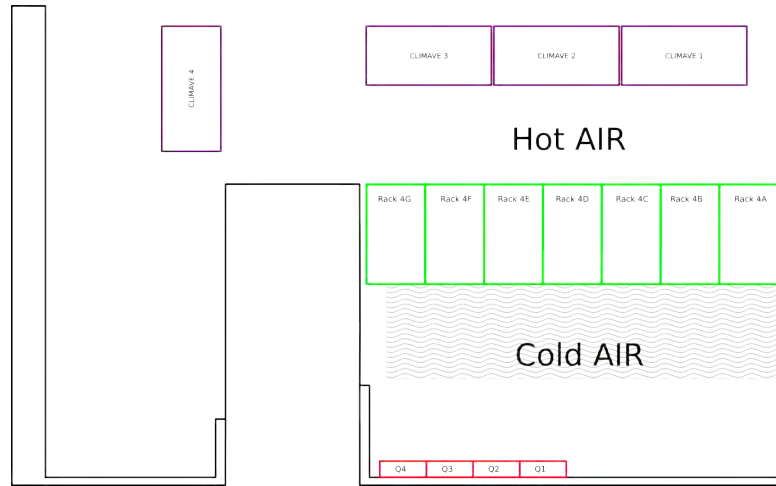


Figure 6: Map of the CRESCO4 facilities.

The cooling system is composed by four independent *Climaveneta i-AFU F04 MOD\_A 50* units; these units are dual circuit systems, featuring a direct expansion circuit with inverter and a secondary water circuit connected to external dry coolers model *BDC-078m*. This technology permits to take advantage of free-cooling when the external conditions are favourable.

The cold air flows through the floor to a confined cold aisle in front of the computing nodes where is heated and then released into the hot aisle. The design of the configuration has been done optimizing and minimizing the heat transfer to the cold aisle; indeed the latter is very well confined and almost isolated from other heat sources. The cooling units take the air from the hot aisle, apply the refrigeration process and send it under the raised floor.

The cooling system is dimensioned with four independent Climaveneta units; the dimensioning takes into account the maximum heat production by computing nodes that is about  $110kW$ , the nominal cooling capacity of each system that is  $50kW$  and the presence of a further machine for redundancy purposes.

In the qualification tests of the system, the HPL benchmark yielded 85 Tflops with a computing electrical power consumption of  $109kW$ , a cooling power consumption of 35 kW and no free-cooling during the benchmark. The PUE (Power Usage Effectiveness) was 1.32 with 0.78 TFlops/kW. The optimization of the free-cooling system settings is currently underway and global results will be available after at least one year of data collection.

### 3.1 Fire suppression system

The fire suppression system consists of a set of aerosol potassium salt extinguishers, that can be automatically or manually activated. The automatic activation is triggered by an electronic fire detection system, based on optical smoke detectors. The detectors react in case of presence of combustion products and the fire control system start an alarm sequence (audio and visual) for a prompt evacuation of the data center.

## 4 Power supply

The utility provides 9kV power to the site main building and transformers convert the power to 400 Vac. In the site main power supply room a system of switchboards feed a 400kVA UPS (Schneider Electric, MGE Galaxy 6000 400kVA/320kW, efficiency at half load 94.4%, with 204 EXIDE P6V1700 batteries) shared between the previous existing CRESCO1, CRESCO2 and the new CRESCO3 and CRESCO4 clusters. Utility faults are backed up by a 500 kVA diesel generator (Cummins Power Generation, C550 D5). With CRESCO4 installation the air conditioning power system has been switched to a dedicated power supply line, backed up in case by another diesel generator (Volvo Penta 485kW). 3 phase power cables (100 mt) connect the site main power room with the main cluster switchboards, located in the entrance hall common to the already existing computer room, hosting CRESCO1, CRESCO2 and CRESCO3 clusters and to the new CRESCO4 computing room (see section 3). In the new computing room we installed 7 racks to host the computing nodes and the network devices; 6 of them (the racks hosting the nodes) are equipped with 4 APC web enabled 3phase 32A PDU while the rack for the network devices is equipped with 2 PDU of the same type. In order to have a redundant power supply system we installed in the computer room 4 panel boards with 8 3phases lines each. In this way, for a single rack each of the 4 PDU is connected to a different panel board. So that the system can tolerate the simultaneous fault of two over four panel boards. The single PDU provides power to the computing elements via short C13-C14 cables.

## 5 Conclusions

We have presented the main architectural features of the new HPC systems CRESCO3 (2016 cores) and CRESCO4 (4864 cores). These facilities have been purchased in the framework of the projects of the Italian National Operational Programme (PON) 2007-2013. The design and realization of these infrastructures is mainly an in-house effort of the ENEA UTICT researchers and technicians. CRESCO3 and CRESCO4 are powerful computing tools at disposal of the scientific community and, with an aggregate computing power of  $\sim 120$  Tflops, are at the moment the main HPC facilities of ENEAGRID.

## References

- [1] <http://www.progettoitacha.it/>.
- [2] <http://www.lamrecor.it/>.
- [3] <http://www.utict.enea.it/it/progetti/utict-e-i-progetti/tedat>.
- [4] <http://www.cresco.enea.it/>.
- [5] Rocchi A., Pierattini S., Bracco G., Migliori S., Beone F., Santoro A., Sciò C., and Podda S. Faro - the web portal to access eneagrid computational infrastructure. In: International Workshop on Science Gateways (IWSG 2010), 2010.
- [6] <http://www.garr.it/>.

# Progress on Inertial Confinement Fusion studies

*Angelo Schiavi\*, Alberto Marocchino, Stefano Atzeni*

*Università degli Studi di Roma "la Sapienza", Dipartimento SBAI  
Via A. Scarpa 14-16, 00161 Roma*

**ABSTRACT.** We report on the activities related to improving the three-dimensional ray tracing module implemented in the Lagrangean hydrodynamics code DUED.

## 1 Introduction

Our group is involved in numerical modelling and simulations related to target design for Inertial Confinement Fusion. We have focused our research activity on the shock-ignition scheme [1], which relies on the generation and collision of two counter propagating shock waves inside the fusion fuel. Travelling to the centre of the plasma, the shock wave increases in strength due to geometric convergence and finally hits a counter-propagating shock reflected from the target inner core. During the collision, the pressure inside the plasma can reach the Gigabar level and could trigger ignition of the reacting compressed fuel. Preliminary numerical investigations using 1D models have demonstrated that the shock-ignition scheme has great potential for achieving high gain implosions. On one hand, there are a few crucial points that need experimental verification (e.g. non-local fast-electron transport inside the plasma), and that are presently beyond the capabilities of existing hydrodynamic codes devoted to fusion energy research. On the other hand, there are important points to be addressed with codes currently available, such as the irradiation symmetry analysis, the gain dependence on the laser beams configuration, the shot-to-shot stability of the target implosion. It is also important to investigate the possibility of achieving high-gain using green-light lasers (second harmonic), increasing the efficiency of laser-to-plasma energy coupling and reducing the damage on the final optics of the system. All these topics are within the capability of our 2D hydrocode DUED which has been recently upgraded with a 3D ray tracing package [2] using MPI communications.

## 2 Progress

In 2013 the group mainly concentrated its efforts on the development of an analytical model for scaling up fusion targets in energy and in wavelength [3]. The CRESCO resources were employed for a preliminary scan of laser irradiation non-uniformity due to the presence of

---

\*Corresponding author. E-mail: [angelo.schiavi@uniroma1.it](mailto:angelo.schiavi@uniroma1.it).



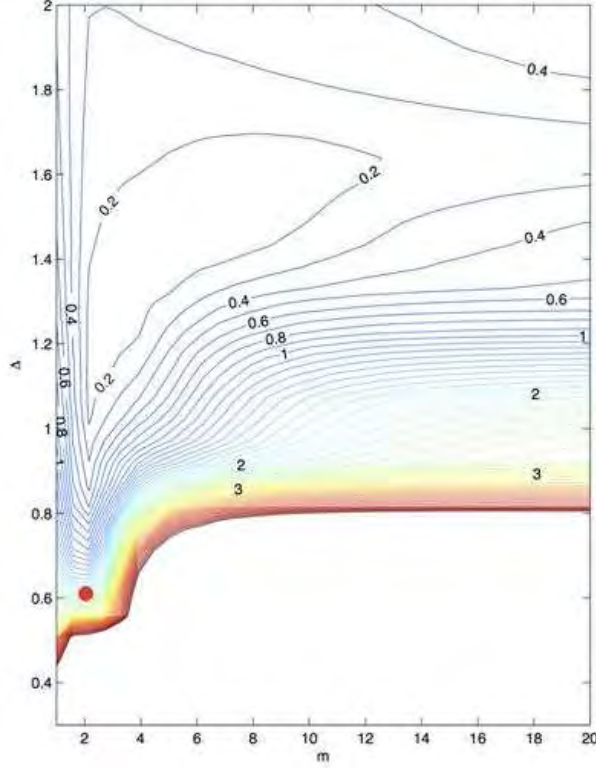


Figure 1: Irradiation asymmetry as a function of beam profile ( $m$ ) and beam cross-section ( $\Delta$ ). Original point design is marked with a red circle.

a preformed coronal plasma at the time of main pulse interaction with the target. This investigation is a continuation study of the parametric scan performed in [2] for the case of hard-sphere illumination. target was irradiated by 48 beams with super-Gaussian profile, and the laser intensity non-uniformity was measured in the layer between critical density  $n_c$  and  $n_c/10$ . The scan was performed by varying the super-Gaussian exponent  $m$  and  $\Delta$ , the ratio of beam waist over initial target radius. The asymmetry map obtained is presented in Fig. 1 for the case of a plasma corona with  $500 \mu\text{m}$  of density scale length. This situation corresponds to the typical plasma parameters during the interaction of the main part of the compression drive in a capsule implosion. It is clearly visible that there is an island of stability (minimum of asymmetry) extending from  $\Delta = 1.2$  to about  $1.4$ , i.e. in a region where the beam waist is slightly larger than the initial shell diameter. The original point design, depicted by a red circle, sits in a region of relatively high asymmetry and large gradient. Hence the simulated irradiation map indicates that the point design should be redefined taking into consideration that the *effective irradiation asymmetry* is not that at  $t=0$  (i.e. no preplasma), but that imprinted on the plasma during the main part of the compression drive.

### 3 Perspectives

Having introduced refraction of laser light in the plasma corona has increased the computing resources needed to perform an online simulation of 2D hydrodynamics evolution coupled to 3D laser ray tracing. We plan to rewrite parts of the ray tracing module in the early 2014 in order to proceed to a significant campaign of simulations for studying the robustness of fusion target implosion using shock ignition when laser pointing errors, beam-to-beam power imbalance and target mispositioning are taken into account.

### References

- [1] Betti R. et al. Physical Review Letters 98 (2007):155001.
- [2] Schiavi A. et al. Europhysics Letters 94 (2011) 35002.
- [3] Atzeni S. and Marocchino A., Schiavi A., and Schurtz G. Energy and wavelength scaling of shock-ignited inertial fusion targets. *New Journal Of Physics*, (15):045004, 2013.

# Application of the MINNI Atmospheric Model System (AMS) at high resolution over Italy

*Mario Adani<sup>2</sup>, Gino Briganti<sup>1\*</sup>, Andrea Cappelletti<sup>1</sup>,  
Massimo D'Isidoro<sup>2</sup>, Mihaela Mircea<sup>2</sup>, Lina Vitali<sup>2</sup>*

<sup>1</sup>*ENEA-UTVALAMB-AIR Territorial Office of Pisa*

<sup>2</sup>*ENEA-UTVALAMB-AIR Bologna Research Centre*

## 1 Introduction

The Italian Integrated Assessment Modelling System for supporting the International Negotiation Process on Air Pollution and assessing Air Quality Policies at national/local level (MINNI [1]), sponsored by the Italian Ministry of the Environment, is operated by UTVALAMB-AIR at ENEA. The MINNI system is composed of an Atmospheric Modelling System (AMS) and the Greenhouse Gas and Air Pollution Interactions and Synergies model over Italy (GAINS-Italy), connected through the Atmospheric Transfer Matrices and RAINS Atmospheric Inventory Link ([www.minni.org](http://www.minni.org)). The main components of AMS are the meteorological model (RAMS [2]), the air quality model (FARM [3], [4]) and the emission module (EMMA [5]). RAMS produces 3D meteorological fields, while EMMA elaborates the emissions over the simulation domain; both meteorology and emissions are used as inputs by FARM [6], which is a 3D K chemical dispersion model, devoted to simulate transport, diffusion and chemical transformations of pollutants, providing in output 3D concentrations and 2D deposition fields. Usually, AMS is used to perform air quality simulations scenarios over Italy at 20 km horizontal resolution and over five sub-domains, including respectively north, centre and south of Italy, Sardinia and Sicily islands, at 4 km horizontal resolution. Recently, the enhanced computational resources resulting from the upgrading of CRESCO facilities, allowed us to investigate model behaviour at resolutions up to 1 km over most of the Italian Peninsula. In this respect, we present here an example of a high resolution simulation, obtained for whole year 2010 over different areas of the Italian domain, focusing over two areas covering part of northern Italy.

## 2 Computational domains and simulations setup

In this exercise, AMS has been applied to simulate hourly meteorology and pollutants concentrations in a nesting cascade at different resolutions: over whole Italy (IT) at 20

---

\*Corresponding author. E-mail: [gino.briganti@enea.it](mailto:gino.briganti@enea.it).

km, northern Italy (NI) at 4 km and at over two sub-domains covering parts of Po Valley and Alps (NO and NE) at 1 km horizontal resolution. Nested domains are depicted in Fig. 1. All the simulation grids have 16 terrain following vertical levels starting from 20 m to 10000 m above the ground. Table 1 summarize the domains sizes.

## 2.1 Meteorological Field Input

	IT (20 km)	NI (4 km)	NO (1 km)	NE (1 km)
NX	67	146	200	165
NY	75	96	160	173
NZ	16	16	16	16
Total (NX*NY*NZ)	80400	224456	512000	456720

Table 1: Number of grid points used at different spatial resolutions. NX refers to longitudinal direction, NY to latitudinal direction and NZ to the vertical levels.

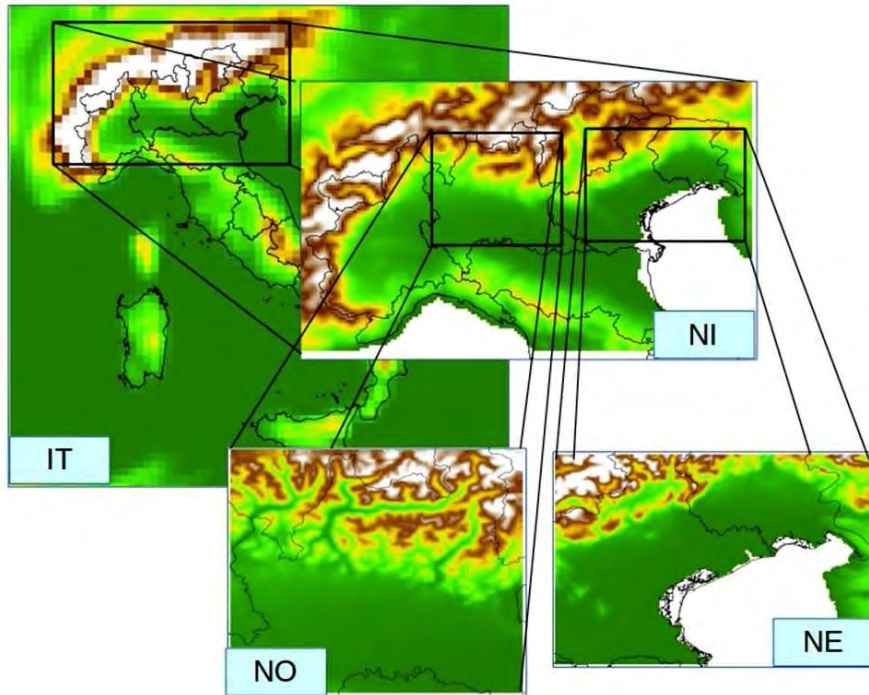


Figure 1: Orography of the nested grids over the 20 km resolution national domain (IT), the 4 km north of Italy sub-domain (NI) and the 1 km high resolution domains (NO, NE).

The meteorological fields have been simulated by means of the prognostic non-hydrostatic Regional Atmospheric Modelling System (RAMS, Version 6.0 [2]), developed at Colorado State University. Initial, boundary conditions and data assimilation have been based on

reanalyses fields produced by means of the RAMS pre-processor ISAN, which uses an optimal interpolation technique. European Centre for Medium-Range Weather Forecast (ECMWF) analyses have been used as background fields and World Meteorological Organisation (WMO) surface stations as observations in the assimilation procedure. A nudging technique has been enabled in RAMS to force runtime the model simulation to the reanalyses. In order to remove any possible drift of the calculated fields with respect to the large-scale analysis and local observations, the simulations have been re-initialized every ten days. RAMS implements a multilayer soil model [7] coupled to the atmospheric model to allow the evaluation of heat and moisture fluxes. For each decadal run, soil temperature and moisture profiles have been initialized using the data relating to the previous run, allowing continuity of soil status during the whole yearly simulation. As an example, temperature fields at lowest model level (20 m above the surface) are depicted in Fig. 2, as simulated at the different resolutions for a given instant. It can be noted that high resolution grids allow a more realistic representation of the field, influenced by the complex orography of the simulation area.

## 2.2 Air Quality Results and Evaluation

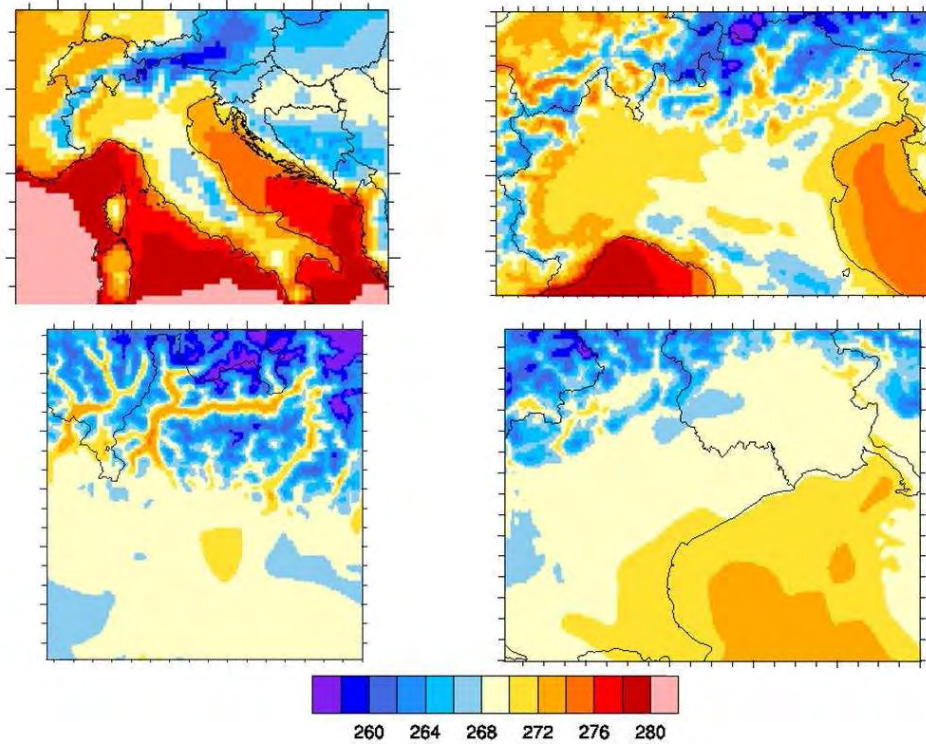


Figure 2: An example of Temperature (K) fields produced by RAMS at different spatial resolutions: 20 km (top, left), 4 km (top, right) and 1 km (bottom panels, NO on the left).

For the 2010 scenario, the emissions fields were computed following the chemical mechanism SAPRC99 with the contributions also of HM (heavy metals) and PAH (polycyclic aromatic hydrocarbons). The input data used was the ISPRA 2010 inventory database for

national emissions and the EMEP 2010 CEIP database for foreign emissions. The biogenic contributions to the emissions fields were computed by MEGAN model, implemented in SURFPRO module [8]. In the Fig. 3 an example of downscaling of 2D (height-integrated) emissions fields (in  $\mu\text{g}/\text{m}^2/\text{s}$ ) is shown. The figure shows clearly the effects of higher resolutions on emissions computations, in relations to the better representations of roads and urban area contributions.

With regard to the dispersion of pollutants, turbulence fields and other microscale boundary layer parameters are determined by means of the SURFPRO module, starting from RAMS fields. Boundary and initial conditions for both gas and aerosol phases pollutants have been provided by the EMEP unified model output (EMEP MSC-W, [emep.int/mscw/index\\_mscw.html](http://emep.int/mscw/index_mscw.html), [9]). At first, the 50 km resolution EMEP MSC-W fields have been suitably remapped to the SAPRC99 chemical model species [10], then they have been interpolated over our 20 km domain. The aerosol fields have been remapped and properly assigned to the three AERO3 bins (Aitken, accumulation and coarse [11]). Boundary and initial conditions for HMs and PAHs have been instead provided by EMEP MSC-E (<http://www.msceast.org/>; [12] [13]) and assigned to both gas and aerosol phases according to AERO3-POPs-Hg model [6]. We have performed off-line nested simulations on the inner domains at higher resolution. In Fig. 4 we can appreciate the effects related to the resolution increasing on annual-averaged nitrogen oxides ( $\text{NO}_x$ ) concentrations (ppb): anthropized areas look more definite during downscaling as consequence of a more accurate emissions distribution. As a first approximation, neglecting the oxidation to nitrates,  $\text{NO}_x$ s can be actually considered as tracers, whose concentration is directly influenced by primary emission of nitrogen oxides.

### 3 Information about Codes, Storage and CPU time

RAMS is an open source code (<http://www.atmet.com/index.shtml>) written in Fortran language. It was compiled in its parallel version and implemented in MVAPICH environment. In order to identify the best performing processor number, several tests have been made. A number of 240 processors resulted to be the best choice for the configuration described above. Running over CRESCO3 (queue `cresco3_72h24`) the whole year 2010 was simulated in 30 days (about 5 min per simulated hour). The same simulation, tested over CRESCO4 (queue `cesco4_16h24`), resulted in an estimated time of 20 days/year using 208 processors (about 3 min/hour). Disk space needed (expressed in Gb) to store all the 3D hourly data in output was 54, 160, 341 and 304 for IT, NI, NE and NO, respectively, over the dedicated filesystem `/gporq1_minini` mounted on CRESCO3-4.

The emission processor EMMA is a set of scripts, makefiles and fortran executables which reads, from a national inventory database, the yearly species-aggregated emissions on a particular administrative units level and projects these emissions on the grid of the domain. Due to the nature of EMMA computation, this module operates on ENEA GRID environment in multiseriial mode and, during the 2013, a significant change has occurred in the multiseriial queues policy by the GRID administrators. During the first part of the year, only the section CRESCO1 was opened to multiseriial queues (CRESCO2 nodes were reserved to parallel jobs); with the opening of CRESCO3 section a new multiseriial queue



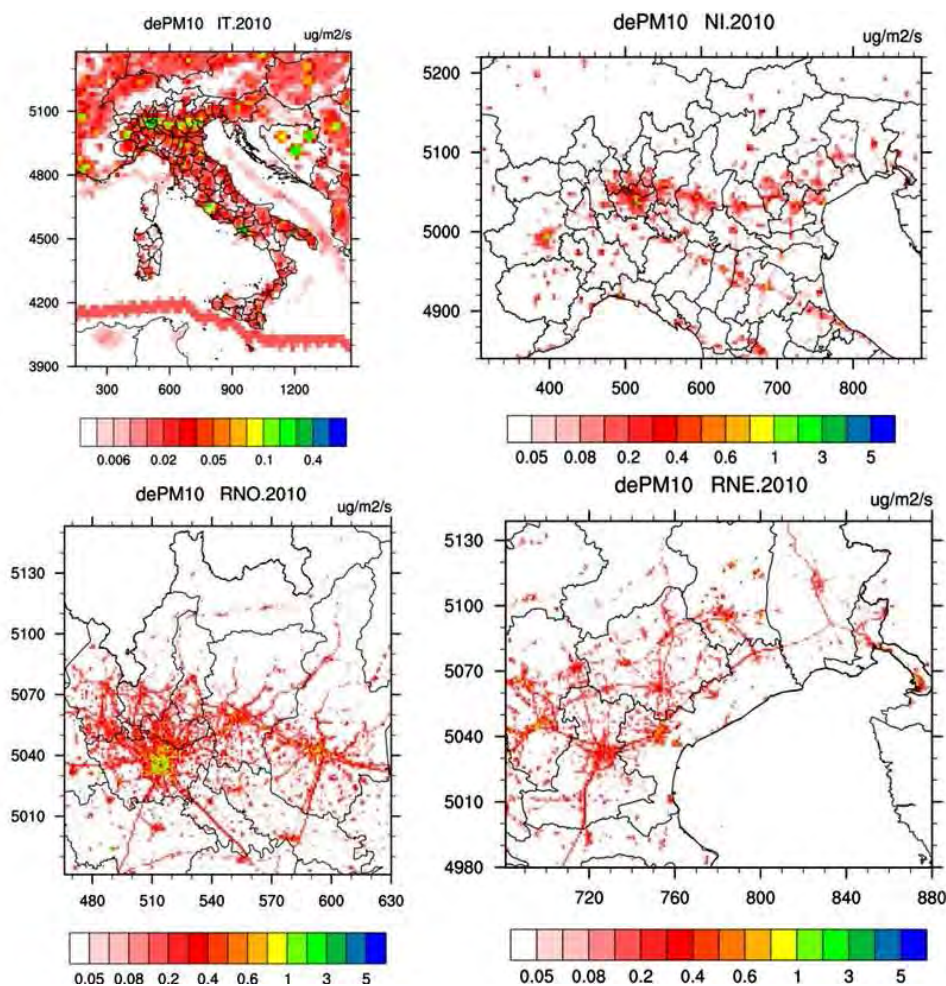


Figure 3: 2010 emission fields, yearly averages, PM10 respectively. 20 km IT, 4 km NI and 1 km RNO and RNE domains.

cresco3\_hXXX has been available for users, with significant enhancement of computational performance by factor of 10 or more. This upgrade allowed to migrate easily from chemical mechanism SAPRC90 to SAPRC99 and SAPRC99 with HM and PAH. However, the improvement of CPU-time for EMMA computations is also due to the update of scripts for jobs submission which now use local and RAM disks as scratch space for intermediate computations, instead of lower I/O throughput devices as shared filesystems.

FARM is a three-dimensional Eulerian model, written in Fortran language, that accounts for the transport, chemical conversion and deposition of atmospheric pollutants. We have used the 4.6 version, in which both MPI and hybrid (OpenMP+MPI) parallelization methods have been implemented. FARM has been indeed recently rewritten [14]: in the new version, both the MPI and hybrid MPI-OpenMP parallelization paradigms have been introduced; moreover, the old OpenMP method has been optimized. We have observed a pretty good scaling of the elapsed time with the number of used processors; we also have identified the optimum number of cores, allowing enough scaling without using a

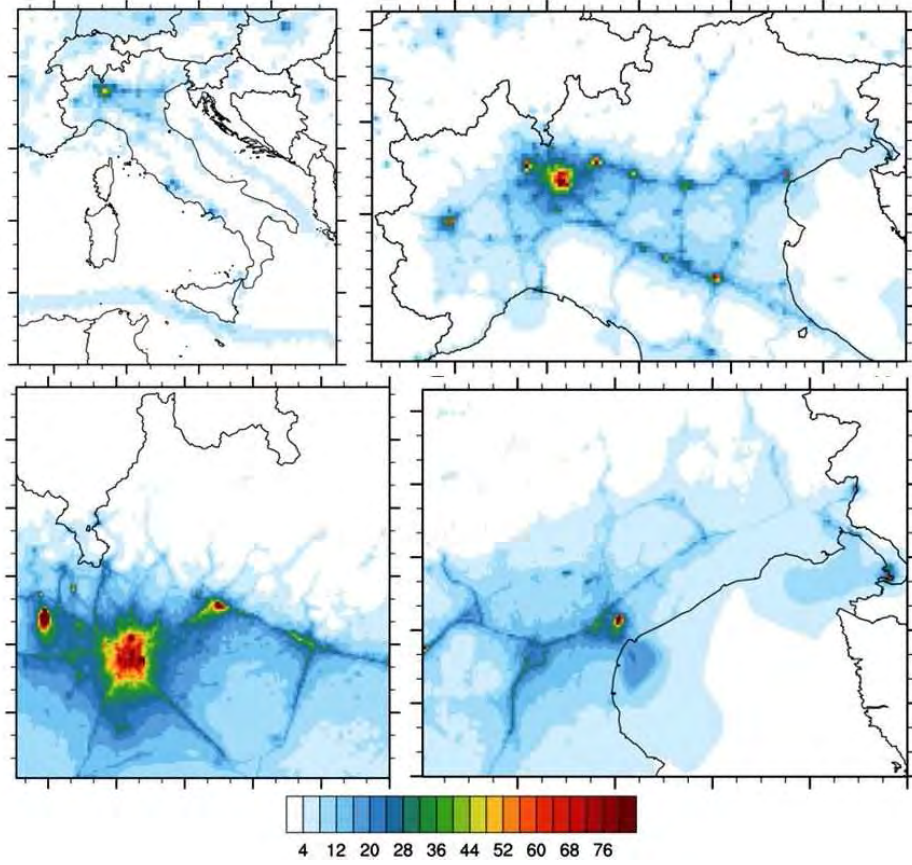


Figure 4: Example of 2010 (annual averaged) concentration fields of NOx: 20 km (top, left), 4 km (top, right) and 1 km (bottom panels).

large amount of computational resources, which is between 48 and 96. Anyhow, from time to time, the choice of the number of cores to be used depends on resources availability. Just to give an order of magnitude, with 48 cores and an integration time step of 300 s, we spend about 0.0002 s/(grid point\*hour). This means that, in order to simulate one whole day for the MINNI North Italy (NI) domain, we need about 20 minutes elapsed time; it's worth to note that old 3.12 FARM OpenMP version with 8 cores (the optimal choice for that version) took about 3.5h [15], namely even one order of magnitude slower. Regards disk usage, we store only float variables on netCDF file, so we have 4 bit/variable. The file dimension is easily calculated by taking into account the number of 2D (n2d) and 3D (n3d) stored variables, the number of dimensions (gridpoints: nx, ny, nz) and considering we have 24 (nt) unlimited dimensions per file (24 hourly data per day):  $dim = 4 \cdot nx \cdot ny \cdot (n2d + nz \cdot n3d) \cdot [bit]$ . Generally, we store 17 2D variables and 144 3D variables, so we obtain about 1.1 GB/daily\_file for 20 km resolution and 3 GB/daily\_file for the 4 km resolution NI. At 1 km, we save 2D fields only. For 1 year, the total storage values are: 400 GB/y for IT, 1 TB/y for NI0, 150 GB/y for NO and 165 GB/y for NE.



## 4 Conclusions

We presented an example of application of the MINNI AMS at high resolution (1 km) over different sub-domains covering parts of the Italian territory, for the whole year 2010. This was possible thanks to the computing facilities provided by CRESCO after the recent upgrades (CRESCO3 and CRESCO4 in 2014). The possibility of reaching such horizontal resolution over Italy will make possible to give more focused, reliable and realistic responses to different stakeholders (e.g. Italian Ministry of Environment, public and private Companies/Agencies) in relation to problems, evaluation and mitigation policies related to air quality. It's worth noting the importance to simulate sources impact at small spatial scales in air quality management planning. In fact, resolution increasing generally improves the performances of the dispersion model, because more meteo structures at smaller scales are resolved (and not introduced by means of mathematical closure assumptions) and the emissions distribution becomes more accurate; this may: i) lead to a better evaluation of the health impact assessment; ii) allow a more detailed identification of the representativity neighbourhood of monitoring stations, iii) help to better understand local source apportionment effects; iv) helps to identify small sources impact.

For the future, the experience made suggests that a further improvement in terms of realism of model simulation could be obtained when the grid model downscaling ( $20\text{ km} \rightarrow 4\text{ km} \rightarrow 1\text{ km}$ ) will be supported by a similar downscaling of national emissions inventories (from NUTS=2 to NUTS=3 administrative level unit) and by the refinement of EMEP grid (from 50 km to  $0.1^\circ$  degree cell size) in order to better exploit the capacities offered by high resolution FARM computations.

## References

- [1] Zanini G., Mircea M., Briganti G., Cappelletti A., Pederzoli A., Vitali L., Pace G., Marri P., Silibello C., Finardi S., and Calori G. The MINNI project: an integrated assessment modeling system for policy making. In *International Congress on Modelling and Simulation*, ISBN: 0-9758400-2-9, pages 2005–2011, Zealand, Melbourne, Australia, 12-15 December 2005.
- [2] Cotton W. R., Pielke R. A., Walko R. L., Liston G. E., Tremback C. J., Jiang H., MC Anelly R. L., Harrington J. Y., Nicholls M. E., Carrio G. G., and MCFADDEN J. P. RAMS 2001: Current status and future directions. *Meteorology and Atmospheric Physics*, 82:5–29, 2003.
- [3] Silibello C., Calori G., Brusasca G., Catenacci G., and Finzi G. Application of a photochemical grid model to milan metropolitan area. *Atmospheric Environment*, 32(11):2025–2038, 1998.
- [4] Gariazzo C., Silibello C., Finardi S., Radice P., Piersanti A., Calori G., Cecinato A., Perrino C., Nusio F., Cagnoli M., Pelliccioni A., Gobbi G. P., and Di Filippo P. A. A gas/aerosol air pollutants study over the urban area of rome using a comprehensive chemical transport model. *Atmospheric Environment*, 41:7286–7303, 2007.

- [5] ARIANET. Emission Manager - processing system for model-ready emission input. User's Guide. Arianet report R2013.19, 2013.
- [6] ARIANET. FARM (Flexible Air quality Regional Model) Model formulation and User's Manual, v. 4.5. Arianet report R2013.24, 2013.
- [7] Walko R. L., Band L. E., Baron J, Kittel T. G. F., Lammers R., Lee T. J., Ojima D. Pielke R. A., Taylor C., Tague C., Tremback C. J., and Vidale P. J. Coupled atmosphere-biophysicshydrology models for environmental modeling. *Journal of Applied Meteorology*, 39:931–944, 2000.
- [8] ARIANET. SURFPRO3 User's Guide (SURFace-atmosphere interface PROcessor, Version 3). Arianet report R2011.31, 2011.
- [9] EMEP. Transboundary acidification, eutrophication and ground level ozone in europe in 2007. EMEP status report 1/2009, joint MSC-W & CCC & CEIP REPORT, ISSN 1504-6109 (PRINT), ISSN 1504-6192 (online), 2009.
- [10] Carter W. P. L. Documentation of the SAPRC-99 chemical mechanism for VOC reactivity assessment. Final report to California Air Resources Board, Contract no. 92-329, and (in part) 95-308, 2000.
- [11] Binkowski F. S. and Roselle S. J. Models-3 community multiscale air quality (CMAQ) model aerosol component 1. Model description. *Journal of Geophysical Research*, 108(D6):4183, 2000.
- [12] Ilyin I., Rozovskaya O., Sokovyh V., Travnikov O., and Aas W. Heavy Metals: Transboundary Pollution of the Environment. EMEP Status Report 2/2009.
- [13] Gusev A., Rozovskaya O., Shatalov V., Sokovyh V., Aas W., and Breivik K. Persistent Organic Pollutants in the Environment. EMEP Status Report 3/2009.
- [14] Marras G. F., Silibello C., and Calori G. A Hybrid Parallelization of Air Quality Model with MPI and OpenMP. In Träff J.L., Benkner S, Dongarra J. (eds.) Recent Advances in the Message Passing Interface. Lecture Notes in Computer Science, 7490, 235-245, Proc. of 19th European MPI Users' Group Meeting, EuroMPI 2012, September 23-26 2012.
- [15] Briganti G. Valutazione delle concentrazioni in aria dei principali inquinanti: CO, SO<sub>2</sub>, NO<sub>x</sub>, PM10, PM2.5, O<sub>3</sub>, COV. Calcolo ad alte prestazioni sul sistema CRESCO: contributi degli utenti 2008-2009, 2010.

# Electronic properties at complex interfaces

*Giovanni Cantele<sup>1\*</sup>, Domenico Ninno<sup>1,2</sup>, Roberto Nunzio D'Amico<sup>1</sup>*

*<sup>1</sup>CNR-SPIN, Dipartimento di Fisica  
Complesso Universitario Monte Sant'Angelo  
Via Cintia, 80126 Napoli, Italy*

*<sup>2</sup>Università degli Studi di Napoli "Federico II", Dipartimento di Fisica  
Complesso Universitario Monte Sant'Angelo  
Via Cintia, 80126 Napoli, Italy*

**ABSTRACT.** In this report, the study of electronic processes and barrier heights at semiconductor-semiconductor and semiconductor-metal interfaces, of interest for applications in (nano)electronics, energy conversion and optoelectronic devices, is presented. Two different systems are chosen, namely, the SrTiO<sub>3</sub>-TiO<sub>2</sub> interface and graphene nanoribbons covalently attached to a metallic substrate. Fundamental properties, following the formation of the interface, are: charge transfer and interface dipole, band offset, role of defects.

It is shown that the local chemistry and the interface stoichiometry play a fundamental role in determining the interface electronic properties. As such, a deep understanding at microscopic level is needed, as provided by accurate first principle approaches.

## 1 Introduction

The most recent advances in thin-film synthesis techniques and two-dimensional materials fabrication has opened new perspectives in the interface physics and its use in (nano)electronics, optoelectronic and energy conversion devices. In particular, the ability of engineering atomically precise complex interfaces, of controlling their stoichiometry and of combining the properties of individual materials into various heterostructures paves the way to new functional devices. Among the many, special mention deserve complex oxide interfaces [1]: a wide range of crystalline structures exhibit, already in the bulk, an incredible variety of physical phenomena, such as piezo-, pyro-, and ferroelectricity, superconductivity, and so on. It is expected that an even more wide range of properties and applications can be observed in atomically sharp oxide heterostructures. Beyond oxide electronics, organic electronic applications are also foreseen, thanks to interfaces with organic layer in devices, such as light-emitting diodes and organic photovoltaic cells [2].

Even more exciting is the physics of two-dimensional materials [3, 4], that has emerged since the discovery of graphene. Graphene nanoribbons (GNR), one dimensional graphene

---

\*Corresponding author. E-mail: giovanni.cantele@spin.cnr.it.

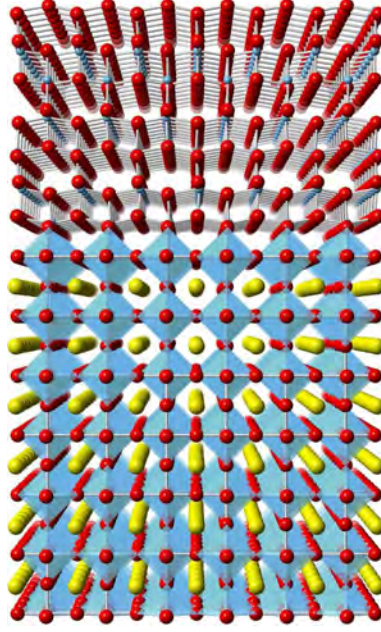


Figure 1: The  $\text{SrTiO}_3\text{--TiO}_2$  interface [5].

stripes, have been shown as promising materials for nanoelectronics: at variance with graphene, that exhibits a zero energy gap, quantum confinement in GNR channels guarantees band energy gaps as large as  $\sim 1$  eV for  $\sim 1$  nm wide stripes. The presence of this gap is fundamental for the realization of a switching device. However, metallic contacts are required in practical applications and the understanding of the metal contact–GNR interaction is of utmost importance for predicting and engineering the device properties.

In this report fundamental properties, arising at complex interfaces, are addressed, choosing as model systems the  $\text{SrTiO}_3\text{--TiO}_2$  oxide-based interface and a GNR-based system, where the GNR is covalently immobilized on the metallic substrate by means of an organic layer.

## 2 Software and computational resources

All calculations have been performed in the framework of Density Functional Theory, as implemented in the open source Quantum Espresso package [6]. This package uses atomic pseudopotentials to mimic the ion cores and plane waves to expand the electronic wave functions and charge density. The periodic supercell approach is used to study low dimensional systems, such as surfaces/interfaces/two-dimensional materials, nanowires, zero-dimensional nanostructures and molecules. As such, vacuum space is needed in these cases, to avoid spurious interactions between the periodic replicas. The number of basis set functions needed to provide converged properties changes with the atomic pseudopotential, number of atoms in the supercell and supercell size. Therefore, huge computational resources are usually needed for the study of interfaces, mostly in the presence of defects.

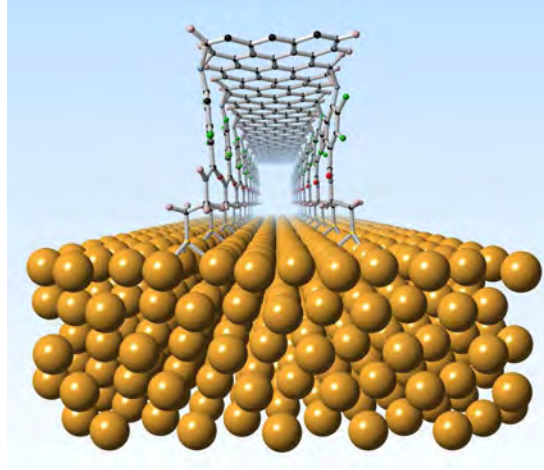


Figure 2: A graphene nanoribbon covalently immobilized on a metallic gold substrate [5].

The results shown in the present report have been obtained with the use of high performance computing facilities, in particular the *CRESCO3* cluster located at the Portici ENEA center. Typical jobs require 64 to 256 computing units and several tens Gb of disk storage (for electronic wave functions and charge density, needed both during the optimization tasks and for post processing purposes). Parallelization is implemented in the used package through the MPI environment.

### 3 Results

#### 3.1 The $\text{SrTiO}_3\text{--TiO}_2$ interface

One of the most important properties that characterize an interface is the band offset, that is, the relative position of the energy levels on the two sides of the interface. In particular, the valence band offset, VBO (the conduction band offset, CBO) can be defined as the difference between the positions of the top valence bands (bottom conduction bands) of the two materials.

X-ray photoelectron spectroscopy has revealed a VBO for the  $\text{SrTiO}_3\text{--TiO}_2$  interface ranging from -0.06 eV to +0.16 eV, even though theoretical predictions ( $\sim 0.5$  eV) largely overestimate such experimental outcomes [7, 8].

The theoretical simulations of this interface, schematically shown in Fig. 1, show that the barrier heights at the interface are lowered by the presence of oxygen vacancies in the near interface region, indicating a possible explanation of the near zero band offsets that have been experimentally observed. Profound modification of the interface electronic structure are induced in the presence of a defected (non stoichiometric) interface, giving indication of a possible tool to tailor the interface properties [9].

### 3.2 GNRs covalently immobilized on a metallic substrate

Recent experiments have made available the possibility of immobilizing graphene and related nanostructure onto either metallic or semiconducting substrates, using an organic layer (thiol-functionalized per-fluorophenyl azide, PFPA) as a coupling agent [10, 11]. A schematic view of the hybrid organic-inorganic heterostructure is shown in Fig. 2.

Large-scale ab initio calculations have allowed to address two fundamental issues, that is, how and to which extent the presence of both the substrate and the covalent functionalization of the GNR modifies the device electronic properties [12, 13]. In particular, it has been shown that: i) the presence of a significant GNR band energy gap is not altered by the presence of the metal-PFPA and PFPA-GNR interfaces, ii) a substantial electrical decoupling between the metal and GNR electronic states shows up, iii) no doping effect (charge transfer from the metal to the GNR) takes place. The results suggest a route for the the engineering and nanopatterning of GNR-based nanodevices.

## References

- [1] Pavlo Zubko, Stefano Gariglio, Marc Gabay, Philippe Ghosez, and Jean-Marc Triscone. Interface Physics in Complex Oxide Heterostructures. *Annu. Rev. Condens. Matter Phys.*, 2(1):141–165, March 2011.
- [2] Hong Li, Paul Winget, and Jean-Luc Brédas. Transparent Conducting Oxides of Relevance to Organic Electronics: Electronic Structures of Their Interfaces with Organic Layers. *Chem. Mater.*, 26(1):631–646, January 2014.
- [3] Ten years in two dimensions. *Nat Nanotechnol*, 9(10):725–725, October 2014.
- [4] Things you could do with graphene. *Nat Nanotechnol*, 9(10):737–737, October 2014.
- [5] Image generated using CrystalMaker®: a crystal and molecular structures program for Mac and Windows. CrystalMaker Software Ltd, Oxford, England (www.crystallmaker.com).
- [6] Paolo Giannozzi, Stefano Baroni, Nicola Bonini, Matteo Calandra, Roberto Car, Carlo Cavazzoni, Davide Ceresoli, Guido L Chiarotti, Matteo Cococcioni, Ismaila Dabo, Andrea Dal Corso, Stefano de Gironcoli, Stefano Fabris, Guido Fratesi, Ralph Gebauer, Uwe Gerstmann, Christos Gougoussis, Anton Kokalj, Michele Lazzeri, Layla Martin-Samos, Nicola Marzari, Francesco Mauri, Riccardo Mazzarello, Stefano Paolini, Alfredo Pasquarello, Lorenzo Paulatto, Carlo Sbraccia, Sandro Scandolo, Gabriele Sclauzero, Ari P Seitsonen, Alexander Smogunov, Paolo Umari, and Renata M Wentzcovitch. QUANTUM Espresso: a modular and open-source software project for quantum simulations of materials. *J Phys-Condens Mat*, 21(39):395502, September 2009.
- [7] A C Tuan, T C Kaspar, T Droubay, J W Rogers, and S A Chambers. Band offsets for the epitaxial TiO<sub>2</sub>/SrTiO<sub>3</sub>/Si(001) system. *Appl Phys Lett*, 83(18):3734, 2003.

- [8] S A Chambers, T Ohsawa, C M Wang, I Lyubinetzky, and J E Jaffe. Band offsets at the epitaxial anatase TiO<sub>2</sub>/n-SrTiO<sub>3</sub>(001) interface. *Surface Science*, 603(5):771–780, March 2009.
- [9] Nunzio Roberto D’Amico, Giovanni Cantele, and Domenico Ninno. First principles calculations of the band offset at SrTiO<sub>3</sub> - TiO<sub>2</sub> interfaces. *Appl Phys Lett*, 101(14):141606–4, January 2012.
- [10] Li-Hong Liu, Michael M. Lerner, and Mingdi Yan. Derivatization of Pristine Graphene with Well-Defined Chemical Functionalities. *Nano Lett*, 10(9):3754–3756, 2010.
- [11] Li-Hong Liu and Mingdi Yan. Functionalization of pristine graphene with perfluorophenyl azides. *J Mater Chem*, 21(10):3273–3276, January 2011.
- [12] Ivo Borriello, Giovanni Cantele, and Domenico Ninno. Graphene nanoribbon electrical decoupling from metallic substrates. *Nanoscale*, 5(1):291, 2012.
- [13] Irina Valitova, Michele Amato, Farzaneh Mahvash, Giovanni Cantele, Antonio Maffucci, Clara Santato, Richard Martel, and Fabio Cicoira. Carbon nanotube electrodes in organic transistors. *Nanoscale*, 5(11):4638, 2013.

# Dynamical Downscaling of GCM Seasonal Forecasts over the Greater Horn of Africa

*Sandro Calmanti\*, Maria Vittoria Struglia*

*ENEA, UTMEA-CLIM*

*Via Anguillarese, 301 - 00123 S.Maria di Galeria (Rome, Italy)*

## 1 Introduction

The FP7 project EUPORIAS (EUropean Provision Of Regional Impact Assessment on a Seasonal-to-decadal timescale) aims to develop a few working prototypes of climate services on a number of key sectors. The Greater Horn of Africa is one of the regions of interest, with a specific focus on agriculture and food security. Precipitation and temperature exhibit better predictability at seasonal timescales over East Africa than regions in the extra-tropics, potentially allowing the use of seasonal forecasts in key sectors of societal relevance. In particular, the potential for rainfall predictability in East Africa has been known for a relatively long-time [1]. Nowadays, SST-based statistical seasonal forecasting algorithms are of common use at the National Meteorological Agency (NMA) of Ethiopia [2]. Seasonal to decadal forecasts are generally available as an ensemble of multi-GCM output, presently made at GCM resolutions of  $\sim 100$ -200 Km. However, climate service applications require information at significantly finer spatial scales, especially over regions characterized by a complex orography such the Greater Horn of Africa. To bring GCM data to such scales some form of downscaling is required. One of the objectives of the EU-FP7 project EUPORIAS is to critically evaluate the hindcast accuracy of both the GCMs (on larger scales; atmosphere and SSTs) and the RCMs (local to the region) against suitable observations. This will assess the utility of dynamical downscaling (DD), combined with statistical methods (SD), to provide seasonal forecast data for impact models over the region. In this context, UTMEA-CLIM has used the CRESCO HPC facilities to conduct a number of sensitivity experiments aiming at the fine tuning of the regional climate model RegCM4 for the region of interest.

## 2 The Regional Climate Model

RegCM4 is open source software developed and maintained by the Earth System Physics Department of ICTP. It is a limited area atmospheric climate model that integrates the 3-dimensional, hydrostatic, primitive equations for the atmosphere using a rectangular grid

---

\*Corresponding author. E-mail: [sandro.calmanti@enea.it](mailto:sandro.calmanti@enea.it).



with uniform horizontal resolution and sigma-coordinates in the vertical (i.e. the vertical coordinate is the atmospheric pressure normalized with the surface pressure). RegCM4 uses a two-dimensional domain decomposition with the model horizontal grid divided into rectangular subdomains, whose dimension depends on the number of assigned CPUs and whose shape is determined in order to be as close as possible to a square with an equal number of grid-points in both directions. The model domain adopted for this study (Fig. 1) has 160x225 grid point on 18 vertical levels. The horizontal resolution for this model domain is about 22 km and it has been chosen in coordination with other partners in the project EUPORIAS, in order to allow a cross-comparison of different models under similar model configurations, aiming at a thorough evaluation of the potential skill in simulating local rainfall patterns. The Ethiopian highlands are the center of the model domain so that lateral boundary conditions have less direct influence on the model behavior over the main focus area of the study. On the other hand, large portions of the Indian ocean are included in the model domain as sea surface temperature is expected to significantly affect local circulation patterns. With this model domain, the optimal resource request to comply with the CRESCO queue policy is to use a domain decomposition on 240 CPUs, so that approximately 3 to 4 years of model simulation can be completed during one queue cycle of 24hours.

### 3 Simulation design

The main objective of the EUPORIAS project is to test the usability of model output in the context of drought early warning where the expected model skill is to capture the inter-annual variability of total cumulated rainfall during the crop season in order to be able to clearly distinguish wet and dry years. The possibility of disaggregating the total rainfall into the sub-seasonal signal is considered as a second order objective. Therefore, the main objective of this preliminary study was to calibrate a selected set of model coefficients of the regional model used to downscale the global fields, in order to optimize the model performance in capturing the inter-annual variability of rainfall during the main crop season in the area. The fine-tuning of the large number of model parameters that may affect rainfall patterns is an extremely demanding challenge. In this report we summarize the results of the analysis by using a simple indicator of the model performances, and by considering a limited number of assumption concerning the key driving factor for affecting the modelled rainfall. In particular the model performance is evaluated by simply using the total June-July-August rainfall over a box encompassing the area from 36E-7N to 43E-13N, covering the highlands of Ethiopia and highlighted with a red box in Fig. 1. We have then considered two important processes that, together with the complex orography of the area, control local rainfall patterns.

First, we consider the parameterization of deep atmospheric convection, which is a key process in determining the total amount of rainfall in the tropics. In this particular area of interest, characterized by significant orographic features, large-scale precipitation, which is determined by the direct condensation of advected moisture plays also an important role. The relative balance between convective and large-scale precipitation is a key ingredient in determining the local rainfall patterns. The model shows a large sensitivity to the

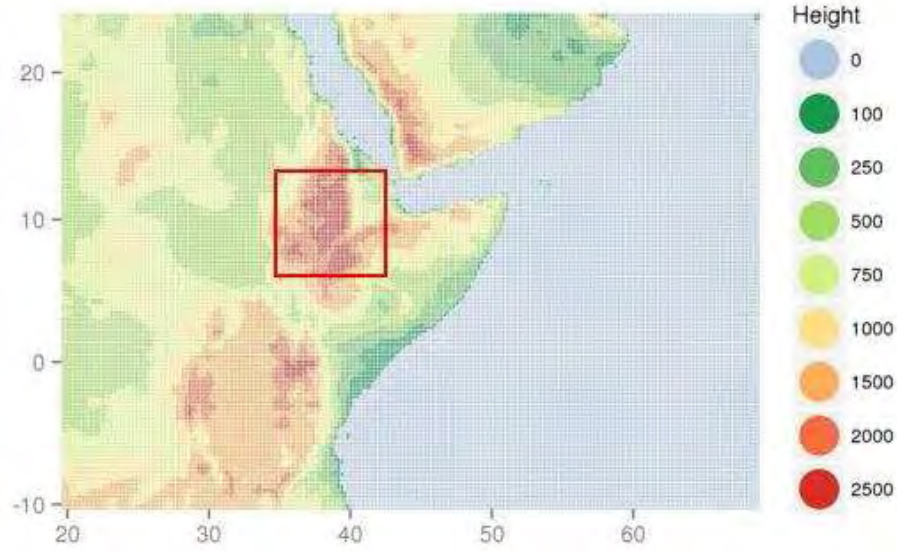


Figure 1: RegCM4 model domain. The model grid as 160x225 grid points. The red box shows the area over which the summer (JJA) total rainfall is computed for the sensitivity analysis.

coefficients implied in the parameterization of deep convection processes. In particular, an important model coefficient is the allowed range of convective heating. When deep convection is activated in the model, the corresponding heating is included in the range  $H_{min} < H_{max}$ . High values of  $H_{min}$  imply that deep-convection is always very efficient in heating the atmosphere and in generating rain-producing clouds. Low values of  $H_{min}$  imply un-efficient convection, and very low values of  $H_{min}$  eventually shut down convection completely. In the a reference simulation (*mxl*), we adopt a model setup already tested in previous studies [3], where the convective heating thresholds are set to  $H_{min} = -250 \text{ K hPa}^{-1}\text{s}^{-1}$  and  $H_{max} = 500 \text{ K hPa}^{-1}\text{s}^{-1}$ . In the other simulations the convective heating is adjusted as indicated in Fig. 2.

A second important factor for the simulation of local atmospheric dynamics is moisture/energy exchange between the atmosphere and the land surface. In particular, latent heat flux during the wet season is an important contributor to the balance of available potential energy which is released during deep convection (and therefore rainfall) events. The moisture/energy exchange between the atmosphere and the land surface is modelled in our configuration of RegCM4 by the Biosphere-Atmosphere Transfer Scheme (BATS), which uses around 20 soil types to describe the fluxes between the soil and the atmosphere [4]. The minimum stomatal resistance ( $rs_{min}$ ) is a key parameter in controlling these fluxes and the model is generally very sensitive to changes in this parameter, which controls evapotranspiration, thereby affecting both the energy and the moisture fluxes. In the default configuration of BATS, the stomatal resistance is set at a rather high value for all the land use types. This corresponds to limited total evapotranspiration and latent heat release. In general, this configuration produces relatively drier atmospheric boundary layer and therefore less energy available for triggering convection. Lower values of the

	MXD	RSMIN00	RSMIN01	RSMIN02	HMIN400	HMIN-500	HMIN-350	HMIN-350_HMAX400
<i>min_convective_heating</i>	-250	-250	-250	-250	<b>400</b>	<b>-500</b>	<b>-350</b>	<b>-350</b>
<i>max_convective_heating</i>	500	500	500	500	500	500	500	<b>400</b>
<i>rsmin/Forest</i>	200	<b>100</b>	<b>100</b>	<b>100</b>	<b>100</b>	<b>100</b>	<b>100</b>	<b>100</b>
<i>rsmin/Crop</i>	200	200	<b>100</b>	<b>100</b>	200	200	200	200
<i>rsmin/Tall Grass</i>	200	200	200	<b>100</b>	200	200	200	200

Figure 2: Summary of the model sensitivity experiments described in this study. Bold fonts indicate the differences between the reference simulation (*mx**d*) and the various sensitivities.

minimum stomatal resistance coefficient (*rsmin*) have been tested for the land use types, which are mostly represented in the considered domain. About 44% of the model domain adopted for this study corresponds to the ocean grid points while 18% of the domain is desert. We have tested the halving of the coefficient (*rsmin*) over forests (10% of the model grid points), tall grass (6%) and crop area (2%). Fig. 2 summarizes the setup of the different simulations discussed in the following section.

## 4 Results

The results of the sensitivity study are summarized in Fig. 3. The model rainfall is compared with different observational datasets: the African Rainfall Climatology (ARC2) is a high resolution satellite rainfall estimate (10x10 km) but is known to underestimate the actual rainfall [5]; the CMAP has a lower resolution but incorporates a larger number of available weather station data. The default configuration (exp. *mx**d*) shows in general excessive rainfall with respect to the observations. A slight improvement can be obtained by lowering the *rsmin* coefficient corresponding to the forest land cover type (exp. *rsmin00*, *rsmin01*, *rsmin02*). However, the reduction in total precipitation is not a persistent feature of these simulation. For example a systematic reduction of the mean JJA rainfall is detected only during the period 2002-2004. The relative contributions of convective and large-scale component of rainfall are comparable to those of the *mx**d* default configuration. The parameters  $H_{min}$  and  $H_{max}$  have a significantly larger effect. In particular, when  $H_{min}$  is set to a high value (exp  $H_{min} = 400$ ), deep-convection is always very efficient and is responsible for the entire rainfall amount, while large scale rainfall is shut-down completely. The inter-annual variability of rainfall increases significantly as well in this case. On the other side, a low value of  $H_{min}$  ( $H_{min} = -350 \text{ K hPa}^{-1}\text{s}^{-1}$ ) corresponds to a weaker convective activity while for  $H_{min} = -500 \text{ K hPa}^{-1}\text{s}^{-1}$  and for lower overall values of the convective heating (e.g.  $H_{min} = -250 \text{ K hPa}^{-1}\text{s}^{-1}$  and  $H_{min} = 500 \text{ K hPa}^{-1}\text{s}^{-1}$ ) convective rainfall shuts down almost completely and the interannual variability of the

total rainfall is dominated by the large-scale contribution.

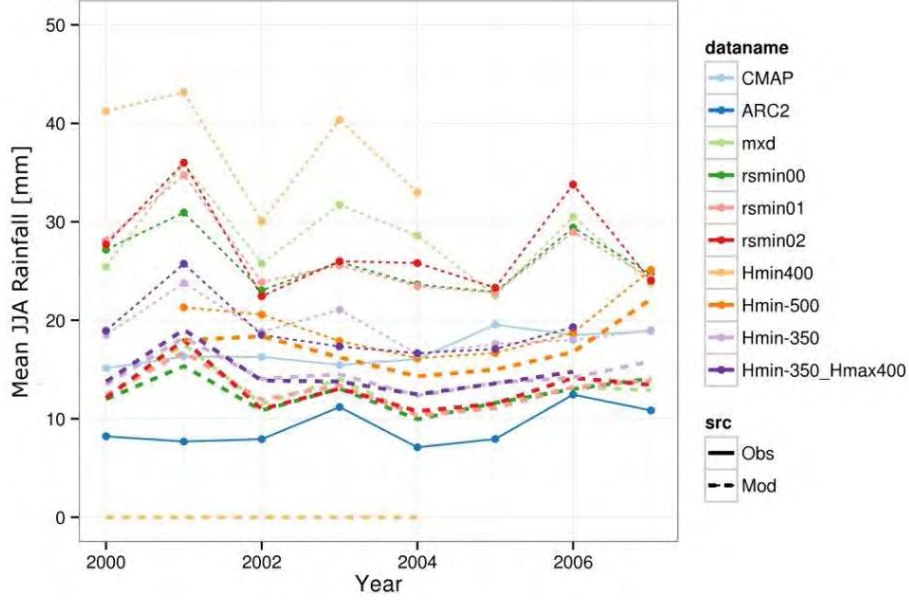


Figure 3: Total seasonal (June-July-August) rainfall averaged over the grid-points inside the red box in Figure 1. Continuous lines are the observational datasets (CMAP and ARC2). The model output is decomposed into total (dashed+circles) and large-scale (thick dashed) components. The difference between the two represents the convective component.

## 5 Conclusions

We have performed a series of sensitivity experiments, aiming at tuning key RegCM4 model coefficients and adjusting the simulated rainfall patterns over Ethiopia. With respect to the relative contribution of convective and large-scale processes to the total amount of precipitation, the results indicate the adjustment of stomatal resistance over of the forest grid points, as well as the adjustment of convective heating thresholds as useful tuning strategies. The observational datasets adopted for the comparison are known to slightly underestimate the total rainfall in this area [5]. However, rather large values of the total rainfall are produced in the sensitivity tests conducted for this study. More in-depth investigation of the large-scale component of total rainfall is required in order to obtain more reliable rainfall patterns to be used has high-resolution drivers of climate impact applications.

## References

- [1] Ogallo L. Rainfall variability in africa. *Monthly Weather Review*, pages 1133–1139, 1979.

- [2] Korecha D. and Barnston A. G. Predictability of june-september rainfall in ethiopia. *Monthly Weather Review*, pages 628–650, 2007.
- [3] Sylla M. B., Gaye A. T., Pal J. S., Jenkins G. S., and Bi X. Q. High resolution simulations of west africa climate using regional climate model (regcm3) with different lateral boundary conditions. *Theoretical and Applied Climatology*, pages 293–314, 2009.
- [4] Dickinson R. E., Henderson-Sellers A., and Kennedy P. J. Biosphere – atmosphere transfer scheme (bats) version 1e as coupled to the ncar community climate model. Technical Note NCAR/TN, 1993.
- [5] Dinku T., Chidzambwa S., Ceccato P., Connor S. J., and Ropelewski C. F. Validation of high-resolution satellite rainfall products over complex terrain. *International Journal of Remote Sensing*, pages 4097–4110, 1993.

# Synchronization phenomena in complex networks

*J.A. Almendral<sup>1,2</sup>, S. Boccaletti<sup>3,4</sup>, R. Gutiérrez<sup>5</sup>, I. Leyva<sup>1,2</sup>,  
J. M. Buldú<sup>1,2</sup>, A. Navas<sup>1</sup>, I. Sendiña-Nadal<sup>1,2\*</sup>*

<sup>1</sup>*Center for Biomedical Technology  
Universidad Politécnica de Madrid, 28223 Madrid, Spain*

<sup>2</sup>*Complex Systems Group  
Universidad Rey Juan Carlos, 28933 Móstoles, Madrid, Spain*

<sup>3</sup>*CNR- Institute of Complex Systems  
Via Madonna del Piano, 10, 50019 Sesto Fiorentino, Florence, Italy*

<sup>4</sup>*The Italian Embassy in Israel  
25 Hamered st., 68125 Tel Aviv, Israel*

<sup>5</sup>*Department of Chemical Physics, Weizmann Institute of Science  
Rehovot 76100, Israel*

**ABSTRACT.** This work is the continuation of that produced in the the periods 2009/2010 and 2010/2011 of use of the ENEA GRID CRESCO system [1, 2] to investigate the role of the connectivity structure among dynamical oscillating systems into the emergence of a collective synchronous behavior.

## 1 Explosive synchronization in complex networks

One of the most intriguing and studied phenomena of dynamics in complex networks is synchronization: the spontaneous organization of networked dynamical units into a collective common dynamics. This process has been extensively related to the role played by the structure and the natural dynamics of each unit. In our studies on this phenomenon we use complex networks of phase oscillators whose instantaneous phase evolves in time according to the simple paradigmatic model of periodic oscillators described by Kuramoto [3]:

$$\dot{\theta}_i = \omega_i + \sigma \sum_{j=1}^N A_{ij} \sin(\theta_j - \theta_i) \quad i = 1, \dots, N, \quad (1)$$

where  $\theta_i$  is the phase of the  $i^{th}$  oscillator with natural frequency  $\omega_i$  and  $\sigma$  is the coupling constant. The topology of the network is uniquely defined by the adjacency matrix  $\mathbf{A}$ ,

---

\*Corresponding author. E-mail: irene.sendina@urjc.es.

since  $A_{ij} = 1$  if node  $i$  is connected with node  $j$  and  $A_{ij} = 0$  otherwise. The degree of a node is defined as  $k_i = \sum_j A_{ij}$ . The node natural frequencies are chosen from a known distribution  $g(\omega)$ . The order parameter quantifying the instantaneous global phase state of the system is defined as  $r(t) = \frac{1}{N} |\sum_{j=1}^N e^{i\theta_j(t)}|$ , and the level of synchronization can be monitored by looking at the value of  $S = \langle r(t) \rangle_T$ , with  $\langle \dots \rangle_T$  denoting a time average over a conveniently large time span  $T$ .

By means of extensive calculations performed in CRESCO, in the last year we have obtained several important results that provide new insights in the relationship between structure and dynamics in the collective dynamics of complex networks. For the numerical integration of our model and the analysis of the results we use homemade *C* codes implementing Runge-Kutta integration algorithms. Extensive serial calculations have been performed for large parameters ranges, diverse network topologies and statistical validation of the results.

In most of the cases synchronization in complex networks emerges as a second order-like, continuous, reversible process. However, several situations have been recently found in which the collective coherent state emerges explosively as a discontinuous transition usually exhibiting hysteresis. Explosive synchronization (ES) have been initially reported in both periodic [4] and chaotic [5] phase oscillators in the particular condition of a heterogeneous degree distribution with positive correlations between the node degree and the corresponding oscillators natural frequency.

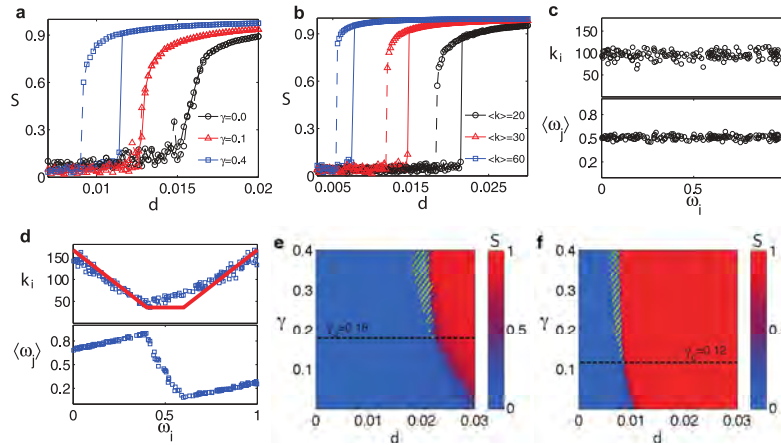


Figure 1: Phase synchronization level  $S$  vs. the coupling strength  $d$ , for different values of  $\gamma$  with  $\langle k \rangle = 40$  (a), and for different values of  $\langle k \rangle$  with  $\gamma = 0.4$  (b). Continuous (dashed) lines refer to the forward (backward) simulations. In panels (c) and (d), the degree  $k_i$  that each node achieves after the network construction is completed (upper plots) and the average of the natural frequencies  $\langle \omega_j \rangle_i$  (bottom plots) vs. the node's natural frequency  $\omega_i$ . Panels (e) and (f) show  $S$  (color coded according to the color bar) in the parameter space  $(d, \gamma)$  for (e)  $\langle k \rangle = 20$  and (f)  $\langle k \rangle = 60$ .

In our recent work [6], we show that ES is not restricted to the above rather limited cases, but it constitutes a generic feature provided that the network is *frequency disassorted*, i.e., the path to synchronization is frustrated by avoiding links between nodes with similar

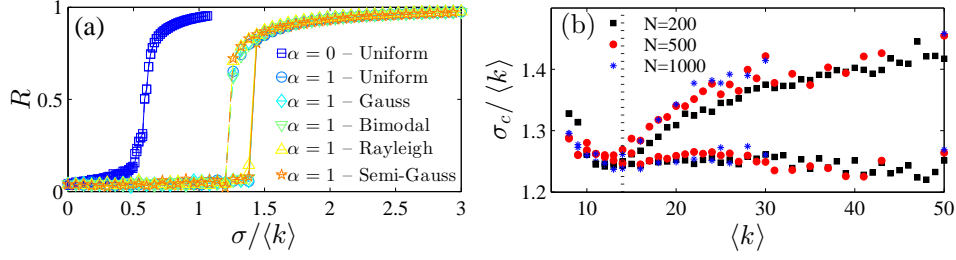


Figure 2: (a) Synchronization transitions for  $N=500$  ER networks,  $\langle k \rangle=30$ , for unweighted case ( $\alpha = 0$ ) (blue squares), and linearly weighted cases ( $\alpha = 1$ ) with several frequency distributions within the range  $[0, 1]$ : uniform, Gaussian, Gaussian-derived, Rayleigh and semi-Gaussian. Solid and dashed lines refer to the forward and backward simulations, respectively. (b) Critical scaled coupling  $\sigma_c / \langle k \rangle$  at the onset of synchronization/desynchronization using a linear weighting procedure  $\Omega_{ij}$  ( $\alpha = 1$ ) as a function of  $\langle k \rangle$  for several ER network sizes  $N$ . Vertical dashed line marks the passage from a smooth to an explosive phase transition. Upper and lower branches correspond to *forward* and *backward* simulations, respectively. Each dot accounts for an average of at least 20 independent runs of uniform frequency distributions.

frequencies. To validate that hypothesis, we construct a random but frequency disassorted network by imposing that a pair of nodes  $i, j$  can be linked only if the condition  $|\omega_i - \omega_j| < \gamma$  is satisfied for a certain threshold  $\gamma$ . Fig. 1 reports the results obtained by setting  $g(\omega)$  as a uniform distribution in the interval  $[0, 1]$ . Panels (a) and (b) show  $S$  as a function of coupling  $d$ , for several values of  $\langle k \rangle$  and  $\gamma$ . A first important result is the emergence of ES in all cases, for sufficiently high values of  $\gamma$ . Panel (d) shows a second relevant result: the spontaneous (and not ad-hoc as in Refs. [4, 5]) emergence of degree-frequency correlation features associated to the passage from a second to a first-order phase transition. Finally, panels (e) and (f) report  $S$  in the  $d - \gamma$  space, for  $\langle k \rangle = 20$  and  $60$ , and show that the rise of ES is, indeed, a generic feature in the parameter space. The horizontal dashed lines separate the two regions where a second-order transition (below the line) and ES (above the line) occurs, while the yellow striped areas correspond to the hysteresis width.

In the above example, we construct the network given a set of frequencies. However, we can extend our hypothesis for the even more general case of a network with a given frequency distribution and architecture. In a more recent work [7] we show that a weighting procedure on the existing links, that combines information on the frequency mismatch of the two end oscillators of a link with that of the link betweenness, has the effect of inducing or enhancing ES for both homogeneous and heterogeneous graph topologies, as well as any symmetric or asymmetric frequency distribution.

For this purpose, we consider the case where in Eq. (1) the adjacency matrix  $\mathbf{A} = \{a_{ij}\}$  is replaced by its weighted counterpart  $\Omega_{ij}^\alpha = a_{ij}|\omega_i - \omega_j|^\alpha$ , being  $a_{ij}$  the elements of the initial adjacency matrix,  $\alpha$  a constant parameter which eventually modulates the weight. The strength of the  $i^{th}$  node (the sum of all its links weights) is then  $s_i = \sum_j \Omega_{ij}^\alpha$ .

In Fig. 2(a) we show how ES is induced in random networks for sufficiently large values



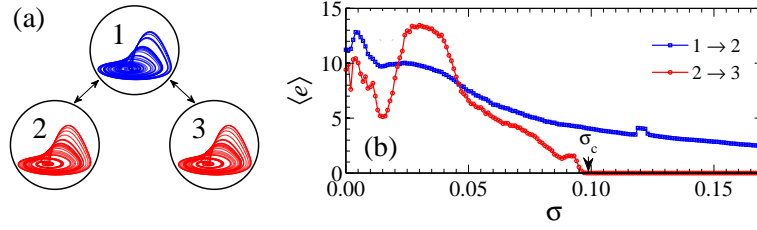


Figure 3: (a) Relay configuration. The autonomous dynamics of the peripheral units (nodes 2 and 3) are identical, whereas that of relay unit (node 1) is different. (b) Synchronization error (defined as the Euclidean distance between phase-space state vectors) between peripheral nodes (blue line) and one peripheral node and the relay unit (red line) as the overall coupling  $\sigma$  is increased.

of  $\langle k \rangle$  and irrespectively on the specific frequency distribution  $g(\omega)$ , as long as they are defined in the same frequency range  $[0, 1]$ .

Further information about the nature and scaling properties of the transition induced by the linear weighting procedure is gained from Fig. 2(b), where it is shown the dependence of the scaled critical coupling  $\sigma_c/\langle k \rangle$  on the average connectivity  $\langle k \rangle$  and on the network size  $N$ . Independently on  $N$ , a dynamical bifurcation exists at  $\langle k \rangle \sim 17$ , corresponding to the passage from a second- to a first-order like phase transition.

## 2 Relay synchronization in complex networks

The study of the structure of complex networks has received much attention at different levels, from the local scale to the global scale that considers the full network as a whole, via a mesoscale where an organization into communities is frequently observed [8]. At the local level, the structure can be studied in terms of *motifs*, i.e. patterns consisting of a few connected nodes, which are the building blocks of the network structure. In our work, we are interested in the *relay configuration* shown in Fig. 3 (a), which is an ubiquitous 3-node motif, whose study predates the modern theory of complex networks due to its relevance in several fields, including neuroscience and optics. Specifically, synchronization in a relay configuration has been the focus of interest for some years, since it was found that when the dynamics of the *relay unit* (node 1 in Fig. 3 (a)) differs from those of the peripheral elements (nodes 2 and 3), still the peripheral nodes are able to synchronize. An example is given in Fig. 3 (b), which shows the synchronization error between nodes 1 and 2 (blue line) and that between the peripheral nodes (red line) in a relay configuration of Rössler oscillators. After a critical coupling  $\sigma_c$  is reached nodes 2 and 3 are in complete synchronization in the absence of any obvious relation between them and node 1. This puzzling phenomenon has been called *relay synchronization*.

In Ref. [9], we shed new light on the nature of relay synchronization by studying the dynamics of the full relay system. We give very strong numerical evidence, based on Lyapunov spectra and phase-space measures, that once the critical coupling strength  $\sigma_c$

is achieved, generalized synchronization between the peripheral nodes and the relay unit arises. Additionally we experimentally show the robustness of relay synchronization and the underlying generalized synchronization.

## References

- [1] Almendral J. A., Bajo R., Boccaletti S., Buldú J. M., Gutiérrez R., Leyva I., Navas A., Papo D., Sendiña-Nadal I., and Zanin M. Synchronization in complex biological networks. In Delinda Piccinelli (Enea) and UTICT-PRA (Cr Frascati), editors, *High Performance Computing on CRESCO infrastructure: research activities and results 2009-2010*, page 33. ENEA, 2011.
- [2] Almendral J. A., Bajo R., Boccaletti S., Buldú J. M., Gutiérrez R., Leyva I., Navas A., Papo D., Sendiña-Nadal I., and Zanin M. Emergent phenomena in biological networks. In Delinda Piccinelli (Enea) and UTICT-PRA (Cr Frascati), editors, *High Performance Computing on CRESCO infrastructure: research activities and results 2010-2011*, page 113. ENEA, 2012.
- [3] Kuramoto Y. *Chemical oscillations, waves and turbulence*. Springer, 1984.
- [4] Gómez-Gardeñes J., Gómez S., Arenas A., and Moreno Y. Explosive synchronization transitions in scale-free networks. *Phys. Rev. Lett.*, 106(12):128701, 2011.
- [5] Leyva I., Sevilla-Escoboza R., Buldú J. M., Sendiña-Nadal I., Gómez-Gardeñes J., Arenas A., Moreno Y., Gómez S., Jaimes-Reátegui R., and Boccaletti S. Explosive first-order transition to synchrony in networked chaotic oscillators. *Phys. Rev. Lett.*, 108:168702, 2012.
- [6] Leyva I., Navas A., Sendiña-Nadal I., Almendral J. A., Buldú J. M., Zanin M., Papo D., and Boccaletti S. Explosive transitions to synchronization in networks of phase oscillators. *Sci. Rep.*, 3, 2013.
- [7] Leyva I., Sendiña-Nadal I., Almendral J. A., Navas A., Olmi S., and Boccaletti S. Explosive synchronization in weighted complex networks. *Phys. Rev. E*, 88:042808, 2013.
- [8] S. Boccaletti, V. Latora, Y. Moreno, M. Chavez, and D.-U. Hwang. Complex networks: Structure and dynamics. *Physics Reports*, 424(4-5):175 – 308, 2006.
- [9] Gutiérrez R., Sevilla-Escoboza R., Piedrahita P., Finke C., Feudel U., Buldú J. M., Huerta-Cuellar G., Jaimes-Reátegui R., Moreno Y., and Boccaletti S. Generalized synchronization in relay systems with instantaneous coupling. *Phys. Rev. E*, 88:052908, 2013.

# Use of Monte Carlo to evaluate signal and radiation damage to Corium Detector in PWR Severe Accident Scenario

*K. W. Burn \**

*ENEA UTFISSM-PRONOC  
Via Martiri di Monte Sole, 4, 40129 Bologna Italy*

## 1 Introduction

The activity of radiation transport by means of Monte Carlo modelling has proceeded along twin tracks: development and application. The development is reported in the following section 2 and the application in section 3. The development is directed at calculating local responses within eigenvalue calculations (as employed in reactor cores or storage arrays of fissile material). The particular application currently considered is that of the monitoring of the corium position in PWR severe accident scenarios. This is carried out in collaboration with IRSN (France).

## 2 Development of Monte Carlo algorithms employed in eigenvalue calculations with the source-iteration approach

Following on from the development of Monte Carlo algorithms for fixed source radiation transport modelling (see for example [1]), the transfer of the algorithms to eigenvalue problems (see for example [2]), has continued, culminating in [3].

This work is directed at: the calculation of spatially limited core monitoring devices within the fissile region of a reactor core; the calculation of any ex-core response (e.g. pressure vessel damage) without making the approximation of decoupling the in-core eigenvalue calculation from the ex-core fixed source calculation; the calculation of small neutron flux detectors placed within or near arrays of spent fuel assemblies. A further application of interest is that of calculating reactivity coefficients from spatially limited perturbations in the fissile zone (e.g. spatially-localized coolant voiding).

For obvious copyright reasons, only the following information can be reproduced:

---

\*Corresponding author. E-mail: [kennethwilliam.burn@enea.it](mailto:kennethwilliam.burn@enea.it).

**Article outline** ☒ Show full outline

Highlights

Abstract

Keywords

1: Introduction

2: Portrayal of the problem

3: The DSA with fixed source problems

3.1: The weight-independent splitt...

3.2: Realization in fixed source pro...

4: Description of the new approach t...

5: Implementation of the new approa...

5.1: Differences between normal M...

5.2: Steps taken

5.3: Realization in eigenvalue probl...

6: Test problems

6.1: PWR 2-D

6.1.1: Varying the length and nu...

6.1.2: Varying the VR according t...

6.2: PWR 3-D

6.2.1: Generating importances th...

6.2.2: Generating importances th...

6.2.3: Generating importances th...

6.2.4: Verifying that the fundame...

6.3: Liquid lead-cooled FR

6.4: PWR 3-D ex-core

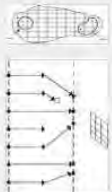
6.4.1: Verifying that the fundame...


7: Conclusions and discussion

Acknowledgments

References

**Figures and tables**







**Annals of Nuclear Energy**

Volume 73, November 2014, Pages 218–240

---

## Optimizing variance reduction in Monte Carlo eigenvalue calculations that employ the source iteration approach

This paper is dedicated to the memory of Lodovico Gasalini (1955–2010) and of Carlo Artoli (1946–2014).

Kenneth W. Burn  

[Show more](#)

DOI: 10.1016/j.anucene.2014.06.040 [Get rights and content](#)

---

**Highlights**

- A variance reduction scheme within Monte Carlo eigenvalue calculations is proposed.
- It is based on the Direct Statistical Approach, already used in fixed source problems.
- Both in- and ex-core local responses are treated.
- Verifications are made that the fundamental mode is not distorted.
- One test problem showed a large advantage over the classical, adjoint-only approach.

---

**Abstract**

The question of variance reduction within the source-iteration scheme of a Monte Carlo eigenvalue calculation is tackled. The trade-off point between improving the statistics of a local response whilst simultaneously not damaging excessively the fundamental mode, the source for the calculation of the local response in the next fission cycle, is found. It is realized that applying less normalizations, i.e. employing superhistories, is advantageous. Realistic test problems, both fast and thermal fission, with in- and ex-core local responses, are treated. There is a good agreement between the predicted and actual gain in efficiency. A single comparison with the classic formalism, based purely on  $\phi^*$ , shows large differences.

**Keywords**

Monte Carlo; Eigenvalue; Source-iteration method; Variance reduction; Direct statistical approach

---

**1. Introduction**

Variance reduction (VR) methods for fixed source Monte Carlo radiation transport calculations have been

### 3 Support to IRSN (Fr) on the DISCOMS Project (monitoring the position of the corium following perforation of the pressure vessel): calculation of neutron and gamma spectra at various positions of the collectrons outside the pressure vessel and estimation of radiation damage to the fibre optics cables

The detection system consists of fibre optics cables and collectrons, monitoring the neutron and gamma fluxes. Both collectrons and fibre optics cables will be placed at a variety of positions outside the pressure vessel in the lower part of the pressure vessel well, the reactor pit, melt discharge channel and spreading area (lined with sacrificial material). The neutron and photon spectra are required at each proposed collectron position for design purposes (type of collectron to be employed, shape of expected signal). The neutron flux and gamma dose are required for radiation damage estimates to the fibre optics cables at a limited number of positions.

This work is underway. As a first step, the "classic" approach of decoupling the in-core eigenvalue calculation from the ex-core fixed source calculation will be made, with the point of decoupling being the fission sites. As a second step, the algorithm described in 1 will be employed. For reasons of confidentiality, very little reporting of this activity can be made at the moment.



Figure 1: Corium spreading test at the French CEA VULCANO facility (UO<sub>2</sub> with some ZrO<sub>2</sub>) (<http://www.iaea.org/NuclearPower/Downloads/INPRO/Files/2010-Feb-DF-WS/15-Teller.pdf>).

## 4 Hardware and software employed in these activities

As far as software is concerned, for the first part of the activity, a patched version of MCNP5 (ver. 1.4) was employed. The patch involved substantial modifications to the original code (the patch was approximately 20500 lines long compared with the original code length of just under 80000).

Instead for the second part of the activity, the superhistory patch is currently just 500 lines. (However subsequent to this work it has been integrated with a modified DSA patch for keff problems and reached more than 22000 lines.) Furthermore a separate stand-alone code is also required that is built around the IMSL version 1.0 library.

Parallelism was exploited as much as possible. A local parallel version of MCNP was used that is built around MPI for IBM AIX POE. The parallelism was maintained in the DSA-patched version. However the stand-alone code built around IMSL is scalar.

Whilst they were running, the sp.5-x (x = 2,3,4,5,6,7,8,10,13) IBM AIX clusters at ENEA, Frascati were employed. At the end of 2013, the IBM AIX machines were withdrawn and

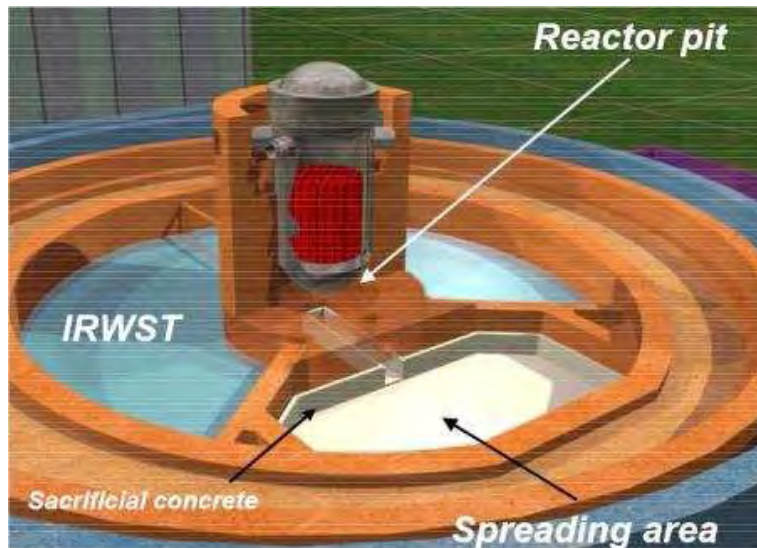


Figure 2: Core melt retention system (<http://www.iaea.org/NuclearPower/Downloads/INPRO/Files/2010-Feb-DF-WS/15-Teller.pdf>).

both the patched MCNP and the stand-alone code, built around IMSL, were moved to the CRESCO LINUX machines.

## References

- [1] Burn K. W. Optimizing monte carlo to multiple responses: the direct statistical approach, 10 years on. *Nucl. Technol.*, (175):138–145, 2011.
- [2] Burn K. W. Use of monte carlo in state-of-the-art pwr design: study of tilt in the enea uam pwr benchmark and development and testing of new algorithms within monte carlo eigenvalue calculations employing the source iteration method. *ENEA-ADPFISS-LP1-015*, 2013.
- [3] Burn K. W. Optimizing variance reduction in monte carlo eigenvalue calculations that employ the source iteration approach. *Ann. Nucl. Energy*, (73):218–240, 2014.

# Boosting conformational sampling in lipid bilayer simulations using Hamiltonian Replica Exchange

Chiara Cardelli<sup>1</sup>, Alessandro Barducci<sup>2</sup>, Piero Procacci<sup>3\*</sup>

<sup>1</sup>*Computational Physics Department  
University of Wien, Sensengasse 8/9 1090 Wien, Austria*

<sup>2</sup>*Laboratoire de Biophysique Statistique  
École Polytechnique Fédérale, CH-1015 Lausanne, Switzerland*

<sup>3</sup>*Chemistry Department  
University of Florence, Via Lastruccia 3 50019 Sesto Fiorentino, Italy*

**ABSTRACT.** In this report we have tested a parallel implementation for the simulation of lipid bilayers at atomistic level, based on a generalized ensemble (GE) protocol where only the torsional degrees of freedom of the alkyl chains of the lipid are scaled. To this aim, we have used our in-house code ORAC where parallelism is implemented exclusively via the Hamiltonian Replica Exchange algorithm (H-REM) with the atomic forces being integrated serially for each simultaneously evolving GE trajectories. The results in terms of configurational sampling enhancement have been compared with a conventional simulation produced with a widespread molecular dynamics code with parallelism based on a domain decomposition approach for parallel computation of the forces. Results show that the proposed thermodynamic-based multiple trajectories parallel protocol for membrane simulations is competitive with the conventional single trajectory domain decomposition approach as far as area and volume fluctuations are concerned while the gain is only moderate for transport/mixing properties, decisively pointing to a mixed strategy as the optimal parallelization approach in lipid bilayer.

## 1 Introduction

Molecular dynamics simulation is an important computational tool for the study of biomolecular systems, such as biological membranes, that have lipid bilayers as main constituents. The recent development of massively parallel environments exploiting high speed communication links such as InfiniBand has nowadays made possible simulations in time range of hundreds of nanosecond of lipid bilayers of the extension in the tens nanometers. Although the indisputable and tremendous gain in the performance with respect to early applications, computational scientists still face a severe length-scale and a time-scale problem in membrane simulation. The actual limits in length and time scale (20-30 nm and  $\simeq 1 \mu\text{s}$

---

\*Corresponding author. E-mail: [procacci@unifi.it](mailto:procacci@unifi.it).



respectively) severely restrain the possibility of studying key properties of bilayers like the bending rigidity via determination of the undulation spectrum and/or cooperative transport phenomena. Both these properties are intimately connected with important biological situations including endocytosis, lipid raft formation and stability, membrane fusions and membrane trafficking.[1, 2] As stated, flat lipid bilayers under periodic boundary conditions provide a simple and effective model system for biological membranes. Nonetheless, the simulations of a hydrated bilayer implies a number of atoms to the least in the order of tens of thousands, resulting in a high wall-time even resorting to efficient parallel algorithms such as the dynamic domain decomposition approach.[3] Typically, on the CRESCO(1-2) platform a moderately sized system, such as a hydrated lipid bilayer of 36 molecules of palmitoyl oleoyl phosphatidylcholine (POPC) per leaflet (about 17000 atoms), can run with a maximum speed of 20-25 nanosecond per day using the popular GROMACS MD program exploiting at most 160 processors with an efficiency of less than 50%. This is so since after a certain processor number threshold, the inter-domain communication overhead dominates over the time spent in the parallelized computation of the forces within each domain. By trading model accuracy and reliability in exchange for computational speed, recent approaches for membrane simulation are based on so-called *coarse-grained* models, where larger molecular units are considered as single particles.[4]

In this report we investigate on the effectiveness of using advanced Hamiltonian Replica exchange schemes with selective scaling of specific degrees of freedom of the system[5, 6, 7] as a mean for boosting configurational sampling in simulations of model membranes at the atomistic level. In this respect, Mori *et al.*[8] have recently proposed a new GE algorithm for membrane systems, based on exchanges between few replicas spanning the surface tension space, from zero of the target replica to higher tensions, obtaining a moderate gain in the convergence time of structural parameters. On the other hand, recent advances in membrane science have highlighted the key importance of lipid flexibility and entanglement in shaping the transport and undulation phenomena in biological membranes.[2]. These molecular properties, in turn, have time scale dynamics that are essentially dictated by the free energy barriers separating, e.g., *gauche* and *trans* states for the dihedral conformation of the torsion around the  $sp^3$  bonds of the alkyl chains in the hydrophobic interior of the bilayer. By selectively scaling, along the replica progression, the energy terms implied in these barriers (i.e. aliphatic torsion angles and 1-4 coulomb and Lennard-Jones interactions), the jump rate for *gauche trans* interconversion can be exponentially increased in the hot replicas, thereby enhancing diffusion and area/volume modulation throughout the GE. This approach should hopefully allow to collect, in few ns or tens of ns time span, a manifold of configurations statistically out of the reach of conventional (single trajectory) simulations.

The present report is organized as follows. In the Section Methods we succinctly describe the system and simulation techniques used in our contributions as well as the basics of the H-REM approach as opposed to the conventional single trajectory technique. In the section Results, we compare configurational properties such as volume and area fluctuations, diffusion and bilayer structure. In Conclusion Section a discussion and conclusive remarks are presented.



## 2 Method

*POPC simulation setup:* The simulations of the lipid bilayer, whether conventional or in the GE, comprised 72 POPC lipid units (36 for leaflet) with approximately 30 water molecules per lipid. The total number of atoms in the system was 16374. The starting PDB configuration was an equilibrated charmm36 configuration, downloaded from ref. [9]. The force field employed is a minor modification[10] of the most recent update of CHARMM parameters for lipids by Jämbeck et al., called *Slipids*, recently developed for fully saturated phospholipids.[11]

All the simulations - both conventional and GE - were performed in the isothermal-isobaric ensemble, NPT, at an external pressure of 0.1 MPa. The pressure was held constant by a Parrinello-Rahman barostat [12], with a  $70\text{ cm}^{-1}$  oscillator frequency and compressibility set to  $5.3 \times 10^{-4}\text{ MPa}^{-1}$  and semi-isotropic stress. The temperature was held at 303 K by means of a Nosé-Hoover thermostat.[13, 14] Electrostatic interactions were treated using Particle Mesh Ewald[15] with a b-spline order parameter of 4 and a grid spacing of 1.2 Å. The TIP3P water model [16] has been used. The switch-off of Lennard-Jones interactions has been set at 13 Å, with no long-range correction.

*H-REM simulation setup:* The GE simulation was performed using the ORAC program[6] running 10 independent sets of 24 GE replica walkers, for a total of 240 parallel processes. The Hamiltonian scaling protocol is identical for each of the 24-walkers sets and involves only the torsion angles around the  $\text{sp}_3$  bonds of the aliphatic chains in the bilayer interior. In Fig. 1 we show the full torsional energy around a C-C bond for the target state (scaling factor 1.0) and for the highest replica (scaling factor 0.3, corresponding to a “torsional temperature” of 1000 K).

The scaling factors for the intermediate states along the replica progression were obtained as the arithmetic mean between a simple linear scaling and the standard scheme given in Ref [5]. In Fig. 1 (right), we report the dihedral angle distributions for the aliphatic torsion angles of the lipid chains in the GE and, in the inset, the jump rate between *gauche* and *trans* state as a function of the scaling state. These properties were determined by performing a 1 ns long GE simulation with no exchanges using the above defined scaling protocol and by averaging on all torsion angles of the alkyl chains of the lipids. As expected, the free energy barrier between *gauche* and *trans* states steadily decreases along the replica progression with jump rate being consequentially boosted exponentially the higher the scaling factors, thereby enhancing the conformational sampling of the bilayer.

For the production run, MPI communication groups are defined only within each of the 24-walkers batteries, that hence run independent GE simulations of 5.5 ns length, accumulating statistics for a total of 55.0 ns on the target state. Each of the 240 exchanging serial simulations are numerically integrated using an efficient multiple time step setup[17, 18], running at a speed of 0.4-0.5 ns/ day on the CRESCO1-2 platforms. The whole GE simulation on 240 processors required about a week of wall clock time on CRESCO2, amounting to a total of  $\simeq 1700$  days of CPU.

*Conventional Simulation set up:* The conventional simulation of POPC bilayer was performed using the GROMACS program[3] (version 4.0.7) using the same physical setup

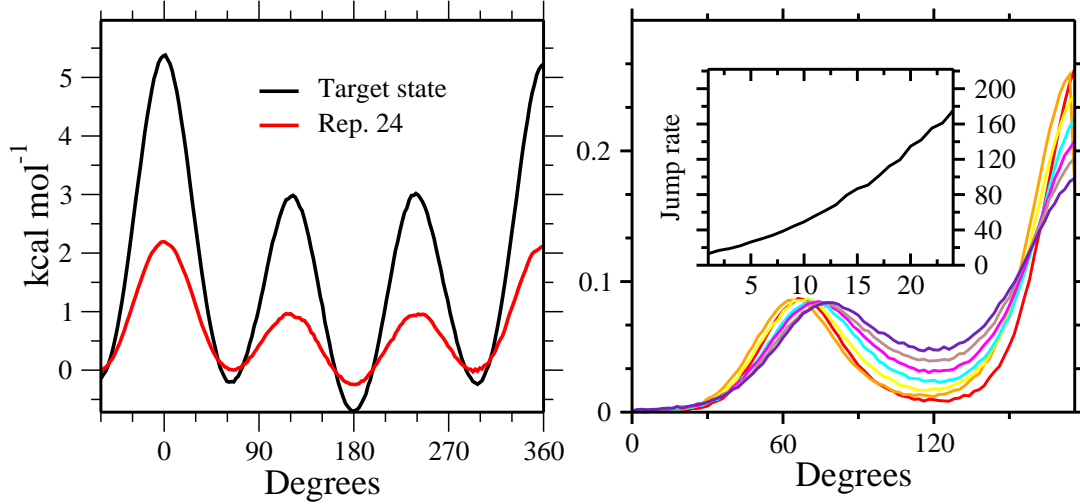


Figure 1: Left: torsional energy round the internal aliphatic C-C bond (Jämbbeck type a3, see Ref. [11]); black trait, target replica; red trait, hottest replica. Right: probability distributions of the dihedral angle averaged on all aliphatic torsion angles in a non exchanging 1 ns GE simulation. Color coded scheme for distributions: from red (target state) to violet (hottest torsional state). In the inset, the jump rate per ns is reported as a function of the scaled state.

previously described. Equations of motion were integrated with a time step of 1 fs. As stated in the introduction, the moderate size of the system (about 17000 atoms) allows to run with a maximum speed of 20-25 ns per day on CRESCO2 using at most 160 processors with an efficiency of less than 50%.

Table 1: Performances of the GROMACS code on the POPC system (16374 atoms). Measures were done on the ENEA-grid CRESCO2 cluster.

Nprocs.	Speed (ns/day)	efficiency
1	0.27	1
32	8.37	0.96
64	14.85	0.85
96	19.296	0.74
160	20.900	0.48

In Table 1 we show the speed up ratio obtained on the POPC system with GROMACS. Starting from the same initial structure, we run two independent 96 processors conventional simulation of the POPC system each lasting 100 ns for about 9 days. The total amount of CPU employed was  $\simeq 1700$  days, i.e. comparable to that used in the H-REM 10-batteries simulations.

### 3 Results

In the following we shall assess the effect of torsional tempering in GE H-REM simulation on two key properties of biological membranes, i.e area fluctuation and lipid diffusion. The former is important for the determination of the bending rigidity of the membrane in the continuum (low wavelength) limit, while the latter determines the mixing rate and equilibration of in-homogeneous systems. In Fig. 2 we compare the time record of the

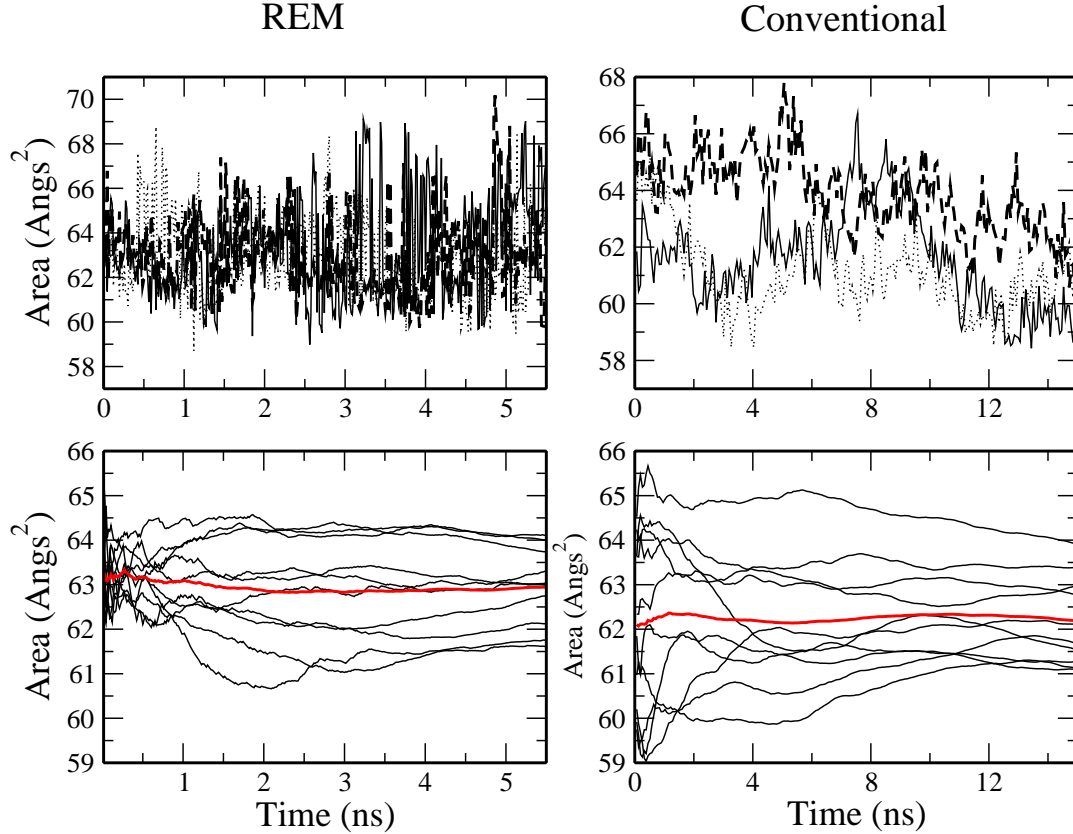


Figure 2: Top: Time record of the area per lipids in REM and conventional simulations. The time record of only three 5.5 ns H-REM batteries and three 15 ps conventional sub-simulations are shown for clarity. Bottom: Area per lipid running averages evaluated in REM for each of the 10 batteries and for the conventional simulation in 15 ns time span taken from two independent 100 ns simulations. The red curve is the cumulative running average over ten 5.5 batteries (REM) and on 200 ns of conventional simulation.

area per lipid for the H-REM and conventional simulation. In REM, the average area over all GE configurations in 5.5 ns appears to have reached a stationary value. Given the variance of the running averages recorded in each of the ten independent batteries, a more accurate results can be straightforwardly attained by simply increasing the number of the independent H-REM simulations with no impact on the wall-clock time. In the H-REM simulation, the fluctuations of the area undergo a clear boost from the GE exchanges,

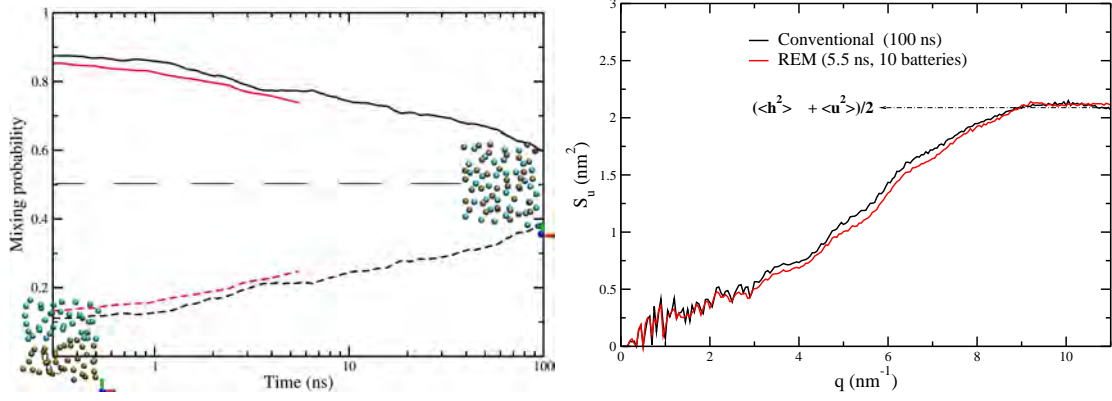


Figure 3: Left panel: Time record of the mixing probability. For the REM data (red curve) the mixing function was averaged over all GE states. Right Panel: Fourier transform of the membrane undulation function[19]  $u(x, y) = \frac{1}{2}[z_1(x, y) + z_2(x, y)]$ .

exhibiting variations up to  $8 \text{ \AA}^2$  in a time as small as the fraction of the picosecond. This is so since the average area per lipid of the hot GE states is sensibly larger than that of the target state increasing up to  $66.7 \text{ \AA}^2$  in the last GE state. These large area states are transmitted through the exchanges in the target replica with the correct Boltzmann weight. The conventional simulation shows in general much smaller fluctuation with respect to REM in the short time scale. Larger fluctuations can only be observed in the super-nanosecond timescale, partly inhibiting the acquisition of a stationary value of the mean and standard deviation of the area in a 100 ns time span.

In Fig. 3 (left) we show the undulation spectrum[19] of the POPC system for H-REM and conventional simulation. The two approaches yield essentially identical results, exhibiting similar trends and the same limiting value at long wavelength. Due to the moderate size of the sample, the  $q^4$  short wavelength behavior[19, 2] could not be observed. On the right of Fig. 3 we show the mixing function for the H-REM and the conventional simulations, obtained by labeling at the start of the run with two different colors two identical sets of phosphorous atoms based on their  $t=0$  y-coordinate. This labeling defines the unmixed zero time state, showed in the bottom left part of the plot. We then evaluate the probability of a phosphorous atom to have the nearest neighbor bearing a different label (or colors) as the simulation proceeds. In the starting state, such probability simply reflects the impact of the surface boundary separating the labeled particles. Clearly, for a perfectly mixed state such probability should tend to 0.5. In the H-REM simulation, because of the exchanges, the time ordered trajectories yield comparable probability evolution and hence one can define a time dependent probability of mixing averaged over the whole GE ensemble. The H-REM protocol produces indeed an apparent moderate acceleration of the mixing speed with respect to the conventional simulation. However, the standard MD at the end of the 100 ns shows a much more pronounced mixing with respect to the final H-REM state at 5.5 ns. Such partly disappointing outcome is due to the fact that the diffusion of the polar heads on the membrane surface is only moderately increased in H-REM via the indirect effect of enhanced torsional *gauche-trans* switching across the GE.

## 4 Conclusions

In Table 2 we finally collect the results obtained with H-REM (10 independent 5.5 24-replicas GE batteries) and the two independent 100 ns simulation conducted conventionally with domain decomposition. The two methods, that uses the same CPU allocation and involve the same wall-clock time, appears to yield in essence the same physical picture of the POPC system, as long as averages lipid area and volume are concerned. Regarding fluctuations, H-REM exhibits a substantial enhancement of the time dependent area variations as well as of the amplitude of the area fluctuation producing a significantly less rigid bilayer compared to the GROMACS outcome. On the other hand H-REM promotes only a moderate increase of the polar head diffusion. These results on the overall suggest to

	$A_L(\text{\AA}^2)$	$V_L(\text{\AA}^3)$	$K_A (10^{-3}Nm^{-1})$	$\frac{1}{2}(\langle h^2 \rangle + \langle u^2 \rangle)$	G/T ratio
<b>HREM simulation</b>	62.9±1.2	1262.0±0.8	164±40	2.10±0.05	0.261
<b>Standard MD simulation</b>	62.2±1.3	1247.7±1.3	388±65	2.10±0.05	0.260
<b>Experiments</b>	64.3 <sup>a</sup> ±1.3	1256 <sup>b</sup>	180-330 <sup>c</sup>	2.1 <sup>a</sup> ±0.1	-

Table 2: Area per lipid ( $A_L$ ), volume per lipid ( $V_L$ ), isothermal area compressibility modulus ( $K_A$ ),  $S_q$  long wavelength limit (see Fig. 3) and *Gauche/Trans* ratio from POPC HREM simulation, standard MD simulation and experiments: **a.** from ref. [20] **b.** from ref. [21] **c.** from ref. [22].

adopt a mixed strategy in H-REM for an optimal allocation of CPU on a parallel platform: “vertical” sampling though independent GE batteries can be reduced by allowing parallel force computation within each GE trajectory, achieving “horizontal” configurational sampling, via increase of the GE simulation time span. For example, based on the data reported in Table 1, on 240 processors, a single 24-replica simulation of the POPC system can in principle be extended up to about 50 ns, using a 10 processor communication group per trajectory for parallel force computation, with little or no degradation of the parallel efficiency. Work in this direction is currently in progress.

## References

- [1] Nagle J. F. and Tristram-Nagle S. Structure of lipid bilayers. *Biochimica et Biophysica Acta (BBA)-Reviews on Biomembranes*, 1469(3):159–195, 2000.
- [2] Watson Max C., Brandt Erik G., Welch Paul M., and Brown Frank L. H. Determining biomembrane bending rigidities from simulations of modest size. *Phys. Rev. Lett.*, 109:028102, Jul 2012.
- [3] Hess Berk, Kutzner Carsten, van der Spoel David, and Lindahl Erik. Gromacs 4: algorithms for highly efficient, load-balanced, and scalable molecular simulation. *Journal of Chemical Theory and Computation*, 4(3):435–447, 2008.
- [4] Marrink S. J., Risselada H. J., Yefimov S., Tieleman D. P., and de Vries A. H. The martini force field: coarse grained model for biomolecular simulations. *The Journal of Physical Chemistry B*, 111(27):7812–7824, 2007.

- [5] Fukunishi H., Watanabe O., and Takada S. On the hamiltonian replica exchange method for efficient sampling of biomolecular systems: application to protein structure prediction. *The Journal of chemical physics*, 116(20):9058–9067, 2002.
- [6] Marsili S., Signorini G. F., Chelli R., Marchi M., and Procacci P. Orac: A molecular dynamics simulation program to explore free energy surfaces in biomolecular systems at the atomistic level. *Journal of computational chemistry*, 31(5):1106–1116, 2010.
- [7] Mitsutake A., Sugita Y., and Okamoto Y. Generalized-ensemble algorithms for molecular simulations of biopolymers. *Peptide Science*, 60(2):96–123, 2001.
- [8] Mori T., Jung J., and Sugita Y. Surface-tension replica-exchange molecular dynamics method for enhanced sampling of biological membrane systems. *Journal of Chemical Theory and Computation*, 9(12):5629–5640, 2013.
- [9] Klauda J. B. Laboratory of molecular & thermodynamic modeling. <http://terpconnect.umd.edu/jbklauda/research/download.html>.
- [10] In the present force field variant, the standard AMBER fudge factors were applied to *all* 14 interactions and only X-H bonds were constrained.
- [11] Jämbeck J. P. M. and Lyubartsev A. P. Derivation and systematic validation of a refined all-atom force field for phosphatidylcholine lipids. *The Journal of Physical Chemistry B*, 116(10):3164–3179, 2012.
- [12] Parrinello M. and Rahman A. Polymorphic transitions in single crystals: A new molecular dynamics method. *Journal of Applied physics*, 52(12):7182–7190, 1981.
- [13] Nosé S. A unified formulation of the constant temperature molecular dynamics methods. *The Journal of Chemical Physics*, 81(1):511–519, 1984.
- [14] Hoover W. G. Canonical dynamics: equilibrium phase-space distributions. *Physical Review A*, 31(3):1695, 1985.
- [15] Essmann U., Perera L., Berkowitz M. L., Darden T., Lee H., and Pedersen L. G. A smooth particle mesh ewald method. *The Journal of Chemical Physics*, 103(19):8577–8593, 1995.
- [16] Jorgensen W. L., Chandrasekhar J., Madura J. D., Impey R. W., and Klein M. L. Comparison of simple potential functions for simulating liquid water. *The Journal of chemical physics*, 79(2):926–935, 1983.
- [17] Procacci P., Darden T. A., Paci E., and Marchi M. Orac: A molecular dynamics program to simulate complex molecular systems with realistic electrostatic interactions. *Journal of computational chemistry*, 18(15):1848–1862, 1997.
- [18] Procacci Piero, Darden Tom, and Marchi Massimo. A very fast molecular dynamics method to simulate biomolecular systems with realistic electrostatic interactions. *The Journal of Physical Chemistry*, 100(24):10464–10468, 1996.

- [19] Brandt Erik G., Braun Anthony R., Sachs Jonathan N., Nagle John F., and Olle Edholm. Interpretation of fluctuation spectra in lipid bilayer simulations. *Biophys J.*, 100:2104–2111, 2011.
- [20] Kučerka N., Nieh M.-P., and Katsaras J. Fluid phase lipid areas and bilayer thicknesses of commonly used phosphatidylcholines as a function of temperature. *Biochimica et Biophysica Acta (BBA)-Biomembranes*, 1808(11):2761–2771, 2011.
- [21] Kučerka N., Tristram-Nagle S., and Nagle J. F. Structure of fully hydrated fluid phase lipid bilayers with monounsaturated chains. *The Journal of membrane biology*, 208(3):193–202, 2006.
- [22] Binder H. and Gawrisch K. Effect of unsaturated lipid chains on dimensions, molecular order and hydration of membranes. *The Journal of Physical Chemistry B*, 105(49):12378–12390, 2001.

# Nuclear Analysis for ITER TBM PORT #16

*Barbara Caiiffi<sup>1\*</sup>, Rosaria Villari<sup>2</sup>*

<sup>1</sup>*Università degli Studi di Genova - Dipartimento di Fisica  
Via Dodecaneso 33, 16143 Genova, Italy*

<sup>2</sup>*ENEA, Fusion Technical Unit, Nuclear Technologies Laboratory  
Via Enrico Fermi 45, 00044 Frascati, Rome, Italy*

**ABSTRACT.** In this report the nuclear analysis of the ITER TBM (Test Blanket Module) Port #16 is presented. The Port is located in the equatorial plane of the reactor and hosts the breeding blanket prototypes containing the lithium to produce tritium. The analysis is focused on the dose rate after the shutdown in the region of the Port where maintenance is planned. The computational method used is called R2S (Rigorous 2 Steps) and is based on the combined calculation of a Monte Carlo code (MCNP) and of a deterministic inventory code (FISPACT). The results of this analysis show dose rates above the design target (which is  $100 \mu\text{Sv/h}$ ), mainly because of the neutron streaming in the gaps and the cross-talk with the Upper and Lower Ports. The analysis, performed on the CRESCO3 cluster, required several 24h runs with 600 core (at least 4/5 for each configuration and region of interest, plus some debugging CPU time). The simulation efficiency spanned from  $10^{-3}$  to 10 particle/(core\*s) according to the type of particle and to the variance reduction technique used.

## 1 Introduction

In ITER life time, the materials of the reactor will undergo huge neutron irradiation, which will cause damages such as displacements in the atomic structure and nuclear heating of sensitive components (e.g superconductor magnetic coils). Furthermore, the neutron irradiation will lead to the activation of the materials, which will become a gamma source also when the reactor will be turned off. For this reason it is of fundamental importance to predict accurately the shutdown dose rate in all the regions where human access is envisaged for maintenance. This analysis, in particular, is dedicated to the assessment of the maintenance area of the TBM Port #16, shown in Fig.1. The TBMs (Test Blanket Module) are mockups of breeding blankets containing lithium in order to produce tritium when irradiated by the neutrons coming from the plasma. ITER will provide a unique opportunity to test these mockups in a real fusion environment. Within these test blankets, viable techniques for ensuring tritium breeding self-sufficiency will be explored. The TBM Port #16, in particular, will host the Helium Cooled Lithium Lead (HCLL) and the Helium Cooled Pebble Bed (HCPB) TBM Sets. The shutdown dose rate calculation was performed

---

\*Corresponding author. E-mail: [caiffi@ge.infn.it](mailto:caiffi@ge.infn.it).



using an original R2S (Rigorous 2 Steps) method. It is based on the combined use of a Monte Carlo code for the transport calculation (MCNP5 v1.6 [1]) and a deterministic code for the material activation calculation ( FISPACT 10.0 [2]). The details of the calculation procedure and of the geometrical models will be described in the following chapters, together with the discussion of the results and the conclusion.

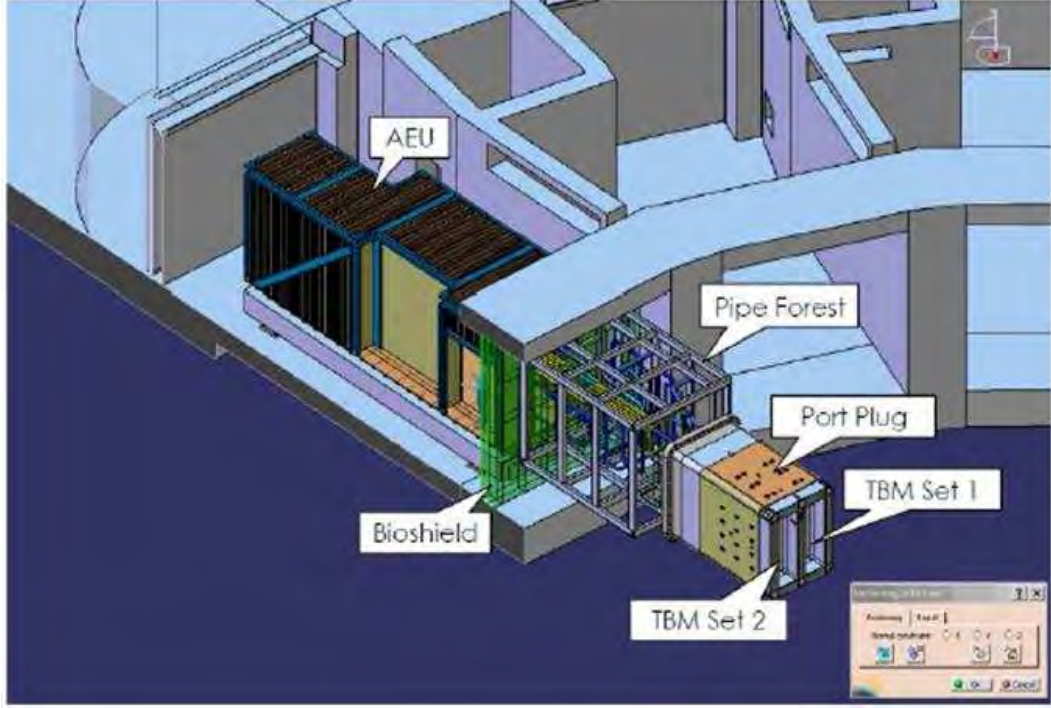


Figure 1: TBM Port design. From the inner part we find the Port Plug region, containing the two TBM Sets inside their TBM Frame. After that, we find the Port Interspace, containing the so called "Pipe Forest" which extends up to the Bioshield.

## 2 Computational Tools

In order to calculate the shutdown dose rate in the region of interest for this analysis, an original R2S method was developed. It is based, following the usual scheme [3], on a Monte Carlo code (MCNP) and on a deterministic code (FISPACT), according to the following procedure: first, a Monte Carlo transport calculation was required to determine the neutron flux and spectrum in all the relevant regions. This step is performed using the code MCNP, which allows a 3-D description of the geometry. The calculations used the ITER Deuterium-Tritium plasma source in [4] normalized to 500 MW of fusion power. Then, the material activation was calculated using a deterministic code, FISPACT. This code follows the decay path of the nuclides induced by the neutron irradiation and provides the corresponding  $\gamma$  spectrum. In this step, the irradiation scenario and the cooling steps of interest can be specified. In particular, the irradiation scenario SA2 [5] was used. Eventually, the activation  $\gamma$  source was used to perform another Monte Carlo calculation

with MCNP and to find the dose rate in the maintenance region.

MCNP simulations have been run on the ENEA CRESCO HPC facility: the MCNP5v1.6 code, linked to the FENDL 2.1 [6] nuclear data libraries, has been compiled on CRESCO3 in its parallel version with Open MPI v 1.5.4 using the Intel compiler suite version 2011 sp1.9.293. Some subroutines MCNP code were modified to perform the gamma transport from an external voxel-segmented source. The analyses performed required several 24-hours-runs on CRESCO3 using 600 cores each: at least 4/5 iterations are necessary for each geometry configuration and for each mesh, plus some debugging CPU time. The high performance computing capability of the CRESCO cluster, together with the application of variance reduction techniques (weight windows) allowed a consistent improvement of the statistics and provided results with sufficient accuracy (statistical errors ranging between within few % and 10% in the area of interest). The simulation efficiency spanned from  $10^{-3}$  to 10 particle/(core\*s) according to the type of particle and to the variance reduction technique used.

### 3 Geometrical Model

The MCNP ITER reference model used in this analysis is Blite v3 [7] and describes a sector of  $40^\circ$  of the reactor with reflecting boundaries. It includes only the main components, while the experimental port equipment should be added according to the type of the analysis. The TBM Ports common features are taken from the analogue analysis performed for the TBM Port #2 in [8].

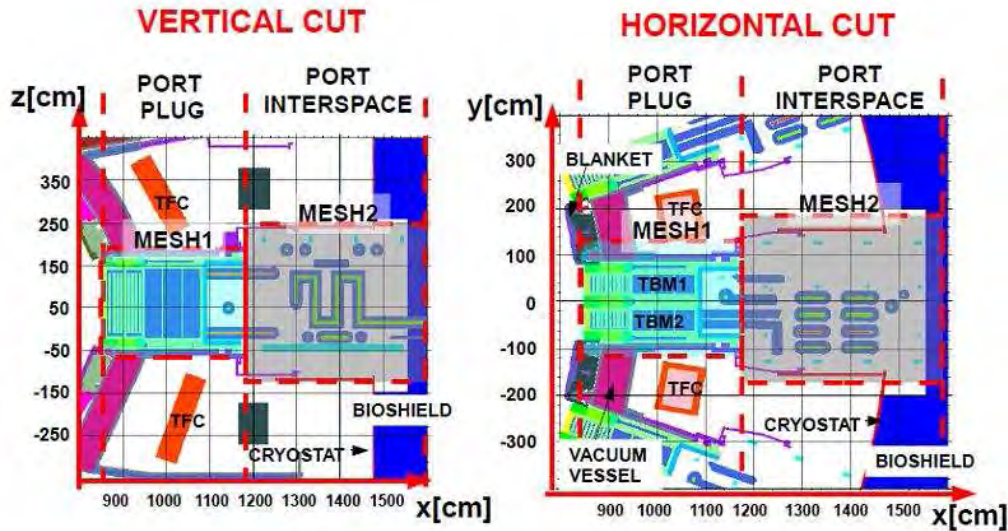


Figure 2: MCNP global model, including the details of the TBM Port #16.

The TBM Port #16 Pipe Forest was prepared starting from the CATIA design, provided by ITER. The pre-processing was performed using Space Claim 2012 [9] while MCAM 4.8 [10] was used for the conversion in an MCNP input file format. The HCLL and HCBP

TBM Sets were adapted starting from the old model in [11]. Some modification was required in order to fit the components to the latest TBM Port Plug design. The final model used in this analysis is shown in Fig. 2. As the geometry is very complicated, all the relevant quantities (neutron flux and spectrum, material composition,  $\gamma$  flux) were averaged over the elements of a mesh, a regular grid laying over the geometry. Two meshes were used, one covering the Port Plug region and the other converting the Port Interspace region.

## 4 Results

The neutron flux and spectrum were calculated with MCNP in all the relevant region. The neutron flux profile across the TBMs (shown in Fig. 3) is reduced by 7 orders of magnitude, from  $10^{14}$  n/cm<sup>2</sup>s to  $3 \cdot 10^7$  n/cm<sup>2</sup>s. At the rear of the TBM back plate, though, the flux has a small increase because of the neutron streaming in the gaps, up to  $10^8$  n/cm<sup>2</sup>s, and remains almost constant in all the Port Interspace.

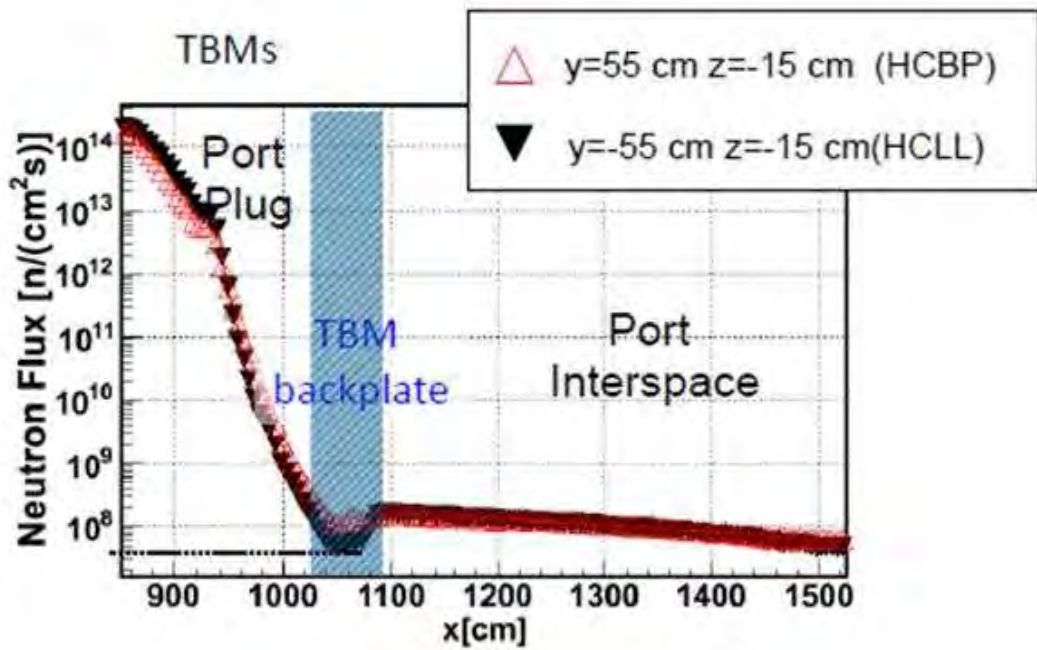


Figure 3: Neutron flux profile within the TBM Port.

The material activation calculation was then performed for each element of the meshes. The most important nuclides were found to be the Co60 (0.05 % in weight in steel SS316), which contribute for the 70% to the total dose rate and the Ta182 (0.01 % in weight in steel SS316), which contribute for the 22%. The shutdown dose rate was calculated with MCNP using a mesh-based  $\gamma$  source. The results, shown in Fig.3, exhibit higher values with respect to the design target (100  $\mu$ Sv/h).

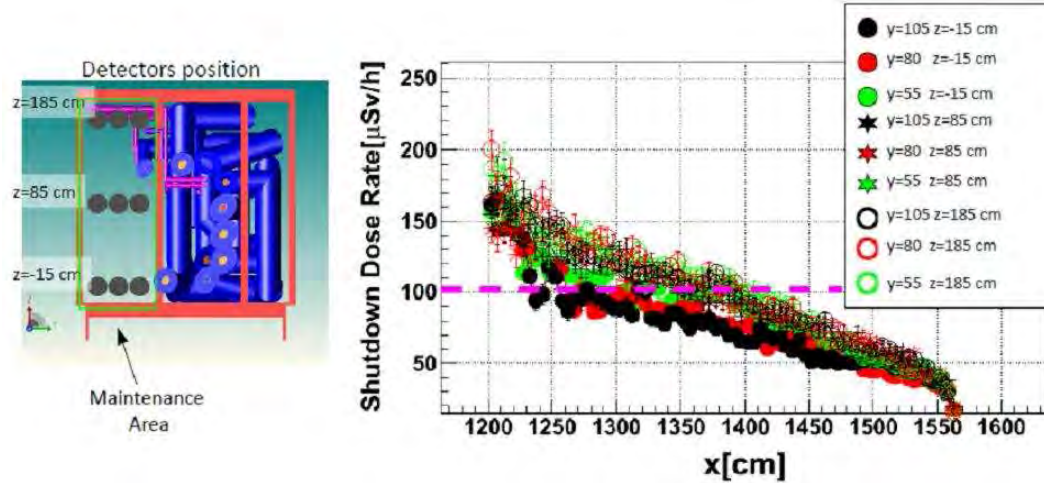


Figure 4: Shutdown Dose Rate profile within the Port Interspace.

## 5 Conclusions

In the present analysis, the shutdown dose rate in the ITER TBM Port #16 was calculated. An original R2S method was created to interface the Monte Carlo code MCNP and the deterministic inventory code FISPACT. The results showed higher dose rate values than the design target limit ( $100 \mu\text{Sv/h}$ ). The effects responsible of the high dose rate, in particular the neutron streaming in the gaps and the cross-talk with the Upper and Lower Ports, must be investigated further in order to find a mitigation procedure. This analysis required several 24h runs with 600 cores on CRESCO3 plus advanced variance reduction techniques to achieve the sufficient statistical accuracy.

## References

- [1] X-5 Monte Carlo Team: MCNP - A General Monte Carlo N-Particle Transport Code, Version 5, Los Alamos National Laboratory, Los Alamos, New Mexico, USA, April 2003.
- [2] Forrest R., FISPACT-2007 User Manual EASY 2007 Documentation Series UKAEA FUS 534.
- [3] Pereslavytset P. and Fischer U. - Fusione Engineering and Design (2013).
- [4] D-T neutron emission rate for standard neutron source for ITER nuclear analysis with MCNP code, IDM 2FV7QR.
- [5] "Recommendation on Plasma scenarios", ITER IDM ITER\_D\_2V3V8G.
- [6] Lopez Al-Dama D. et al., 2004 "FENDL-2.1: update of an evaluated nuclear data library for fusion applications", Report INDC(NDS)-46 (Vienna: IAEA).

- [7] "ITER Neutronic model: B-lite v3", R121217 ITER IDM 9KKVQR (2012).
- [8] Final Report on Neutronic Analysis of the ITER TBM PP (CDR) IDM JR5EZH (October 2013).
- [9] <http://www.spaceclaim.com/en/>.
- [10] Wu Y., FDS Team - "CAD-based interface programs for fusion neutron transport simulation", Fus. Eng. Des. 84 (2009) 1987-1992.

# Simulation of a Square Boiling Channel Using NEPTUNE\_CFD

*Antonio Cervone\**

*ENEA, UTFISSM/SICIS  
Via Martiri di Monte Sole 4, 40129 Bologna, Italy*

**ABSTRACT.** This report describes a set of simulations that have been performed using the CRESCO platform in order to model the boiling flow of a refrigerant that flows through a vertical square channel. Some experimental data on the setup are available and they are used to assess to performance of the NEPTUNE\_CFD code.

## 1 Introduction

This report is aimed at the description of the numerical simulations that have been performed on the CRESCO cluster about a boiling flow in a vertical square channel. This work is performed in the framework of the NURESAFE project (Grant Agreement: 323263), an EURATOM FP7 project that has started at the beginning of 2013 and that lasts 3 years.

The contribution of ENEA in this project covers two different Work Packages, in particular one of them is WP2.4 that is the *Validation, Verification and Application* task of the boiling flow models implemented in the computational fluid dynamics (CFD) codes inside the NURESAFE platform [1]. ENEA is performing simulation of the experimental facility that will be described in the next section using both NEPTUNE\_CFD and TransAT, the two CFD reference code in the platform for two-phase flows.

The results that will be shown in the report are still under development, as the project is still active, and will not display any quantitative result since the project agreement requires for all the simulation results to be restricted to the project partners.

In the following, we will describe in details only the NEPTUNE\_CFD simulations, since that code is the only one that has been installed in the CRESCO3 cluster.

## 2 Experimental Facility

The experimental facility that is used as a validation test for the Neptune\_CFD and TransAT codes is described in details in [2] and it is hosted at the Texas A&M University, Texas. It consists of a rectangular channel with a cross section of 7.6 mm by 8.7 mm and a total

---

\*Corresponding author. E-mail: [antonio.cervone@enea.it](mailto:antonio.cervone@enea.it).



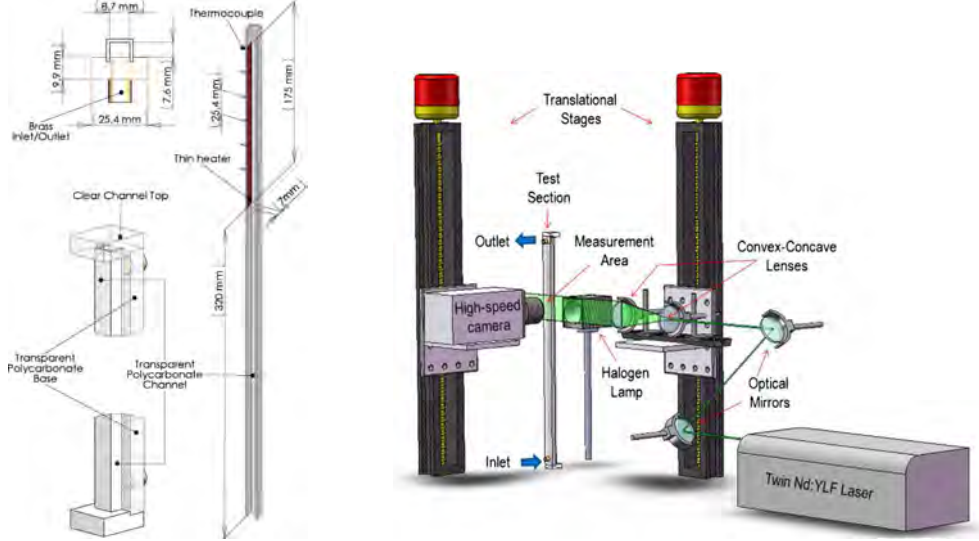


Figure 1: Experimental facility geometrical setup (left) and acquisition system (right).

Table 1: HFE-301 Physical Properties of Interest at Ambient Pressure.

Property	Phase	Symbol	Value	Unit
Saturation Temperature	—	$T_s$	307.15	K
Density	liquid	$\rho_l$	1400	Kg/m <sup>3</sup>
Viscosity	liquid	$\mu_l$	4.48e-4	Pa.s
Thermal Conductivity	liquid	$k_l$	7.5e-2	W/(m.K)
Specific Heat Capacity	liquid	$c_{pl}$	1300	J/(Kg.K)
Latent Heat of Evaporation	—	$h_v$	1.42e5	J

vertical length of 530 mm. The pipe is made of transparent polycarbonate, in order to allow high-speed camera recordings, and there is an heating plate 175 mm long and 7 mm large attached on the inner side of the pipe 320 mm away from the inlet. A balsa wood insulator is used to avoid thermal losses.

The geometrical setup is shown on the left side of Fig. 1, with details on the inlet and outlet sections. The dimensions have been selected in order to properly approximate coolant channels inside boiling and pressurized nuclear reactors. The acquisition system of the facility is also shown in Fig. 1 on the right side. It is made up of an high-speed high-resolution camera, high-speed high-power laser, a continuous halogen lamp and particle flow tracers. The experiments were analyzed using Particle Tracking Velocimetry (PTV) in order to reconstruct liquid phase velocity profiles. The measuring section is located 455 mm from the inlet, in the upper part of the heated section, where the turbulent profile is completely developed.

The fluid that is used is HFE-301 [3]. This is a cryogenic fluid that was selected by the experimenters because it scales well with respect to thermodynamic properties of

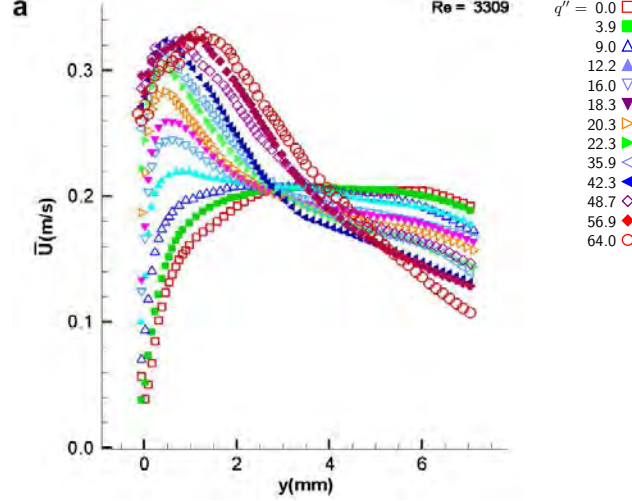


Figure 2: Experimental velocity profiles with  $Re = 3309$  and different heat fluxes.

water in the regimes that can be found inside a pressure vessel of a Pressurized Water Reactor (PWR). The physical properties of this fluid that are relevant for two-phase CFD simulation are reported in Table 1. Many experiments have been performed in this facility. Three different value of the incoming flow rate have been used, that correspond to three different Reynolds numbers of 3309, 9926 and 16549. All three regimes are fully turbulent. For each of this flow rates, many different heat fluxes have been applied to the heating plate, ranging from 0 to 64  $KW/m^2$ . The results for the lower Reynolds number and all the heat fluxes are shown in Fig. 2.

### 3 Code Capabilities and Performances

The NEPTUNE\_CFD code is developed by a consortium of French associations: EDF, CEA, IRSN and AREVA[4]. The aim of the code is to use state-of-the-art technology in the CFD simulation of two-phase flows in order to assess and analyze safety issues in water-cooled nuclear power reactor.

The code is based on the widely-adopted finite volume approach, that is a well-established numerical approximation that is often used in fluid dynamics. NEPTUNE\_CFD shares its core components with CODE\_SATURNE [5], another software developed mainly by EDF that has been recently open-sourced. This code is limited to single-phase modelization.

The code has a large selection of turbulence models that can be used: from the simple *mixing length* model, through well-established  $k - \epsilon$  variants, up to second-order methods such as the *Reynolds Stress Model (RSM)*. The code is also MPI-enabled and uses internal algorithms for the numerical solution of the discretized problem. Since the code does not rely on external libraries, such as the low-level BLAS, LAPACK, or the high level PETSc, the parallel performance is sub-optimal and the scalability is limited to a small number of cores. No assessment on the code parallel performances have been conducted in the past, but they are scheduled for the near future.



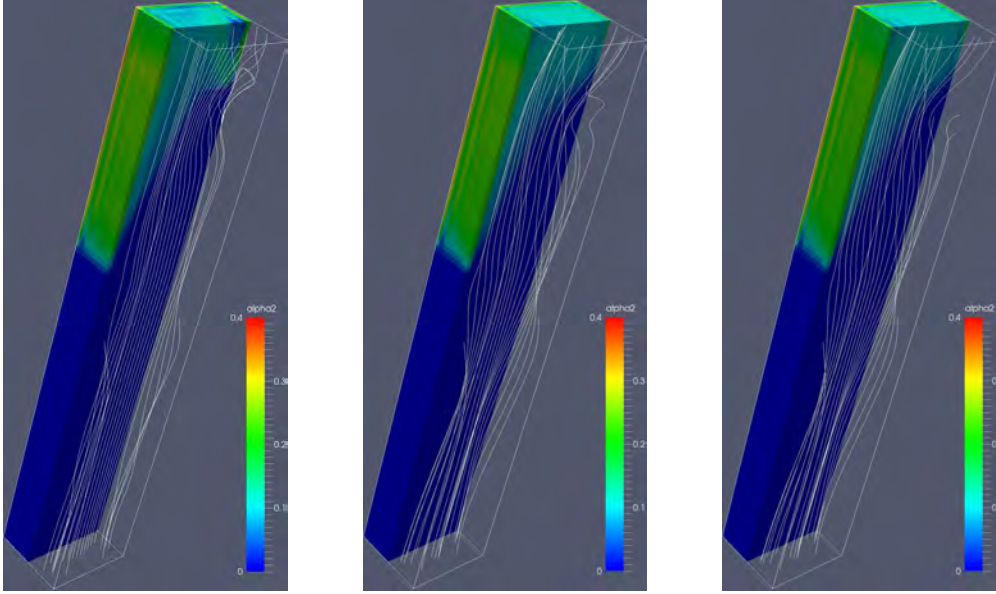


Figure 3: Void fraction and velocity field (stream lines) for the case  $Re = 3309$  and  $q'' = 20.3 \text{ KW}$  at three different time steps. The height of the channel has been compressed by a factor of 10.

The biggest difference between `CODE.SATURNE` and `NEPTUNE_CFD` is in the two-phase modeling. `NEPTUNE_CFD` includes advanced models that are able to simulate boiling flows, condensation and in general every process that includes a change of phase between liquid and gas. The approach that is used is the two-fluid model, where the bubbles (or droplets) are not explicitly reconstructed, but they are taken into account as a dispersed phase. A recent development has been the introduction of an interface tracking algorithm that is capable of capturing explicitly the interface of the bubbles. This is important when the bubble size is significantly higher than the grid size.

## 4 Numerical Simulations

The computational domain that has been considered includes the whole test section. The computational mesh is produced using the `SALOME` platform meshing tool. An uniform mesh step of 0.5 mm across the section is selected, while the step in the axial direction is of 5 mm.

The simulation setup features an RSS turbulence model for the liquid phase. The vapor phase is modeled as a dispersed phase and its turbulence is obtained from the liquid phase with the Large Inclusion Model. An important model is the one that takes into account for the momentum transfer between the two phase: in this case we used the Ishii drag, the Zuber added mass and the Tomiyama SMD lift models. The transport of the interfacial area uses the Ruyer & Seiler source term. The nucleate boiling model is set up with the Extended Kurul-Podowski model and Mimouni wall function model for two-phase flows.

In Fig. 3 some qualitative results are depicted for the case with the lower Reynolds number ( $Re = 3309$ ) and an intermediate value of the heat flux ( $q'' = 20.3$  KW). With this setup, there is an important production of vapor near the heated wall. The generation and detachment of bubbles from the wall generates an acceleration of the flow near that wall, due to the smaller density of the vapor phase. This gives rise to distorted velocity profiles with a maximum near the heated wall as highlighted by the experimental results.

## References

- [1] NURESAFE website. <http://www.nuresafe.eu/>.
- [2] Estrada-Perez C.E. and Hassan Y.A. PTV experiments of subcooled boiling flow through a vertical rectangular channel. *International Journal of Multiphase Flow*, 36(9):691–706, 2010.
- [3] 3M Novec 7000. *HFE-301 3M Product information*, 2009.
- [4] Guingo M. and Team NeptuneCFD Development. Validation note of NeptuneCFD 2.0 for NURESAFE members. Technical report, EDF, 2014.
- [5] Code\_Saturne website. <http://code-saturne.org/>.

# CFD testing of a conventional gas turbine burner operating in oxy-fuel combustion

*G. Calchetti\*, A. Di Nardo†*

*ENEA UTTEI-COMSO*

*Advanced Technologies for Energy and Industry Technical Unit  
Sustainable Combustion Processes Laboratory*

**ABSTRACT.** There is a growing interest in oxy-combustion for carbon capture and storage (CCS). Emission reduction and lower costs of flue gas cleanup represent additional benefits of such technology. Recirculated combustion products, consisting mainly of CO<sub>2</sub> and H<sub>2</sub>O, are used for diluting the oxidizer stream and keep low temperature levels. Injection of steam is also an alternative. Aim of the work is to verify the functioning of a conventional gas turbine burner in oxy-fuel operating conditions.

## 1 Introduction

The characteristics of oxy-fuel combustion with recycled flue gas differ from air combustion in several aspects, primarily related to the higher CO<sub>2</sub> levels and system effects due to the recirculated flow. To sustain the flame and attain a similar adiabatic flame temperature, the O<sub>2</sub> concentration must be higher, typically 30%, with respect air-combustion (i.e. 21%). Stable combustion and low turbine inlet temperature can be obtained simultaneously by optimizing the ratio of oxygen to CO<sub>2</sub> supplies in the oxidizer mixture to the combustion chamber. This requires that about 60% of the flue gas is recycled. Since the exhaust gases contain high proportions of CO<sub>2</sub> and H<sub>2</sub>O, higher gas emissivities are expected. The volume of gases passing through the burner is reduced and the volume of flue gas (after recycling) is reduced by about 80%, while flue gas density is increased. As oxy-fuel combustion combined with sequestration must provide power to several significant unit operations, such as flue gas compression, that are not required in a conventional plant without sequestration, oxy-fuel combustion/sequestration is less efficient per unit of energy produced.

---

\*Corresponding author. E-mail: [giorgio.calchetti@enea.it](mailto:giorgio.calchetti@enea.it).

†Corresponding author. E-mail: [antonio.dinardo@enea.it](mailto:antonio.dinardo@enea.it).

## 2 Combustor Description

The combustor under study is designed for combustion in air. It has a power of 300 kWt and consists of an outer flame tube that encloses the volume for the air flow. Within this is placed the inner flame tube, which actually contains the flame. In the final part of the inner flame tube there are nine dilution inlets, in order to decrease the outlet temperature of the flue gas, to avoid turbine blades damage and to lower the emission of CO and NO<sub>x</sub> completing the oxidation reactions. The fuel supply takes place along two different lines: the nozzles of the pilot line are coaxial to the combustion chamber and introduce the fuel in the primary zone, while the main line introduces the fuel in a bladed swirler chamber before entering the secondary zones. Here the air and the fuel coming from the main duct are mixed. The air enters the combustor in countercurrent with respect to the combustion gases flow, through the gap between the outer and inner flame tube. Part of the incoming air is sent to the dilution holes, while the remaining part, flowing outside of the combustion chamber, is sent to the pilot and the main. With respect to the reference condition relative to the air case (Fig. 1), there were made some variations of the oxidizer CO<sub>2</sub>/O<sub>2</sub> flow rate and O<sub>2</sub> concentration. The total flow rate, for the first series of simulations, was partitioned as follows: 3% to the pilot, 40% to the main flow and 57% to the dilution (that is the same percentages of the air combustion case); then the flow rates were fixed independently. The operating pressure is 409025 Pa and the temperature of the inner flame tube was kept fixed at 1000 K, as well as the amount of fuel flow for both the main and the pilot.

CO <sub>2</sub> /O <sub>2</sub>	
MAIN	0.3050 kg/s 870 K
PILOT	0.0226 kg/s 870 K
DILUIZIONE	0.4379 kg/s 870 K
CH <sub>4</sub>	
MAIN	0.005942
PILOT	0.001025 kg/s 300 K

Figure 1: Reference operating conditions.

## 3 Simulations

The CFD simulations were made by means of ANSYS-FLUENT 12.0 software. The summary of the tests is shown in the Fig. 2. The computational grid is partly tetrahedral (in the area of the pilot and near the walls of the inner flame tube) and in part hexahedral (in the central part of the chamber), for a total of about 1.3 Mcells. As turbulence model we used the k- $\epsilon$ , while for chemical reactions the EDC model in conjunction with the SMOOKE mechanism (17 species and 46 reactions) was adopted. We use the P1 as radiation model. In order to assess the accuracy of the mechanism, simulations were performed using a PLUG-FLOW reactor, comparing the results obtained with the complete GRI-MECH 3.0 (325 reactions and 53 species) [1] and the SMOOKE reduced mechanism [2].

It can be seen that the results are very close, except that the GRI is a little faster, in terms of ignition delay and laminar flame speed. The simulations were performed on the CRESCO2 cluster for 128 CPU. The amount of storage needed was about 10 GB.

	F	CO <sub>2</sub> /O <sub>2</sub> %	$\Phi$	DIL
CASO 1	1.2	75/25	0.47	CO <sub>2</sub> /O <sub>2</sub>
CASO 2	1.5	75/25	0.60	CO <sub>2</sub> /O <sub>2</sub>
CASO 3	1.5	65/35	0.40	CO <sub>2</sub> /O <sub>2</sub>
CASO 4	1.5	75/25	0.60	CO <sub>2</sub>
CASO 5	1.7	79/21	0.82	CO <sub>2</sub>
CASO 6	2	79/21	1	CO <sub>2</sub>
CASO 7	2	79/21	1	-
CASO 8	2	77/23	0.90	CO <sub>2</sub>
CASO 9	2	75/25	0.83	CO <sub>2</sub>
CASO 10	2.4	74/26	1	CO <sub>2</sub>
CASO 11	2.4	70/30	0.83	CO <sub>2</sub>

Figure 2: Reference operating conditions.

## 4 Results

The fluid-dynamic field is characterized by the presence of a torus like vortex near the exit of the burner, typical of all swirled systems, and a recirculation zone, less significant for the dynamics of the flame, limited to the base of the combustion chamber and adhering to the walls (Fig. 3). It is also present a stagnation area halfway between the top of the torus like vortex and the area where the dilution jets flows into the chamber. The average residence time is of the order of  $2 \times 10^{-2}$  s. In Fig. 4 is shown how the CO mass fraction, intermediate product of combustion, is slowly converted to CO<sub>2</sub>. In Fig. 5 is reported the OH map, which represents a marker of the reaction zone. The first simulation, not shown in Fig. 2, was performed with the same flow rates of the air reference case, simply by replacing the nitrogen with the carbon dioxide. The result was the extinction of the flame. We proceeded by reducing the flow rate of CO<sub>2</sub> by a factor F for different concentrations of O<sub>2</sub> at fixed power (Fig. 6). For F=1.2, the minimum concentration of O<sub>2</sub> was found to be around 25%. In this case the average temperature in the combustion chamber were quite low, with many unburned species at the burner outlet. Even for F=1.5 it was not possible to go below 25%, however, with temperatures more acceptable than the previous case. From this point onwards, the dilution was made only with CO<sub>2</sub>. In fact the solution in which two different CO<sub>2</sub> flows, one enriched with oxygen for the premix+pilot and the other without oxygen for the dilution, may be the most simple and practicable in view of a redesign of the system in order to contain and virtually eliminate the waste of O<sub>2</sub>. For F=1.7 we got a good reduction of oxygen, up to 21%, with an equivalence ratio of 0.82 and therefore a substantial saving of oxygen. To prevent the flame extinction and simultaneously have stoichiometric conditions it is necessary to reach the value F=2. CO emissions are higher than in the case of combustion in air. However this is not due to the cooling produced by the diluent flow. In fact, as we can see for the case number 7, in the absence of dilution the emissions are substantially unchanged. Even for F=2.4, where we have higher average temperatures, the situation does not improve. This depends on the

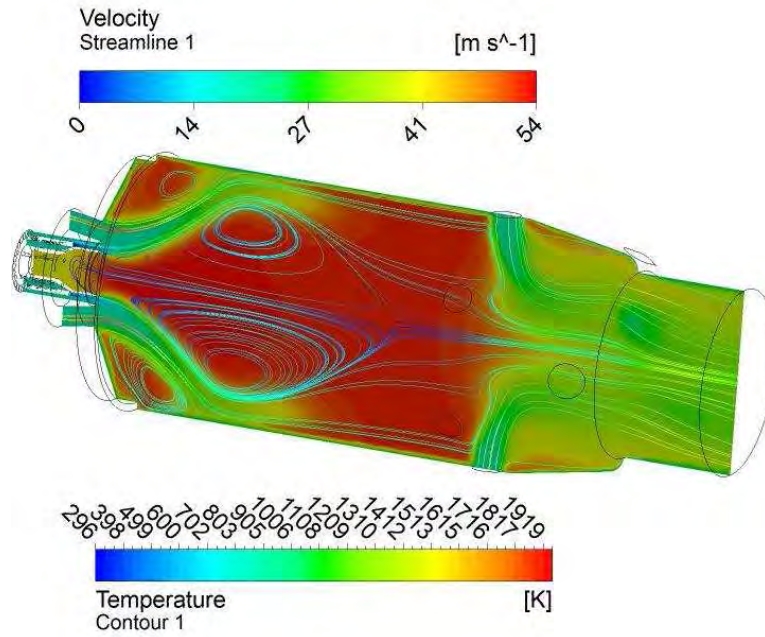


Figure 3: Path lines and temperature field.

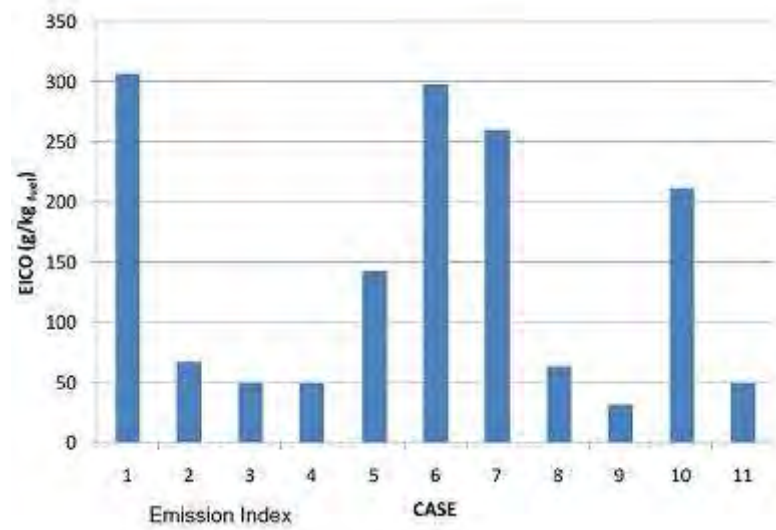


Figure 4: CO mass fraction.

higher CO<sub>2</sub> concentration. In this case, the equilibrium concentration of CO is higher while the rate of reaction of CO is slower. From the kinetic point of view the CO<sub>2</sub> competes with O<sub>2</sub> for atomic hydrogen H, leading to the formation of CO through the reaction CO<sub>2</sub>+H → CO+OH. The reaction of CO<sub>2</sub> with the type CH<sub>x</sub> radicals play also a significant role. The competition of CO<sub>2</sub> for the radicals H with the most important chain branching reaction H+O<sub>2</sub> → O+OH, significantly reduces the concentration of the radicals O, H and OH.

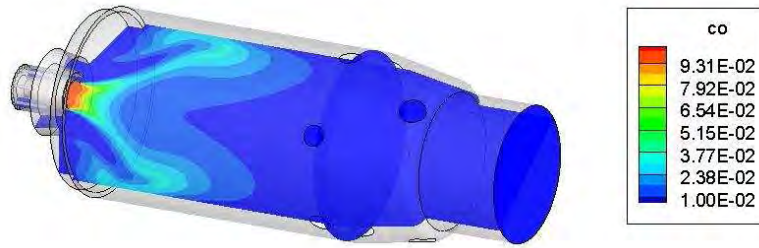


Figure 5: OH mass fraction.

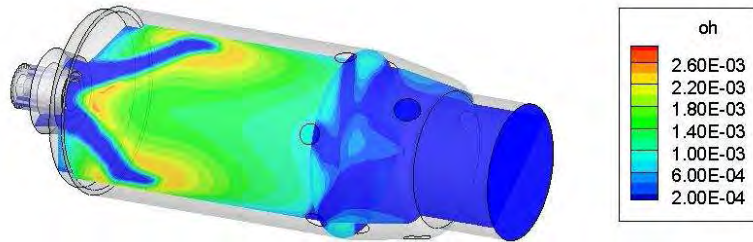


Figure 6: CO emission index.

This causes an overall reduction of the rate of reaction. High levels of CO lead to a loss of efficiency and corrosion problems. In all the studied cases we can see that only the increase in the equivalence ratio, i.e. working with  $O_2$  excess, reduces CO emissions.

## References

- [1] <http://www.nuresafe.eu/>.
- [2] Smooke M. D., Puri I. K., and Seshadri K. Proc. Combust. Inst., 21, pp. 1783-1792., 1986.



# Contributions to CRESCO Annual Report 2013

*Fabio Paglia<sup>\*</sup>, Daniele Schiariti<sup>†</sup>*

*Avio S.p.A., Via Ariana, km 5.2, 00034 Colleferro (Roma)*

**ABSTRACT.** Different numerical CFD activities have been performed by AVIO using the GRID ENEA on the CRESCO platform during the last year, in order to perform challenging simulations and to improve AVIO computational capability and simulation accuracy. These activities have been performed in the frame of Vega, Vega Evolution, Ariane 6 programs and tactical propulsion. The CFD activities have been focused on different topics:

- Blast wave at the lift off
- External aerodynamic
- Boil-off in a tank

## 1 Blast wave at the lift off

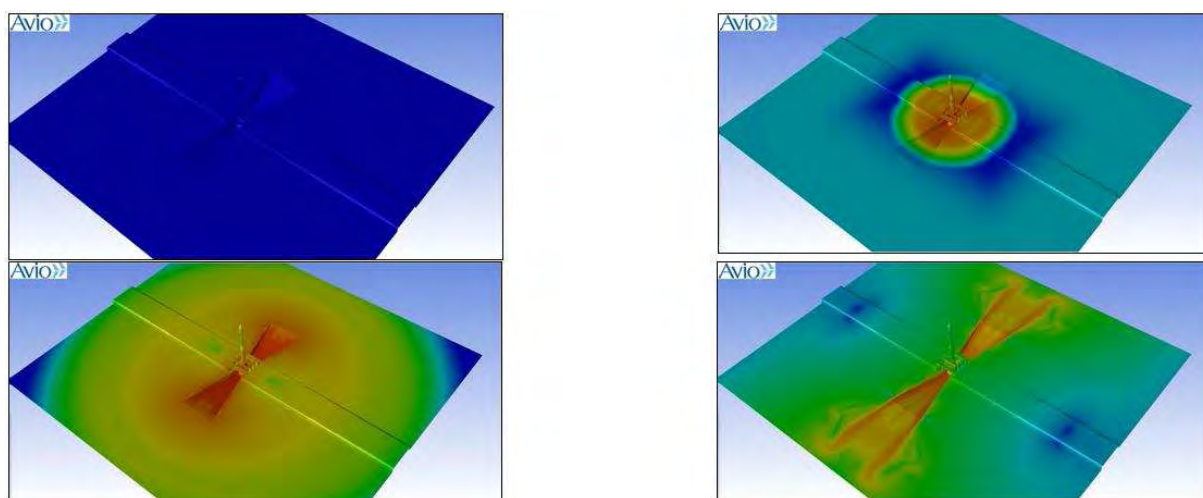


Figure 1: Blast wave CFD simulation.

The effect on the pressure field due to the blast wave, generated at the ignition of the first stage of Vega Launcher, has been assessed. Taking into account that the fluid-dynamic behaviour is strongly unsteady, the CPU effort has been very elevated. Thanks to the use

---

<sup>\*</sup>Corresponding author. E-mail: [fabio.paglia@avio.com](mailto:fabio.paglia@avio.com).

<sup>†</sup>Corresponding author. E-mail: [daniele.schiariti@avio.com](mailto:daniele.schiariti@avio.com).



of GRID ENEA it has been possible to increase the grid size resolution, obtaining a better evaluation of the flow field around the launcher, reducing the computational time.

## 2 External aerodynamic

### 2.1 Vega Evolution

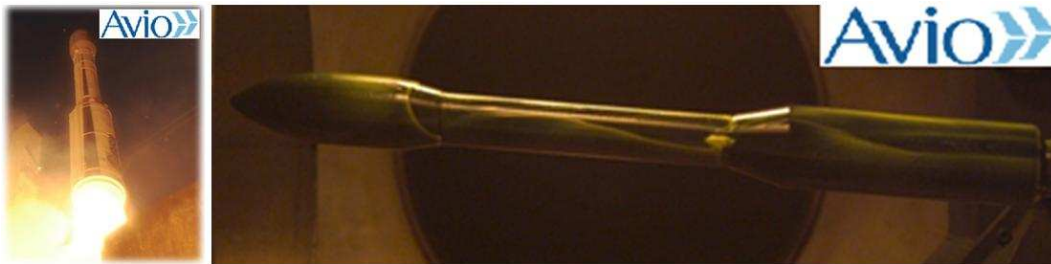


Figure 2: Vega launcher - wind tunnel aerodynamic tests.



Figure 3: Vega aerodynamic mesh.

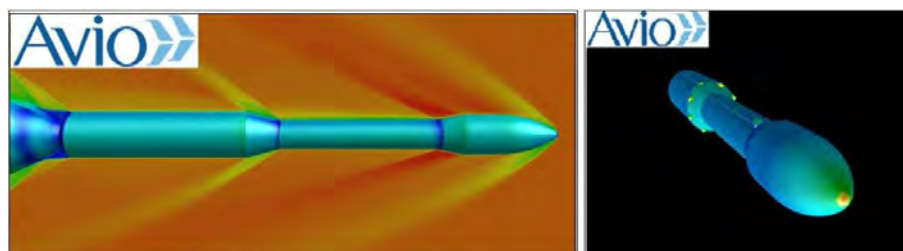


Figure 4: Vega aerodynamic CFD simulation.

Vega evolution aerodynamic data-package has been built taking into account numerical results and Vega experience. Distributed aerodynamic coefficient trend has been obtained starting from available Vega aerodynamic data-package. For each region of the launcher,

a dedicated law/trend has been obtained. The structured mesh used in the simulations, with about 15ML of cells, has allowed to increase significantly the computational accuracy reaching a difference with respect to the wind tunnel results lower than 5%.

## 2.2 Tactical propulsion

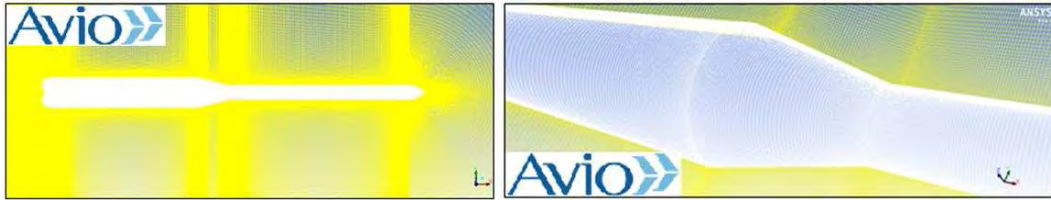


Figure 5: Tactical propulsion simulation - mesh.

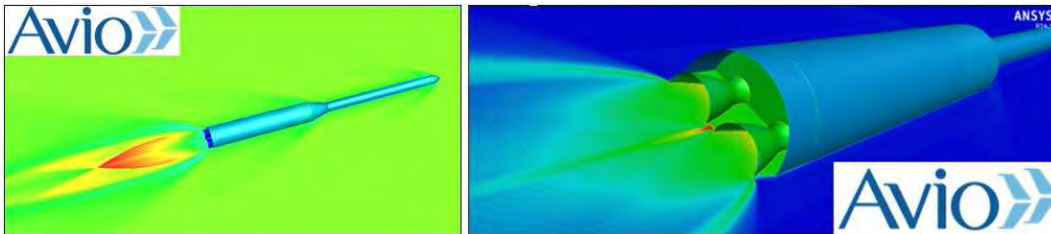


Figure 6: Tactical propulsion simulation - CFD simulation.

The base drag numerical simulation and the interaction with the solid rocket motor plume is a very challenging task. In order to obtain an accurate resolution of the numerical model, a complete structured mesh of about 21ML of computational cells has been adopted during the analysis.

## 2.3 Ariane evolution

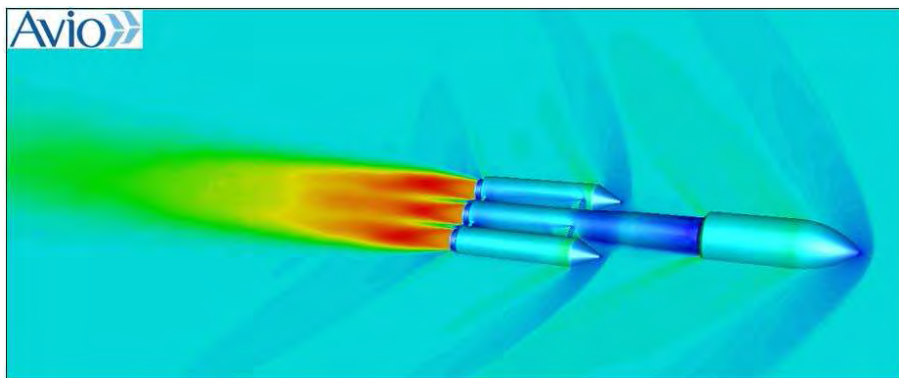


Figure 7: Ariane 6 aerodynamic CFD simulation.

The aerodynamic of Ariane launcher has been simulated, taking into account the base drag and the plume effects, with a structured mesh with about 22ML of computational cells and second order accuracy, in order to obtain an accurate solution. Such numerical model needed of a strong numerical effort and the use of GRID ENEA has allowed to reduce the computational time and to reach the required mesh resolution.

### 3 Boil off

The aim of the boil off study has been to evaluate the phase transition phenomena inside to a cryogenic tank. The boil off mechanism has been modelled using the evaporation-condensation approach available in Ansys code and performing an unsteady simulation, that has allowed to estimate the transition from liquid to gas phase and the Rayleigh-Bènard motion inside the tank.

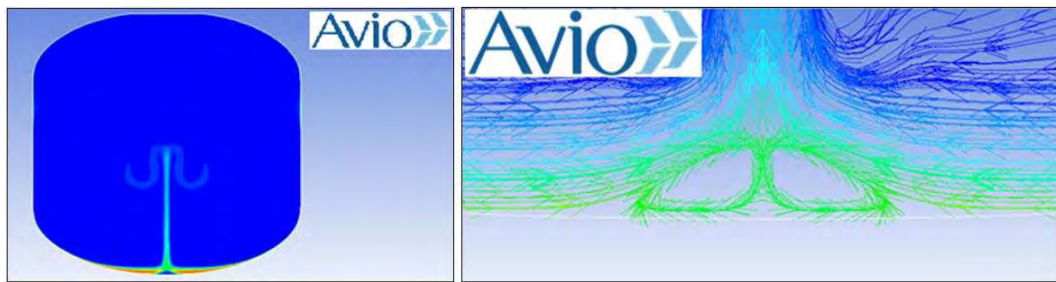


Figure 8: Boil off CFD- Rayleigh-Bènard motion.

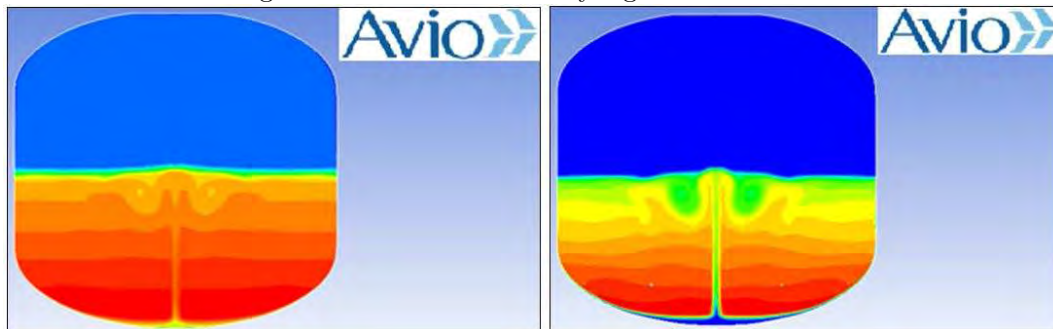


Figure 9: Boil off CFD.

# Sodium fast reactor core design using MCNPX<sup>TM</sup> code and CRESCO HPC infrastructure

*Carlo Parisi\*, Giulia Abbate, Benedetto Fresilli*

*ENEA Casaccia Research Center, UTFISST  
Via Anguillarese 301 – 00123 Rome, Italy*

**ABSTRACT.** In the framework of the *PELGRIMM* FP-7 European project, core design verification of a Generation IV Sodium Fast Reactor core, sphere-packed fuelled, was achieved. Core modelling and static neutronic calculations by Monte Carlo code MCNPX were performed, estimating main physical parameters, power distribution and variation of the heavy metal masses as function of fuel burnup and Minor Actinides concentrations. Parallel calculations using CRESCO HPC infrastructure were run, using up to 600 cores. In this way, several sensitivities calculations and final reference results were obtained and shared with other tasks of *PELGRIMM* project.

## 1 Introduction

*PELGRIMM* FP-7 European project [1] addresses Minor-Actinide (MA) bearing oxide fuel developments for Sodium Cooled Fast Reactors (SFR). Both options, MA homogeneous recycling with driver fuels containing MA and heterogeneous recycling of UO<sub>2</sub> fuels with high MA contents are investigated.

In the framework of such Project, ENEA-UTFISST is involved in the safety assessment of the sphere-packed fuelled cores. Such studies are conducted on Core Configuration #2, developed in the previous FP-7 CP-ESFR (European Sodium Fast Reactor) project. This core configuration includes a large sodium plenum, therefore achieving a reduced positive sodium void worth.

The specific task of ENEA-UTFISST is to provide the static behavior of reactor Core Configuration #2 loaded with sphere-pack fuel, performing detailed neutronic analyses as function of burnup and of MA concentration.

In particular, the objectives are:

- main neutronic parameters as function of fuel burnup:
  - Reactivity variation during 2050 Effective Full Power Days (EFPD) of irradiation ( $k_{\text{eff}}$ ),

---

\*Corresponding author. E-mail: [carlo.parsi@enea.it](mailto:carlo.parsi@enea.it).

Calculation type	PC based Intel i7-3770 CPU 3.40 GHz 4 cores	CRESCO-2 based 512 processors
Core Criticality	13 hrs	N/A
Assembly-by-Assembly Power Distribution	16.6 days	21 hrs
Burnup (2050 EFPD)	~3 weeks	~39 hrs

Table 1: Calculation times.

- Effective Delayed Neutron Fraction ( $\beta_{\text{eff}}$ ),
- Reactivity Coefficients (mainly Sodium void and Doppler coefficients),
- Control Rods worth, or Control and Safety Device (CSD) and Direct Shut-down Device (DSD) worth;
- power distribution, assembly by assembly at different steps of the fuel cycle;
- variation of Heavy Metal masses during irradiation.

## 2 Tools and hardware

### 2.1 Neutronic tool: Monte Carlo code MCNPX

To obtain such results with an elevated level of accuracy, ENEA set up a detailed Monte Carlo model of the SFR, using Monte Carlo code MCNPX, developed at Los Alamos National Laboratory (USA), [2].

Choice of such tool was based on the following considerations:

- use of continuous-energy neutron cross section libraries for neutron transport (ENDF-B/VII.0, [3]) → no approximation in the energy domain;
- capability of modelling the reactor core including its components with high level of details (up to pin level for the nuclear fuel) → no significant code-imposed geometrical simplifications;
- capability to directly perform depletion calculations (CINDER [4] depletion module directly integrated into the MCNPX code);
- possibility to compile the code in a parallel computational infrastructure like CRESCO supercomputer.

## 2.2 CRESCO calculations

Particle transport codes based on Monte Carlo methods have the drawback of requiring simulation of hundreds of millions / sometime billions of particles histories in order to get a relatively small statistical error associated to the final result. Therefore, availability of an high performance computing (HPC) machine is required when dealing with Monte Carlo codes and complex problems like design of a nuclear reactor core.

Capabilities of performing parallel calculations using MCNPX are based on the exploitation of the MPI protocol. The used version of MCNPX (v. 2.7.0) did not allow the setting-up of multi-threading. The code was compiled on CRESCO-2 machine, using 64-bit Intel Fortran Compiler and OpenMPI libraries. Maximum resources allocated for a production calculation were 600 cores (902 threads) and 446.5 GB of memory. Speed-up of runs was relevant when comparing CRESCO performance with that of a modern 4-cores PC (see Table 1).

## 3 Modelling

The following figures give an idea of the level of details achieved in modelling the SFR using MCNPX. Fig. 1 shows the radial and axial views of the reactor while Fig. 2 shows details of the nuclear fuel, control devices and reflectors.

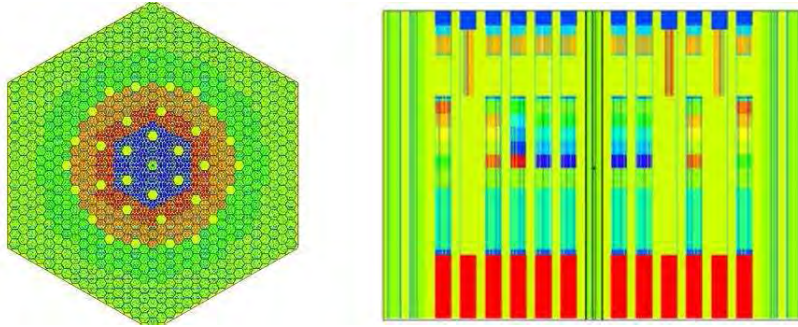


Figure 1: Core x-y view (left) and x-z view (right).

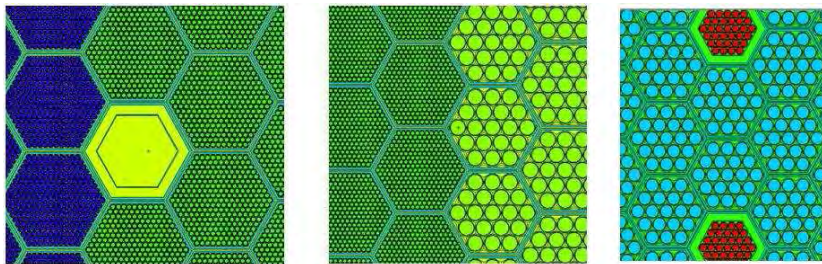


Figure 2: Core particulars: Inner/Outer core border (left), Outer core/Radial Reflector border (center) and DSD + Top Absorber (right).



## 4 Final results

Results allowed to track the evolution of neutronic parameters of an SFR core, fuelled with sphere-packed fuel. In Fig. 3, the core reactivity trend and the reactor MA masses as function of burnup and of the initial Americium concentrations are shown, as examples. In Fig. 4 core power distribution at Beginning of Life and at End of Cycle #5 are instead shown. Results demonstrated that sphere-packed fuel should not significantly affect neutronic parameters, while initial Americium concentration influences both safety parameters (sodium void, Doppler coefficient and delayed neutron fraction) and the amount of MA being burned during the fuel cycle. All these results obtained by the MCNPX – CRESCO calculations are being used by other project participants for initializing and performing dynamic safety analyses of the SFR. Ultimate goal will be quantification of safety margins of a Gen. IV SFR core loaded with innovative fuels.

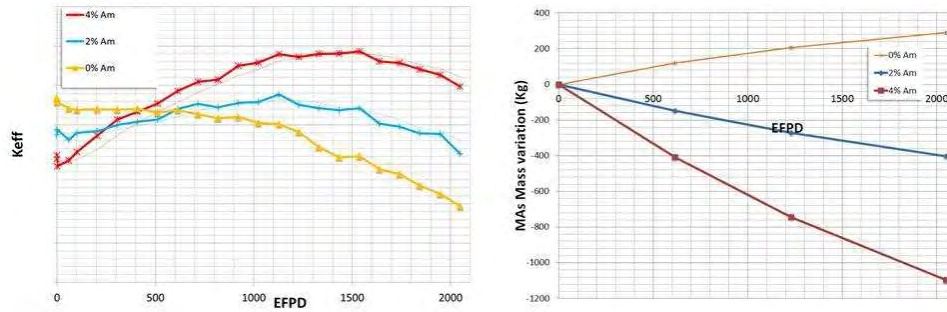


Figure 3: Core reactivity (left) and MA mass variation as function of fuel burnup and of Americium concentrations.

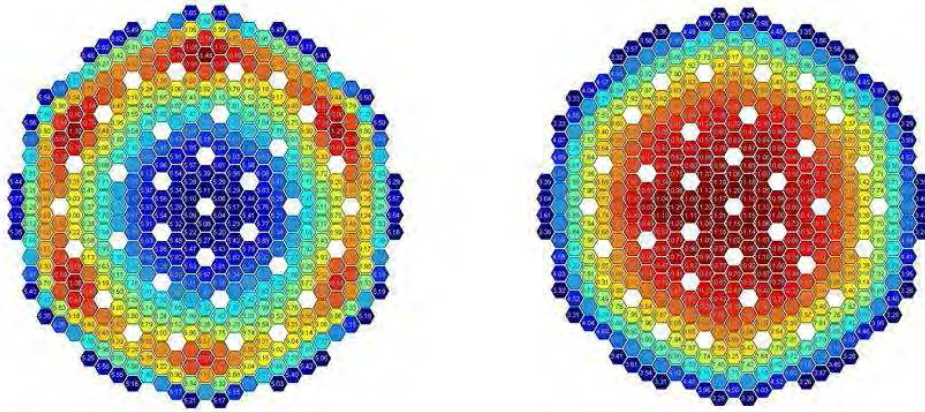


Figure 4: Assembly power distribution at Beginning of Life and at the End of Cycle #5 for SFR core + 4% Am content.

## References

- [1] EU-FP7. *PELGRIMM*—pellets versus granulates: Irradiation, manufacturing & modelling. *Grant Agreement Annex I* -, "Description of Work". Collaborative project No. 295664 FP7-Fission-2011.
- [2] Pelowitz D. B. et al. MCNPX<sup>tm</sup> users manual, version 2.7.0. *LA-CP-11-00438*, Los Alamos National Laboratory, USA, April 2011.
- [3] Chadwick M. B. et al. NDF/B-VII.0: Next generation evaluated nuclear data library for nuclear science and technology. , *Nuclear Data Sheets, Volume 107, Issue 12 pp. 2931-3060*. Archived at Brookhaven National Laboratory (<http://www.nndc.bnl.gov>), 2006.
- [4] Fensin M. L., Hendricks J. S., and Anchaie S. The enhancements and testing for the MCNPX 2.6.0 depletion capability. *Nuclear Technology, vol. 170*, 2010.



# Hydrogen diffusion in rutile TiO<sub>2</sub>

*Radojka Vujasin<sup>1</sup>, Jasmina Grbović Novaković<sup>1</sup>,  
Simone Giusepponi<sup>2</sup> and Nikola Novaković<sup>1\*</sup>*

<sup>1</sup>*VINČA Institute of Nuclear Sciences,  
POB 522, 11001 Belgrade, Serbia*

<sup>2</sup>*ENEA Casaccia Research Center, UTICT-HPC  
Via Anguillarese 301 – 00123 Rome, Italy*

**ABSTRACT.** The hydrogen interaction with the TiO<sub>2</sub> (110) surface has been investigated using pseudopotential and PAW methods with addition of GGA+U, as implemented in Abinit code. The hydrogen diffusion behaviour and thermodynamic properties were calculated by means of full relaxation of structure in every step of bulk diffusion. The results show the existence of potential barriers close to every atomic layer, the trends of barriers and overall system energy lowering away from surface. This goes in favour of previously experimental findings of TiO<sub>2</sub> low surface H coverage and easy diffusion of hydrogen into the TiO<sub>2</sub> bulk.

## 1 Introduction

TiO<sub>2</sub> attracts a lot of interest because of its non-toxicity and safe usage. This material is used as a white pigment and for optical coating [1], in environmental applications TiO<sub>2</sub> is used as a photocatalyst for air and water purification and as a self-cleaning surface [2] and for hydrogen production, using photochemical splitting of water [3]. Modified TiO<sub>2</sub> films could also be promising alternative for spin-based electronic devices [4]. Due to its electronic and optical properties, TiO<sub>2</sub> is known as a good catalyst [5, 6]. It was shown that addition of metal oxides cause improvement of kinetic properties of this material [6, 7, 8, 9, 10]. Several numerical studies on hydrogen motion through oxide surface has been done to understand the mechanism of the reaction [11, 12]. Yin *et al.* [13] have investigated hydrogen coverage on TiO<sub>2</sub> (110) surface under different experimental conditions of exposure to atomic hydrogen. They obtained that maximum H monolayer coverage on TiO<sub>2</sub> (110) surface is only 70% at room temperature, regardless of applied partial pressure of hydrogen. The same group confirmed that during heating of the hydrogenated sample, H atoms migrates *into* TiO<sub>2</sub> bulk. This is unusual behaviour, since desorption of H<sub>2</sub> (or H<sub>2</sub>O) molecules into the gas phase is common characteristic of hydroxylated oxide surface. The same results were obtained by Kowalski *et al.* [14]. Filippone *et al.* carried out research which showed that hydrogen behaves as a deep donor in rutile phase and

---

\*Corresponding author. E-mail: novnikc@vinca.rs.

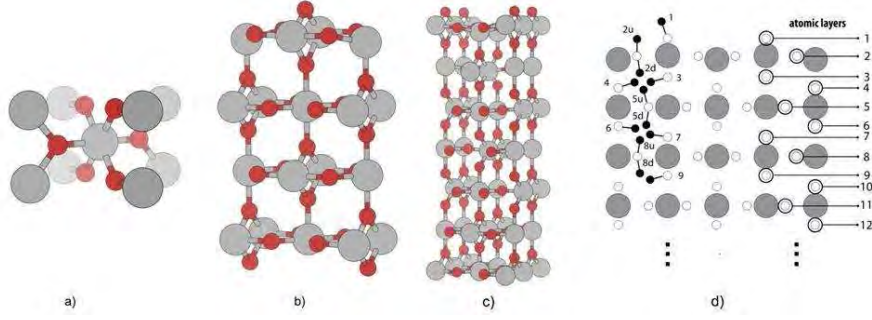


Figure 1: Rutile unit cell and slab supercells used in calculations.

forms an  $\text{OH}^+$  complex by interaction of H atom with oxygen vacancy, where H formed bond with a prevailing ionic character [15]. They have showed that electronic localization effects treatment have major influence on nature of bonding and charge distribution due to hydrogen incorporation. Also,  $\text{Ti}^{+3}$  species are formed as a result of localization of H and  $\text{OH}^+$  electronic levels on some Ti neighbours.

## 2 Details of calculations and results

Investigation of atomic hydrogen behaviour on rutile  $\text{TiO}_2$  (110) surface and in the near-surface region were done using Troullier–Martins norm-conserving pseudopotentials (PP) and projected augmented waves (PAW) methods available in Abinit code [16, 17, 18]. Additionally, GGA+U method was used for the treatment of localized states of Ti. Bulk calculations were performed to check the validity of chosen methods.

In case of pseudopotential calculations smaller (1x1)(110) cell with 12 atomic layers and 25 atoms (with hydrogen) was constructed, while in case of PAW calculations, larger (2x1)(110) slab supercell with 21 atomic layers with total of 85 atoms was used. The slab supercells are presented in Fig.1. The surface of the supercells was separated from its periodic image in direction perpendicular to the (110) surface by 15 Å of vacuum). The final cell parameters of supercells were  $a=2.9812$  Å,  $b=6.6124$  Å,  $c=27.5172$  Å and  $a=5.9779$ ,  $b=6.6124$  Å,  $c=37.0424$  Å, for smaller and larger cell, respectively. Three bottom layers were fixed to simulate the bulk. The rest of supercell atoms were subject to the relaxation of atomic positions.

The energy cut-off of the plane wave basis set was 816 eV in all cases. Only gamma  $k$  point was used in the whole Brillouin zone. All calculations were performed on ENEA–GRID facilities Crescof01 in Frascati and Cresco2 in Portici using 72 nodes. Abinit code was compiled on site using MPI wrapper for Intel Fortran compiler and MKL libraries.

H atoms are initially positioned at distances corresponding to short O–H bond (approximately 1 Å). Configurations corresponding to the same O–H bond are marked with additional letter index **u** and **d** for H “up” and “down” orientations, respectively. Some configurations after relaxation of forces are found to be degenerated, in a sense that H atoms, initially bound to one O atom, are found bounded after relaxation to the other O

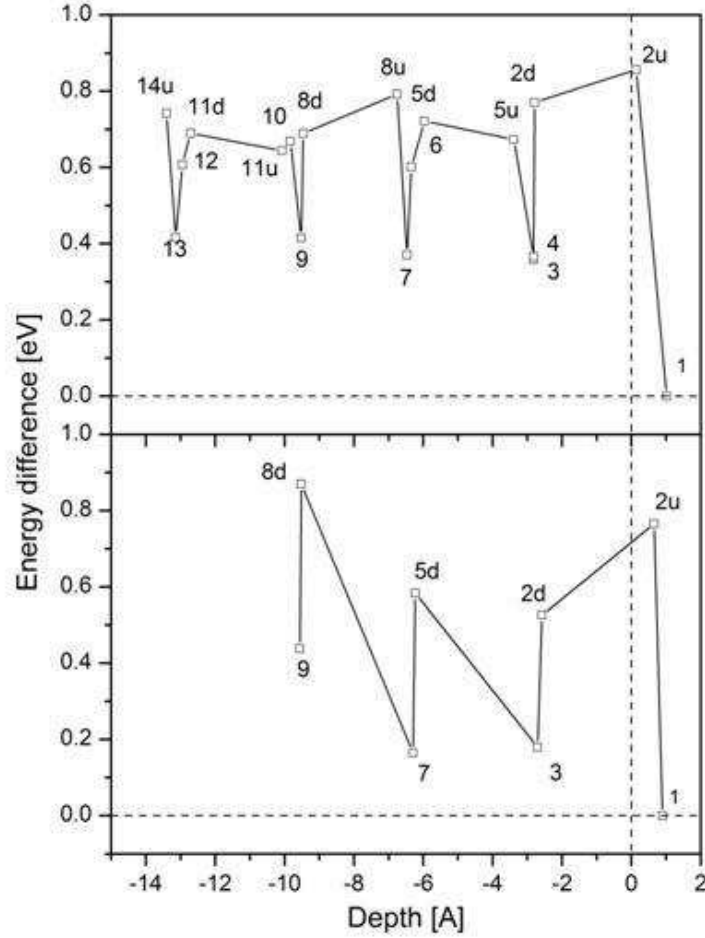


Figure 2: Slab system energy change as a function of hydrogen atom distance from the surface.

atom. The pairs of such configurations are **3** and **4**, **2d** and **5u**, **6** and **7**, **5d** and **8u** in (1x1)(110) case. In case of larger cell, similar situation occurred for configurations **3** and **4**, but the energy and H atom position difference were large enough for these configurations to be treated separately. Introduction of H atom cause severe distortion of surrounding atom sites, due to electrostatic interaction of bare H in formed OH group. On surface (configuration **1**) in PP calculation, H atom forms a bond with two-fold bonded O ( $O_{2s}$ ) atom, which deviates from initial surface normal position for more than  $75^\circ$ . This effect was not observed in case of PAW calculation for the same configuration. Hydrogen causes deviation and bending of neighbor O–Ti bonds in all other configurations. This is not that pronounced in case of PAW calculations.

Opposite non-bonding O atoms are always attracted to almost bare bonded H atom. Thus formed O–H–O sequence of atoms is almost collinear, with distances sum close to  $2.6 \text{ \AA}$ . The O–H distances for configuration **1** and **2u**, where the opposite O atoms are missing, are very close to distance found for OH group, known to be  $0.96 \text{ \AA}$ . For all remaining configurations this distance is considerably longer, (up to  $1.13 \text{ \AA}$  for configuration **5d**).

This is a consequence of attracting electrostatic interaction, mostly with opposite O atom. The absence of degeneration in case of larger supercell (PAW calculation) means that the effect is a consequence of high H concentration and H–H interaction. PAW results show that O–H bond varies less, ranging from 0.96 to 1.04 Å.

In Fig. 2, the energy differences as function of H distance from surface are given for both PAW (top) and PP (bottom) calculations. Energy differences were shown on x axis, with energy of configuration **1** used as reference, marked with horizontal line. As distance reference from surface, z-coordinate of O<sub>2s</sub> atom in slab supercell without H was used, marked as vertical short-dashed line. The characteristic periodic dependence of energy on hydrogen position depth is visible. The effect is more pronounced in case of PAW calculations, where degeneration of above mentioned opposite configurations was not observed.

In case of PP calculations the jump of H atom from O<sub>2s</sub> to O atom in second layer is followed by increase in energy of about 0.76 e. The next two steps, orientation switch from **2u** to **2d** position and jump to neighbor O atom in first basin below surface are energetically more preferable. In the first interlayer basin, **2d** and **3** are preferable over **5u** and **4**, respectively. Also, **5u**–**5d** orientation switch is not energetically favorable, but subsequent jump to **7** is. Energy increase in configurations **8d** and **9** can be attributed to vicinity of bottom surface and fixed three atomic layers playing the role of the bulk. Because of that, the relaxation in this region is not complete, the system is under residual stress, and consequently the electronic energy is higher. This is the reason why we have extended supercell along z-axis in PAW calculations. In case of PAW calculated values, configurations labeled with **u** and **d** indices are energetically less favorable than configurations where hydrogen is bounded to one of two O atoms within given cavity. **1**–**2u** transition is accompanied with change of energy similar to PP value (approximately 0.8 eV). All further changes whenever H jump to or from O positioned in densely populated layer are smaller, ranging from 0.1 to 0.4 eV. The periodicity of energy is established already in 3-rd and 4-th atomic layer, meaning that influence of surface is contained to few layers closest to the vacuum.

## Acknowledgements

We acknowledge the ENEA–HPC team for supporting our computational activities on the ENEA–GRID infrastructure. This work was supported the Ministry of Education, Science and Technological Development of the Republic of Serbia under the Grant III 45003. The authors express their gratitude to COST Action MP1103 *Nanostructured Materials for Solid State Hydrogen Storage*.

## References

- [1] Diebold U. The surface science of titanium dioxide. *Surf. Sci. Rep.* 48, pages 53–229, 2003.

- [2] Fujishima A., Rao T. N., and Tryk D. A. Titanium dioxide photocatalysis. *J. Photochem Photobiol C: Photochem Rev*, pages 1–21, 2000.
- [3] Fujishima A. and Honda K. Electrochemical photolysis of water at a semiconductor electrode. *Nature* 238, pages 37–38, 1972.
- [4] Matsumoto Y., Murakami M., Shono T., Hasegawa T., Fukumura T., Kawasaki M., Ahmet P., Chikyow T., Koshihara S., and Koinuma H. Room-temperature ferromagnetism in transparent transition metal-doped titanium dioxide. *Science* 291, pages 854–856, 2001.
- [5] Henderson M. A. A surface science perspective on  $\text{TiO}_2$  photocatalysis. *Surf. Sci. Rep.* 66, pages 185–297, 2011.
- [6] Croston D. L., Grant D. M., and Walker G. S. The catalytic effect of titanium oxide based additives on the dehydrogenation and hydrogenation of milled  $\text{MgH}_2$ . *J. Alloys Compd.* 492, pages 251–258, 2010.
- [7] Oelerich W. and Klassen T. and Bormann R. Metal oxides as catalysts for improved hydrogen sorption in nanocrystalline Mg-based materials. *J. Alloys Compd.* 315, pages 237–242, 2001.
- [8] Polanski M. and Bystrzycki J. Comparative studies of the influence of different nano-sized metal oxides on the hydrogen sorption properties of magnesium hydride. *J. Alloys Compd.* 486, pages 697–701, 2009.
- [9] Hirate H., Morinaga M., Yukawa H., and Nakai H. Atomization energy approach to the quantitative evaluation of catalytic activities of metal oxides during dehydrogenation of  $\text{MgH}_2$ . *J. Alloys Compd.* 509S, pages S612–5, 2011.
- [10] Jung K. S., Kim D. H., Lee E. Y., and Lee K. S. Hydrogen sorption of magnesium hydride doped with nano-sized  $\text{TiO}_2$ . *Catal. Today* 120, pages 270–275, 2007.
- [11] Leconte J., Markovits A., Skall M. K., Minot C., and Belmajdoub A. Periodic ab initio study of the hydrogenated rutile  $\text{TiO}_2$  (110) surface. *Surf. Sci.* 497, pages 194–204, 2002.
- [12] Chen H. T., Choi M., Liu M., and Lin M. C. A theoretical study of surface reduction mechanisms of  $\text{CeO}_2$  (111) and (110) by  $\text{H}_2$ . *Chem. Phys. Chem.*, pages 849–855, 2007.
- [13] Yin X. L., Calatayud M., Qiu H., Wang Y., Birkner A., Minot C., and Wöll Ch. Diffusion versus desorption: complex behavior of h atoms on an oxide surface. *Chem. Phys. Chem.* 9, pages 253–256, 2008.
- [14] Kowalski P. M., Meyer B., and Marx D. Composition, structure, and stability of the rutile  $\text{TiO}_2$  (110) surface: Oxygen depletion, hydroxylation, hydrogen migration, and water adsorption. *Phys. Rev. B* 79:115410, 2009.
- [15] Filippone F., Mattioli G., Alippi P., and Amore Bonapasta A. Properties of hydrogen and hydrogen-vacancy complexes in the rutile phase of titanium dioxide. *Phys. Rev. B* 80, page 245203, 2009.

- [16] Bottin F., Leroux S., Knyazev A., and Zerah G. Large scale ab initio calculations based on three levels of parallelization. *Comput. Mat. Science* 42, pages 329–336, 2008.
- [17] Gonze X., Amadon B., Anglade P. M., Beuken J. M., Bottin F., Boulanger P., Bruneval F., Caliste D., Caracas R., Cote M., Deutsch T., Genovese L., Ghosez Ph., Giantomassi M., Goedecker S., Hamann D. R., Hermet P., Jollet F., Jomard G., Leroux S., Mancini M., Mazevet S., Oliveira M. J. T., Onida G., Pouillon Y., Rangel T., Rignanese G. M., Sangalli D., Shaltaf R., Torrent M., Verstraete M. J., Zerah G., and Zwanziger J. W. Abinit: First-principles approach of materials and nanosystem properties. *Comput. Phys. Commun.* 180, pages 2582–2615, 2009.
- [18] Gonze X., Rignanese G. M., Verstraete M., Beuken J. M., Pouillon Y., Caracas R., Jollet F., Torrent M., Zerah G., Mikami M., Ghosez Ph., Veithen M., Raty J. Y., Olevano V., Bruneval F., Reining L., Godby R., Onida G., Hamann D. R., and Allan D. C. A brief introduction to the abinit software package. *Z. Kristallogr.* 220, pages 558–562, 2005.

# CeO<sub>2</sub> electronic properties from first principles: an introductory study

*F. Rizzo\*, G. de Marzi, L. Morici*

*ENEA, UTFUS-COND C.R. Frascati  
Via E. Fermi 45, 00044, Frascati (Rm), Italy*

**ABSTRACT.** The electronic structure of bulk cerium oxide  $CeO_2$  has been investigated using Density Functional Theory (DFT) calculations. The bands structure and the corresponding Density Of States (DOS) have been calculated along high-symmetry paths. In order to properly take into account the strongly correlated character of cerium 4f electronic states, we adopted the DFT+U method with a value of  $U = 4.5eV$  for the on-site Coulomb repulsion and exchange energy; our results have been compared with the bare structure calculations and the literature outcomes. Finally, the implementation of a 96-atoms supercell description of the bulk cerium oxide has been started. This supercell structure will allow the study of both reduced ( $CeO_{2-\delta}$ ) and zirconium doped ( $Ce_{1-x}Zr_xO_2$ ) ceria structures.

## 1 Introduction

Recently, the study of structural and electronic properties of cerium oxides ( $CeO_2$  and  $Ce_2O_3$ ) has attracted a huge interest. In fact, the technological interest in catalysis processes due to the remarkable ceria oxygen storage capacity has motivated several theoretical and computational works [1] - [3].

On the other hand,  $CeO_2$  epitaxial thin films are widely used as seed layers for  $YBCO$  ( $YBa_2Cu_3O_{7+x}$ ) films in the realization of high quality coated conductors [4] - [6]. Starting from a metallic substrate, a (00l)-oriented  $CeO_2$  layer is usually grown by physical (pulsed laser deposition) or chemical methods (metal-organic deposition) on the top of a complex architecture in order to ensure a high quality (00l) growth of a superconductor  $YBCO$  layer. In fact, due to the high chemical compatibility between ceria and  $YBCO$  and to the low value for the mismatch between their lattice parameter,  $CeO_2$  is widely recognized as one of the most suitable  $YBCO$  seed layer.

In this perspective, it is particularly important to study the behaviour of the structural and electronics properties of the  $CeO_{2-\delta}$  compound as a function of its oxygen content,  $\delta$ . In fact, the presence of significant stress in the structure may lead to the formation of cracks during the cerium oxide deposition process, thus resulting in a pronounced worsening of the whole coated conductor performances. Also the effect of doping, such as in the case of  $Ce_{1-x}Zr_xO_2$  compounds [7], may substantially affect the structure stability.

---

\*Corresponding author. E-mail: [francesco.rizzo@enea.it](mailto:francesco.rizzo@enea.it).

In this work first-principles calculations based on Density Functional Theory (DFT) are employed for a preliminary study of the properties of stoichiometric bulk  $CeO_2$ . A Hubbard repulsion term with energy value  $U = 4.5eV$  is added to the self-consistent hamiltonian calculation in order to properly take into account the strongly localized character of  $4f - Ce$  electronic states [10]. After preliminary convergence studies, which allow to determine the optimized value for the lattice parameter, the electronic properties of the structure are evaluated and compared with data available in literature. In particular, both the calculated energy bands and the electronic Density Of States (DOS) exhibit a good agreement with previously published works. In order to study the variation of the structural and electronic properties in both a reduced  $CeO_{2-\delta}$  and doped  $Ce_{1-x}Zr_xO_2$  cases, a supercell description is needed. Therefore, a 2X2X2 representation is implemented.

## 2 Computational resources

The computations were performed using the ENEA-CRESCO computational structure. The electronic and structural characteristics of  $CeO_2$  have been calculated by means of the Kohn-Sham density functional theory representation. This representation, being the only affordable for ab-initio computations on complex quantum systems, is inherently heavy in terms of resource usage; furthermore, the computational load is strongly dependent on the material's complexity. The intrinsic cell symmetries can significantly reduce the computation complexity, but they can rarely be applied to conventional systems, with the exception of few elementary case studies. The system of our interest, namely the  $CeO_2$ , benefited of the material cell symmetry for computational savings. We submitted our jobs both to the CRESCO-Portici parallel queues and to the CRESCO-Frascati system. A disk quota of 1 TB was attributed to our account in order to carry out our simulations, and the standard ab-initio Quantum-Espresso-4.3.2 open source code has been installed and used. The Quantum espresso code may be freely downloaded from <http://www.quantum-espresso.org/> as source code. It can be installed by way of CRESCO fortran 95 outfit compiler, takes speed advantages from BLAS, LAPACK and FFT installed libraries and MPI parallelization.

## 3 Methodology

$CeO_2$  exhibits a  $Fm3m$  fluorite lattice structure.  $Ce$  atoms are placed in a face centered cubic lattice and  $O$  atoms occupy tetrahedral lattice sites, as shown in Fig. 1.

The experimental value for the equilibrium lattice parameter is  $a_{exp} = 5.411\text{\AA}$ . Our self-consistent first-principles calculations have been performed using the open source Quantum Espresso suite [8]. DFT calculations have been done in the framework of the generalized gradient approximation (GGA) for the electron exchange and correlation terms, using the Perdew-Burke-Ernzerhof functionals (PBE) [9]. In addition, in order to correctly take into account the localized character of the  $4f - Ce$  electrons DFT+U calculations have been performed. The Hubbard energy term has been set to the value  $U = 4.5\text{ eV}$ , according to Fabris *et al.* [10].



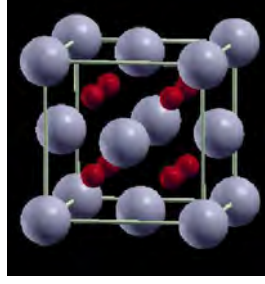


Figure 1:  $CeO_2$  crystal structure. Ce atoms are placed in a fcc-like structure, whereas O atoms are represented by small red spheres.

After a preliminary convergence study, the cut-off energy for the plane waves expansion of Kohn-Sham orbitals has been set to the value of 40 Ry. Similarly, the final Brillouin zone (BZ) sampling has been achieved through a 6X6X6 Monkhorst-Pack (MP) grid. For the study of oxygen defective and/or doped bulk ceria, a 96-atoms 2X2X2 supercell description has been adopted. In this case a 2X2X2 MP k-point sampling scheme has been used.

## 4 Results

The equilibrium properties of face-centered cubic  $Fm - 3m$  fluorite-like bulk  $CeO_2$  have been firstly investigated. In Fig. 2 the cell total energy behaviour as a function of the lattice parameter  $a$  is shown. Energy values have been fitted considering a II order Birch's equation of state [11] in order to obtain the equilibrium optimized value for the lattice parameter  $a_{th} = 5.518 \text{ \AA}$  corresponding to the energy minimum. The relative difference between  $a_{exp}$  and  $a_{th}$  is less than  $\Delta = 2 \%$  suggesting that this DFT analysis carefully describes the bulk  $CeO_2$  structural properties.  $\Delta$  magnitude is partially due to the value chosen for the Hubbard term  $U$ . In fact, it has been verified that a  $U$  lower value would give a better agreement between  $a_{exp}$  and  $a_{th}$ . However, the value  $U = 4.5 \text{ eV}$  suggested by previous first-principles calculations [10] and which allows a better matching between experimental and calculated electronic properties has been finally adopted. Also, it is worth to point it out that the calculated bulk modulus  $B_0 = 1.76 \text{ Gbar}$  is in good agreement with previous analysis.

The electronic properties have been investigated by calculating the band structure along a path  $\lambda$  crossing several high symmetry points of the Brillouin zone, as depicted in Fig. 3.

Fig. 3 compares the electronic dispersions calculated by considering the Hubbard repulsive energy term (red), associated with  $Ce$  atoms, with energy bands evaluated without taking into account for it (blue). The corresponding DOSs are also shown. Valence bands below the Fermi level ( $E_F = 11.26 \text{ eV}$  and set to zero in the graph) are slightly affected by the presence of the  $U$  term. On the other hand, the Hubbard term plays a significant role for the energy bands placed above  $E_F$ : a group of bands located around  $E = 2 \text{ eV}$  shrinks with respect to the  $U = 0$  case; in addition, all the bands at higher energy undergo a red-shift towards lower values. An indirect energy gap  $\Delta E \sim 2.1 \text{ eV}$  opens between the

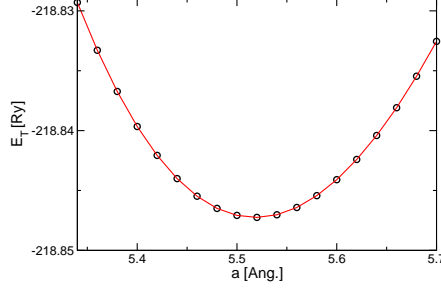


Figure 2: Cell energy (black circles) behaviour as function of the lattice parameter. Energy values have been fitted using a II order approximation of the Birch's equation of state (red line).

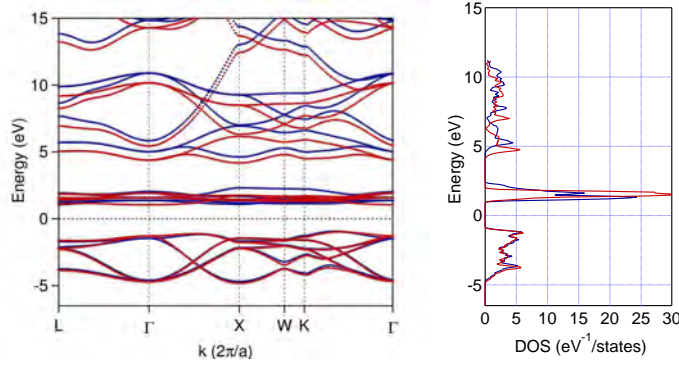


Figure 3:  $CeO_2$  energy bands along the high-symmetry  $k$ -space path  $\lambda : L \rightarrow \Gamma \rightarrow X \rightarrow W \rightarrow K \rightarrow \Gamma$ .

valence and the conduction electronic bands, and the overall behaviour of the electronic states is in a very good agreement with recent results [12].

The effect of the Hubbard term is clearly evident in the density of state. The magnitude of the peak above the Fermi level increases. In order to understand the role of the strongly correlated  $Ce$  electronic states it is useful to consider the total DOS projected over the different atomic orbitals, as shown in Fig. 4.

The intense peak above  $E_F$  is almost completely due to the  $4f - Ce$  electronic states. Fig. 4 reveals the nature  $2p - O-4f - Ce$  of the indirect energy gap. Furthermore, a second gap  $\Delta E_1 \sim 5$  eV between  $2p - O-4f - Ce$  is observed, in agreement with analogous studies [13].

Finally, in order to study reduced systems and  $Zr$  doped bulk ceria, the 96-atoms  $CeO_2$  supercell shown in Fig. 5 has been built starting from the conventional cubic unit cell.

Such supercell-based approach is essential for an accurate study of the doping-dependence of both the structural and the electronic properties of  $CeO_2$  systems. A  $2X2X2$   $CeO_2$  supercell contains 32  $Ce$  atoms, thus allowing to explore small doping levels (such as  $x \sim (3\%, 6\%, 9\%)$ ) usually found in experimental  $Ce_{1-x}Zr_xO_2$  compounds. However, the increased cell complexity obviously results on a greater demand of computational resources and time-consuming calculations. Preliminary results obtained for the  $CeO_2$  supercell electronic structure show full agreement with the standard 12-atoms cell description.

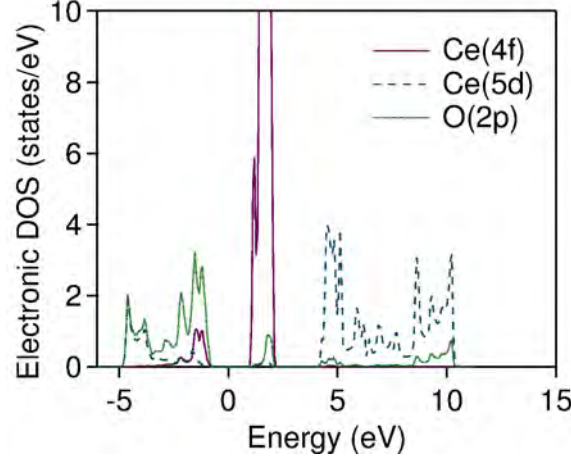


Figure 4: Partial density odd states pDOS for  $4f - Ce$  (purple line),  $5d - Ce$  (blue dashes) and  $2p - O$  (green dots) states.

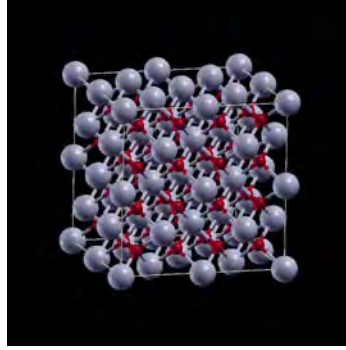


Figure 5: 96-atoms  $CeO_2$  supercell representation.

## 5 Conclusions and future work

A comprehensive first-principle study of bulk  $CeO_2$  has been carried out to determine both the structural and electronic properties of this fluorite-like oxide. GGA+U calculation strategy has been adopted, with a Coulomb energy value of  $U = 4.5$  eV, which allows to reproduce with a good accuracy the experimental data and theoretical studies already published in literature. The recent introduction of a 96-atoms supercell description will allow to study of the structure stability and the electronic properties of both oxygen defective and  $Zr$  doped ceria structures.

## References

- [1] Skorodumova N. V., Ahuja R., Simak S. I., Abrikosov I. A., Johansson B., and Lundqvist B. V., Phys. Rev. B. 64, 115108 (2001).

- [2] Desaunay T., Ringuede A., Cassir M., Labat F., Adamo C., Surf. Sci. 606 (2012) 305.
- [3] Da Silva J. L. F., Ganduglia-Pirovano M. V., and Suaer J., Phys. Rev. B. 75, 045121 (2007).
- [4] Boikov Yu. A., Claeson T., and Ertz D., Phys. Rev. B. 56, 11312 (1997).
- [5] van Wijck M. A. A. M., Verhoeven M. A. J., Reuvekamp E. M. C. M., Gerritsma G. J., Blank D. H. A., and Rogalla H., Appl. Phys. Lett. 68, 553 (1996).
- [6] Varesi E., Celentano G., Petrisor T., Boffa V., Ciontea L., Galluzzi V., Gambardella U., Mancini A., Rufoloni A., and Vannozzi A., Supercond. Sci. Technol. 16, 498 (2003).
- [7] Yang Z., Woo T. K., and Hermansson K., J. Chem. Phys. 124, 224704 (2006).
- [8] Giannozzi P., Baroni S., Bonini N., Calandra M., Car R., Cavazzoni C., Ceresoli D., Chiarotti G. L., Cococcioni M., Dabo I., Dal Corso A., de Gironcoli S., Fabris S., Fratesi G., Gebauer R., Gerstmann U., Gougoussis C., Kokalj A., Lazzeri M., Martin-Samos L., Marzari N., Mauri F., Mazzarello R., Paolini S., Pasquarello A., Paulatto L., Sbraccia C., Scandolo S., Sclauzero G., Seitsonen A. P., Smogunov A., Umari P., and Wentzcovitch R. M., Journal of Physics: Condensed Matter 39, 395502 (2009).
- [9] Perdew J. P., Burke K., and Ernzerhof M., Phys. Rev. Lett. 77, 3865 (1996).
- [10] Fabris S., de Gironcoli S., Baroni S., Vicario G., and Balducci G., Phys. Rev. B. 72, 237102/1 (2005).
- [11] Birch F., Phys. Rev., 71, 809 (1947).
- [12] Sevik C., and Cagin T., Phys. Rev. B, 80, 014108 (2009).
- [13] Loschen C., Carrasco J., Neyman K. M., and Illas F., Phys. Rev. B, 75, 035115 (2007).

# Magneto-Thermo-Structural optimization of the Large-Bore 8T Superconducting Magnet for the Nafassy Test Facility

*Giordano Tomassetti<sup>1\*</sup>, Michele Perrella<sup>2</sup>, Alessandro Anemona<sup>3</sup>,  
Valentina Corato<sup>1</sup>, Antonio della Corte<sup>1</sup>*

<sup>1</sup>*ENEA-UTFUS-COND*

*Via Enrico Fermi 45, 00044, Frascati (RM), Italy*

<sup>2</sup>*University of Salerno, Dipartimento di Fisica*

*Via Ponte don Melillo, 84084, Fisciano (SA), Italy*

<sup>3</sup>*Italian Consortium for Applied Superconductivity*

*Via Enrico Fermi 45, 00044, Frascati (RM), Italy*

**ABSTRACT.** The "NAFASSY" (NAtional FAcility for Superconducting SYstems) facility is designed to test wound conductor samples under high field conditions at variable temperature. Due to its unique features, it's reasonable to figure out that in the near future NAFASSY will have a preeminent role at international level in the qualification of long coiled cables in operative conditions. The magnetic system consists of a large warm bore background solenoid, made up of three series connected grading sections obtained by winding three different Nb3Sn Cable in Conduit Conductors. Thanks to the financial support of the Italian Ministry for University and Research the low-field coil is currently under production. The design has been properly modified to allow the system to operate also as a stand-alone facility, with an inner bore diameter of 1144 mm. This magnet is able to provide about 7 T on its axis and about 8 T close to the insert inner radius, giving the possibility to perform test relevant for large size NbTi or medium-field Nb3Sn conductors. The magneto-thermo-structural optimization of the 8T magnet is here reported.

## 1 Introduction

The NAFASSY test facility is designed to test long superconducting samples at variable temperature, ranging from 4.2 K to 10 K, in presence of a transversal magnetic field. The facility is going to be built at the University of Salerno, in the Southern Italy, thanks to the financial support of the Italian Ministry for University and Research (MIUR) under the National Operative Projects call. Although the original project [1] included a large bore 15 T background solenoid made up of three series connected grading sections, obtained by winding three different Nb3Sn Cable in Conduit Conductors (CICCs), only the outer

---

\*Corresponding author. E-mail: [giordano.tomassetti@enea.it](mailto:giordano.tomassetti@enea.it).

solenoid is currently under production. As a stand-alone facility, the NAFASSY magnet is able to provide about 7 T on its axis and about 8 T close to the insert inner radius (572 mm), giving the possibility to perform test relevant for large size NbTi or medium-field Nb3Sn conductors, as well as small magnets. The large bore allows to coil cables with a diameter up to 60 mm without damaging them. In addition, the warm bore gives the opportunity to change the sample without warming up the background solenoid.

## 2 The NAFASSY facility

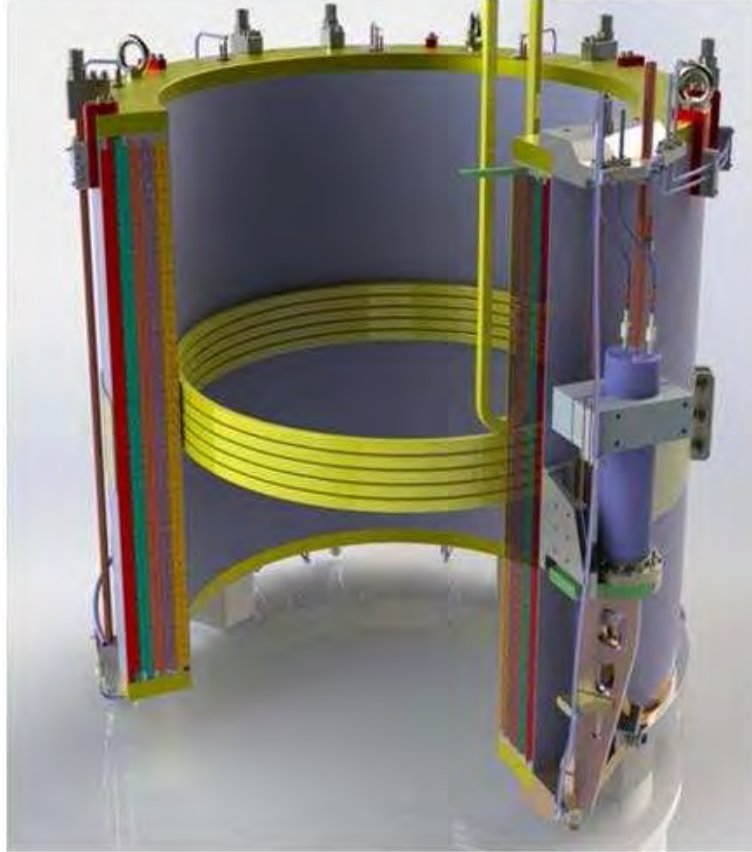


Figure 1: Artist view of the NAFASSY magnet, with a long coiled sample inside.

The core of the NAFASSY facility is a large warm bore superconducting solenoid, obtained by winding a rectangular Cable-In-Conduit Conductor (CICC). The conductor will be cooled by forced flow supercritical He at  $T_{inlet} = 4.5$  K and fed by a current  $I_{op} = 20$  kA through HTS current leads. In these operating conditions the coil provides up to 8 T of background (BG) magnetic field. The system is optimized in order to test long coiled samples in orthogonal field, as shown in Fig. 1. Samples will be allocated into a thermally de-coupled cryostat to allow their insertion/extraction without warming up the BG coil, with significant saving of time and money while operating the facility. In the present configuration the sample can be fed with a maximum current of 50 kA at 12 V, even if the

power supply allows to provide up to 100 kA at 6 V for testing coils with higher critical current,  $I_c$ . Finally, the sample is cooled through a secondary refrigerating line whose temperature can be varied by heating the forced flowing helium from 4.5 K to 10 K, to evaluate the sample current sharing temperature,  $T_{cs}$ .

### 3 Magneto-thermo-structural optimization

The A finite element (FE) model of the magnet has been developed in ANSYS to simulate the magneto-thermo-structural response under operating conditions [2]. The FE model takes advantage of the axial symmetry of the magnet allowing a 2D modelling with the use of PLANE13 and INFIN110 elements for the magnetic analysis and PLANE42 elements for the thermo-structural analysis using the axial symmetric option. The total number of FE exceeded one million elements. The capability of the FE code to perform the coupled magnetic and thermo-structural analyses has allowed the use of the same mesh, making easier the application of the Lorentz forces, resulting from the magnetic analysis as structural loads in the thermo-mechanical model. Under the assumptions introduced to implement the mentioned FE model, the structure has shown to be over-dimensioned in terms of the 316LN Stainless Steel (SS) jacket thickness. In particular, FE analyses have demonstrated stress conditions far below critical values. Using the Von Mises yield criterion, the maximum stress induced in the 316LN SS jacket was about 500 MPa. Yield stress for 316LN is about 900 MPa at 4.2 K. Using a safety factor of 1.5, this leads to a possible maximum safe operating stress of 600 MPa which is yet far from the induced stress (501 MPa) with a 2.5 mm jacket thickness, as foreseen in the original design [1]. In order to reduce the use of expensive SS material, a numerical optimization process has been implemented with the aim of minimizing the total amount of SS used for the jacket while ensuring structural integrity under operating conditions. From a mathematical point of view, the optimization process is stated as below:

$$\begin{aligned} \min \quad & \text{Weight}_{jacket}(\text{th}_{jacket}) \\ \text{with } \left\{ \begin{array}{l} \sigma_{VM,jacket} \leq \sigma_{max,s.s.} \\ \tau_{insulation} \leq \tau_{max,insul.} \end{array} \right. \end{aligned}$$

The weight of the SS jacket is minimized as a function of the jacket thickness  $\text{th}_{jacket}$  with constraints on the induced Von Mises stress in the jacket ( $\sigma_{VM,jacket}$ ) to be below the  $\sigma_{max,s.s.} = 600$  MPa and the induced shear stresses into the insulation layer ( $\tau_{insulation}$ ) to be below the maximum allowable for the specific material ( $\tau_{max,insul.} = 50$ MPa). As posed, the optimization process is solved using an evolutionary algorithm named Minimized Computational Effort Particle Swarm Optimization (MCEPSO), specifically developed to minimize the computational effort of the optimization itself [3]. As a result of the optimization process (Table 1), a solution was found corresponding to a reduction of the SS jacket thickness from the initially proposed value of 2.5 mm to a value of 2.1 mm,

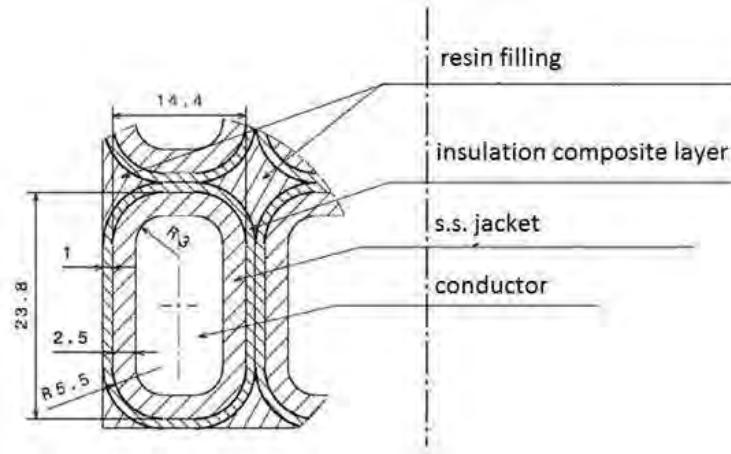


Figure 2: Schematic of the design variables used in the optimization with the original shape.

achieving a jacket overall weight reduction of 17%, from 2289 kg (original configuration) to 1890 kg (optimized configuration). The maximum magnetic field varies slightly from 7.74 T to 7.85 T in the optimized configuration, with a negligible +1.4%. At the same time the induced shear stress in the insulation layer of the optimized configuration is 24.9 MPa (Fig. 3), well below the limit of  $\tau_{max,insul.} = 50$  MPa, and the the computed maximum Von Mises stress amounts to 599 MPa (Fig. 4).

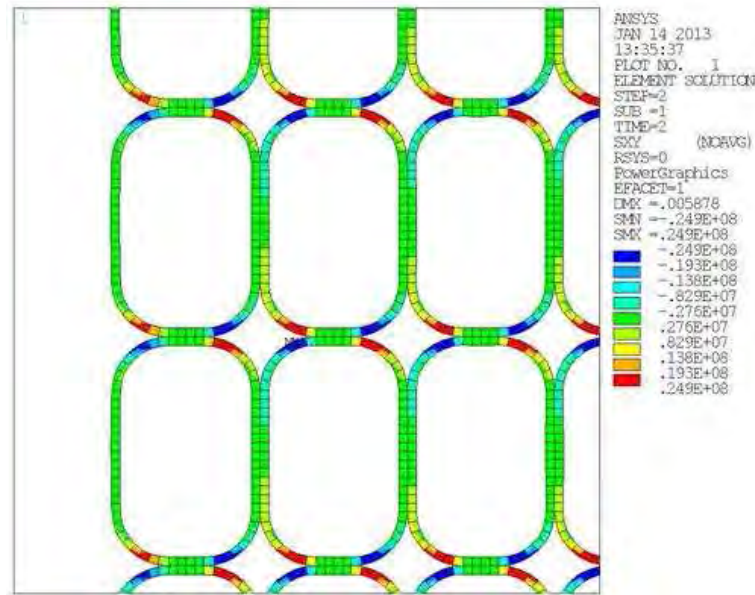


Figure 3: Insulation layer induced maximum shear stress area.



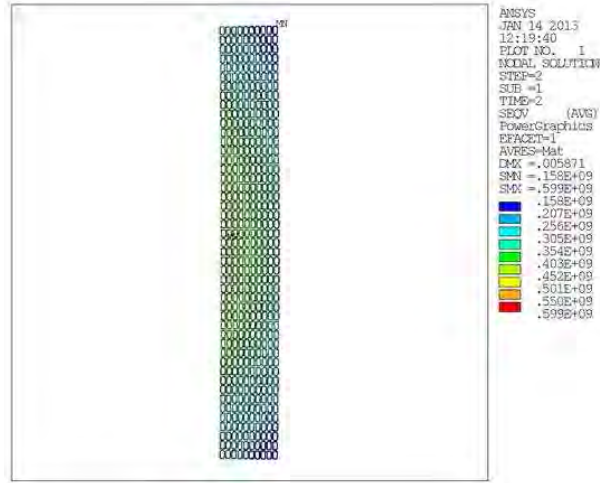


Figure 4: SS jacket induced von Mises stress.

	Original configuration	Optimized configuration
S.S. Jacket thickness [mm]	2.5	2.1
Jacket overall weight [Kg]	2289	1890
Max Magnetic field [T]	774	7.85
Max Von Mises Stress in S.S. jacket [MPa]	501	599
Max Shear Stress in insulation layer [MPa]	34.2	24.9

Table 1: Comparison between the original and optimized configurations.

## 4 Conclusions

The NAFASSY facility is designed to be the unique in Europe allowing the qualification of long coiled cables in medium field at variable temperature. Presently the superconducting conductor has been manufactured and the 8 T magnet is under construction. The completion of the facility, including the new building, the refrigerator and the two power suppliers, is foreseen during 2015. After commissioning, NAFASSY facility will be available for superconducting tests. Thanks to the present study, a 17% weight reduction of SS needed for the jacket structure was achieved.

## References

- [1] Della Corte A. et al. Enfasi: Conceptual design of a 15 t large bore superconducting test facility. *IEEE Transactions on Applied Superconductivity*, (19):1548–1551, 2009.
- [2] Cricrì G. and Perrella M. Valutazione dello stato tensionale nello strato isolante di un magnete superconduttore. Proceedings of National Conference 42° AIAS, 11-14 September, Salerno, Italy.
- [3] Tomassetti G. and Cagnina L. Particle swarm algorithms to solve engineering problems: A comparison of performance. *Journal of Engineering*, 2013.

Edito dall'ENEA  
Unità Centrale Relazioni – Servizio Comunicazione  
Lungotevere Thaon di Revel, 76 – 00196 Roma  
*[www.enea.it](http://www.enea.it)*

Stampa: Laboratorio tecnografico – Centro Ricerche ENEA Frascati  
Gennaio 2015

